ABSTRACT

Title of Dissertation: PLATE AND MICRO-SCALE STRUCTURES: ANALYSIS AND EXPERIMENTS

Mary Elizabeth Vechery

Directed By: Dr. B. Balachandran, Professor and Associate Chair of Mechanical Engineering

Within this work, plate and micro-scale structures are studied. Methodologies are developed to analyze the laminate stiffness, residual forces, moments and stresses, and deformations in these thin composite laminate structures to facilitate better designs, enable device characterization, and enhance device performance. Specific devices studied in this work are cantilevered and clamped-clamped PZT resonators of various lengths, widths, and laminate thicknesses. In order to better understand the behavior of these devices, analytical and experimental methods have been developed. The analytical methods are based on linear and nonlinear beam and plate models, with reduced-order models developed to study dynamic behavior. Parameter identification techniques have been applied to characterize residual stress induced deformation of micro-scale structures. Extensive data has been collected through careful experiments to aid the development of identification techniques and to determine device deflections and individual device residual stress values.

An analytical model has been developed to describe the behavior of thin composite laminate plate-like structures. Since an exact solution for plate mode shapes does not exist for all boundary conditions, appropriate combinations of orthogonal functions are assumed for the mode shapes of a plate with all edges simply supported or all edges clamped. These functions make the development of reduced-order models possible for these boundary conditions. In addition, these plate-like structures are asymmetric isotropic laminates. A procedure was applied to calculate the stiffness, forces and moments for a laminate comprised of multiple isotropic layers regardless of symmetry. Parametric identification techniques were developed to identify system parameters and to characterize residual stress induced deformation in plate and micro-scale structures. These techniques are based on linear and nonlinear beam models and reduced-order methodologies, and they enable the first characterization of residual stress in PZT micro scale devices post-fabrication and release processing. The obtained results indicate that post-release residual stress measurements in devices can be considerably different from the corresponding measurements made before release.

PLATE AND MICRO-SCALE STRUCTURES: ANALYSIS AND EXPERIMENTS

By

Mary Elizabeth Vechery

Dissertation submitted to the Faculty of the Graduate School of the
University of Maryland, College Park, in partial fulfillment
of the requirements for the degree of
Doctor of Philosophy
2008

Advisory Committee:
Professor B. Balachandran, Chair
Professor A. Baz
Professor A. Dasgupta
Assistant Professor M. Yu
Professor S. Lee (Dean's Representative)

© Copyright by
Mary Elizabeth Vechery
2008

Dedication

This dissertation is dedicated to my friends and family who supported me all these years in accomplishing my goal of a PhD in Mechanical Engineering. I very much consider my friends my family and every one of my friends has played an important part in assisting me in reaching my educational goals. Especially, I dedicate this dissertation to my twin sister Martha, my brother Jim, my Indian brothers Rohit and Rocky, my brother-in-law Jeff, my sister-in-law Anita, my father John, my grandfather Al, my grandmother Eileen, my grandfather Neale, and most of all my mother, Terri, who's undying support was and is my rock. Thank-you everyone for your support for this was very much a group family effort.

Acknowledgements

First, I would like to thank Professor Balachandran for the opportunity to pursue my PhD in Mechanical Engineering at the University of Maryland. I want to thank him for his friendship, guidance, mentorship and extreme patience me as I have pursued and completed my education. In addition, I would like to thank my dissertation committee, Professor Baz, Professor Dasgupta, Assistant Professor Yu and Professor Lee for there guidance and support throughout this process. I would also to thank Professor Baz for giving me the opportunity to start my PhD in this department, conduct research under him, and friendship and mentorship as well. I would like to thank my research group as well, especially Andrew Dick for his friendship, support and assistance with my research. In addition, I would also like to thank my group at the Army Research Laboratory. Specifically, Madan Dubey, Paul Amirtharaj, and John Costanza for the opportunity to work, learn, and conduct research at the Lab, my group mates Jeff Pulskamp, Luke Currano, Ron Polcawich and Brett Piekarski for all their assistance in teaching about design and fabrication of MEMS devices, John, Ritchie, Chris and Wayne for all their help in fabrication and Mark Wood for his friendship and many hours discussing research, cards, family, and rock-climbing. Partial support was received for this work through the Army Research Labortary, Adelphi, MD and ARO Grant No. W911NF0510076 and ARO Grant No. W911NF0710215 and is gratefully acknowledged. Finally, I would like to thank my family and friends, for without them and their support, this goal of my PhD wouldn't have been possible.

Table of Contents

Dedication ... ii
Acknowledgements ... iii
Table of Contents ... iv
List of Tables ... vii
List of Figures ... viii

1 INTRODUCTION AND BACKGROUND ... 1
1.1 Micro-scale Structures ... 1
1.2 Residual Stress Approximations in Thin-films ... 5
1.3 Static Techniques: Residual Stress Identification via Deflection or Curvature Measurements ... 13
1.4 Dynamic Techniques: Parametric Identification of MEMS Device System Parameters and Residual Stress Identification ... 26
1.5 Scope and Organization of Dissertation ... 30

2 LINEAR AND NONLINEAR ANALYSIS OF COMPOSITE BEAMS AND PLATES ... 32
2.1 Euler-Bernoulli Theory for Thin Beams ... 32
2.2 Linear Equilibrium Equation for Thin Plates: Static Equilibrium ... 37
2.3 Nonlinear Equilibrium Equation for a Thin Plate ... 40
2.4 Classical Laminated Plate Theory: Dynamic Case ... 43

3 LAMINATE STIFFNESS ANALYSES ... 46
3.1 General Laminate Stiffness Formulae ... 46
3.2 Single Layer Plates ... 48
3.3 Symmetric Laminates ... 51
3.4 Asymmetric Laminates ... 54
3.5 Generalized Laminate Stiffness Scheme ... 58

4 REDUCED-ORDER MODELS FOR PLATE-LIKE STRUCTURES ... 68
4.1 Thin Composite Laminate Beams ... 68
4.2 Thin Composite Laminate Plates ... 70
4.3 Separation of Variables – Motivation for Plate Mode-Shape Approximations ... 72
4.4 Von Karman Strain Field and Compatibility Equation ... 74
4.5 Solution to Compatibility Equation ... 77
4.6 Special Case: Composite Laminate Plate With All Edges Simply Supported ... 78
4.7 Special Case: Composite Laminate Plate With All Edges Clamped ... 88

5 FABRICATION OF MEMS DEVICES AND EXPERIMENTAL ARRANGEMENTS.. 94
5.1 Fabrication of MEMS Devices 94
5.1.1 Thin-film Deposition 94
5.1.2 Device Layouts 96
5.1.3 Fabrication / Release Processes 102
5.2 Wafer Bow Stress Measurements 106
5.3 Woollam Ellipsometer 107
5.4 Optical Profilometer...109
5.5 Dynamic Experiment Setup 111

6 RESIDUAL STRESS INDUCED DEFORMATION IN MEMS CANTILEVERS 113
6.1 MEMS Cantilever Description 114
6.2 One-Dimensional Analysis of MEMS Cantilevers............................114
6.3 MEMS Cantilever Laminate Stiffness and Residual Force/Moment Description 116
6.4 Residual Stress Induced Deformation and Preliminary Results 118
6.5 Neutral Axis Location and Its Effect on Residual Stress Deformation, Residual Force, Moment and Laminate Stiffness Calculations...122

7 CHARACTERIZATION OF RESIDUAL STRESSES IN MEMS DEVICES 140
7.1 Static Technique: Wafer Bow Measurements and Stoney's Formula 140
7.2 Static Technique: Residual Stress Identification in MEMS Cantilevers 142
7.3 Dynamic Technique: Parametric Identification of MEMS Resonators...147
7.4 Static technique: Parametric Identification of MEMS Resonators...151

8 COMPARISON OF TECHNIQUES, DISCUSSION AND RESULTS.......... 156
8.1 Results From Wafer Bow Measurements and Stoney's Formula......156
8.2 Results From the Static Technique Applied to MEMS Cantilevers 159
8.3 Results From Dynamic Technique Applied to MEMS Clamped-Clamped Resonators...171
8.4 Results From the Static Technique: Parametric Identification of MEMS Resonators 176

9 SUMMARY, CONCLUDING REMARKS AND SUGGESTIONS FOR FUTURE WORK.. 179
9.1 Plate-Like Structure Modeling and Reduced-Order Methodologies..179

9.2 Isotropic Laminate Stiffness Calculations 180
9.3 Characterization of Residual Stress Induced Deformation in Plate and Micro-Scale Structures. 182
9.4 Summary/Contributions and Suggestions for Future Work..............184

A1 REDUCED-ORDER MODELS FOR PLATE-LIKE STRUCTURES: METHODOLOGY UTILIZING OPPOSING BEAM MODES 188
A2 MATLAB PROGRAM: CRITICAL FORCE AND STRESSES.....................191
A3 MATLAB PROGRAM: CALCULATING RESIDUAL STRESS VALUES FROM SECTION 7.1..192
A4 MATLAB PROGRAM: BISECTION METHOD FOR ROOTS IN SECTION 7.4..195
A5 MATHEMATICA SPREADSHEET: REDUCED-ORDER MODEL FOR PLATE WITH ALL EDGES SIMPLY-SUPPORTED (INPUTS ONLY) 197
A6 MATHEMATICA SPREADSHEET: REDUCED-ORDER MODEL FOR PLATE WITH ALL EDGES CLAMPED (INPUTS ONLY) 201

REFERENCES 206

List of Tables

Table 6.1: *h* locations for various zero axis starting positions. 125

Table 6.2: Zero axis positions 125

Table 7.1: Residual stress range (MPa) for identification scheme 145

Table 8.1: Results from wafer bow measurements and Stoney's formula 157

Table 8.2: Thin-film layer stresses and composite stress calculation 158

Table 8.3: Wafer #1 and Wafer #2: cantilever widths, lengths, tip deflections 165

Table 8.4: Wafer #3 and Wafer #4: cantilever widths, lengths, tip deflections 165

Table 8.5: Wafer #5: cantilever widths, lengths, tip deflections 166

Table 8.6: Thin-film layer thicknesses by wafer 170

List of Figures

FIGURE 1.1:	RESONATOR EXHIBITING DEFORMATION [2].	2
FIGURE 1.2:	BENDING OF STEEL RULE DUE TO DEPOSITION OF NICKEL.	6
FIGURE 1.3:	SOLID AND DASHED LINES INDICATE LOCUS OF POINTS WHERE STONEY'S FORMULA OVERESTIMATES AND UNDERESTIMATES CURVATURE BY 10% [22].	8
FIGURE 1.4:	ERROR IN PERCENTAGE IN APPLYING STONEY'S FORMULA TO THICKER FILMS [23].	9
FIGURE 1.5:	ERROR IN PERCENTAGE IN APPLYING ATKINSON'S FORMULA TO THICKER FILMS [23].	9
FIGURE 1.6:	ERROR IN PERCENTAGE IN APPLYING BRENNER-SENDEROFF'S APPROXIMATION [23].	10
FIGURE 1.7:	THE EFFECT OF FILM THICKNESS ON STONEY'S FORMULA FOR VARIOUS TEMPERATURES OR STRESSES [19].	11
FIGURE 1.8:	THE EFFECT OF FILM THICKNESS ON CHEN AND OU'S FORMULA FOR VARIOUS TEMPERATURES OR STRESSES [19].	11
FIGURE 1.9:	40 MM THICK SILANE-BASED PECVD OXIDE FILM CYCLED AT 500˚C [26].	13
FIGURE 1.10:	NATURAL, COMPRESSED AND POST-BUCKLED STATE OF A MICRO MACHINED BEAM [3].	14
FIGURE 1.11:	COMPARISON OF MEASURED AND PREDICTED PROFILES OF BEAMS WITH LENGTHS IN THE PREBUCKLING (48 MM), TRANSITION (56 MM) AND POSTBUCKLING (72 MM) REGIONS. MEASURED RESULTS ARE TAKEN OVER SIX BEAMS. [3].	15
FIGURE 1.12:	BILAYER CANTILEVER SCHEMATIC OF FANG AND WICKERT [4].	16

FIGURE 1.13:	VARIATION OF RESIDUAL STRAIN WITH ALCU FILM THICKNESS. DATA POINTS AVERAGED OVER FIVE SAMPLES ([3], [4], [5]).	17
FIGURE 1.14:	RESIDUAL STRESS Σ VERSUS MICROBRIDGE LENGTH FOR .45 MM AND .62 MM THICK SiO_2 FILM [27].	19
FIGURE 1.15:	DEFLECTION OF THE BASE LAYER OF A BILAYER CANTILEVER [28].	20
FIGURE 1.16:	DEFLECTION OF COMPOSITE BILAYER CANTILEVER [16].	20
FIGURE 1.17:	COMPARING DEFLECTION BEFORE AND AFTER ADDITIONAL THIN-FILMS ARE DEPOSITED [12].	22
FIGURE 1.18:	COMPARISON OF SIMULATIONS OF HOU AND CHEN'S MODEL [12] (STRAIGHT LINES) AND MIN AND KIM'S (DASHED LINES) MODEL APPROXIMATING THE RESIDUAL STRESS IN AN ADDITION THIN-FILM LAYER [28] VERSUS THE DEFLECTION IN THE COMPOSITE CANTILEVERED BEAM. BEAMS ARE ASSUMED 100 MM LONG, E_1 AND E_2 ARE 105 GPA AND 70 GPA, THE BASE LAYER THICKNESS IS H_2 = 2 MM, AND THREE ADDITIONAL FILM LAYER THICKNESSES ARE CONSIDERED H_1 = 300. 600, 900 A, AND THE DEFLECTION IN THE SINGLE LAYER CANTILEVER IS ASSUMED TO BE W_2 = -1.0 MM. (HOU AND CHEN [12]).	25
FIGURE 1.19:	FREQUENCY – RESPONSE SPECTRUM OF AYELA *ET AL.* [32].	28
FIGURE 2.1:	DIFFERENTIAL BEAM ELEMENT.	33
FIGURE 2.2:	DIFFERENTIAL DISTANCES AND ROTATION ANGLE OF ROTATING BEAM ELEMENT.	34
FIGURE 2.3:	PLATE ELEMENT.	38
FIGURE 2.4:	DEFORMED PLATE ELEMENT WITH MEMBRANE FORCES.	41
FIGURE 3.1:	SYMMETRIC LAMINATE SCHEME.	51

Figure 3.2: Fibers in each layer of this composite laminate have different orientations. 56

Figure 3.3: Fibers in each layer of this composite laminate have different orientations. 56

Figure 3.4: Unsymmetric laminate scheme. 58

Figure 3.5: Symmetric laminate with three isotropic layers. 59

Figure 3.6: Asymmetric laminate with three isotropic layers. 62

Figure 3.7: Asymmetric laminate with three isotropic layers and neutral axis location. 64

Figure 3.8: Asymmetric laminate with three isotropic layers and neutral axis location. 66

Figure 4.1: General plate element exhibiting stretching. 75

Figure 4.2: Thin laminate plate with simply supported boundaries. 79

Figure 4.3: Thin laminate plate with clamped boundaries. 88

Figure 5.1: Device layout in grid pattern on silicon wafer. 96

Figure 5.2: Varying layered cantilevered resonators. 97

Figure 5.3: 20 mm wide PZT cantilevers with lengths varying from 100 to 900 mm long. 98

Figure 5.4: Die representation of microresonators. Three rows of 20, 35 and 50 mm wide resonators ranging in lengths of 100 mm to 1000 mm are present. 99

Figure 5.5: Schematic exhibiting SiO_2 and PZT resonators. 101

Figure 5.6: Silicon resonator exhibiting various stages of release. 102

FIGURE 5.7: MASK #1 DEFINING THE TOP ELECTRODE AREA. (A) FULL STACK CANTILEVERED RESONATORS WITH TOP PLATINUM ELECTRODE. (B), (C), (D) SiO_2/TIPT/PZT, SiO_2/TIPT, SiO_2 CANTILEVER WITH NO TOP ELECTRODE LAYER. 103

FIGURE 5.8: MASK #2 DEFINING PZT AND BOTTOM PT AREA TO BE ION MILLED. 103

FIGURE 5.9: MASK #3 DEFINING AREA FOR WET ETCHING AND PZT REMOVAL. 104

FIGURE 5.10: MASK #4 DEFINING AREA FOR ETCHING SiO_2. 104

FIGURE 5.11: XeF_2 ETCHING RELEASING RESONATORS. 105

FIGURE 5.12: FULL STACK RESONATOR AND SiO_2 RESONATOR POST-FABRICATION AND RELEASE. 106

FIGURE 5.13: INSTRUMENTATION USED FOR WAFER BOW MEASUREMENT IN THIN-FILMS [2]. 107

FIGURE 5.14: WOOLLAM ELLIPSOMETER USED FOR MEASURING THIN-FILM THICKNESSES [40]. 108

FIGURE 5.15: TYPICAL ELLIPSOMETRY CONFIGURATION, WHERE LINEARLY POLARIZED LIGHT IS REFLECTED FROM THE SAMPLE SURFACE AND THE POLARIZATION CHANGE IS MEASURED TO DETERMINE SAMPLE RESPONSE [40]. 108

FIGURE 5.16: VEECO OPTICAL PROFILOMETER [2]. 110

FIGURE 5.17: EXPERIMENTAL SET FOR DYNAMIC EXPERIMENTS AT THE MARYLAND MEMS LABORATORY. 111

FIGURE 5.18: LINEAR AND NONLINEAR FREQUENCY RESPONSE OF A PZT RESONATOR, 900 MM LONG, 35 MM WIDE. 112

FIGURE 6.1: COMPOSITE LAMINATE PLATE RESOLVED TO A LAMINATE BEAM FOR SPATIALLY ONE DIMENSIONAL ANALYSIS. 113

FIGURE 6.2: PZT CANTILEVER [6]. 114

FIGURE 6.3: LAMINA EXHIBITING STRESSES DEFINED VIA HOOKE'S LAW. 115

FIGURE 6.4:	ASYMMETRIC LAMINATE SCHEMATIC OF MEMS CANTILEVER.	117
FIGURE 6.5:	TIP DEFLECTIONS FOR MEMS CANTILEVERS.	121
FIGURE 6.6:	TIP DEFLECTIONS FOR MEMS CANTILEVERS.	122
FIGURE 6.7:	LAMINATE BEAM SHOWING NEUTRAL AXIS LOCATION, Z_N AND VARIOUS OTHER LOCATIONS FOR THE ZERO AXIS STARTING POSITION.	123
FIGURE 6.8:	CANTILEVER DEFLECTIONS (MM) VERSUS CANTILEVER LENGTHS (MM) FOR NINE DIFFERENT ZERO AXIS LOCATIONS, AND THREE STIFFNESS METHODS (COUPLED – STRAIGHT BLACK LINE, UNCOUPLED – DASHED LINE, NEUTRAL AXIS – STRAIGHT BLACK LINE INCLUDED, EXPERIMENTAL DATA - DOTTED).	126
FIGURE 6.9:	ZERO AXIS LOCATIONS (MM) VERSUS CURVATURES TAKEN FROM THIN LAMINATE CURVATURE CALCULATIONS FROM EQUATIONS 6.14.	127
FIGURE 6.10:	COUPLING STIFFNESSES B FOR EACH INDIVIDUAL LAMINATE LAYER CALCULATED VIA METHOD #1 FOR ANY ZERO AXIS POSITION. ES_{SIO2} IS THE COUPLING STIFFNESS FOR THE SIO_2 LAYER, ES_{PT} IS THE COUPLING STIFFNESS FOR THE PLATINUM LAYER, ES_{PZT} IS THE COUPLING STIFFNESS FOR THE PZT LAYER, ES_{PT} IS THE COUPLING STIFFNESS FOR THE TOP PT LAYER.	130
FIGURE 6.11:	COUPLED STIFFNESSES $[B]$ ARE ZERO (COMPOSITE) AND CALCULATED VIA METHOD #3. ES_{SIO2} IS THE COUPLING STIFFNESS FOR THE SIO_2 LAYER, ES_{PT} IS THE COUPLING STIFFNESS FOR THE PLATINUM LAYER, ES_{PZT} IS THE COUPLING STIFFNESS FOR THE PZT LAYER, ES_{PT} IS THE COUPLING STIFFNESS FOR THE TOP PT LAYER.	131
FIGURE 6.12:	EXTENSIONAL STIFFNESSES CALCULATED VIA METHOD #1. EA_{SIO2} IS THE EXTENSIONAL STIFFNESS FOR THE SIO_2 LAYER, EA_{PT} IS THE EXTENSIONAL STIFFNESS FOR THE PLATINUM LAYER, EA_{PZT} IS THE EXTENSIONAL STIFFNESS FOR THE PZT LAYER, EA_{PT}	

	IS THE EXTENSIONAL STIFFNESS FOR THE TOP PT LAYER.	132
FIGURE 6.13:	EXTENSIONAL STIFFNESSES CALCULATED VIA METHOD #3. EA_{SIO2} IS THE EXTENSIONAL STIFFNESS FOR THE SIO_2 LAYER, EA_{PT} IS THE EXTENSIONAL STIFFNESS FOR THE PLATINUM LAYER, EA_{PZT} IS THE EXTENSIONAL STIFFNESS FOR THE PZT LAYER, EA_{PT} IS THE EXTENSIONAL STIFFNESS FOR THE TOP PT LAYER.	133
FIGURE 6.14:	BENDING STIFFNESSES CALCULATED VIA METHOD #1. EI_{SIO2} IS THE BENDING STIFFNESS FOR THE SIO_2 LAYER, EI_{PT} IS THE BENDING STIFFNESS FOR THE PLATINUM LAYER, EI_{PZT} IS THE BENDING STIFFNESS FOR THE PZT LAYER, EI_{PT} IS THE BENDING STIFFNESS FOR THE TOP PT LAYER.	134
FIGURE 6.15:	BENDING STIFFNESSES CALCULATED VIA METHOD #1. EI_{SIO2} IS THE BENDING STIFFNESS FOR THE SIO_2 LAYER, EI_{PT} IS THE BENDING STIFFNESS FOR THE PLATINUM LAYER, EI_{PZT} IS THE BENDING STIFFNESS FOR THE PZT LAYER, EI_{PT} IS THE BENDING STIFFNESS FOR THE TOP PT LAYER.	135
FIGURE 6.16:	RESIDUAL MOMENTS CALCULATED VIA METHOD #1. MR_{SIO2} IS THE RESIDUAL MOMENT FOR THE SIO_2 LAYER, MR_{PT} IS THE RESIDUAL MOMENT FOR THE PLATINUM LAYER, MR_{PZT} IS THE RESIDUAL MOMENT FOR THE PZT LAYER, MR_{PT} IS THE RESIDUAL MOMENT FOR THE TOP PT LAYER.	136
FIGURE 6.17:	RESIDUAL MOMENTS CALCULATED VIA METHOD #3. MR_{SIO2} IS THE RESIDUAL MOMENT FOR THE SIO_2 LAYER, MR_{PT} IS THE RESIDUAL MOMENT FOR THE PLATINUM LAYER, MR_{PZT} IS THE RESIDUAL MOMENT FOR THE PZT LAYER, MR_{PT} IS THE RESIDUAL MOMENT FOR THE TOP PT LAYER.	137
FIGURE 6.18:	RESIDUAL FORCES CALCULATED VIA METHOD #1. NR_{SIO2} IS THE RESIDUAL FORCE FOR THE SIO_2 LAYER, NR_{PT} IS THE RESIDUAL FORCE FOR THE PLATINUM LAYER, NR_{PZT} IS THE RESIDUAL FORCE FOR THE PZT LAYER, NR_{PT} IS THE RESIDUAL FORCE FOR THE TOP PT LAYER.	138

FIGURE 6.19: RESIDUAL FORCES CALCULATED VIA METHOD #3. NR_{SIO2} IS THE RESIDUAL FORCE FOR THE SIO_2 LAYER, NR_{PT} IS THE RESIDUAL FORCE FOR THE PLATINUM LAYER, NR_{PZT} IS THE RESIDUAL FORCE FOR THE PZT LAYER, NR_{PT} IS THE RESIDUAL FORCE FOR THE TOP PT LAYER. 139

FIGURE 7.1: MEMS CANTILEVERS EXHIBITING LARGE CURVATURES. 142

FIGURE 7.2: MEMS CANTILEVERS EXHIBITING LARGE CURVATURES. 142

FIGURE 7.3: RESIDUAL STRESS IDENTIFICATION PROCESS. 146

FIGURE 7.4: SCHEMATIC OF A CLAMPED-CLAMPED MICRO RESONATOR WITH PARTIAL TOP PLATINUM LAYERS. 147

FIGURE 7.5: REPRESENTATION FREQUENCY-RESPONSE CURVES THAT AID IN DETERMINING VARIOUS PARAMETERS: 150

FIGURE 7.6: RESONATOR TREATED AS A LONG THIN STRUCTURE UNDER A COMPRESSIVE LOAD. 151

FIGURE 8.1: CANTILEVER TIP DEFLECTION DATA. ASTERISKS REPRESENT EXPERIMENTALLY MEASURED TIP DEFLECTIONS; STRAIGHT LINE REPRESENTS ANALYTICALLY PREDICTED TIP DEFLECTIONS. 161

FIGURE 8.2: CANTILEVER TIP DEFLECTION DATA. ASTERISKS REPRESENT EXPERIMENTALLY MEASURED TIP DEFLECTIONS, STRAIGHT LINE REPRESENTS ANALYTICALLY PREDICTED TIP DEFLECTIONS. 162

FIGURE 8.3: OPTICAL PROFILOMETER SCAN OF THREE CANTILEVERED RESONATORS. (A) 250 MM LONG, 20 MM WIDE PZT RESONATOR. (B) 300 MM LONG, 20 MM WIDE PZT RESONATOR. (C) 300 MM LONG, 20 MM WIDE SIO_2 RESONATOR. OBTAINED VIA OPTICAL PROFILOMETER AT THE ARMY RESEARCH LABORATORY, ADELPHI, MD. 163

FIGURE 8.4: Y PROFILE FROM OPTICAL PROFILOMETER SCAN. . OBTAINED VIA OPTICAL PROFILOMETER AT THE ARMY RESEARCH LABORATORY, ADELPHI, MD. 164

FIGURE 8.5:	COMPOSITE RESIDUAL STRESSES FOR INDIVIDUAL CANTILEVERED DEVICES APPROXIMATED FROM THE STATIC TECHNIQUE GIVEN IN SECTION 7.2.	167
FIGURE 8.6 (A) & (B):	INDIVIDUAL WAFER COMPOSITE RESIDUAL STRESS (*COMP. RS*) IN COMPARISON TO CANTILEVERED DEVICE RESIDUAL STRESS (*DEVICE RS*).	168
FIGURE 8.7 (A) & (B):	INDIVIDUAL WAFER COMPOSITE RESIDUAL STRESS (*COMP. RS*) IN COMPARISON TO CANTILEVERED DEVICE RESIDUAL STRESS (*DEVICE RS*).	168
FIGURE 8.8 (A) & (B):	INDIVIDUAL WAFER COMPOSITE RESIDUAL STRESS (*COMP. RS*) IN COMPARISON TO CANTILEVERED DEVICE RESIDUAL STRESS (*DEVICE RS*).	169
FIGURE 8.9 (A) & (B):	INDIVIDUAL WAFER COMPOSITE RESIDUAL STRESS (*COMP. RS*) IN COMPARISON TO CANTILEVERED DEVICE RESIDUAL STRESS (*DEVICE RS*).	169
FIGURE 8.10:	LINEAR AND NONLINEAR FREQUENCY-RESPONSE OF A PZT RESONATOR, 900 MM LONG AND 35 MM WIDE.	171
FIGURE 8.11:	SAMPLE RESULTS OBTAINED FROM THE DYNAMIC TECHNIQUE FOR A SINGLE RESONATOR.	172
FIGURE 8.12:	AXIAL FORCE CALCULATED VIA THE DYNAMIC TECHNIQUE FOR VARYING LENGTHS AND WIDTHS (SQUARES) AND THE AXIAL FORCE CALCULATED VIA WAFER BOW MEASUREMENTS AND STONEY'S FORMULA.	174
FIGURE 8.13:	RESIDUAL STRESS CALCULATED VIA THE DYNAMIC TECHNIQUE FOR VARYING LENGTHS AND WIDTHS (SQUARES) AND THE AXIAL FORCE CALCULATED VIA WAFER BOW MEASUREMENTS AND STONEY'S FORMULA.	175
FIGURE 8.14:	DEFLECTION PROFILES FOR A 300 MM AND 700 MM LONG RESONATORS UNDER VARIOUS LEVELS OF RESIDUAL STRESS.	177
FIGURE 8.15 (A,B):	CRITICAL FORCE AND RESIDUAL STRESSES OBTAINED FROM THE STATIC TECHNIQUE OF SECTION 7.4.	177

FIGURE 8.16 (A,B): AXIAL FORCE AND RESIDUAL STRESS RESULTS FOR STONEY'S FORMULA, THE DYNAMIC TECHNIQUE OF SECTION 7.3 AND THE STATIC TECHNIQUE OF SECTION 7.4. 178

FIGURE 9.1: LAMINATE BEAM SHOWING NEUTRAL AXIS LOCATION, Z_N AND VARIOUS OTHER LOCATIONS FOR THE ZERO AXIS STARTING POSITION. 181

1 INTRODUCTION AND BACKGROUND

In this chapter, background information and prior research on residual stress in micro-scale structures is discussed. Background information related to plate analysis is provided in Chapter 2. The scope and organization of this dissertation is also provided.

1.1 Micro-scale Structures

Residual stress deformation in micro-scale structures is considered in this work. Residual stress can arise from the deposition of thin-films below their flow temperatures as well as the mismatch of the coefficients of thermal expansions among thin-film lamina layers. Fabrication processes requiring extreme temperatures exacerbate these problems and this can also lead to substantial thin-film stresses.

There are two major types of residual stresses, namely, intrinsic residual stress and thermal residual stress. Intrinsic residual thin-film stress either originates from strained regions within the films (grain boundaries, dislocations, voids, impurities, etc.), or at the film/substrate and film/vacuum interfaces, or is due to dynamic processes such as re-crystallization and inter-diffusion [1]. In addition to intrinsic stress, thermal residual stress is an important issue as well. Thermal residual stress is highly dependent on the geometrical shape change during the growth of the film.

The effects of residual stress are often detrimental to microelectromechanical (MEMS) structures. This stress induces axial stretching and bending moments within the film layers, which in turn, cause unwanted deflections or deformations.

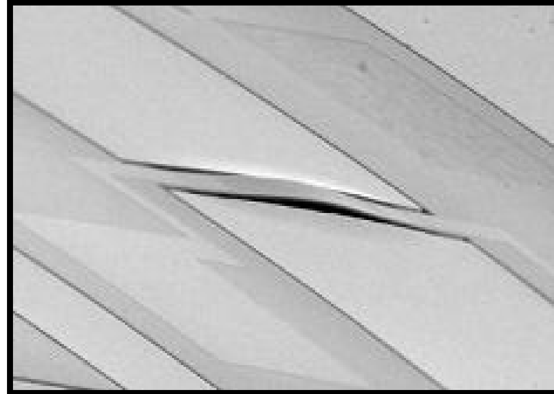

Figure 1.1: Resonator exhibiting deformation [2].

A representative deformation observed in a micro-resonator device is shown in Figure 1.1. Such deformations may cause structural defects or impede device performance in MEMS devices after release. For example, a MEMS switch that is deformed via residual stress may now require too high of a voltage to close. For this reason, as thin-films are being deposited, it is necessary to accurately measure, characterize, and control residual stress. Modeling of actual residual stress that occurs in thin-films and MEMS devices is extremely difficult. Experimental thin-film stress measurements can have extreme variation from run-to-run or wafer-to-wafer. This variation can lead to miscalculations in device deflections, material parameters, and operability. Past measurement techniques have focused on a specific fabrication process or single/bilayer thin-film structures.

To study and accurately characterize residual stress in thin-films and MEMS structures, two things are necessary, one, an accurate model, and second, techniques and

experiments that use this model to characterize residual stress in these structures. MEMS structures have often been modeled with linear or nonlinear beam models. One of the first early work was that of Fang and Wickert ([3], [4], [5]) where the static deflection of a clamped-clamped resonator is modeled with

$$[EI]w_{,xxxx} + [EA]\left(\varepsilon - \frac{1}{2L}\int_0^L \left(w_{,x}^2\right)dx\right)w_{xx} = 0 \tag{1.1}$$

where $[EI]$ is stiffness due to bending, $[EA]$ is stiffness due to stretching, w is the transverse displacement and the last part of equation (1.1) is a nonlinearity due to axial stretching. In addition, Pulskamp, Wickenden, Polcawich, Piekarski, and Dubey [6] modeled the static deflection of a cantilevered device as

$$\frac{\dfrac{d^2w}{dx^2}}{\left(1+\left(\dfrac{dw}{dx}\right)^2\right)^{\frac{3}{2}}} = \frac{M(x)}{EI}$$

(1.2 a,b)

$$w(x) = \frac{1}{2}\left(\frac{M(x)}{EI}\right)x^2$$

In equation (1.2 a), the curvature is nonlinear and needs a numerical method to solve for w. Equation (1.2 b) is already integrated for the static transverse deflection. In addition, many analyses have used a linear form of equation (1.1) for buckling analysis ([3], [4], [5], [7], [8], [9])

$$[EI]w_{,xxxx} + Pw_{xx} = 0 \tag{1.3}$$

where P is the axial force acting along the beam length. Finally, these equilibrium equations have often been put in the form of reduced-order models similar to [10]

$$\overline{m} * \ddot{z}(t) + \overline{c}\dot{z}(t) + kz(t) + \alpha_3 z^3(t) = F\, cos(\omega t) \tag{1.4}$$

$$\begin{aligned} \overline{m} &= \int_{l_{n-1}}^{l_{b=n}} \phi_n(x)\left[\rho A_n \phi_n(x)\right] dx \\ \overline{c} &= \int_{l_{n-1}}^{l_{b=n}} \phi_n(x)\left[c\phi_n(x)\right] dx \\ \overline{k} &= \int_{l_{n-1}}^{l_{b=n}} \phi_n(x)\left[EI\phi_n(x) - P_o \phi_n''\right] dx \end{aligned} \tag{1.5}$$

for the purpose of linear and nonlinear frequency-response analysis, often around the fundamental mode of vibration. In equation (1.4) and (1.5), $\phi_n(x)$ is considered the model mode shape function.

In addition to beam models, micro-scale structures can take the form of a thin laminate plate. Hou and Chen ([11],[12]) studied the width effect on ultra wide cantilevers. A linear curvature model was used to predict the static deflection in their cantilevers; however, they used formulae for calculating beam stiffnesses from thin laminate plate theory and noted improvements in the model predictions. Though many micro-scale devices can take on the form and dimensions suited for a plate model, beam models are often used for simplification purposes. However, in the packaging field, printed wiring boards are often modeled with plate-like models and methodologies. These applications in the packaging field are on a macro-scale and maybe used on a micro scale for MEMS devices. Such work is that of Suhir ([13],[14]) who evaluates the dynamic response of a flexible rectangular thin plate to an acceleration at its support contour as well as periodic shocks. He ([15], [16]. [17]) took Suhir's models and expanded them to include

symmetric multi-laminate schemes that more accurately describe the make up of a printed wiring board. Plate models can potentially play an important role in the modeling and response of micro-scale structures. For example, cantilevers often have large deflections in comparison to a clamped-clamped resonator. It's been noted by Hou and Chen ([11],[12]) that not only do certain types of cantilevers deflect along the axial length direction, but curvatures exist across the widths as well. This means that plane strain assumptions made for a cantilever aren't possible, and further analysis can aid in better predictive models of these plate-like micro-scale structures.

In addition to accurate modeling of micro-scale structures, it is necessary to develop identification techniques capable of predicting stress that occurs during thin-film deposition, stress that occurs immediately post-fabrication and release processes, stress that occurs with the application of applied voltages, and stress that occurs during various static and dynamic loadings. These techniques involve linear and nonlinear beam and plate models, and are they solved numerically so that additional studies can be conducted. Experiment data are used as inputs into these techniques as well as to verify results of simulations. Identification techniques and uses will be further covered in the next few Sections.

1.2 Residual Stress Approximations in Thin-films

Past work has focused on approximating residual stress in thin-films, usually post deposition of the thin-film on a substrate. The first such work was that of G. Stoney [18]. Stoney investigated stresses in metallic films deposited electrolytically. Stoney

discovered that when nickel was deposited on a very thin sheet of steel (102mm long/12mm wide/.32 mm thick), bending of up to four millimeters occurred (

Figure 1.2).

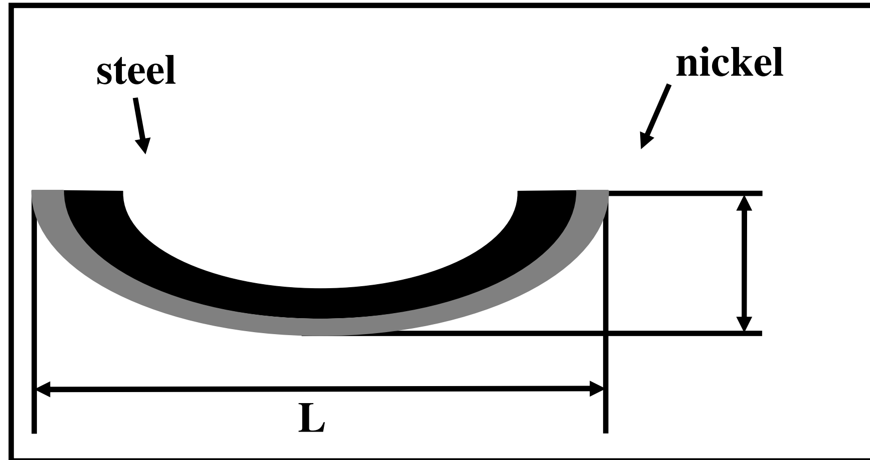

Figure 1.2: Bending of steel rule due to deposition of nickel.

Stoney then developed a formula based on linear beam theory for converting stress induced curvatures into residual thin-film values.

$$P = \frac{4}{3} E \frac{(d^2 + td)z}{tL^2} \tag{1.6}$$

where P is the axial force, E is the Young's modulus, d is the thickness of the steel, t is the thickness of the deposited nickel, Z is the deflection of the steel, and L is the length of the structure. Equation (1.6) is used to calculate the thin-film stress in the deposited nickel layer. This formula is commonly used today for approximating thin-film stress in any number of deposited layers. After each individual thin-film layer stress value is

calculated, a composite value for the entire thin-film or structure may be calculated via volumetric averaging.

Although Stoney's formula is valuable in many cases, its applicability can be limited because of its basis in linear mechanics [19]. Modifications to Stoney's formula have been proposed by Brenner and Senderoff [20] and Atkinson [21]. Freund, Floro and Chasen [22] relaxed Stoney's main assumptions that the film is very thin in comparison to the substrate and that the deformations are infinitesimally small. By utilizing the expression for the elastic strain energy and radial and transverse strains, they obtained

$$U(r,z)=\frac{E}{2(1-\upsilon)}\left[\varepsilon_{rr}(r,z)^2+\varepsilon_{\theta\theta}(r,z)^2+2\upsilon\varepsilon_{rr}(r,z)*\varepsilon_{\theta\theta}(r,z)\right] \tag{1.7}$$

$$\begin{aligned}\varepsilon_{rr}&=u'(r)-zw''(r)+\varepsilon_m\\ \varepsilon_{\theta\theta}&=\frac{u(r)}{r}-\frac{zw'(r)}{r}+\varepsilon_m\end{aligned} \tag{1.8}$$

equations (1.7) and (1.8) are inserted into the total potential energy in order to derive the expression for the substrate curvature.

$$\kappa=\frac{6\varepsilon_m}{h_{substrate}}hm\left[\frac{1+h}{1+hm\left(4+6h+4h^2\right)+h^4m^2}\right] \tag{1.9}$$

where $h=h_{film}/h_{substrate}$ and $m=M_{film}/M_{substrate}$. Freund *et al.* [22] then compares Equation (1.9) to Stoney's curvature relation, κ_{ST}, and shows that

$$\left|\frac{\kappa-\kappa_{ST}}{\kappa_{ST}}\right|\leq\frac{1}{10} \tag{1.10}$$

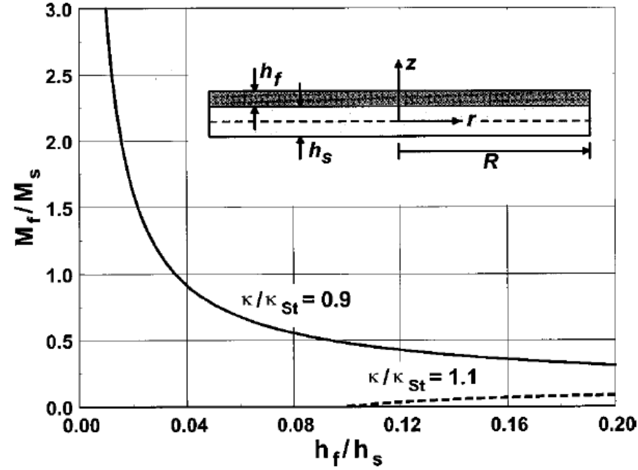

Figure 1.3: Solid and dashed lines indicate locus of points where Stoney's formula overestimates and underestimates curvature by 10% [22].

in Figure 1.3. Here the solid and dashed lines represent the locus of points where Stoney's formula is estimates the curvature within 10% of the formula derived by Freund *et al*. [22]. The region in between these lines represents the area where Stoney's formula is valid within 10%.

In addition to the work of Freund *et al.*, Klein [23] developed a formula based off of general theory of elastic interactions in multilayer laminates for thin-film stress, and used this formula to develop a correction factor for Stoney's formula

$$\sigma_{Klein} = \underbrace{\left[\frac{1+\gamma\delta}{1+\delta}\right]}_{Correction} \sigma_{Stoney} \tag{1.11}$$

where γ is the ratio of the biaxial moduli and δ is the ratio of the layer thicknesses. Klein emphasizes that it's straightforward to extend Stoney's formula to be valid in situations involving thick films with ratios less than 0.1.

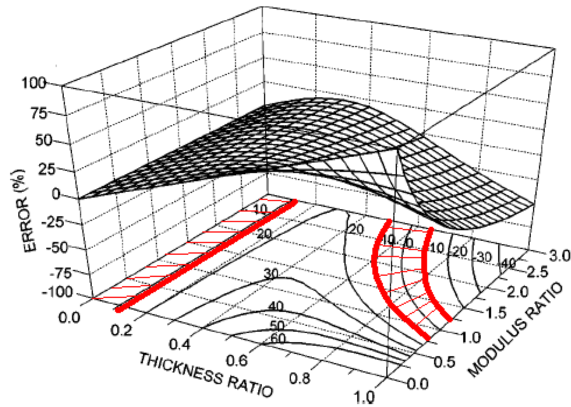

Figure 1.4: Error in percentage in applying Stoney's formula to thicker films [23].

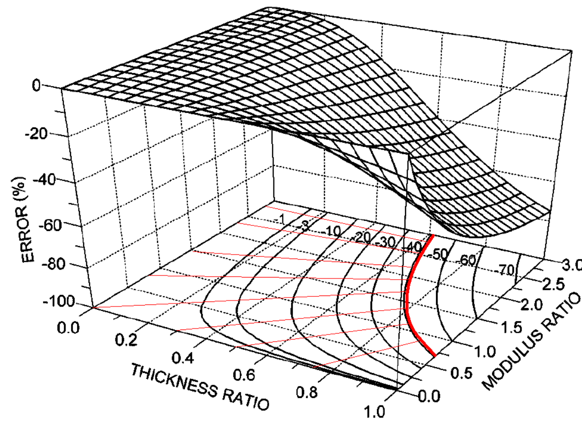

Figure 1.5: Error in percentage in applying Atkinson's formula to thicker films [23].

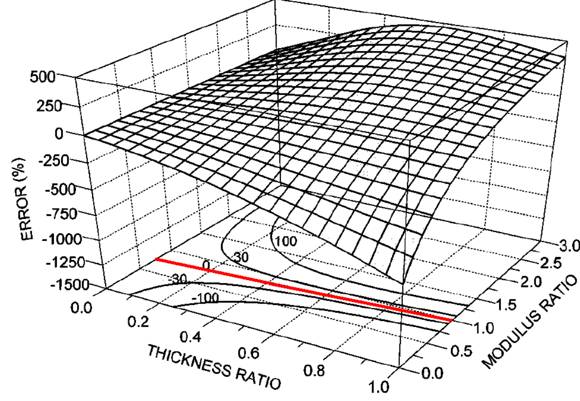

Figure 1.6: Error in percentage in applying Brenner-Senderoff's approximation [23].

Klein also notices that Atkinson's [21] proposed modification yields improved results for ratios up to 0.4, and those expressions provided by Brenner-Senderoff [20] yield large errors and should be avoided for thicker films. Besides the thin-film stress characterization of Stoney, Brenner-Senderoff, Atkinson. Freund and Klein, Chen and Ou [19] assumed a shaped energy-based approach to improve the curvature/stress conversion by simultaneously considering effects of geometrical nonlinearity and mid-plane offsets. Via this approach, a conversion factor is defined,

$$K_N = \frac{E_f\left(B_f - 2C_0\left(d_s + \frac{1}{2}d_f - d_{np}\right)\right)}{(1-\upsilon_f)(C_0L^2 + C_2L^4)} \tag{1.12}$$

where E_f is the thin-film Young's modulus, B_f, C_0 and C_2 are predetermined coefficients, d_s and d_f are the thicknesses of the thin-film and substrate, d_{np} is the mid-plane offset, υ_f is the poisson's ratio of the thin-film and L is the length of the rule to be considered. Chen and Ou compare equation (1.12) to the conversion factor of Stoney

$$K_{Stoney} = \frac{film\ stress}{measured\ bow} = \frac{E_s d_s^3}{3(1-\upsilon_s)L^2 d_f^2\left(1+\frac{d_s}{d_f}\right)} \quad (1.13)$$

and analyze the error between the two for tick films and that of a finite element model.

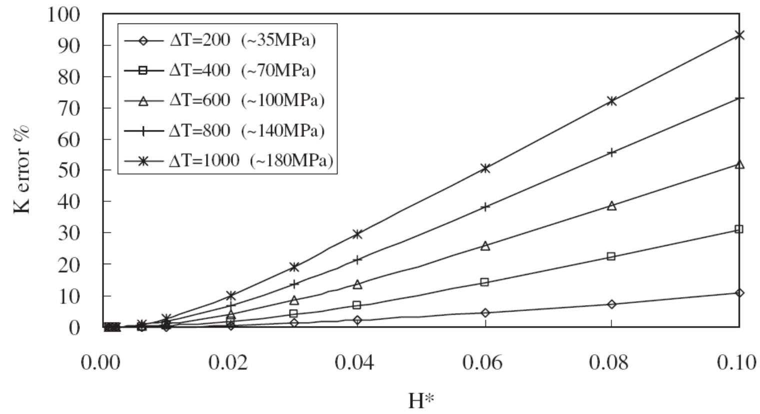

Figure 1.7: The effect of film thickness on Stoney's formula for various temperatures or stresses [19].

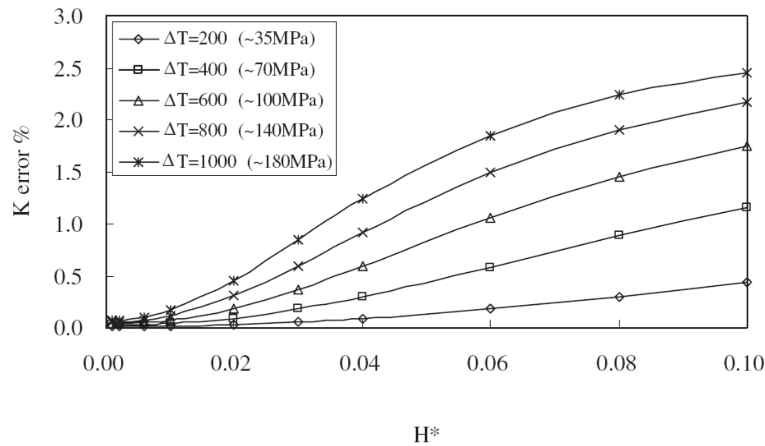

Figure 1.8: The effect of film thickness on Chen and Ou's formula for various temperatures or stresses [19].

Results from these comparisons are shown in Figure 1.7 and Figure 1.8 where H^* is the ratio of film to substrate thicknesses. Chen and Ou's expressions clearly produce much lower errors than that of Stoney for large thicknesses and most temperatures.

Zhang, Chen, Ghodssi, Ayon, Spearing [24] and Zhang, Chen, Spearing ([25], [26]) also studied residual stress effects on thin-films while temperature was being cycled. Motivation for Zhang *et al.* ([24], [25], [26]) comes from the need to elucidate factors contributing to residual stress, deformation and fracture of silicon oxide films so as to refine fabrication processes for manufacturing MEMS. In the studies of Zhang *et al.* ([24], [25], [26]), PECVD oxide films were deposited by using a five-station continuous plasma processing system. Thermal cycling tests were conducted and the *in situ* wafer curvature was measured between room temperature and 500˚C by using a KLA-Tencor™ FLX-2320 system with a ramp rate of 5˚C/min. Some results are shown in Figure 1.9 for a 40 μm oxide film with respect to temperatures ranging from room temperature to 500˚C. The dependence of residual stress on temperature is highly nonlinear with a significant amount of hysteresis during the first thermal cycle.

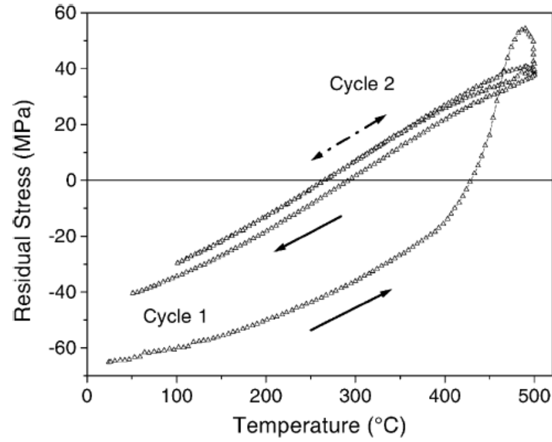

Figure 1.9: 40 μm thick silane-based PECVD oxide film cycled at 500˚C [26].

1.3 Static Techniques: Residual Stress Identification via Deflection or Curvature Measurements

In addition to the characterization of residual stress in thin-films, residual stress has also been characterized in microelectromechanical systems post-fabrication and post-release processes. In 1994, Fang and Wickert [3], the finite amplitude of a clamped-clamped beam was predicted by modeling the nonlinear dependence of the out-of-plane deformation on compressive residual stress (Figure 1.10).

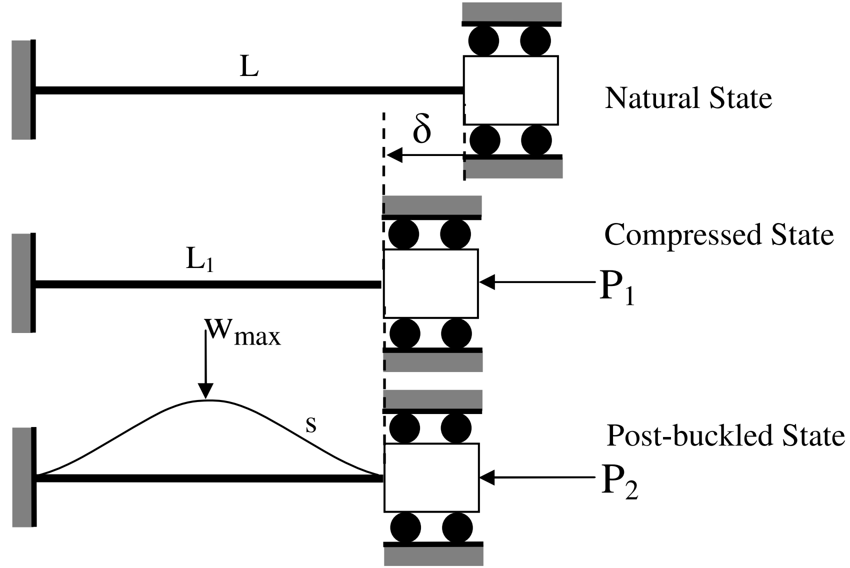

Figure 1.10: Natural, compressed and post-buckled state of a micro machined beam [3].

The axial load in the post-buckled state is given by

$$P_2 = EA\left(\underbrace{\varepsilon}_{\substack{\textit{Stretching}\text{ due to} \\ \text{axial compression}}} - \underbrace{\frac{1}{2L}\int_0^L w_{,x}^2 dx}_{\substack{\text{Stretching due to} \\ \text{transverse deflection}}} \right) \tag{1.14}$$

and the governing static equation of motion describing transverse deflection is given by

$$EIw_{,xxxx} + EA\left(\varepsilon - \frac{1}{2L}\int_0^L w_{,x}^2 dx \right) w_{,xx} = 0 \tag{1.15}$$

The solution to the eigenvalue problem, the simplified version of equation (1.15) $\left(EIw_{,xxxx} + EA\varepsilon w_{,xx} = 0 \right)$, provides

$$P_c = \frac{4\pi^2 EI}{L_c^2} \tag{1.16}$$

where P_c is the critical residual axial load due to compression. The profile of the beam at critical loading is

$$w = \frac{1}{2} w_{\max} \left(1 - \cos\left(\frac{2\pi x}{L}\right)\right) \tag{1.17}$$

SiO_2 beams were fabricated with lengths ranging from 30 μm to 140 μm, and width and thickness of 15 μm and 2 μm, and profiles were compared to those obtained from equation (1.17) and results obtained are shown in Figure 1.11.

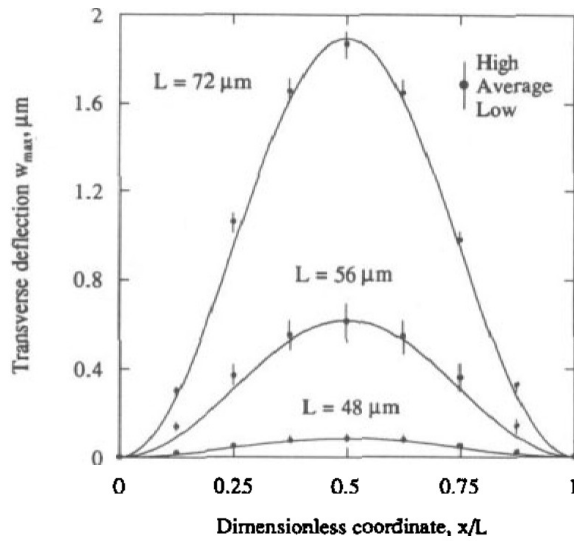

Figure 1.11: Comparison of measured and predicted profiles of beams with lengths in the prebuckling (48 μm), transition (56 μm) and postbuckling (72 μm) regions. Measured results are taken over six beams. [3].

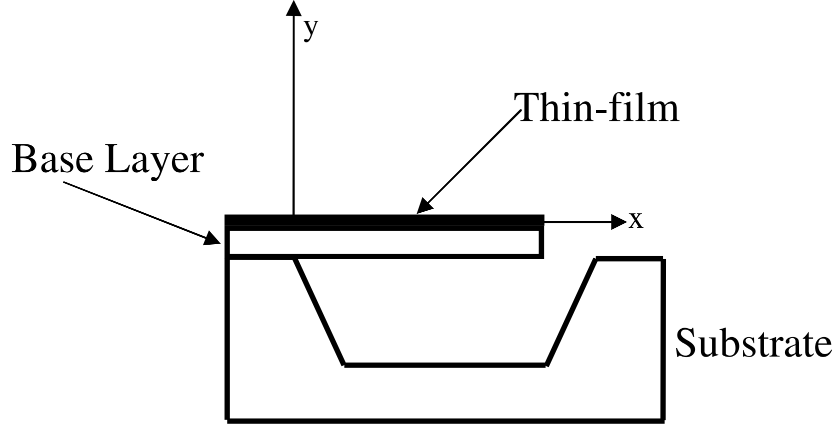

Figure 1.12: Bilayer cantilever schematic of Fang and Wickert [4].

In 1995, Fang and Wickert [4] moved from single single-layer SiO_2 beams to bilayer AlCu and diamond like carbon films deposited on premade SiO_2 cantilevers (Figure 1.12). Fang and Wickert utilize the strain-deflection model

$$\begin{aligned} \frac{t_B}{R} &= \frac{2c_1}{(1+c_2)} \\ c_1 &= \frac{Et\varepsilon_F - c_2(Et+1)}{Et^2-1} \\ c_2 &= \frac{E^2t^4\varepsilon_F + 3Et^2\varepsilon_F + 4Et\varepsilon_F + \varepsilon_1(Et^2-1)}{3(Et^2-1)^2 - 4(Et+1)(Et^3+1)} \end{aligned} \tag{1.18}$$

where $E=E_F/E_B$ and $t=t_F/t_B$ are the nondimensional moduli and thicknesses, $\varepsilon_1=t_B/2r$, and R is the radius of curvature. Once constants are known and the radius of curvature is measured, Fang and Wickert solved equation (1.18) for the residual strain, ε_F. Representative results are shown in Figure 1.13 where it is clear that for thicker AlCu films the residual strain tends to be more compressive.

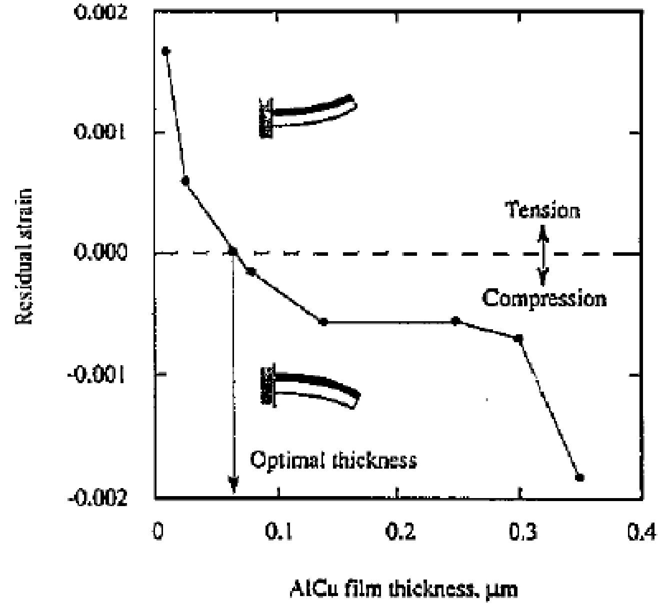

Figure 1.13: Variation of residual strain with AlCu film thickness.

Data points averaged over five samples ([3], [4], [5]).

Fang *et al*. [5] finally extend their analyses to include gradient residual stresses with application to single layer SiO_2 cantilevers. They represent the residual stress in a thin-film via the polynomial

$$\sigma_{total} = \sum_{k=0}^{\infty} \sigma_k \left(\frac{y}{h/2} \right)^2 \tag{1.19}$$

where $y \in (-y/2, y/2)$ is the coordinate across the thickness, *h*, with the origin chosen at the film's midplane. Higher order terms are neglected and equation (1.19) becomes

$$\sigma_{total} \approx \sigma_0 + \sigma_1 \left(\frac{y}{h/2} \right) \tag{1.20}$$

where σ_0 represents the constant mean stress and σ_1 represents the gradient stress.

Similar to Fang and Wickert ([3], [4], [5]), Nicu, Temple-Boyer, Berguad, Schied and Martinez [27] SiO_2 microfabricated clamped-clamped beams under buckling due to compressive residual stress. The deflected SiO_2 beams indicated the presence of residual stress. These deflections were them measured via atomic force microscopy. The potential energy stored in the buckled beam was computed and the residual stress value was determined by considering the measured buckling maximal deflection and by making approximations too the shape of the micro-beam deflection curve. This energy approach permits one to compute the residual stress value many times for the different lengths micro-bridges by using the same thin-film under compressive residual stress. The shape of this deflection curve is chosen as

$$y(x) = \frac{A}{2}\left(1 + cos\frac{2\pi x}{L_0}\right) \tag{1.21}$$

and the critical residual stress is obtained as

$$\sigma_{cr} = \frac{\pi^2}{3}E\left(\frac{h}{L_0}\right)^2 \tag{1.22}$$

where E is the Young's modulus, h the film thickness and L_0 the beam length. Nicu *et al*. approximated the SiO_2 residual stress in 300 μm long beams as -191 ± 9 MPa and -185 ± 7 MPa for 0.45 μm and 0.62 μm thick films and varying lengths (Figure 1.14)

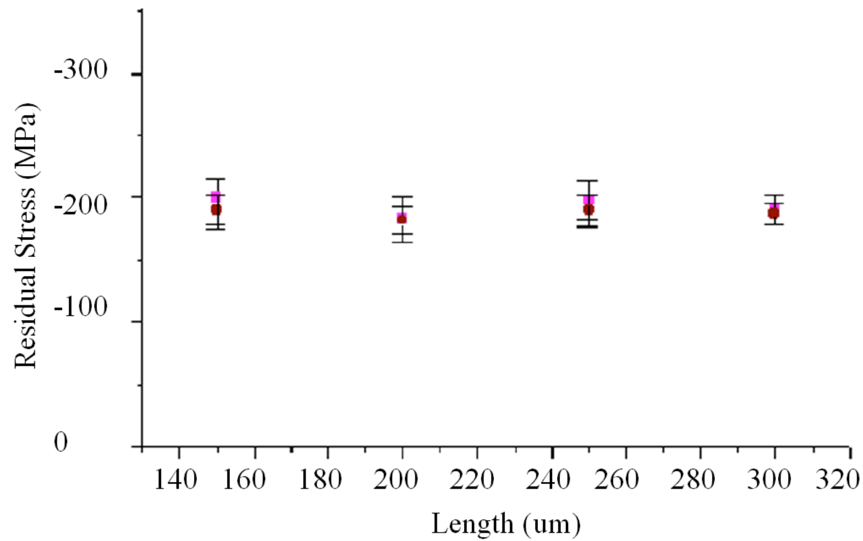

Figure 1.14: Residual stress σ versus microbridge length for .45 μm and .62 μm thick SiO_2 film [27].

Min and Kim [28] approached approximating residual stress in cantilevers via experimentally measured micro-cantilever tip deflections as model inputs, instead of using curvature or bow measurements. In order to model their composite bilayer beams, the composite beam is first considered at a single-layer beam (Figure 1.15), a thin-film is deposited, and then, the composite beam is considered as a bilayer beam (Figure 1.16).

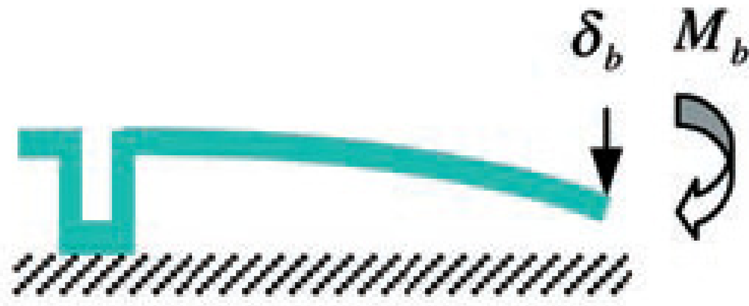

Figure 1.15: Deflection of the base layer of a bilayer cantilever [28].

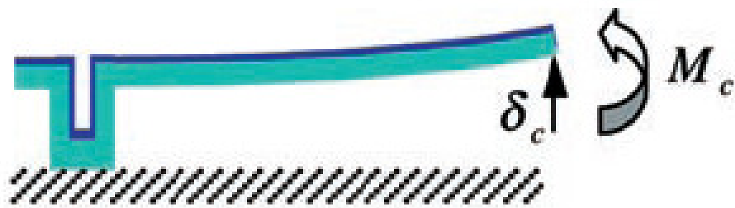

Figure 1.16: Deflection of composite bilayer cantilever [16].

Based on small deflection theory, the applied moments, M_b and M_c shown in Figure 1.15 and Figure 1.16, are described as

$$\begin{aligned} M_b &= \frac{2E_b}{L^2} I_b \delta_b \\ M_C &= \frac{2E_c}{L^2} I_c \delta_c \end{aligned} \qquad (1.23)$$

The induced moments for the single and bilayer cantilever can also be calculated as

$$M_C = \sigma_a w_a t_a \left(t_b + \frac{t_a}{2} - y_c \right)$$
$$M_b = \sigma_b w_b t_b \left(y_c - \frac{t_b}{2} \right) \tag{1.24}$$

The applied moment in the additional film is found by subtracting the moment in the single-layer cantilever from that of the composite cantilever (equation (1.25)).

$$M_C - M_b = \sigma_a w_a t_a \left(t_b + \frac{t_a}{2} - y_c \right) - \sigma_b w_b t_b \left(y_c - \frac{t_b}{2} \right) \tag{1.25}$$

Inserting equation (1.23) into equation (1.25), and solving for σ_a, results in a formula for the additionally deposited thin-film

$$\sigma_a = \frac{\left(2E_b / L^2\right)\left(I_c \delta_c - I_b \delta_b\right) + \sigma_b w_b t_b \left(y_c - \left(t_b / 2\right)\right)}{w_a t_a \left(t_b + \left(t_a / 2\right) - y_c\right)} \tag{1.26}$$

where σ_a is the residual stress of an additional film layer, σ_b is the residual stress of the base layer, E is the Young's modulus, w is the width, L is the cantilever length, I is the moment of inertia, and y_c is the neutral axis location. By using this formula, several parameter variations and simulations are carried out. These simulations are verified in the data for fabricated aluminum/gold and aluminum/titanium cantilevers.

Hou and Chen ([11], [12]) expand upon Min and Kim's work [28] to incorporate the width effect on stress-induced bending of micromachined bilayer cantilevers. Polysilicon/chromium cantilevers are considered and the residual stress in the chromium layer is exploited to deform the test cantilevers. The residual stresses in Hou and Chen ([11]) are calculated via Fang and Wickert ([3], [4]), equation (1.1).

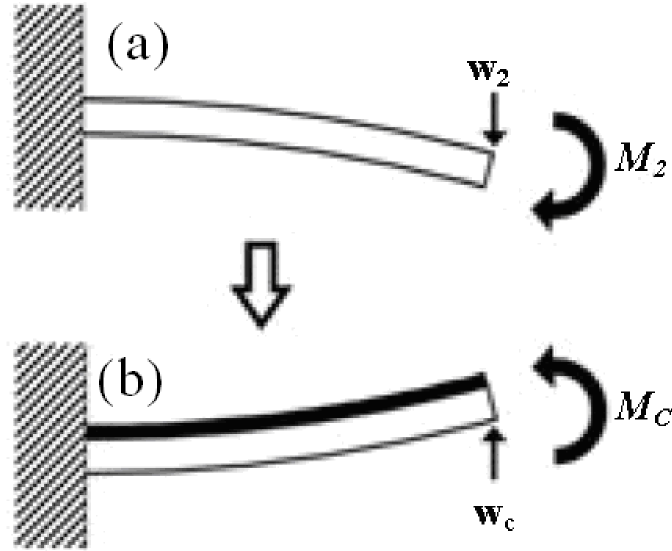

Figure 1.17: Comparing deflection before and after additional thin-films are deposited [12].

A three dimensional finite element model was used to analyze and compare residual stress values and cantilever deflection profiles to that of fabricated polysilicon/chromium cantilevers. Hou *et al*. expands the work in [11] and that of Min and Kim [28] analytically to include width effect on ultra-wide polysilicon/chromium cantilevers ([11], [12]). Hou *et al*. ([11], [12]) begin their methodology via a single layer and bilayer cantilever model (Figure 1.17).

In general, a cantilever's moment can defined as a function of its flexural rigidity and transverse deflection,

$$
\begin{aligned}
M_x &= D\frac{d^2 w}{dx^2} \\
D &= \frac{Eh^3}{12\left(1-\upsilon^2\right)}
\end{aligned}
\tag{1.26}
$$

and integrating results in an expression representing the tip deflection of a cantilever.

$$w(L) = \frac{1}{2}\kappa L^2 \tag{1.27}$$

where D is the flexural rigidity, E is the Young's modulus, h is the layer thickness, υ is the Poisson's ratio and κ is the beam curvature. Noting that

$$\frac{M_x}{D} = \frac{d^2 w}{dx^2} = \kappa = \frac{2w(L)}{L^2} \tag{1.28}$$

A general expression for the moment in a cantilever beam becomes

$$M_x = D\frac{2W_{tip}}{L^2} \tag{1.29}$$

where W_{tip} represents the deflection of the tip of the cantilever. In Figure 1.17 (a) and (b), the single and bilayer cantilevers' tip deflections, moment expressions and flexural rigidity are given by

$$\begin{aligned} w_2 &= \frac{1}{2}\kappa_{x2}L^2 & w_c &= \frac{1}{2}\kappa_{xc}L^2 \\ D_2 &= \frac{E_2 h_2^3}{12(1-\upsilon_2^2)} & D_c &= \frac{E_1 h_1^3}{12(1-\upsilon_1^2)}K_2 \\ M_{x2} &= D_2\frac{2w_2}{L^2} & M_{xc} &= D_c\frac{2w_c}{L^2} \end{aligned} \tag{1.30}$$

where K_2 is an expression comprised of thickness, Young's modulus and Poisson's ratio values for the bilayer cantilever. If the moment from the single layer cantilever is subtracted from the moment expression for the bilayer cantilever (Similar to that of Min *et al*., equation (1.25)),

$$M_C - M_2 = \sigma_1 h_1 \left(h_2 + \frac{h_1}{2} - z_C \right) - \sigma_2 h_2 \left(z_C - \frac{h_2}{2} \right) \qquad (1.31)$$

an expression for the residual stress in the additional film may be obtained as

$$\sigma_1 = \frac{\frac{2}{L^2}(D_C w_C - D_2 w_2) + \sigma_2 h_2 \left(z_C - \frac{h_2}{2} \right)}{h_1 \left(h_2 + \frac{h_1}{2} - Z_C \right)} \qquad (1.32)$$

The main difference between the approaches of Hou *et al*. and Min *et al*. is that Hou *et al*. calculate the flexural rigidity of the ultra wide cantilevered beams using expressions for the plate stiffnesses. Simulations are shown in (Figure 1.18).

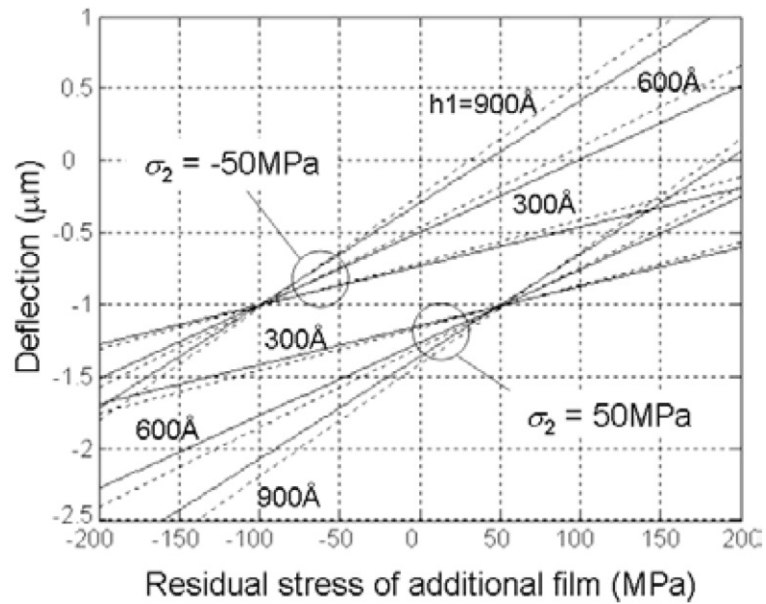

Figure 1.18: Comparison of simulations of Hou and Chen's model [12] (straight lines) and Min and Kim's (dashed lines) model approximating the residual stress in an addition thin-film layer [28] versus the deflection in the composite cantilevered beam. Beams are assumed 100 μm long, E_1 and E_2 are 105 GPa and 70 GPa, the base layer thickness is h_2 = 2 μm, and three additional film layer thicknesses are considered h_1 = 300. 600, 900 A, and the deflection in the single layer cantilever is assumed to be w_2 = -1.0 μm. (Hou and Chen [12]).

1.4 Dynamic Techniques: Parametric Identification of MEMS Device System Parameters and Residual Stress Identification

In addition to s*tatic techniques*, *dynamic techniques* are also useful in determining device residual stress values. Dynamic techniques are especially useful in determining system parameters such as modal mass, damping, linear and nonlinear stiffnesses, and forcing amplitudes. Dynamic characterization of MEMS devices was carried out by Piekarski, DeVoe, Dubey, Kaul, and Conrad [29]. Piezoelectric actuation and sensing of a suspended beam MEMS resonant filter was demonstrated and resonance frequencies are observed for various dimensions. With these PZT resonators, linear frequency data may be taken for various poling voltages and time and the axial force, and hence, the residual stress in the structures. In the work of Jaksic and Boltezar [30], parameter identification for a single-degree-of-freedom system was carried out. The free acceleration response of the system was studied in order to estimate the parameters in the equation of motion. Yahiaoui and Bosseboeuf [31] modeled cantilever beams using finite element analysis software and conducted material characterization with an experimental setup designed for the vibration spectra measurements of micromechanical devices and microoptoelectromechanical systems (MOEMS). A beam correction factor was found that includes the width effect from the plate stiffness in the natural frequency calculations.

In the work of Ayela and Fournier [32], resonance sensors were used with high mechanical Q factors based on a vibrating element acting as a harmonic oscillator. Ayela *et al*. modeled these resonators as

$$\frac{d^2x}{dt^2} + \frac{\lambda}{a}\frac{dx}{dt} + \omega_0^2 x = -\beta x^3 + \frac{F}{a}\cos(\omega t) \tag{1.33}$$

where x is the transverse displacement, λ is the damping factor, a is the inertial coefficient (kg), ω_0 is the natural frequency, β is the nonlinear stiffness coefficient, F is the forcing amplitude and ω is the excitation frequency. Free standing silicon resonators were electrostatically excited in the flexural or fundamental mode. In the anharmonic mode with $\beta \neq 0$ and close to the resonance frequency, the relation between the frequency ω and the main amplitude A is

$$\left[\left(\varepsilon - XA^2\right)^2 + \lambda^2\right]A^2 = \Gamma \tag{1.34}$$

and from equation (1.34) one can find

$$\frac{dA}{d\varepsilon} = \frac{A\left(XA^2 - \varepsilon\right)}{\varepsilon^2 + \lambda^2 + XA^2\left(3XA^2 - 4\varepsilon\right)} \tag{1.35}$$

This derivative used to locate maximum amplitudes for frequency values that correspond to forward and backward sweeps. In addition, by analyzing these parameters as well as parameters describing the location, forcing and amplitude where jumps in the frequency response occur, system parameters for the weakly nonlinear system are determined. Some of these parameters are shown in Figure 1.19 for a general linear and nonlinear frequency response.

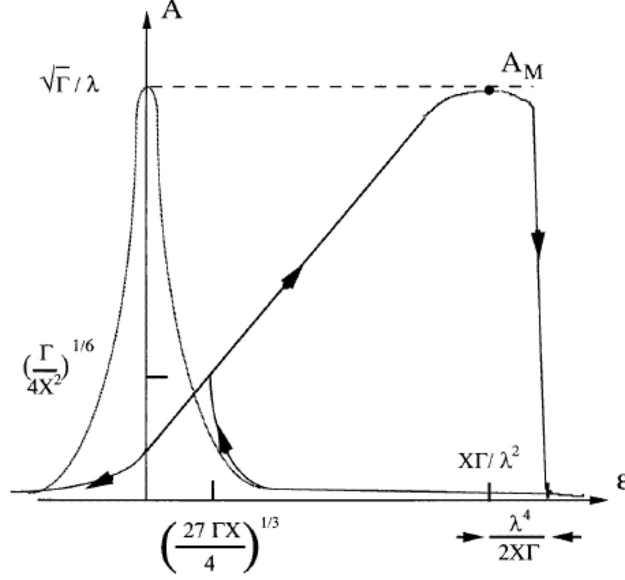

Figure 1.19: Frequency – response spectrum of Ayela *et al.* [32].

Malatkar and Nayfeh [33] presented a procedure for the identification of parameters on the basis of a single-mode response of a spatially continuous system. Malatkar *et al.* modeled a cantilever with the following equation

$$\begin{aligned} m\ddot{v} + c_v\dot{v} + \hat{c}\dot{v}|\dot{v}| + EIv^{iv} &= ma_b\cos(\Omega t) - EI\left[v'\left(v'v''\right)'\right]' \\ &-\frac{1}{2}m\left\{v'\int_l^s\left[\frac{\partial^2}{\partial t^2}\int_0^s v'^2 ds\right]ds\right\}' \end{aligned} \tag{1.36}$$

where *m* is the beam mass, *l* is the beam length, *E* is the Young's modulus, *I* is the area moment of inertia, *v(s,t)* is the transverse displacement, *s* is the arclength, *t* is time, a_b is the acceleration of the supported end of the beam, c_v is the coefficient of linear viscous damping, $\hat{c}$ is the coefficient for quadratic damping, and Ω is the excitation frequency. The method of multiple scales is used to obtain a first order approximation to the response and the approximation and the modulation equations are given by

$$
\begin{aligned}
v(s,t) &\approx \in a(t)\cos(\Omega t-\gamma)\phi_s(s)+\ldots \\
a' &= -\mu a-\frac{1}{2}\alpha_d c a^2+\frac{f}{2\omega_n}\sin\gamma \\
a\gamma' &= \sigma a-\frac{\alpha}{4\omega_n}a^3+\frac{f}{2\omega_n}\cos\gamma
\end{aligned}
\tag{1.37}
$$

where μ is the modal damping coefficient, α are the nonlinear stiffness coefficients, f is forcing amplitude, and $\Phi(s)$ represents the linear mode shape of the undamped system. These equations are then used to examine the frequency-response of a system. The parameter values of the system can then be estimated by a least-square curve fitting the experimental frequency-response data.

Finally, Dick, Balachandran, DeVoe and Mote [10] devised a parameter identification scheme based on device frequency response. Dick *et al*. observed nonlinear behavior in experimentally measured frequency-response of microresonators. A least squares parameter identification scheme was devised in combination with the analytical model

$$
\overline{m}\ddot{x}+\overline{c}\dot{x}+kz+\alpha_3 z^3=F\,cos(\omega t) \tag{1.38}
$$

(m and c are the modal mass and damping, k is the linear stiffness, α_3 is the nonlinear stiffness, F is the forcing amplitude and ω is the excitation frequency). in order to determine system parameters for the micro-resonators considered.

Although considerable work on determining residual stress in micro-scale structures has been done before, the determination of residual stress post-release and pre release states has not been given careful consideration before. This is addressed here.

1.5 Scope and Organization of Dissertation

Within this dissertation, plate models and their applications to the residual stress deformation in micro-scale structures are explored. Analytical models are developed to study the deformation and stresses in these devices. Reduced-order models are developed to aid in analysis of frequency-response data. Micro-scale cantilevered PZT structures and clamped-clamped PZT structures are fabricated to validate and enhance these models. Experiments were performed to collect data from these devices to aid in validation of models. Parametric identification schemes were developed to analyze the residual stress and system parameters. Through these studies, a greater understanding of plate-like micro-scale structures has been gained and multiple methods that can be used to analyze them have been developed.

The organization of this dissertation is as follows. In Chapter 2, the development of linear and nonlinear thin composite laminate beam and plate models are presented. In Chapter 3, symmetric and asymmetric laminate schemes are described. Chapter 4 contains reduced-order linear and nonlinear beam models as well as a technique meant for developing reduced-order models for a plate that is either simply supported on all edges or clamped on all edges. In Chapter 5, a description on the fabrication processes, used in this work, for micro-scale cantilevers and clamped resonators as well as descriptions on all experimental arrangements are provided. In Chapter 6, residual stress induced deformation is analyzed in MEMS cantilevers as well as neutral axis location and its effect on residual force/moment/stress and laminate stiffness calculations. Following that, in Chapter 7, four different techniques based on models and methodologies presented in earlier chapters are presented and the results obtained are

discussed. Finally, concluding remarks and suggestions for future work are presented in Chapter 9. Appendices containing the programs used in the calculations as well as other particulars are included along with the references.

2 LINEAR AND NONLINEAR ANALYSIS OF COMPOSITE BEAMS AND PLATES

In this chapter, a Newtonian approach is first taken to derive the Euler-Bernoulli beam equation. Later, a linear equilibrium equation describing transverse deflections of a thin plate is developed. This linear plate model is expanded to include nonlinear stretching at its mid plane. Finally, classical laminate plate theory is presented.

2.1 Euler-Bernoulli Theory for Thin Beams

To begin the derivation of the equilibrium equation for an Euler-Bernoulli thin beam, first apply the Newtonian approach to the beam element in Figure 2.1 and sum the forces in the vertical direction,

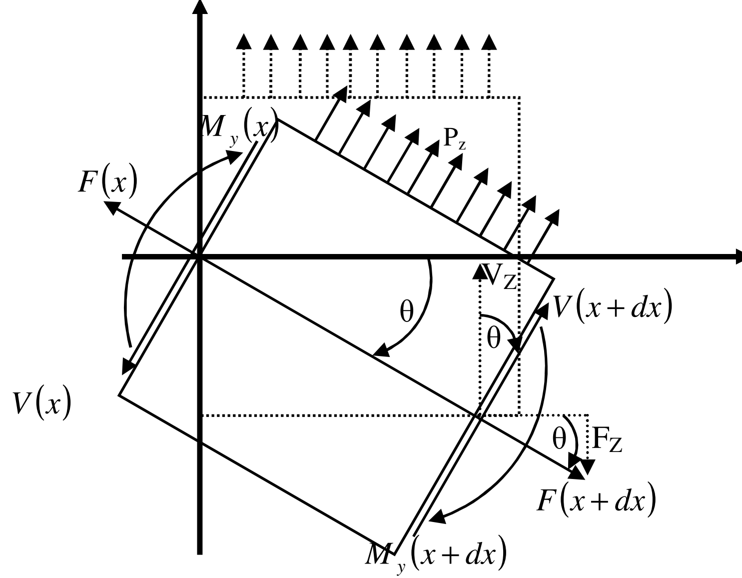

Figure 2.1: Differential beam element.

$$
\begin{aligned}
m\frac{\partial^2 w(x,t)}{\partial t^2} &= \sum(F_z) \\
&= F(x)\sin(\theta) - \left\{(F\sin(\theta)) + \frac{\partial}{\partial x}(F\sin(\theta))\right\} \\
&+ \left\{(V\cos(\theta)) + \frac{\partial}{\partial x}(V\cos(\theta))\right\} - V(x)\cos(\theta) + P_z dx \\
&= -\frac{\partial}{\partial x}(F\sin(\theta)) + \frac{\partial}{\partial x}(V\cos(\theta)) + P_Z(x,t)
\end{aligned}
\tag{2.1}
$$

For “small” angles, equation (2.1) becomes

$$
m\frac{\partial^2 w(x,t)}{\partial t^2} = -\frac{\partial}{\partial x}(F\theta) + \frac{\partial V}{\partial x} + P_Z(x,t) \tag{2.2}
$$

Summing the moments about the end of the beam element, one obtains

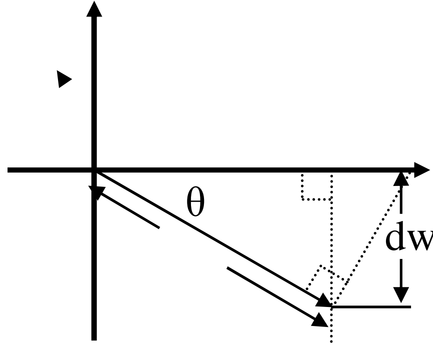

Figure 2.2: Differential distances and rotation angle of rotating beam element.

$$
\begin{aligned}
& -M_y(x)+M_y(x+dx)-V(x)\cos(\theta)dx=0 \\
& -M_y(x)+\left\{M_y(x)+\frac{\partial M_y}{\partial x}dx\right\}-V(x)dx=0 \\
& \frac{\partial M_y}{\partial x}dx-V(x)dx=0 \qquad (2.3) \\
& \frac{\partial M_y}{\partial x}-V(x)=0
\end{aligned}
$$

Solving equation (2.3) for the shear force, *V(x)*,

$$
\begin{aligned}
V(x) &= \frac{\partial M_y}{\partial x} \\
\frac{\partial V}{\partial x} &= \frac{\partial^2 M_y}{\partial x^2}
\end{aligned} \qquad (2.4)
$$

and inserting equation (2.4) into equation (2.2) results in

$$
m\frac{\partial^2 w(x,t)}{\partial t^2}=-\frac{\partial}{\partial x}(F\theta)+\frac{\partial^2 M_y}{\partial x^2}+P_Z(x,t) \qquad (2.5)
$$

The rotation angle, θ, can be related to the transverse displacement, w, by examining Figure 2.2., that is

$$sin(\theta) = -\frac{\partial w}{\partial x} \tag{2.6}$$

If the rotation angle θ is assumed small,

$$\theta = -\frac{\partial w}{\partial x} \tag{2.7}$$

Next, inserting equation (2.7) into (2.5) and noting that the force, F, is constant results in

$$\begin{aligned} m\frac{\partial^2 w(x,t)}{\partial t^2} &= -\frac{\partial}{\partial x}\left(F\left(-\frac{\partial w}{\partial x}\right)\right) + \frac{\partial^2 M_y}{\partial x^2} + P_Z(x,t) \\ m\frac{\partial^2 w(x,t)}{\partial t^2} &= F\frac{\partial^2 w}{\partial x^2} + \frac{\partial^2 M_y}{\partial x^2} + P_z(x,t) \end{aligned} \tag{2.8}$$

The bending moment, M_y, is related to the bending displacement via (2.9

$$M_y = (EI)\left(-\frac{\partial^2 w}{\partial x^2}\right) \tag{2.9}$$

and noting that $F = N_R$, where N_R is a *constant* force resultant due to residual stress, then the nonlinear equilibrium equation for a thin beam becomes

$$m\frac{\partial^2 w(x,t)}{\partial t^2} = F\frac{\partial^2 w}{\partial x^2} + \frac{\partial^2}{\partial x^2}\left((EI)\left(-\frac{\partial^2 w}{\partial x^2}\right)\right) + P_Z(x,t)$$

$$m\frac{\partial^2 w(x,t)}{\partial t^2} - N_R \frac{\partial^2 w}{\partial x^2} + (EI)\frac{\partial^4 w}{\partial x^4} = P_Z(x,t) \tag{2.10}$$

If large curvatures are present, then (2.9 becomes

$$\begin{aligned} M_y &= -(EI)\frac{\partial^2 w}{\partial x^2}\left(1 + \left(\frac{\partial w}{\partial x}\right)^2\right)^{-\frac{3}{2}} \\ &= -(EI)\frac{\partial^2 w}{\partial x^2}\left(1 - \frac{3}{2}\left(\frac{\partial w}{\partial x}\right)^2 + \cdots\right) \end{aligned} \tag{2.11}$$

The second derivative of the first two terms (2.11 are

$$\frac{\partial^2 M_y}{\partial x^2} = \frac{\partial^2}{\partial x^2}\left[-(EI)\frac{\partial^2 w}{\partial x^2}\left(1 - \frac{3}{2}\left(\frac{\partial w}{\partial x}\right)^2 + \cdots\right.\right] \tag{2.12}$$

and equation (2.10) becomes

$$m\frac{\partial^2 w(x,t)}{\partial t^2} - N_R \frac{d^2 w}{dx^2} + \frac{\partial^2}{\partial x^2}\left[(EI)\frac{\partial^2 w}{\partial x^2}\left(1 - \frac{3}{2}\left(\frac{\partial w}{\partial x}\right)^2 + \cdots\right.\right] - P_z(x,t) = 0 \tag{2.13}$$

Equation (2.13) is the nonlinear equilibrium equation describing the transverse displacement of a thin beam in its entirety. If all nonlinear terms in equation (2.13) are neglected, the equilibrium equation becomes

$$m\frac{\partial^2 w(x,t)}{\partial t^2} - N_R \frac{\partial^2 w}{\partial x^2} + (EI)\frac{\partial^4 w}{\partial x^4} = P_z(x,t) \tag{2.14}$$

Equation (2.14) will be used in later chapters for finding a general solution in terms of the transverse displacement *w(x,t)*, analyzing system natural frequencies and mode shapes, buckling analysis, and residual stress identification utilizing the residual force, N_R.

2.2 Linear Equilibrium Equation for Thin Plates: Static Equilibrium

To begin the derivation of the equation of motion of a thin plate, one must first consider some basic assumptions. First, the stress analysis of a thin plate can involve solutions of differential equations in three-dimensions and can be quite complex to determine. But, for many applications, applying Kirchhoff's classical theory of thin plates can yield sufficiently accurate results without the need to carry out a full, three-dimensional stress analysis [34]. The underlying assumptions are as follows:

1. The material is linear, homogeneous, isotropic, linear elastic, and follows Hooke's Law
2. The plate is initially flat
3. The thickness of the plate is constant and very small in comparison to its other dimensions
4. The mid-plane of the thin plate remains unstrained
5. Straight lines normal to the mid-plane before bending, remain straight, normal, and undeformed during bending ($\sigma_{xz}, \sigma_{yz}, \sigma_{zz}$ are negligible and the normal strain ε_z is assumed to be zero).

The above assumptions are common for a *linear* classical thin plate. In order to derive the differential equation of motion of a thin plate, one first considers the plate element shown in Figure 2.3. The *M*'s and *Q*'s are the mechanically applied moments and forces, and *p* is a generally applied transverse force. To begin, the force balance along the z-direction leads to:

$$p(x,y)dxdy + Q_x dy + Q_y dx - \left(Q_x + \frac{\partial Q_x}{\partial x}dx\right)dy - \left(Q_y + \frac{\partial Q_y}{\partial y}dy\right)dx = 0 \quad (2.15)$$

Dividing by dx dy, canceling out terms and taking limits as dx → 0 and dy → 0, results in

$$\frac{\partial Q_x}{\partial x} + \frac{\partial Q_y}{\partial y} = p(x,y) \quad (2.16)$$

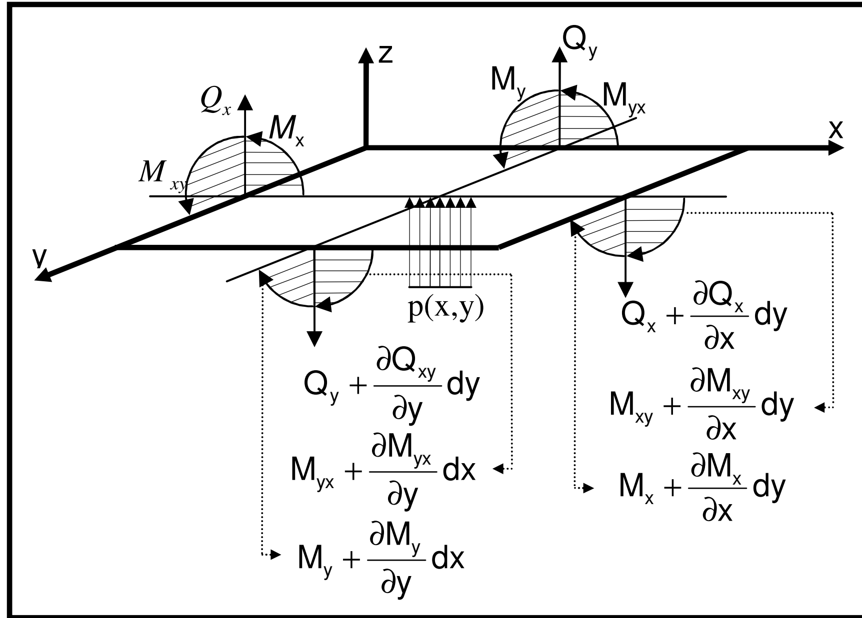

Figure 2.3: Plate Element.

A moment balance about the x-axis results in

$$
\begin{aligned}
&M_y dx - \left(M_y + \frac{\partial M_y}{\partial y} dy \right) dx + \left(M_{xy} + \frac{\partial M_{xy}}{\partial x} dx \right) dy - M_{xy} dy \\
&+ \left(Q_y + \frac{\partial Q_y}{\partial y} dy \right) dxdy + \left(Q_x + \frac{\partial Q_x}{\partial x} dx \right) dy \frac{dy}{2} - Q_x dy \frac{dy}{2} \\
&+ p(x, y) dxdy \frac{dy}{2} = 0
\end{aligned}
\tag{2.17}
$$

Again, dividing by dx and dy, canceling out terms and taking the limits dx → 0 and dy → 0, results in:

$$
\frac{\partial Q_y}{\partial y} = \frac{\partial^2 M_y}{\partial y^2} - \frac{\partial^2 M_{xy}}{\partial x \partial y} \tag{2.18}
$$

Likewise, a moment balance about the y-axis results in

$$
\frac{\partial Q_x}{\partial x} = \frac{\partial^2 M_x}{\partial x^2} - \frac{\partial^2 M_{yx}}{\partial x \partial y} \tag{2.19}
$$

After substituting from the moment balance equations, (2.18) and (2.19) into the force balance equation (2.16), one obtains

$$
\frac{\partial^2 M_x}{\partial x^2} - 2 \frac{\partial^2 M_{yx}}{\partial x \partial y} + \frac{\partial^2 M_y}{\partial y^2} = p(x, y) \tag{2.20}
$$

One defines the moments as

$$
\begin{aligned}
M_x &= -D\left(w_{xx} + \nu w_{yy}\right) \\
M_y &= -D\left(\nu w_{xx} + w_{yy}\right) \\
M_{xy} &= -D\left(-(1-\nu) w_{xy}\right)
\end{aligned}
\tag{2.21}
$$

D is the flexural rigidity of the thin plate, ν is the Poisson's ratio, and w_{xx}, w_{yy}, and w_{xy} are the plate curvatures, written in terms of the transverse deflection, w. When equations (2.21) are inserted into (2.20), the result is the static linear differential equation governing a thin isotropic plate subjected to transverse loading:

$$w_{xxxx} + 2w_{xxyy} + w_{yyyy} = \frac{p(x,y)}{D} \tag{2.22}$$

2.3 Nonlinear Equilibrium Equation for a Thin Plate

Plate deflections are usually assumed "small" in comparison to the thickness of the plate. By increasing the magnitude of the deflections beyond a certain level, the relationship between the external load and the deflection is no longer linear [34]. Due to large deflections, the stretching of the mid-plane now needs to be taken into consideration. To account for large deflections, nonlinear theory needs to be considered. According to Kirchhoff's theory, if the deflection in the z-direction is greater than 1/5 of the plate's

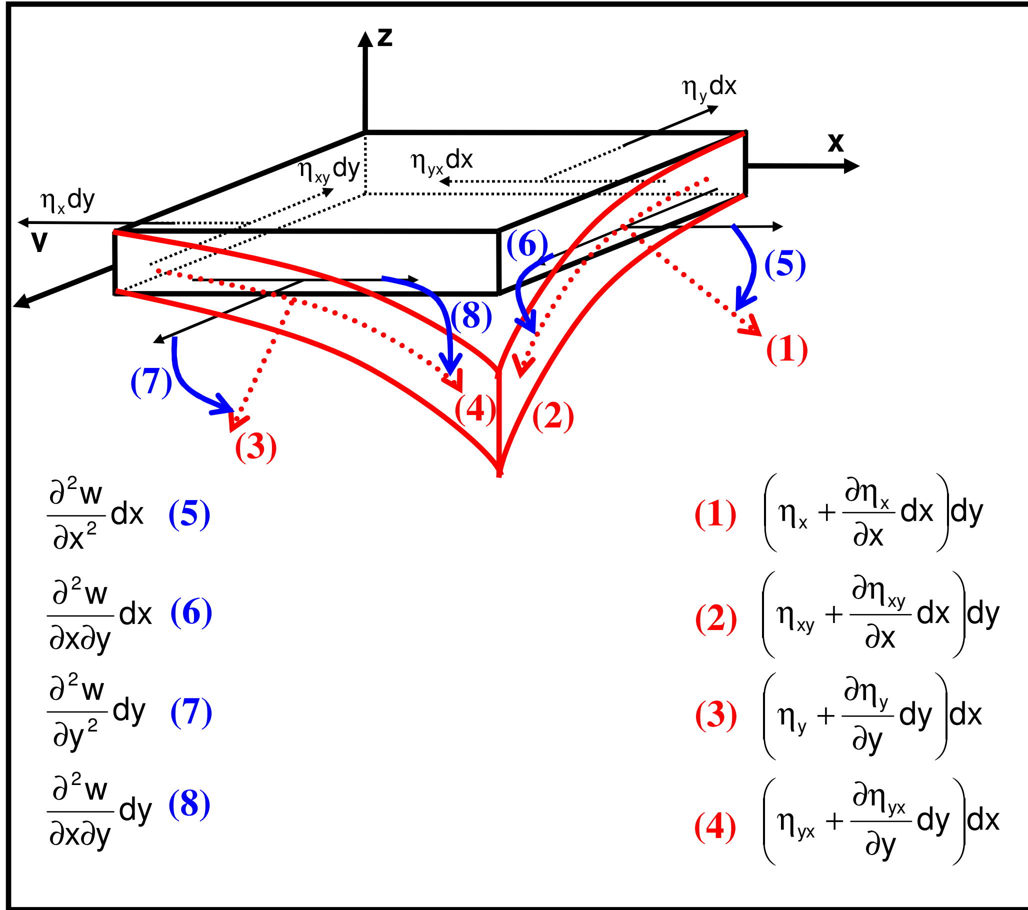

Figure 2.4: Deformed plate element with membrane forces.

thickness, then the deformation is considered to be nonlinear. Linear deformation theory neglects the straining of the mid-surface of the plate and the corresponding in-plane stresses, whereas in nonlinear deformation theory, one does not. To incorporate the membrane forces, consider the plate element shown in Figure 2.4.

The expressions (1) through (4) in Figure 2.4 are the membrane forces and the expressions (5) through (8) are the curvatures if the plate element is in bending. Now, consider the projections of the membrane forces in the z-direction, as given in [34], that is,

$$P_{membrane} = \sum F_Z \quad = \left[\eta_x + \frac{\partial \eta_x}{\partial x} dx\right] dy \left(\frac{\partial^2 w}{\partial x^2} dx\right) + \left[\eta_y + \frac{\partial \eta_y}{\partial y} dy\right] dx \left(\frac{\partial^2 w}{\partial y^2} dy\right) + \left[\eta_{xy} + \frac{\partial \eta_{xy}}{\partial x} dx\right] dy \left(\frac{\partial^2 w}{\partial x \partial y} dx\right) + \left[\eta_{yx} + \frac{\partial \eta_{yx}}{\partial y} dy\right] dx \left(\frac{\partial^2 w}{\partial y \partial x} dy\right) = 0 \tag{2.23}$$

If equation (2.23) is divided by dx dy throughout, and the limits as dx $\rightarrow$ 0 and dy $\rightarrow$ 0 are considered, equation (2.23) becomes

$$\eta_x \frac{\partial^2 w}{\partial x^2} + \eta_y \frac{\partial^2 w}{\partial y^2} + 2\eta_{xy} \frac{\partial^2 w}{\partial x \partial y} = P_{membrane} \tag{2.24}$$

Thus the effect of the membrane forces on the transverse deflection is equivalent to a fictitious lateral force [34]. Introducing the Airy stress function $\Phi(x, y)$ [34] and

$$\Phi_{xx} = \eta_y \quad \Phi_{yy} = \eta_x \quad \Phi_{xx} = -\eta_{xy} \tag{2.25}$$

and the nonlinear differential equation describing the static deflection of a thin plate subjected to large deflections becomes

$$w_{xxxx} + 2w_{xxyy} + w_{yyyy} = \frac{1}{D}\left[p(x, y) + \Phi_{xx} w_{yy} + \Phi_{yy} w_{xx} - 2\Phi_{xy} w_{xy}\right] \tag{2.26}$$

Comparing equation (2.26) with equation (2.22), it is mentioned that equation (2.26) includes the membrane force terms. To obtain the equation governing dynamic equilibrium, inertia forces would have to be included and the time variable *t* would also need to be introduced.

2.4 Classical Laminated Plate Theory: Dynamic Case

Classical laminated plate theory (CLPT) is an extension of classical plate theory [35]. In CLPT, it's assumed that the Kirchhoff hypothesis holds and that the displacement kinematics are of the form

$$\begin{aligned} u(x,y,z,t) &= u_o(x,y,t) - z\frac{\partial w_o}{\partial x} \\ v(x,y,z,t) &= v_o(x,y,t) - z\frac{\partial w_o}{\partial y} \\ w(x,y,z,t) &= w_o(x,y,t) \end{aligned} \tag{2.27}$$

where u, v, and w are the displacements along the x, y, and z directions, respectively, u_o, v_o, and w_o are the translational displacements along the respective directions and z*(dw/dx) and z*(dw/dy) are due to the rotations about the x and y axes. The Euler-Lagrange equations are obtained by substituting expressions for the potential energy U, the virtual work done by applied forces W, and the kinetic energy T into the extended Hamilton's principle

$$\int_{t_1}^{t_2} (\delta U - \delta W - \delta T)dt = 0 \tag{2.28}$$

As in [35], by inserting the energy expressions and setting the coefficients of the virtual displacements δu_o, δv_o, and δw_o equal to zero separately provides the Euler-Lagrange equations as

$$\delta u_o \quad \Rightarrow \quad \frac{\partial N_{xx}}{\partial x} + \frac{\partial N_{xy}}{\partial y} = I_0 \frac{\partial^2 u_o}{\partial t^2} - I_1 \frac{\partial^2}{\partial t^2}\left(\frac{\partial w_o}{\partial x}\right)$$

$$\delta v_o \quad \Rightarrow \quad \frac{\partial N_{xy}}{\partial x} + \frac{\partial N_{yy}}{\partial y} = I_0 \frac{\partial^2 v_o}{\partial t^2} - I_1 \frac{\partial^2}{\partial t^2}\left(\frac{\partial w_o}{\partial y}\right)$$

$$\delta w_o \quad \Rightarrow \quad \frac{\partial^2 M_{xx}}{\partial x^2} + 2\frac{\partial^2 M_{xy}}{\partial x \partial y} + \frac{\partial^2 M_{yy}}{\partial y^2} + N(w_o) + q$$

$$= I_o \frac{\partial^2 w_o}{\partial t^2} - I_2 \frac{\partial^2}{\partial t^2}\left(\frac{\partial^2 w_o}{\partial x^2} + \frac{\partial^2 w_o}{\partial y^2}\right) + I_1 \frac{\partial^2}{\partial t^2}\left(\frac{\partial^2 u_o}{\partial x^2} + \frac{\partial^2 v_o}{\partial y^2}\right) \tag{2.29}$$

where the inertia properties have also been considered. In equation (2.29), if the equation corresponding to δu_0 is solved for $\partial^2 u_o / \partial t^2$ and likewise, the equation corresponding to δv_0 is solved for $\partial^2 v_o / \partial t^2$, and then both of these expressions are inserted into the equation corresponding to δw_0, one obtains

$$\begin{aligned}
&\frac{\partial^2 M_{xx}}{\partial x^2} + 2\frac{\partial^2 M_{xy}}{\partial x \partial y} + \frac{\partial^2 M_{yy}}{\partial y^2} + N(w_o) + q - I_o \frac{\partial^2 w_o}{\partial t^2} \\
&= \left(-I_2 + \frac{I_1^2}{I_0}\right)\frac{\partial^2}{\partial t^2}\left(\frac{\partial^2 w_o}{\partial x^2} + \frac{\partial^2 w_o}{\partial y^2}\right) \\
&+ \frac{I_1}{I_0}\left(\frac{\partial^2 N_{xx}}{\partial x^2} + 2\frac{\partial^2 N_{xy}}{\partial x \partial y} + \frac{\partial^2 N_{yy}}{\partial y^2}\right)
\end{aligned} \tag{2.30}$$

where

$$N(w_o) = \frac{\partial}{\partial x}\left(N_{xx}\frac{\partial w_o}{\partial x} + N_{xy}\frac{\partial w_o}{\partial y}\right) + \frac{\partial}{\partial y}\left(N_{xy}\frac{\partial w_o}{\partial x} + N_{yy}\frac{\partial w_o}{\partial y}\right) \tag{2.31}$$

and

$$[I_0 \quad I_1 \quad I_2] = \sum_k^N \int_{-h_1}^{h_2} \rho_{ij}^{(k)} [1 \quad z \quad z^2] dz \tag{2.32}$$

I_2 is often ignored since it does not contribute to lower vibration modes (but can contribute to higher order vibration modes). The force and moment relations for classical laminate plate theory are given by

$$\begin{Bmatrix} N_{xx} \\ N_{yy} \\ N_{xy} \end{Bmatrix} = \begin{bmatrix} A_{11} & A_{12} & A_{16} \\ A_{12} & A_{22} & A_{26} \\ A_{16} & A_{26} & A_{66} \end{bmatrix} \begin{Bmatrix} \varepsilon_{xx}^{o} \\ \varepsilon_{yy}^{o} \\ \varepsilon_{xy}^{o} \end{Bmatrix} + \begin{bmatrix} B_{11} & B_{12} & B_{16} \\ B_{12} & B_{22} & B_{26} \\ B_{16} & B_{26} & B_{66} \end{bmatrix} \begin{Bmatrix} \varepsilon_{xx}^{1} \\ \varepsilon_{yy}^{1} \\ \varepsilon_{xy}^{1} \end{Bmatrix}$$

(2.33)

$$\begin{Bmatrix} M_{xx} \\ M_{yy} \\ M_{xy} \end{Bmatrix} = \begin{bmatrix} B_{11} & B_{12} & B_{16} \\ B_{12} & B_{22} & B_{26} \\ B_{16} & B_{26} & B_{66} \end{bmatrix} \begin{Bmatrix} \varepsilon_{xx}^{o} \\ \varepsilon_{yy}^{o} \\ \varepsilon_{xy}^{o} \end{Bmatrix} + \begin{bmatrix} D_{11} & D_{12} & D_{16} \\ D_{12} & D_{22} & D_{26} \\ D_{16} & D_{26} & D_{66} \end{bmatrix} \begin{Bmatrix} \varepsilon_{xx}^{1} \\ \varepsilon_{yy}^{1} \\ \varepsilon_{xy}^{1} \end{Bmatrix}$$

where the strain-displacement relations take the form

$$\begin{Bmatrix} \varepsilon_{xx}^{o} \\ \varepsilon_{yy}^{o} \\ \varepsilon_{xy}^{o} \end{Bmatrix} = \underbrace{\begin{Bmatrix} \dfrac{\partial u_o}{\partial x} + \dfrac{1}{2}\left(\dfrac{\partial w_o}{\partial x}\right)^2 \\ \dfrac{\partial v_o}{\partial y} + \dfrac{1}{2}\left(\dfrac{\partial w_o}{\partial y}\right)^2 \\ \dfrac{\partial u_o}{\partial y} + \dfrac{\partial v_o}{\partial x} + \dfrac{\partial w_o}{\partial x}\dfrac{\partial w_o}{\partial y} \end{Bmatrix}}_{\text{Membrane Strains}} \qquad \begin{Bmatrix} \varepsilon_{xx}^{1} \\ \varepsilon_{yy}^{1} \\ \varepsilon_{xy}^{1} \end{Bmatrix} = \underbrace{\begin{Bmatrix} \dfrac{\partial^2 w_o}{\partial x^2} \\ \dfrac{\partial^2 w_o}{\partial y^2} \\ \dfrac{\partial^2 w_o}{\partial x \partial y} \end{Bmatrix}}_{\text{Curvature Strains}} \tag{2.34}$$

([34], [35]). Equations (2.30) through (2.34) effectively describe the dynamics of a general, nonlinear, laminated, composite plate.

3 LAMINATE STIFFNESS ANALYSES

In this chapter, general laminate stiffness formulae are presented. These are followed by schemes for calculating stiffnesses in single and multi-layer laminates with either a symmetric layout or an asymmetric layout. Finally, a general laminate stiffness scheme is presented to calculate the stiffnesses for an isotropic laminate, regardless of the number of layers, material types or symmetry involved.

3.1 General Laminate Stiffness Formulae

Though laminate strains are continuous through thickness, the stresses are not due to the change in material coefficients through each lamina. Integration of the stresses through the laminate thickness requires lamina wise integration [35]. The force and moment resultants for a generalized laminate are given by

$$
\begin{aligned}
\begin{Bmatrix} N_{xx} \\ N_{yy} \\ N_{xy} \end{Bmatrix} &= \sum_{k=1}^{N} \int_{z_k}^{z_{k+1}} \begin{Bmatrix} \sigma_{xx} \\ \sigma_{yy} \\ \sigma_{xy} \end{Bmatrix} dz \\
&= \sum_{k=1}^{N} \int_{z_k}^{z_{k+1}} \begin{bmatrix} Q_{11} & Q_{12} & Q_{16} \\ Q_{12} & Q_{22} & Q_{26} \\ Q_{16} & Q_{26} & Q_{66} \end{bmatrix} \begin{Bmatrix} \varepsilon_{xx}^{(0)} + z\varepsilon_{xx}^{(1)} \\ \varepsilon_{yy}^{(0)} + z\varepsilon_{yy}^{(1)} \\ \varepsilon_{xy}^{(0)} + z\varepsilon_{xy}^{(1)} \end{Bmatrix} dz \\
&= \begin{bmatrix} A_{11} & A_{12} & A_{16} \\ A_{12} & A_{22} & A_{26} \\ A_{16} & A_{26} & A_{66} \end{bmatrix} \begin{Bmatrix} \varepsilon_{xx}^{(0)} \\ \varepsilon_{yy}^{(0)} \\ \varepsilon_{xy}^{(0)} \end{Bmatrix} + \begin{bmatrix} B_{11} & B_{12} & B_{16} \\ B_{12} & B_{22} & B_{26} \\ B_{16} & B_{26} & B_{66} \end{bmatrix} \begin{Bmatrix} \varepsilon_{xx}^{(1)} \\ \varepsilon_{yy}^{(1)} \\ \varepsilon_{xy}^{(1)} \end{Bmatrix}
\end{aligned}
\tag{3.1}
$$

and similarly

$$\begin{Bmatrix} M_{xx} \\ M_{yy} \\ M_{xy} \end{Bmatrix} = \begin{bmatrix} B_{11} & B_{12} & B_{16} \\ B_{12} & B_{22} & B_{26} \\ B_{16} & B_{26} & B_{66} \end{bmatrix} \begin{Bmatrix} \varepsilon_{xx}^{(0)} \\ \varepsilon_{yy}^{(0)} \\ \varepsilon_{xy}^{(0)} \end{Bmatrix} + \begin{bmatrix} D_{11} & D_{12} & D_{16} \\ D_{12} & D_{22} & D_{26} \\ D_{16} & D_{26} & D_{66} \end{bmatrix} \begin{Bmatrix} \varepsilon_{xx}^{(1)} \\ \varepsilon_{yy}^{(1)} \\ \varepsilon_{xy}^{(1)} \end{Bmatrix} \tag{3.2}$$

Here, A is the extensional stiffness matrix, D is the bending stiffness matrix,and B is the bending-extensional coupling stiffness matrix of the laminate. They are determined as

$$\begin{aligned} \left(A_{ij} \quad B_{ij} \quad D_{ij}\right) &= \int_{-\frac{h}{2}}^{\frac{h}{2}} Q_{ij} \left[1 \quad z \quad z^2\right] dz = \sum_{k=1}^{N} \int_{-\frac{h}{2}}^{\frac{h}{2}} Q_{ij} \left[1 \quad z \quad z^2\right] dz \\ A_{ij} &= \sum_{k=1}^{N} Q_{ij}^{(k)} \left(z_{k+1} - z_k\right) \\ B_{ij} &= \frac{1}{2} \sum_{k=1}^{N} Q_{ij}^{(k)} \left(z_{k+1}^2 - z_k^2\right) \\ D_{ij} &= \frac{1}{3} \sum_{k=1}^{N} Q_{ij}^{(k)} \left(z_{k+1}^3 - z_k^3\right) \end{aligned} \tag{3.3}$$

The coefficients, Q_{ij}, can be written as

$$\begin{aligned} Q_{11} &= \frac{E_1}{1 - \nu_{12}\nu_{21}} & Q_{22} &= \frac{E_2}{1 - \nu_{12}\nu_{21}} \\ Q_{12} &= \frac{\nu_{12}E_2}{1 - \nu_{12}\nu_{21}} = \frac{\nu_{21}E_1}{1 - \nu_{12}\nu_{21}} & Q_{66} &= G_{12} = \frac{E_1}{2(1 + \nu_{12})} \end{aligned} \tag{3.4}$$

where E_1 and E_2 are the Young's modulus, ν_{12} and ν_{21} are the Poisson's ratios, and G_{12} is the shear modulus. If a laminate is made of several layers, each of whose material axes is oriented arbitrarily, the constitutive equations in each layer must be transformed as

$$
\begin{aligned}
\overline{Q}_{11}^{(k)} &= Q_{11} cos^4\theta + 2(Q_{12}+2Q_{66}) sin^2\theta cos^2\theta + Q_{22} sin^4\theta \\
\overline{Q}_{12}^{(k)} &= (Q_{11}+Q_{22}-4Q_{66}) sin^2\theta cos^2\theta - Q_{12}(sin^4\theta + cos^4\theta) \\
\overline{Q}_{22}^{(k)} &= Q_{11} sin^4\theta + 2(Q_{12}+2Q_{66}) sin^2\theta cos^2\theta + Q_{22} cos^4\theta \\
\overline{Q}_{16}^{(k)} &= (Q_{11}-Q_{12}-2Q_{66}) sin\theta cos^3\theta + (Q_{12}-Q_{12}+2Q_{66}) sin^3\theta cos\theta \\
\overline{Q}_{26}^{(k)} &= (Q_{11}-Q_{12}-2Q_{66}) sin^3\theta cos\theta + (Q_{12}-Q_{12}+2Q_{66}) sin\theta cos^3\theta \\
\overline{Q}_{66}^{(k)} &= (Q_{11}+Q_{22}-2Q_{12}-2Q_{66}) sin^2\theta cos^2\theta + Q_{66}(sin^4\theta + cos^4\theta)
\end{aligned} \tag{3.5}
$$

where the rotation angle is θ.

3.2 Single Layer Plates

Single Isotropic Layer

For a single isotropic layer (principal material coordinates coincide with those of the plate) the laminate stiffnesses become

$$
\begin{aligned}
A_{11} &= \frac{Eh}{1-v^2} \quad A_{12} = vA_{11} \quad A_{22} = A_{11} \quad A_{66} = \frac{1-v}{2} A_{11} \\
D_{11} &= \frac{Eh^3}{12(1-v^2)} \quad D_{12} = vD_{11} \quad D_{22} = D_{11} \quad D_{66} = \frac{1-v}{2} D_{11}
\end{aligned} \tag{3.6}
$$

The plate constitutive equations for classical and first-order theories become

$$
\begin{Bmatrix} N_{xx} \\ N_{yy} \\ N_{xy} \end{Bmatrix} = \begin{bmatrix} A_{11} & vA_{11} & 0 \\ vA_{11} & A_{11} & 0 \\ 0 & 0 & \frac{1-v}{2} A_{11} \end{bmatrix} \begin{Bmatrix} \varepsilon^o_{xx} \\ \varepsilon^o_{yy} \\ \varepsilon^o_{xy} \end{Bmatrix} = \frac{Eh}{1-v^2} \begin{bmatrix} 1 & v & 0 \\ v & 1 & 0 \\ 0 & 0 & \frac{1-v}{2} \end{bmatrix} \begin{Bmatrix} \varepsilon^o_{xx} \\ \varepsilon^o_{yy} \\ \varepsilon^o_{xy} \end{Bmatrix} \tag{3.7}
$$

$$\begin{Bmatrix} M_{xx} \\ M_{yy} \\ M_{xy} \end{Bmatrix} = \begin{bmatrix} D_{11} & vD_{11} & 0 \\ vD_{11} & D_{11} & 0 \\ 0 & 0 & \frac{1-v}{2}D_{11} \end{bmatrix} \begin{Bmatrix} \varepsilon^{1}_{xx} \\ \varepsilon^{1}_{yy} \\ \varepsilon^{1}_{xy} \end{Bmatrix} = \frac{Eh^3}{12\left(1-v^2\right)} \begin{bmatrix} 1 & v & 0 \\ v & 1 & 0 \\ 0 & 0 & \frac{1-v}{2} \end{bmatrix} \begin{Bmatrix} \varepsilon^{o}_{xx} \\ \varepsilon^{o}_{yy} \\ \varepsilon^{o}_{xy} \end{Bmatrix}$$

Since the $[B]$ matrix has zero entries, it is clear that there is no coupling between bending and extensional motions.

Single Specially Orthotropic Layer

For a single specially orthotropic layer (material coordinates also lined up with plate coordinates), the laminate stiffnesses become

$$\begin{array}{llll} A_{11} = Q_{11}h & A_{12} = Q_{12}h & A_{22} = Q_{22}h & A_{66} = Q_{66}h \\ D_{11} = \frac{Q_{11}h^3}{12} & D_{12} = \frac{Q_{12}h^3}{12} & D_{22} = \frac{Q_{22}h^3}{12} & D_{66} = \frac{Q_{66}h^3}{12} \end{array} \tag{3.8}$$

where the plane stress reduced stiffnesses are given by

$$\begin{array}{c} Q_{11} = \frac{E_1}{1-v_{12}v_{21}} \qquad Q_{12} = \frac{v_{12}E_2}{1-v_{12}v_{21}} \qquad Q_{22} = \frac{E_2}{1-v_{12}v_{21}} \\ Q_{66} = G_{12} = \frac{E_1}{2\left(1+v_{12}\right)} \end{array} \tag{3.9}$$

The plate constitutive equations for classical and first-order theories become

$$\begin{Bmatrix} N_{xx} \\ N_{yy} \\ N_{xy} \end{Bmatrix} = h \begin{bmatrix} Q_{11} & Q_{12} & 0 \\ Q_{12} & Q_{22} & 0 \\ 0 & 0 & Q_{66} \end{bmatrix} \begin{Bmatrix} \varepsilon^{o}_{xx} \\ \varepsilon^{o}_{yy} \\ \varepsilon^{o}_{xy} \end{Bmatrix} = h \begin{bmatrix} \frac{E_1}{1-v_{12}v_{21}} & \frac{v_{21}E_2}{1-v_{12}v_{21}} & 0 \\ \frac{v_{21}E_2}{1-v_{12}v_{21}} & \frac{E_2}{1-v_{12}v_{21}} & 0 \\ 0 & 0 & \frac{E_1}{2\left(1+v_{12}\right)} \end{bmatrix} \begin{Bmatrix} \varepsilon^{o}_{xx} \\ \varepsilon^{o}_{yy} \\ \varepsilon^{o}_{xy} \end{Bmatrix}$$

(3.10)

$$\begin{Bmatrix} M_{xx} \\ M_{yy} \\ M_{xy} \end{Bmatrix} = \frac{h^3}{12}\begin{bmatrix} Q_{11} & Q_{12} & 0 \\ Q_{12} & Q_{22} & 0 \\ 0 & 0 & Q_{66} \end{bmatrix}\begin{Bmatrix} \varepsilon^o_{xx} \\ \varepsilon^o_{yy} \\ \varepsilon^o_{xy} \end{Bmatrix} = \frac{h^3}{12}\begin{bmatrix} \frac{E_1}{1-\nu_{12}\nu_{21}} & \frac{\nu_{21}E_2}{1-\nu_{12}\nu_{21}} & 0 \\ \frac{\nu_{21}E_2}{1-\nu_{12}\nu_{21}} & \frac{E_2}{1-\nu_{12}\nu_{21}} & 0 \\ 0 & 0 & \frac{E_1}{2(1+\nu_{12})} \end{bmatrix}\begin{Bmatrix} \varepsilon^1_{xx} \\ \varepsilon^1_{yy} \\ \varepsilon^1_{xy} \end{Bmatrix}$$

Again, since the $[B]$ matrix has zero entries, it is clear that there is no coupling between bending and extensional motions.

Single Generally Orthotropic Layer

For a single generally orthotropic layer (principal material coordinates do not coincide with those of the plate), the laminate stiffnesses become

$$A_{ij} = \overline{Q}_{ij}h \quad D_{ij} = \frac{\overline{Q}_{ij}h^3}{12} \tag{3.11}$$

where the equations for transforming the coefficients are shown in equations (3.5). The equations for the laminate plate become

$$\begin{Bmatrix} N_{xx} \\ N_{yy} \\ N_{xy} \end{Bmatrix} = \begin{bmatrix} A_{11} & A_{12} & A_{16} \\ A_{12} & A_{22} & A_{26} \\ A_{16} & A_{26} & A_{66} \end{bmatrix}\begin{Bmatrix} \varepsilon^{(0)}_{xx} \\ \varepsilon^{(0)}_{yy} \\ \varepsilon^{(0)}_{xy} \end{Bmatrix}$$

(3.12)

$$\begin{Bmatrix} M_{xx} \\ M_{yy} \\ M_{xy} \end{Bmatrix} \quad \begin{bmatrix} D_{11} & D_{12} & D_{16} \\ D_{12} & D_{22} & D_{26} \\ D_{16} & D_{26} & D_{66} \end{bmatrix} \begin{Bmatrix} \varepsilon_{xx}^{(1)} \\ \varepsilon_{yy}^{(1)} \\ \varepsilon_{xy}^{(1)} \end{Bmatrix}$$

3.3 Symmetric Laminates

When lamination scheme, material properties and locations are symmetric about the mid-plane, the laminate is called a symmetric laminate (see Figure 3.1). In Figure 3.1, h is the total thickness of all laminates included. Due to the symmetry of the laminate, the coupling stiffnesses B_{ij} are zero, and with this assumption, one can simplify the equation of motion.

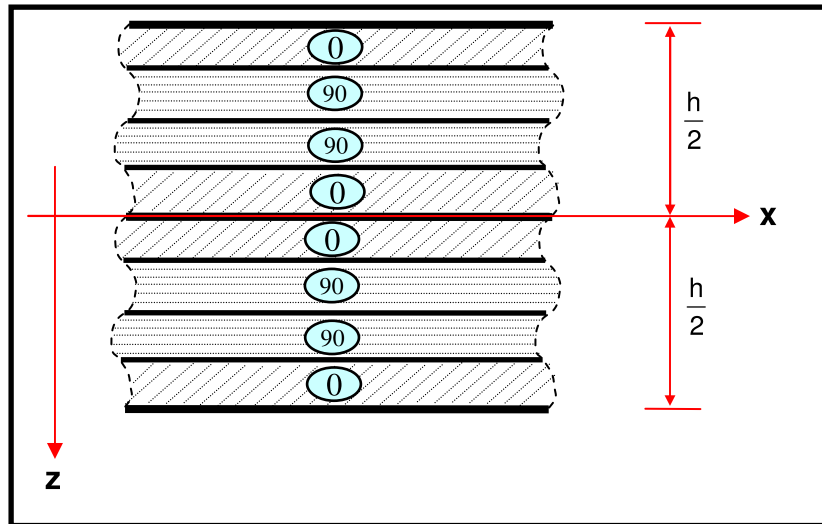

Figure 3.1: Symmetric laminate scheme.

Multiple Isotropic Layers

Similarly to a single isotropic layer, the stiffnesses and constitutive equations for a symmetric laminate with multiple isotropic layers become

$$\overline{Q}_{11}^{(k)} = \overline{Q}_{22}^{(k)} \frac{E^{(k)}}{1-\nu_{(k)}^2} \quad \overline{Q}_{16}^{(k)} = \overline{Q}_{26}^{(k)} = 0 \quad \overline{Q}_{12}^{(k)} = \frac{\nu_{(k)} E^{(k)}}{1-\nu_{(k)}^2} \quad \overline{Q}_{66}^{(k)} = \frac{E^{(k)}}{2\left(1+\nu_{(k)}\right)}$$

(3.13)

where E and ν are the Young's modulus and Poisson's ratio. The forces and moments are

$$\begin{Bmatrix} N_{xx} \\ N_{yy} \\ N_{xy} \end{Bmatrix} = \begin{bmatrix} A_{11} & A_{12} & 0 \\ A_{12} & A_{11} & 0 \\ 0 & 0 & A_{66} \end{bmatrix} \begin{Bmatrix} \varepsilon_{xx}^{o} \\ \varepsilon_{yy}^{o} \\ \varepsilon_{xy}^{o} \end{Bmatrix}$$

(3.14)

$$\begin{Bmatrix} M_{xx} \\ M_{yy} \\ M_{xy} \end{Bmatrix} = \begin{bmatrix} D_{11} & D_{12} & 0 \\ D_{12} & D_{22} & 0 \\ 0 & 0 & D_{66} \end{bmatrix} \begin{Bmatrix} \varepsilon_{xx}^{1} \\ \varepsilon_{yy}^{1} \\ \varepsilon_{xy}^{1} \end{Bmatrix}$$

Multiple Specially Orthotropic Layers

Stiffnesses of symmetric laminates with multiple specially orthotropic layers can be derived similarly from a single layer as

$$\overline{Q}_{11}^{(k)} = \frac{E_1^{(k)}}{1 - v_{12}^{(k)} v_{21}^{(k)}} \qquad \overline{Q}_{12}^{(k)} = \frac{v_{12}^{(k)} E_2^{(k)}}{1 - v_{12}^{(k)} v_{21}^{(k)}} \qquad \overline{Q}_{22}^{(k)} = \frac{E_2}{1 - v_{12} v_{21}}$$

$$Q_{66}^{(k)} = G_{12}^{(k)} = \frac{E_1^{(k)}}{2\left(1 + v_{12}^{(k)}\right)} \tag{3.15}$$

where the constitutive equations are

$$\begin{Bmatrix} N_{xx} \\ N_{yy} \\ N_{xy} \end{Bmatrix} = \begin{bmatrix} A_{11} & A_{12} & 0 \\ A_{12} & A_{11} & 0 \\ 0 & 0 & A_{66} \end{bmatrix} \begin{Bmatrix} \varepsilon^{o}_{xx} \\ \varepsilon^{o}_{yy} \\ \varepsilon^{o}_{xy} \end{Bmatrix}$$

(3.16)

$$\begin{Bmatrix} M_{xx} \\ M_{yy} \\ M_{xy} \end{Bmatrix} = \begin{bmatrix} D_{11} & D_{12} & 0 \\ D_{12} & D_{22} & 0 \\ 0 & 0 & D_{66} \end{bmatrix} \begin{Bmatrix} \varepsilon^{1}_{xx} \\ \varepsilon^{1}_{yy} \\ \varepsilon^{1}_{xy} \end{Bmatrix}$$

Multiple Generally Orthotropic Layers

Stiffnesses of symmetric laminates with multiple generally orthotropic layers can be derived similarly from a single layer as

$$A_{ij} = \overline{Q}_{ij}^{(k)} h \quad D_{ij} = \frac{\overline{Q}_{ij}^{(k)} h^3}{12} \tag{3.17}$$

where the forces and moments are

$$g\begin{Bmatrix} N_{xx} \\ N_{yy} \\ N_{xy} \end{Bmatrix} = \begin{bmatrix} A_{11} & A_{12} & 0 \\ A_{12} & A_{11} & 0 \\ 0 & 0 & A_{66} \end{bmatrix} \begin{Bmatrix} \varepsilon^{o}_{xx} \\ \varepsilon^{o}_{yy} \\ \varepsilon^{o}_{xy} \end{Bmatrix}$$

(3.18)

$$\begin{Bmatrix} M_{xx} \\ M_{yy} \\ M_{xy} \end{Bmatrix} = \begin{bmatrix} D_{11} & D_{12} & 0 \\ D_{12} & D_{22} & 0 \\ 0 & 0 & D_{66} \end{bmatrix} \begin{Bmatrix} \varepsilon^{1}_{xx} \\ \varepsilon^{1}_{yy} \\ \varepsilon^{1}_{xy} \end{Bmatrix}$$

3.4 Asymmetric Laminates

Anti Symmetric Laminates

From a modeling standpoint, symmetric laminates are generally more desirable than anti symmetric laminates, because the bending-extensional coupling stiffness matrix, B, does not have to be considered. This, in turn, simplifies the constitutive equations for the laminate and the second-order, nonlinear, partial differential equation that results. However, in many applications, this is not a reasonable assumption. A representative anti symmetric laminate is shown in Figure 3.2. In a case such as in Figure 3.2 all types of stiffness components need to be included in the constitutive equations, that is

$$\begin{Bmatrix} N_{xx} \\ N_{yy} \\ N_{xy} \end{Bmatrix} = \begin{bmatrix} A_{11} & A_{12} & A_{16} \\ A_{12} & A_{22} & A_{26} \\ A_{16} & A_{26} & A_{66} \end{bmatrix} \begin{Bmatrix} \varepsilon^{(0)}_{xx} \\ \varepsilon^{(0)}_{yy} \\ \varepsilon^{(0)}_{xy} \end{Bmatrix} + \begin{bmatrix} B_{11} & B_{12} & B_{16} \\ B_{12} & B_{22} & B_{26} \\ B_{16} & B_{26} & B_{66} \end{bmatrix} \begin{Bmatrix} \varepsilon^{(1)}_{xx} \\ \varepsilon^{(1)}_{yy} \\ \varepsilon^{(1)}_{xy} \end{Bmatrix}$$

$$\begin{Bmatrix} M_{xx} \\ M_{yy} \\ M_{xy} \end{Bmatrix} = \begin{bmatrix} B_{11} & B_{12} & B_{16} \\ B_{12} & B_{22} & B_{26} \\ B_{16} & B_{26} & B_{66} \end{bmatrix} \begin{Bmatrix} \varepsilon_{xx}^{(0)} \\ \varepsilon_{yy}^{(0)} \\ \varepsilon_{xy}^{(0)} \end{Bmatrix} + \begin{bmatrix} D_{11} & D_{12} & D_{16} \\ D_{12} & D_{22} & D_{26} \\ D_{16} & D_{26} & D_{66} \end{bmatrix} \begin{Bmatrix} \varepsilon_{xx}^{(1)} \\ \varepsilon_{yy}^{(1)} \\ \varepsilon_{xy}^{(1)} \end{Bmatrix} \tag{3.19}$$

However, suppose that this general class of anti symmetric laminates must have an even number of orthotropic layers, and opposite pairs of layers having identical thicknesses and exactly opposite orientations as pictured below in Figure 3.3.

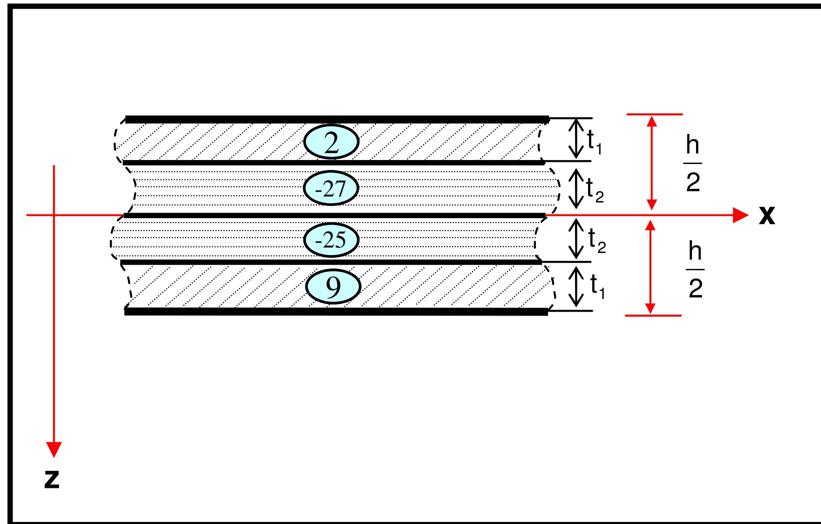

Figure 3.2: Fibers in each layer of this composite laminate have different orientations.

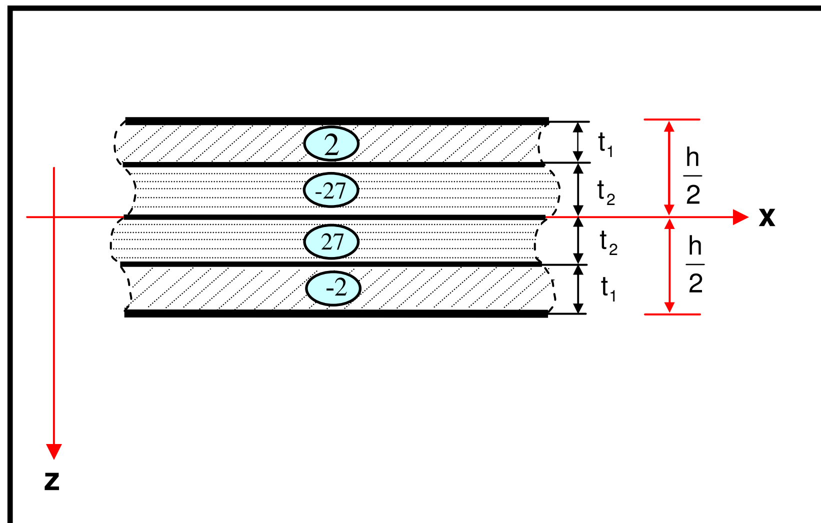

Figure 3.3: Fibers in each layer of this composite laminate have different orientations.

Then,the constitutive equations become

$$\begin{Bmatrix} N_{xx} \\ N_{yy} \\ N_{xy} \end{Bmatrix} = \begin{bmatrix} A_{11} & A_{12} & 0 \\ A_{12} & A_{22} & 0 \\ 0 & 0 & A_{66} \end{bmatrix} \begin{Bmatrix} \varepsilon_{xx}^{(0)} \\ \varepsilon_{yy}^{(0)} \\ \varepsilon_{xy}^{(0)} \end{Bmatrix} + \begin{bmatrix} B_{11} & B_{12} & B_{16} \\ B_{12} & B_{22} & B_{26} \\ B_{16} & B_{26} & B_{66} \end{bmatrix} \begin{Bmatrix} \varepsilon_{xx}^{(1)} \\ \varepsilon_{yy}^{(1)} \\ \varepsilon_{xy}^{(1)} \end{Bmatrix}$$

$$\begin{Bmatrix} M_{xx} \\ M_{yy} \\ M_{xy} \end{Bmatrix} = \begin{bmatrix} B_{11} & B_{12} & B_{16} \\ B_{12} & B_{22} & B_{26} \\ B_{16} & B_{26} & B_{66} \end{bmatrix} \begin{Bmatrix} \varepsilon_{xx}^{(0)} \\ \varepsilon_{yy}^{(0)} \\ \varepsilon_{xy}^{(0)} \end{Bmatrix} + \begin{bmatrix} D_{11} & D_{12} & 0 \\ D_{12} & D_{22} & 0 \\ 0 & 0 & D_{66} \end{bmatrix} \begin{Bmatrix} \varepsilon_{xx}^{(1)} \\ \varepsilon_{yy}^{(1)} \\ \varepsilon_{xy}^{(1)} \end{Bmatrix} \quad (3.20)$$

Unsymmetric Laminates

An unsymmetric laminate is the most general case of a laminate. In this laminate, no sense of symmetry exists. Multiple material layers exist, in even or odd numbers. Thicknesses are not necessarily equal to or symmetric about the neutral axis and the neutral axis is not always at the mid-line of the laminate layers. For the cases considered in this dissertion, an unsymmetric laminate scheme with multiple isotropic layers will be investigated (Figure 3.4). Specifically, because there is no symmetry in the layer thicknesses (t_1, t_2, t_3, t_4), coupling between extension and bending is present and has to

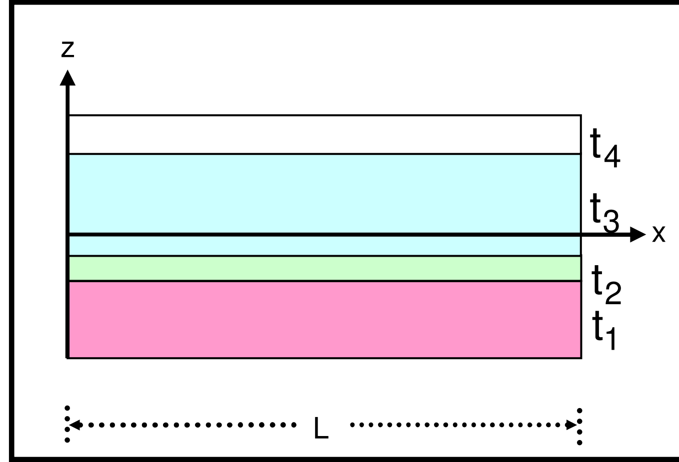

Figure 3.4: Unsymmetric laminate scheme.

be accounted for. In addition, the neutral axis is no longer at the mid-plane of the laminate. The force and moment resultants become

$$\begin{Bmatrix} N_{xx} \\ N_{yy} \\ N_{xy} \end{Bmatrix} = \begin{bmatrix} A_{11} & A_{12} & 0 \\ A_{12} & A_{22} & 0 \\ 0 & 0 & A_{66} \end{bmatrix} \begin{Bmatrix} \varepsilon_{xx}^{(0)} \\ \varepsilon_{yy}^{(0)} \\ \varepsilon_{xy}^{(0)} \end{Bmatrix} + \begin{bmatrix} B_{11} & B_{12} & 0 \\ B_{12} & B_{22} & 0 \\ 0 & 0 & B_{66} \end{bmatrix} \begin{Bmatrix} \varepsilon_{xx}^{(1)} \\ \varepsilon_{yy}^{(1)} \\ \varepsilon_{xy}^{(1)} \end{Bmatrix}$$

$$\begin{Bmatrix} M_{xx} \\ M_{yy} \\ M_{xy} \end{Bmatrix} = \begin{bmatrix} B_{11} & B_{12} & 0 \\ B_{12} & B_{22} & 0 \\ 0 & 0 & B_{66} \end{bmatrix} \begin{Bmatrix} \varepsilon_{xx}^{(0)} \\ \varepsilon_{yy}^{(0)} \\ \varepsilon_{xy}^{(0)} \end{Bmatrix} + \begin{bmatrix} D_{11} & D_{12} & 0 \\ D_{12} & D_{22} & 0 \\ 0 & 0 & D_{66} \end{bmatrix} \begin{Bmatrix} \varepsilon_{xx}^{(1)} \\ \varepsilon_{yy}^{(1)} \\ \varepsilon_{xy}^{(1)} \end{Bmatrix} \tag{3.21}$$

It is clear from equation (2.21) that the coupling exists, not just from material orthotropy, but rather from the laminate heterogeneity [36].

3.5 Generalized Laminate Stiffness Scheme

As was shown in Section 3.3, symmetric laminates are laminates where the lamination scheme, material properties and locations are symmetric about the mid-plane as well as

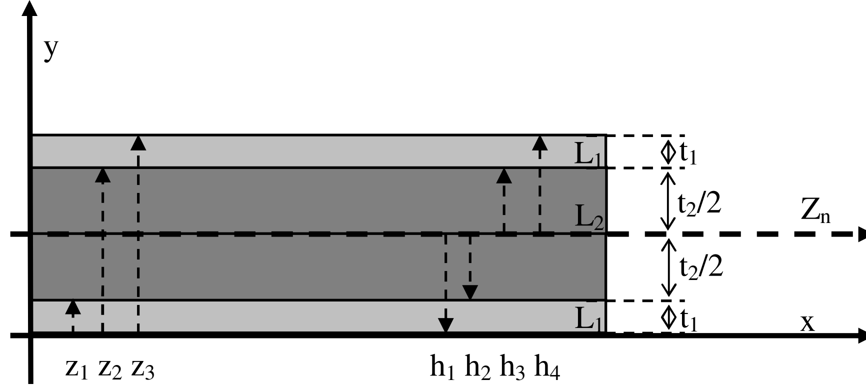

Figure 3.5: Symmetric laminate with three isotropic layers.

the neutral axis is in the same location as the mid-plane (Figure 3.5). Asymmetric laminates are not symmetric about its center axis, can have multiple material layers with varying thickness values. In this sction, the author presents a generalized laminate stiffness scheme that can be used to calculate the laminate stiffness for any number of material types and thicknesses, regardless of symmetry.

To begin, a representative symmetric laminate example with three laminate layers is shown in Figure 3.5. From Figure 3.5, two schemes are possible for defining laminate stiffnesses. If the x-axis is assumed to be at the bottom of the laminate, z_n can be written in terms of the layer thicknesses as

$$\begin{aligned} z_1 &= t_1 \\ z_2 &= t_1 + t_2 \\ z_3 &= 2t_1 + t_2 \end{aligned} \tag{3.22}$$

The extensional, coupling and bending stiffnesses can be written as

$$[EA]_{tot} = z = bEh\Big|_{h_n}^{h_{n+1}} = \sum_{k=1}^{N} b_k E_k \left(h_{k+1} + h_k\right) \tag{3.23}$$

$$[ES]_{tot} = \int_z bEzdz = bE\frac{1}{2}h^2\Big|_{h_n}^{h_{n+1}} = \frac{1}{2}\sum_{k=1}^{N} b_k E_k \left(h_{k+1}^2 - h_k^2\right) \quad (3.24)$$

$$[EI]_{tot} = \int_z bEz^2dz = bE\frac{1}{3}h^3\Big|_{h_n}^{h_{n+1}} = \frac{1}{3}\sum_{k=1}^{N} b_k E_k \left(h_{k+1}^3 - h_k^3\right) \quad (3.25)$$

When (3.22) is inserted into equations (3.23), (3.24) and (3.25), the stiffness expressions become

$$\begin{aligned}[EA]_{tot} &= bE_1(z_1 - 0) + bE_2(z_2 - z_1) + bE_1(z_3 - z_2) \\ &= bE_1(t_1) + bE_2(t_2) + bE_1(t_1) \\ &= 2E_1A_1 + E_2A_2\end{aligned} \quad (3.26)$$

$$\begin{aligned}[ES]_{tot} &= \frac{1}{2}bE_1\left(z_1^2 - 0\right) + \frac{1}{2}bE_2\left(z_2^2 - z_1^2\right) + \frac{1}{2}bE_1\left(z_3^2 - z_2^2\right) \\ &= \frac{1}{2}b(2t_1 + t_2)(2E_1t_1 + E_2t_2)\end{aligned} \quad (3.27)$$

$$\begin{aligned}[EI]_{tot} &= bE_1\left(z_1^3 - 0\right) + bE_2\left(z_2^3 - z_1^3\right) + bE_1\left(z_3^3 - z_2^3\right) \\ &= \frac{1}{3}b\left(E_1t_1^3 + E_2\left(-t_1^3 + (t_1 + t_2)^3\right) + E_3\left(-(t_1 + t_2)^3 + (2t_1 + t_2)^3\right)\right)\end{aligned} \quad (3.28)$$

One important observation to note is that equation (3.27) is nonzero. This clearly indicates for a symmetric laminate that coupling exists when the starting axis is anywhere but the midline or neutral axis of the laminate. If these calculations are taken about the center axis, or neutral axis, Z_n, h_n becomes

$$
\begin{aligned}
h_1 &= -\left(t_1 + \frac{t_2}{2}\right)\\
h_2 &= -\left(\frac{t_2}{2}\right)\\
h_3 &= \left(\frac{t_2}{2}\right)\\
h_4 &= \left(t_1 + \frac{t_2}{2}\right)
\end{aligned}
\tag{3.29}
$$

and the stiffness expressions become

$$
\begin{aligned}
[EA]_{tot} &= bE_1(h_2 - h_1) + bE_2(h_3 - h_2) + bE_1(h_4 - h_3)\\
&= bE_1(t_1) + bE_2(t_2) + bE_1(t_1)\\
&= E_1A_1 + E_2A_2 + E_1A_1
\end{aligned}
$$

$$
[EA]_{tot} = 2E_1A_1 + E_2A_2 \tag{3.30}
$$

$$
\begin{aligned}
[ES]_{tot} &= \frac{1}{2}bE_1(h_2^2 - h_1^2) + \frac{1}{2}bE_2(h_3^2 - h_2^2) + \frac{1}{2}bE_1(h_4^2 - h_3^2)\\
&= \frac{1}{2}bE_1(-t_1^2 - t_1t_2) + \frac{1}{2}bE_2\left(\frac{t_2^2}{4} - \frac{t_2^2}{4}\right)\\
&+ \frac{1}{2}bE_1(t_1^2 + t_1t_2)\\
&= 0
\end{aligned}
\tag{3.31}
$$

$$
\begin{aligned}
[EI]_{tot} &= bE_1(h_2^3 - h_1^3) + bE_2(h_3^3 - h_2^3) + bE_1(h_4^3 - h_3^3)\\
&= \frac{1}{3}bE_1\left(t_1^3 + \frac{3t_1^2t_2}{2} + \frac{3t_1t_2^2}{4}\right) + \frac{1}{3}bE_2\left(\frac{t_2^3}{4}\right)\\
&+ \frac{1}{3}bE_1\left(t_1^3 + \frac{3t_1^2t_2}{2} + \frac{3t_1t_2^2}{4}\right)\\
&= \frac{1}{12}b\left(E_2t_2^3 + 2E_1t_1\left(4t_1^2 + 6t_2t_2 + 3t_2^2\right)\right)
\end{aligned}
$$

$$
[EI]_{tot} = \frac{1}{12}E_2A_2t_2^2 + \frac{1}{12}2E_1A_1\left(4t_1^2 + 6t_2t_2 + 3t_2^2\right) \tag{3.32}
$$

Clearly,equation (3.31) shows that coupling between extensional and bending stiffnesses does not exist for a symmetric laminate and may be neglected when the starting axis is

taken about the neutral axis of the structure. This can greatly simplify the governing equation of motion for a plate or beam by making it possible to neglect unnecessary linear and nonlinear terms due to coupling.

However, similar to Figure 3.5, if an asymmetric laminate with three isotropic layers is considered (Figure 3.6),

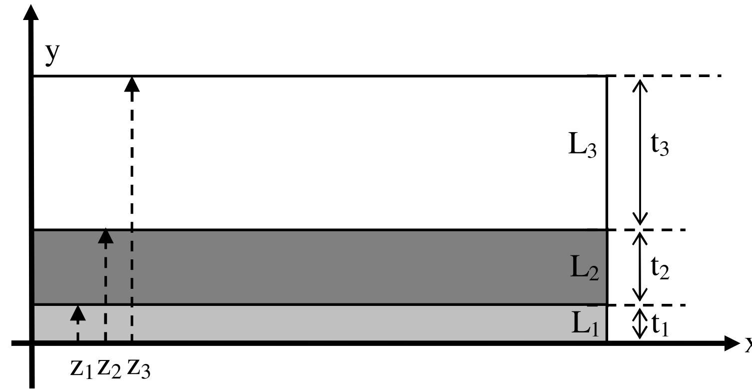

Figure 3.6: Asymmetric laminate with three isotropic layers.

then z_n in terms of the layer thicknesses become

$$\begin{aligned} z_1 &= t_1 \\ z_2 &= t_1 + t_2 \\ z_3 &= t_1 + t_2 + t_3 \end{aligned} \tag{3.33}$$

the extensional stiffness, coupled stiffness and bending stiffness become

$$\begin{aligned} [EA]_{tot} &= bE_1(z_1 - 0) + bE_2(z_2 - z_1) + bE_3(z_3 - z_2) \\ &= b(E_1 t_1 + E_2 t_2 + E_3 t_3) \end{aligned} \tag{3.34}$$

$$\begin{aligned} [ES]_{tot} &= \frac{1}{2} bE_1(z_1^2 - 0) + \frac{1}{2} bE_2(z_2^2 - z_1^2) + \frac{1}{2} bE_3(z_3^2 - z_2^2) \\ &= \frac{1}{2} b\left(E_1 t_1^2 + E_2 t_2(2t_1 + t_2) + E_3 t_3(2t_1 + 2t_2 + t_3)\right) \end{aligned} \tag{3.35}$$

$$
\begin{aligned}
[EI]_{tot} &= \frac{1}{3}bE_1\left(z_1^3 - 0\right) + \frac{1}{3}bE_2\left(z_2^3 - z_1^3\right) + \frac{1}{3}bE_3\left(z_3^3 - z_2^3\right) \\
&= \frac{1}{3}b\left(E_1t_1^3 + E_2\left(-t_1^3 + (t_1 + t_2)^3\right) + E_3\left(-(t_1 + t_2)^3 + (t_1 + t_2 + t_3)^3\right)\right)
\end{aligned} \tag{3.36}
$$

Equation (3.35) indicates that for an asymmetric laminate that coupling exists when the starting axis is taken at the bottom of the laminate. However, in the case of an asymmetric laminate, the neutral axis is not in the center of the laminate. The neutral axis is dependent on the Young's modulus of each laminate layer, thickness and may be calculated as

$$
\begin{aligned}
Z_n = \frac{ES_{tot}}{EA_{tot}} &= \frac{\frac{1}{2}bE_L h^2\Big|_{h_n}^{h_{n+1}}}{bE_L h\Big|_{h_n}^{h_{n+1}}} \\
&= \frac{\frac{1}{2}b\left(E_1t_1^2 + E_2t_2(2t_1 + t_2) + E_3t_3(2t_1 + 2t_2 + t_3)\right)}{b\left(E_1t_1 + E_2t_2 + E_3t_3\right)}
\end{aligned} \tag{3.37}
$$

Defining h_n about the neutral axis as shown in Figure 3.7,

$$
\begin{aligned}
h_1 &= -Z_n \\
h_2 &= z_1 - Z_n \\
h_3 &= z_2 - Z_n \\
h_4 &= z_3 - Z_n
\end{aligned} \tag{3.38}
$$

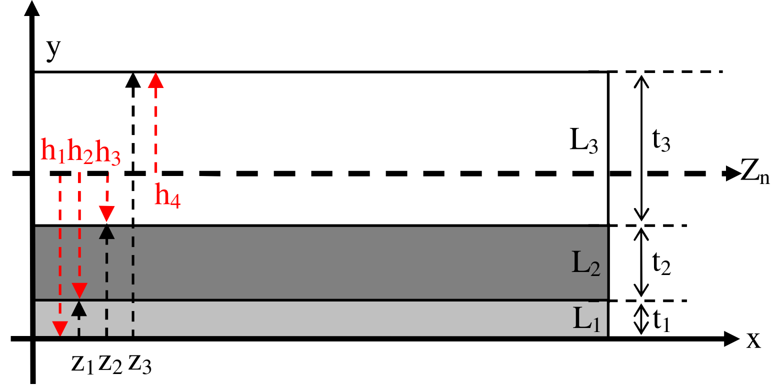

Figure 3.7: Asymmetric laminate with three isotropic layers and neutral axis location.

First,considering the extensional stiffness,

$$\begin{aligned}[EA]_{tot} &= bE_1(h_2-h_1)+bE_2(h_3-h_2)+bE_3(h_4-h_3) \\ &= bE_1((z_1-Z_n)-(-Z_n))+bE_2((z_2-Z_n)-(z_1-Z_n)) \\ &\quad +bE_3((z_3-Z_n)-(z_2-Z_n)) \\ &= bE_1t_1+bE_2t_2+bE_3t_3\end{aligned} \tag{3.39}$$

it is clear that the neutral axis location cancels out, and that the extensional stiffness in equation (3.39) is not dependent on neutral axis location and is equivalent to equation (3.34).

If the coupled and bending stiffness is revisited,

$$
\begin{aligned}
[ES]_{tot} &= \frac{1}{2}bE_1\left(h_2^2 - h_1^2\right) \\
&+ \frac{1}{2}bE_2\left(h_3^2 - h_2^2\right) \\
&+ \frac{1}{2}bE_3\left(h_4^2 - h_3^2\right) \\
&= \frac{1}{2}bE_1\left((z_1 - Z_n)^2 - (-Z_n)^2\right) \\
&+ \frac{1}{2}bE_2\left((z_2 - Z_n)^2 - (z_1 - Z_n)^2\right) \\
&+ \frac{1}{2}bE_3\left((z_3 - Z_n)^2 - (z_2 - Z_n)^2\right) \\
&= 0
\end{aligned}
\tag{3.40}
$$

$$
\begin{aligned}
[EI]_{tot} = b\Big(&E_1^2 t_1^4 + E_2^2 t_2^4 + E_3^2 t_3^4 \\
&+ 2E_2E_3t_2t_3\left(2t_2^2 + 3t_2t_3 + 2t_3^2\right) \\
&+ 2E_1t_1 \\
&\quad \Big(E_2t_2\left(2t_1^2 + 3t_1t_2 + 2t_2^2\right) \\
&\quad + E_3t_3\big(2t_1^2 + 6t_1t_2 + 6t_2^2 \\
&\quad + 3t_1t_3 + 6t_2t_3 + 2t_3^2\big)\Big)\Big) \\
&\quad /\left(12\left(E_1t_1 + E_2t_2 + E_3t_3\right)\right)
\end{aligned}
\tag{3.41}
$$

Clearly, for an asymmetric laminate, using the neutral axis in stiffness calculations will eliminate coupling between bending and extension.

To generalize stiffness calculations for symmetric or asymmetric laminates with an indefinite number of isotropic layers, first define z_n (Figure 3.8),

$$
\begin{aligned}
z_1 &= t_1 \\
z_2 &= t_1 + t_2 \\
z_3 &= t_1 + t_2 + t_3 \\
&\vdots \\
z_n &= t_1 + t_2 + t_3 + \cdots + t_n
\end{aligned}
\tag{3.42}
$$

The neutral axis location, for a general laminate, may be calculated as

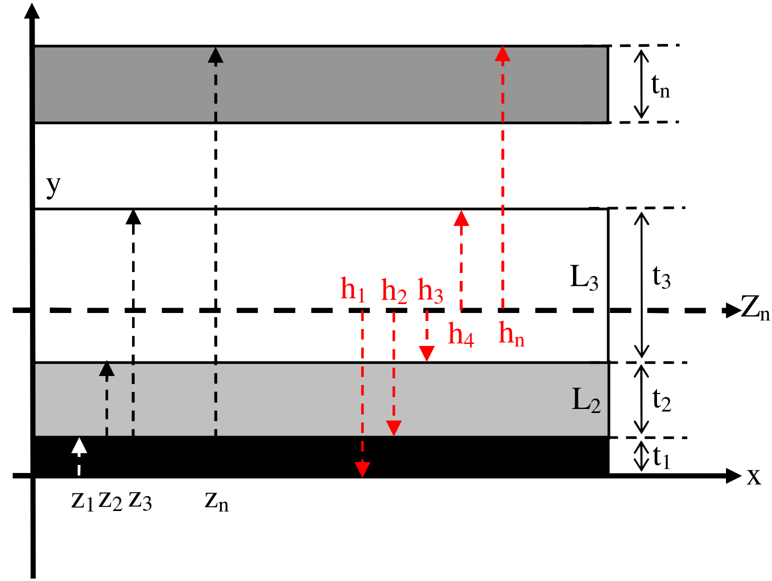

Figure 3.8: Asymmetric laminate with three isotropic layers and neutral axis location.

$$Z_{neutralaxis} = \frac{ES_{tot}}{EA_{tot}} = \frac{\frac{1}{2}\sum_{k=1}^{N} b_k E_k \left(h_{k+1}^2 + h_k^2\right)}{\sum_{k=1}^{N} b_k E_k \left(h_{k+1} + h_k\right)}$$

$$= \frac{\frac{1}{2} b_1 E_1 \left(z_2^2 + z_1^2\right) + \frac{1}{2} b_2 E_2 \left(z_2^2 + z_2^2\right) + \frac{1}{2} b_3 E_3 \left(z_4^2 + z_3^2\right) + \cdots + \frac{1}{2} b_n E_n \left(z_n^2 + z_{n-1}^2\right)}{b_1 E_1 \left(z_2 + z_1\right) + b_2 E_2 \left(z_3 + z_2\right) + b_3 E_3 \left(z_4 + z_3\right) + \cdots + b_n E_n \left(z_n + z_{n-1}\right)} \tag{3.43}$$

Once the location of the neutral axis location is known, the distances, h_n, are

$$
\begin{aligned}
h_1 &= -Z_n \\
h_2 &= z_1 - Z_n \\
h_3 &= z_2 - Z_n \\
h_4 &= z_3 - Z_n \\
&\vdots \\
h_n &= z_n - Z_n
\end{aligned}
\tag{3.44}
$$

and the extensional stiffness can be defined as

$$[EA]_{tot} = bE_1t_1 + bE_2t_2 + bE_3t_3 + \cdots + bE_nt_n$$

$$[EA]_{tot} = b \sum_{k=1}^{n=\#Layers} E_k t_k \tag{3.45}$$

$$[ES]_{tot} = 0 \tag{3.46}$$

$$
\begin{aligned}
[EI]_{tot} = \; & = \frac{1}{2} bE_1 \left((z_1 - Z_n)^2 - (-Z_n)^2 \right) \\
& + \frac{1}{2} bE_2 \left((z_2 - Z_n)^2 - (z_1 - Z_n)^2 \right) \\
& + \frac{1}{2} bE_3 \left((z_3 - Z_n)^2 - (z_2 - Z_n)^2 \right) \\
& \vdots \\
& + \frac{1}{2} bE_n \left((z_n - Z_n)^2 - (z_{n-1} - Z_n)^2 \right)
\end{aligned}
$$

$$[EI]_{tot} = \frac{1}{2} \sum_{k=1}^{n=\#Layers} bE_k \left((z_k - Z_n)^2 - (z_{k-1} - Z_n)^2 \right) \tag{3.46}$$

4 REDUCED-ORDER MODELS FOR PLATE-LIKE STRUCTURES

In this chapter, a reduced-order model is first presented for a thin composite laminate beam. Following that, reduced-order models are developed for plate structures, Since the variables in the plate equation are not separable, a procedure is developed to develop and approximate solution to the plate mode shapes and static stress function (Airy's function). Two special cases are considered, namely, a plate with all edges simply supported and all edges clamped.

4.1 Thin Composite Laminate Beams

The objective here is to determine a reduced-order model describing the transverse displacement of a thin beam with some given boundary conditions. If equation (2.13) is revisited

$$m\frac{\partial^2 w(x,t)}{\partial t^2} - N_R\frac{\partial^2 w}{\partial x^2} + \frac{\partial^2}{\partial x^2}\left[(EI)\frac{\partial^2 w}{\partial x^2}\left(1-\frac{3}{2}\left(\frac{\partial w}{\partial x}\right)^2 + \cdots\right]\right] - P_z(x,t) = 0 \qquad (4.1)$$

and all nonlinear terms are neglected, equation (4.1) becomes

$$\frac{\partial^2 w(x,t)}{\partial t^2} + \left(\frac{EI}{m}\right)\frac{\partial^4 w(x,t)}{\partial x^4} = 0 \qquad (4.2)$$

The transverse displacement may be defined as

$$W(x,t) = w(x) f(t) \tag{4.3}$$

and if inserted into the linear equilibrium equation (4.2),

$$\frac{EI}{m} \frac{d^4 w(x)}{dx^4} \frac{1}{\mathrm{w(x)}} = -\frac{1}{f(t)} \frac{d^2 f(t)}{dt^2} = \omega^2 \tag{4.4}$$

Equation (4.4) clearly indicates that the deflection variable x is separable from the time variable t and exact solutions exist for $w(x)$ and $f(t)$.

If the transverse displacement $w(x,t)$ is redefined as

$$W(x,t) = \Psi_n(x) f(t) \tag{4.5}$$

where Ψ_n represents general mode shapes for any beam boundary condition. If equation (4.5) is inserted into the nonlinear equilibrium equation for a thin beam (4.1) and the external loading is considered, (4.1) becomes

$$\begin{aligned} & m\Psi_n(x) \frac{d^2 f(t)}{dt^2} \\ & - N_R \frac{d^2 \Psi_n(x)}{dx^2} f(t) \\ & + EI \frac{d}{dx^2} \left(\frac{d^2 \Psi_n(x)}{dx^2} - \frac{3}{2} (EI) \left(\frac{d\Psi_n(x)}{dx} \right)^2 + \cdots \right) f^3(t) \\ & - P_z(x,t) = 0 \end{aligned} \tag{4.6}$$

In order to apply the method of weighted residuals [37] and complete the reduced-order model, a set of weighting functions is chosen similar to Ψ_n is chosen as Ψ_m. If equation (4.6) is multiplied by Ψ_m and integrated over the beam length, x, equation (4.6) becomes

$$a\ddot{f}(t)+bf(t)+cf^{3}(t)=Q$$

$$a=\int_{0}^{l} m\Psi_n(x)\Psi_m(x)dx$$

$$b=\int_{0}^{l}\left(N_R\left(-\frac{d^2\Psi_n(x)}{dx^2}\right)+(EI)\frac{d^4\Psi_n(x)}{dx^4}\right)\Psi_m(x)dx$$

$$c=\int_{0}^{l} EI\frac{d}{dx^2}\left(-\frac{3}{2}(EI)\left(\frac{d\Psi_n(x)}{dx}\right)^2+\cdots\right)\Psi_m(x)dx$$

$$Q=\int_{0}^{l} P_z(x,t)\Psi_m(x)dx$$

(4.7)

where the over dots in equation (4.7) indicate time derivatives. Equation (4.7) is considered to be a reduced-order model for a thin beam, in the form of an undamped Düffing oscillator. In the damped case, an addition term and coefficient would be present in equation (4.7). In addition, here is assumed that a single mode dominates the response in using equation (4.5).

4.2 Thin Composite Laminate Plates

To begin reduction of the model describing the transverse displacement of a thin plate, First consider the equilibrium equation (Section 2.1) with no outside forces ($P_Z = 0$) and neglecting the nonlinear inplane forces,

$$I_o\frac{\partial^2 W}{\partial t^2}-\frac{\partial^2 M_x}{\partial x^2}-2\frac{\partial^2 M_{yx}}{\partial x\partial y}-\frac{\partial^2 M_y}{\partial y^2}=0 \quad (4.8)$$

If the stiffnesses are calculated via the general scheme presented in Section 3.5, then coupling between extensional and bending stiffnesses can be assumed negligible, the bending stiffness is calculated around the laminate's neutral axis, and the moment-curvature relation is defined as

$$\begin{Bmatrix} M_{xx} \\ M_{yy} \\ M_{xy} \end{Bmatrix} = \begin{bmatrix} D_{11} & D_{12} & D_{16} \\ D_{12} & D_{22} & D_{26} \\ D_{16} & D_{26} & D_{66} \end{bmatrix} \begin{Bmatrix} \varepsilon^1_{xx} \\ \varepsilon^1_{yy} \\ \varepsilon^1_{xy} \end{Bmatrix} \tag{4.9}$$

where the curvatures are defined as

$$\begin{Bmatrix} \varepsilon^1_{xx} \\ \varepsilon^1_{yy} \\ \varepsilon^1_{xy} \end{Bmatrix} = \begin{Bmatrix} -\dfrac{\partial^2 W}{\partial x^2} \\ -\dfrac{\partial^2 W}{\partial y^2} \\ -2 * \dfrac{\partial^2 W}{\partial x \partial y} \end{Bmatrix} \tag{4.10}$$

and assuming each layer is isotropic, the bending stiffnesses are defined as

$$\begin{bmatrix} D_{11} & D_{12} & D_{16} \\ D_{12} & D_{22} & D_{26} \\ D_{16} & D_{26} & D_{66} \end{bmatrix} = \begin{bmatrix} D_{11} & vD_{11} & 0 \\ vD_{11} & D_{11} & 0 \\ 0 & 0 & \dfrac{1-v}{2} D_{11} \end{bmatrix} = \frac{Eh^3}{12\left(1-v^2\right)} \begin{bmatrix} 1 & v & 0 \\ v & 1 & 0 \\ 0 & 0 & \dfrac{1-v}{2} \end{bmatrix} \tag{4.11}$$

For simplicity, the moment-curvature relation will be written as

$$\begin{Bmatrix} M_{xx} \\ M_{yy} \\ M_{xy} \end{Bmatrix} = \begin{bmatrix} D_{11} & D_{12} & 0 \\ D_{12} & D_{22} & 0 \\ 0 & 0 & D_{66} \end{bmatrix} \begin{Bmatrix} -\dfrac{\partial^2 W}{\partial x^2} \\ -\dfrac{\partial^2 W}{\partial y^2} \\ -2 * \dfrac{\partial^2 W}{\partial x \partial y} \end{Bmatrix} \tag{4.12}$$

If equation (4.12) is inserted into equation (4.8),

$$I_O \frac{\partial^2 W}{\partial t^2} + D_{11} \frac{\partial^4 W}{\partial x^4} + 2(D_{12} + 2D_{66}) \frac{\partial^4 W}{\partial x^2 \partial y^2} + D_{22} \frac{\partial^4 W}{\partial x^4} = 0 \tag{4.13}$$

From equation (4.11) it is seen that $D_{22} = D_{11}$, $D_{12} = \upsilon D_{11}$ and $D_{66} = (1 - \upsilon)/2 * D_{11}$ and the equilibrium equation describing the transverse displacement of a thin isotropic laminate plate becomes

$$I_O \frac{\partial^2 W}{\partial t^2} + D_{11} \left(\frac{\partial^4 W}{\partial x^4} + 2 \frac{\partial^4 W}{\partial x^2 \partial y^2} + \frac{\partial^4 W}{\partial x^4} \right) = 0 \tag{4.14}$$

4.3 Separation of Variables – Motivation for Plate Mode-Shape Approximations

Since the equilibrium equation is a function of three variables, length *x*, width *y* and time *t*, it is convenient if the length and width dependence is first assumed to be separable from the dependence on time *t* as

$$W(x, y, t) = F_1(x, y) F_2(t) \tag{4.15}$$

Inserting equation (4.15) into (4.14), the author obtains

$$I_o F_1(x,y)\frac{d^2F_2(t)}{dt^2}$$
$$+D_{11}F_2(t)\left(\frac{d^4F_1(x,y)}{dx^4}+2\frac{d^4F_1(x,y)}{dx^2dy^2}+\frac{d^4F_1(x,y)}{dy^4}\right) \tag{4.16}$$
$$=0$$

along with the appropriate boundary conditions. Rearranging position variables on one side and time dependent variables on the other, equilibrium equation (4.16) becomes

$$-I_o\frac{1}{F_2(t)}\frac{d^2F_2(t)}{dt^2}$$
$$=D_{11}\frac{1}{F_1(x,y)}\left(\frac{d^4F_1(x,y)}{dx^4}+2\frac{d^4F_1(x,y)}{dx^2dy^2}+\frac{d^4F_1(x,y)}{dy^4}\right) \tag{4.17}$$
$$=\omega_{n1}^2$$

where ω_{n1}^2 is a set of constant values referred to as characteristic values or eigenvalues. From equation (4.17) its clear that the length dependent variables can be separated from time as

$$-I_o\frac{\partial^2F_2(t)}{\partial t^2}+\omega_{n1}^2F_2(t)=0 \tag{4.18}$$

$$D_{11}\left(\frac{\partial^4F_1(x,y)}{\partial x^4}+2\frac{\partial^4F_1(x,y)}{\partial x^2\partial y^2}+\frac{\partial^4F_1(x,y)}{\partial y^4}\right)-F_1(x,y)\omega_{n1}^2=0 \tag{4.19}$$

To determine where the length *X* is separable from the width *Y*, let

$$F_1(x,y)=X(x)Y(y) \tag{4.20}$$

and inserting equation (4.20) into (4.19). This leads to

$$D_{11}\left(\frac{d^4X(x)}{dx^4}Y(y)+2\frac{d^2X(x)}{dx^2}\frac{d^2Y(y)}{dy^2}+X(x)\frac{d^4Y(y)}{dy^y}\right)-X(x)Y(y)\omega_{n1}^2=0$$

(4.21)

and grouping X and Y terms

$$D_{11}\left(\frac{d^4X(x)}{dx^4}\frac{1}{X(x)}\right)+2D_{11}\underbrace{\left(\frac{1}{X(x)}\frac{d^2X(x)}{dx^2}\frac{1}{Y(y)}\frac{d^2Y(y)}{dy^2}\right)}_{\text{Makes Equation UNSEPARABLE}}=\frac{1}{Y(y)}\frac{d^4Y(y)}{dy^y}+\omega_{n1}^2$$

(4.22)

Clearly, the second term in equation (4.22) makes the equation unseparable. In other words, the dependence on the length x cannot be separated from the dependence on the width y. An exact solution for equation (4.19) does not exist for arbitrary boundary conditions.

4.4 Von Karman Strain Field and Compatibility Equation

Before the nonlinear plate equation of (2.26) can reduced to the form of the Düffing oscillator, the relationship between the static stress function $\Phi(x,y)$ and the transverse displacement $W(x,y)$ needs to be examined. When considering linear plate theory based on Kirchhoff's assumptions, the theory is valid for cases when the transverse deflections are much less then the thickness of the plate. The extension to large deflections, where nonlinear terms are retained, was first provided by von Karman [38]. First, consider the general plate element shown in Figure 4.1.

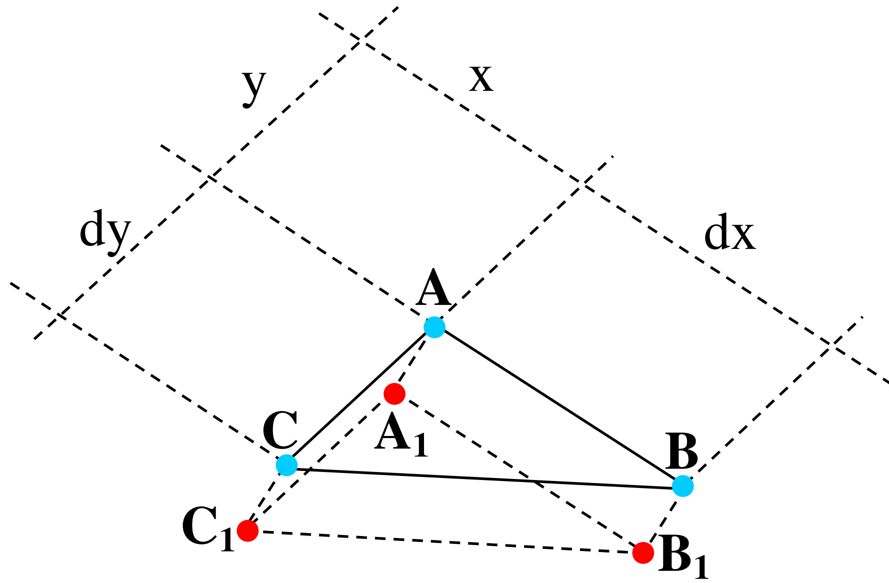

Figure 4.1: General plate element exhibiting stretching.

In Figure 4.2, the points A, B, and C denote the original plate element, and A_1, B_1, and C_1 signify the plate element that is deformed due to stretching. The axial strain in the x-direction can be defined as ([34], [35]).

$$\begin{aligned} \varepsilon_x &= \frac{A_1B_1 - AB}{AB} \\ &= \frac{\partial u}{\partial x} + \frac{1}{2}\left(\frac{\partial w}{\partial x}\right)^2 \end{aligned} \tag{4.23}$$

where A_1B_1 represents the line segment connecting points A_1 and B_1, and *AB* is the line segment connecting the points *A* and *B*. In equation (4.23), the axial strain ε_x effectively describes the stretching of line segment AB. The additional nonlinear strains are defined similarly as

$$\varepsilon_{yy} = \frac{\partial v}{\partial y} + \frac{1}{2}\left(\frac{\partial w}{\partial y}\right)^2 \tag{4.24}$$

$$\varepsilon_{xy} = \frac{\partial u}{\partial y} + \frac{\partial v}{\partial x} + \frac{\partial w}{\partial x}\frac{\partial w}{\partial y} \tag{4.25}$$

If the compatibility equation is considered

$$\frac{\partial^2 \varepsilon_x}{\partial y^2} + \frac{\partial^2 \varepsilon_y}{\partial x^2} = \frac{\partial^2 \varepsilon_{xy}}{\partial x \partial y} \tag{4.26}$$

and the strains given by equations (4.23), (4.24) and (4.25) are inserted into equation (4.26), equation (4.26) becomes

$$\frac{\partial^2 \varepsilon_{xx}}{\partial y^2} + \frac{\partial^2 \varepsilon_{yy}}{\partial x^2} - \frac{\partial^2 \varepsilon_{xy}}{\partial x \partial y} = \left(\frac{\partial^2 w}{\partial x \partial y}\right)^2 - \frac{\partial^2 w}{\partial x^2}\frac{\partial^2 w}{\partial y^2} \tag{4.27}$$

To obtain the nonlinear strain compatibility equation (4.27) in terms of the static stress function, Φ, the force-strain relation must be considered as

$$\begin{Bmatrix} N_{xx} \\ N_{yy} \\ N_{xy} \end{Bmatrix} = \begin{bmatrix} A_{11} & A_{12} & A_{16} \\ A_{12} & A_{22} & A_{26} \\ A_{16} & A_{26} & A_{66} \end{bmatrix} \begin{Bmatrix} \varepsilon^o_{xx} \\ \varepsilon^o_{yy} \\ \varepsilon^o_{xy} \end{Bmatrix} \tag{4.28}$$

Since an isotropic laminate is considered, equation (4.28) becomes

$$\begin{Bmatrix} N_{xx} \\ N_{yy} \\ N_{xy} \end{Bmatrix} = \begin{bmatrix} A_{11} & A_{12} & 0 \\ A_{12} & A_{22} & 0 \\ 0 & 0 & A_{66} \end{bmatrix} \begin{Bmatrix} \varepsilon^o_{xx} \\ \varepsilon^o_{yy} \\ \varepsilon^o_{xy} \end{Bmatrix} \tag{4.29}$$

Inserting the static stress function into equation (4.29) and solving for the axial and shear strains,

$$\begin{Bmatrix} \varepsilon^o_{xx} \\ \varepsilon^o_{yy} \\ \varepsilon^o_{xy} \end{Bmatrix} = \begin{bmatrix} A_{11} & A_{12} & 0 \\ A_{12} & A_{11} & 0 \\ 0 & 0 & A_{66} \end{bmatrix}^{-1} \begin{Bmatrix} N_{xx} \\ N_{yy} \\ N_{xy} \end{Bmatrix} = \begin{bmatrix} a_{11} & a_{12} & 0 \\ a_{12} & a_{11} & 0 \\ 0 & 0 & a_{66} \end{bmatrix} \begin{Bmatrix} \Phi_{yy} \\ \Phi_{xx} \\ -\Phi_{xy} \end{Bmatrix} \tag{4.30}$$

Noting that for an isotropic laminate, the elements of the stiffness matrix in equation (4.30) are such that $A_{22} = A_{11}$, $A_{12} = \upsilon * A_{11}$ and $A_{66} = (1-\upsilon)/2 * A_{11}$. If the strains defined by equation (4.30) are inserted into equation (4.27), the result is the compatibility equation that holds for the nonlinear strain-displacement field and the relationship between the static stress function and the transverse deflection *w*. This result reads as

$$\begin{aligned} \Phi_{xxxx} + 2\Phi_{xxyy} + \Phi_{yyyy} &= \left(\frac{1}{a_{11}}\right)\left[\left(\frac{\partial^2 w}{\partial x \partial y}\right)^2 - \frac{\partial^2 w}{\partial x^2}\frac{\partial^2 w}{\partial y^2}\right] \\ &= \left(\frac{1}{A_{11}}\right)\left(\frac{1}{1-\upsilon^2}\right)\left[\left(\frac{\partial^2 w}{\partial x \partial y}\right)^2 - \frac{\partial^2 w}{\partial x^2}\frac{\partial^2 w}{\partial y^2}\right] \\ &= (A)\left[\left(\frac{\partial^2 w}{\partial x \partial y}\right)^2 - \frac{\partial^2 w}{\partial x^2}\frac{\partial^2 w}{\partial y^2}\right] \end{aligned} \tag{4.31}$$

4.5 Solution to Compatibility Equation

The compatibility equation, (4.31), is now a fourth order partial differential equation whose solution, $\Phi(x, y)$, is broken into two parts, the particular and complimentary solutions; that is

$$\phi(x,y) = \underbrace{\phi_P(x,y)}_{Particular\ Soln} + \underbrace{\phi_C(x,y)}_{Complimentary\ Soln} = \underbrace{F(x,y)}_{Particular\ Soln} + \underbrace{\frac{1}{2}C^1_{ij}x^2 + \frac{1}{2}C^2_{ij}y^2}_{Complimentary\ Soln} \tag{4.32}$$

that can be solved in terms of the free (unforced) response (complimentary function)

$$\Phi_{C,xxxx} + 2\Phi_{C,xxyy} + \Phi_{C,yyyy} = 0 \qquad (4.33)$$

and the forced response (particular solution) as

$$\Phi_{P,xxxx} + 2\Phi_{P,xxyy} + \Phi_{P,yyyy} = \left(\frac{1}{a_{11}}\right)\left(\left(\frac{\partial^2 w}{\partial x \partial y}\right)^2 - \frac{\partial^2 w}{\partial x^2}\frac{\partial^2 w}{\partial y^2}\right) \qquad (4.34)$$

The coefficients C_{ij}^1 and C_{ij}^2 of the complimentary function are solved by applying the plate boundary conditions. In order to derive a solution to the compatibility equation, an expression must first be defined for the transverse displacement, $W(x, y)$. However, as was discussed in Section 4.3, the length dependent and time dependence are not separable in a general case. An approximation is necessary for the transverse displacement *W*. Once $W(x, y)$ and $\Phi(x, y)$ are known, these expressions can be insertedinto the equilibrium equation, and the equilibrium equation is reduced via Galerkin's Method, to the form of a reduced-order model given by the undamped Düffing oscillator.

4.6 Special Case: Composite Laminate Plate With All Edges Simply Supported

In this Section, a composite laminate plate with all edges simply-supported is considered ([15], [16], [17], [13], [14]) .

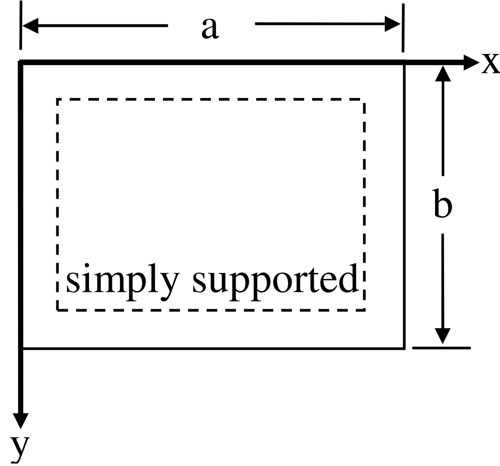

Figure 4.2: Thin laminate plate with simply supported boundaries.

The boundary conditions for a simply supported plate are

$$\begin{array}{llll} w(x,0,t)=0 & w(x,b,t)=0 & w(0,y,t)=0 & w(a,y,t)=0 \\ M_{xx}(0,y,t)=0 & M_{xx}(a,y,t)=0 & M_{yy}(x,0,t)=0 & M_{yy}(x,b,t)=0 \end{array} \tag{4.35}$$

and for a thin isotropic laminate, the moment-curvature relation is

$$\begin{Bmatrix} M_{xx} \\ M_{yy} \\ M_{xy} \end{Bmatrix} = \begin{bmatrix} D_{11} & \upsilon D_{11} & 0 \\ \upsilon D_{11} & D_{11} & 0 \\ 0 & 0 & \frac{1-\upsilon}{2} D_{11} \end{bmatrix} \begin{Bmatrix} -\frac{\partial^2 W}{\partial x^2} \\ -\frac{\partial^2 W}{\partial y^2} \\ -2\frac{\partial^2 W}{\partial x \partial y} \end{Bmatrix} \tag{4.36}$$

The *Navier* method expands the transverse displacement w into a double trigonometric Fourier series in terms of unknown parameters. The choice of trigonometric functions is those that satisfy boundary conditions. The externally applied load, $q(x, y)$, is similarly expanded. On substitution of the displacement and load expansions into the governing

equation of motion should result in an invertible set of algebraic equations. Otherwise, a Navier solution cannot be developed for that problem [35].

The boundary conditions in equation (4.35) are then satisfied by the Navier definition of the transverse displacement as

$$W(x, y, t) = \sum_{m}^{\infty}\sum_{n}^{\infty} W_{mn}(t)\sin(\alpha_m x)\sin(\beta_n y) \tag{4.37}$$
$$\alpha_m = \frac{m\pi}{a} \quad \beta_n = \frac{n\pi}{b}$$

If equation (4.37) is inserted into (4.31),

$$\begin{aligned}\Phi_{xxxx} + 2\Phi_{xxyy} + \Phi_{yyyy} &= \left(\frac{1}{a_{11}}\right)\left[\left(\frac{\partial^2 \mathrm{w}}{\partial \mathrm{x}\partial \mathrm{y}}\right)^2 - \frac{\partial^2 \mathrm{w}}{\partial \mathrm{x}^2}\frac{\partial^2 \mathrm{w}}{\partial \mathrm{y}^2}\right] \\ &= \sum_{m}\sum_{n}\left(\frac{1}{a_{11}}\right)\alpha_m^2\beta_n^2 W^2(t)(\cos[\alpha_m x]\cos[\alpha_n y] \\ &- \sin[\alpha_m x]\sin[\alpha_n y]) \\ &(\cos[\alpha_m x]\cos[\alpha_n y] + \sin[\alpha_m x]\sin[\alpha_n y])\end{aligned} \tag{4.38}$$

and if its rewritten in terms of the particular solution, several trigonometric identities through Mathematica (see appendices) are used, the compatibility equation can be rewritten as

$$\begin{aligned}&\Phi_{\mathrm{P,xxxx}} + 2\Phi_{\mathrm{P,xxyy}} + \Phi_{\mathrm{P,yyyy}} \\ &= \sum_{m}\sum_{n}\frac{1}{2}\left(\frac{1}{a_{11}}\right)\alpha_m^2\beta_n^2 W_{mn}^2(t)(\cos[2\alpha_m x] + \cos[2\beta_n y])\end{aligned} \tag{4.39}$$

Next, a particular solution, Φ, is chosen similar to the right side of equation (4.39) as

$$\Phi_{\mathrm{P}}(x, y) = \sum_{m}\sum_{n} F_1 \cos[2\alpha_m x] + F_2 \cos[2\beta_n y] \tag{4.40}$$

where F_1 and F_2 are unkown coefficients. If equation (4.40) is inserted into the left side of (4.39)

$$\begin{aligned} &16\alpha_m^4 F_1 \cos(2\alpha_m x) + 16\beta_n^4 F_2 \cos(2\beta_m y) \\ &= \frac{1}{2}\left(\frac{1}{a_{11}}\right)\alpha_m^2 \beta_n^2 W_{mn}^2(t)(\cos[2\alpha_m x] + \cos[2\beta_n y]) \end{aligned} \tag{4.41}$$

and it can be seen that the coefficients for equation (4.40 become

$$\begin{aligned} F_{1mn} &= \frac{1}{32a_{11}} \frac{\beta_n^2}{\alpha_m^2} W^2(t) \\ F_{2mn} &= \frac{1}{32a_{11}} \frac{\alpha_m^2}{\beta_n^2} W^2(t) \end{aligned} \tag{4.42}$$

From equations (4.40) and (4.42), the particular solution Φ_P exists, but does not satisfy the boundary conditions. The complimentary function is solved such that the solution to the compatibility equation, Φ, satisfies all boundary conditions. The complimentary function is chosen following He, [15], [16] and [17], as

$$\Phi_C(x, y) = \frac{1}{2} C_{ij}^1 x^2 + \frac{1}{2} C_{ij}^2 y^2 \tag{4.43}$$

and the complete solution to the compatibility equation becomes

$$\begin{aligned} \Phi(x, y) = \sum_m \sum_n \Bigg[&\frac{1}{2} C_{mn}^1 x^2 + \frac{1}{2} C_{mn}^2 y^2 \\ &+ \left(\frac{1}{32a_{11}} \frac{\beta_n^2}{\alpha_m^2} W^2(t)\right)\cos[2\alpha_m x] \\ &+ \left(\frac{1}{32a_{11}} \frac{\alpha_m^2}{\beta_n^2} W^2(t)\right)\cos[2\beta_n y] \Bigg] \end{aligned} \tag{4.44}$$

From the force-strain relation of equation (4.30), the axial strains may be written as

$$\begin{aligned} \varepsilon_x &= a_{11}\Phi_{yy} + a_{12}\Phi_{xx} = u_x + \frac{1}{2}(w_x)^2 \\ \varepsilon_x &= a_{12}\Phi_{yy} + a_{22}\Phi_{xx} = v_y + \frac{1}{2}(w_y)^2 \end{aligned} \tag{4.45}$$

If the derivatives of Φ are written as

$$\begin{aligned} \Phi_{xx} &= \Phi_{P,xx} + C_{ij}^{1} \\ \Phi_{yy} &= \Phi_{P,yy} + C_{ij}^{2} \end{aligned} \tag{4.46}$$

and inserted into equation (4.45), the coefficients to the complimentary function may be solved as

$$\begin{Bmatrix} C_{ij}^{2} \\ C_{ij}^{1} \end{Bmatrix} = [A] \begin{Bmatrix} u_{o,x} + \frac{1}{2}w_x^2 \\ v_{o,y} + \frac{1}{2}W_y^2 \end{Bmatrix} - \begin{Bmatrix} \Phi_{P,yy} \\ \Phi_{P,xx} \end{Bmatrix} \tag{4.47}$$

where the $[A]$ is the extensional stiffness matrix previously defined. The coefficients to the complimentary function clearly are a function of the transverse displacement, $W(x,y)$, the static stress function $\Phi(x,y)$ and the axial deflections u_x and u_y. Expressions and approximations for the transverse displacement, $W(x,y)$, equation (4.37), and the static stress function $\Phi(x,y)$, equation (4.40), can be inserted into equation (4.47), however, a known expression for the axial strains do not exist. Therefore, the boundary conditions will be applied to analyze the axial strains. If equation (4.47) is integrated over the plate boundaries,

$$\begin{Bmatrix} C_{ij}^2 \\ C_{ij}^1 \end{Bmatrix} = \left(\frac{1}{ab}\right)\int_0^a\int_0^b [A]\begin{Bmatrix} u_{o,x} \\ v_{o,y} \end{Bmatrix} dydx + \left(\frac{1}{ab}\right)\int_0^a\int_0^b \left[[A]\begin{Bmatrix} \frac{1}{2}w_x^2 \\ \frac{1}{2}W_y^2 \end{Bmatrix} - \begin{Bmatrix} \Phi_{P,yy} \\ \Phi_{P,xx} \end{Bmatrix} \right] dydx \tag{4.48}$$

and the axial strains are integrated once

$$\left(\frac{1}{ab}\right)\int_0^a\int_0^b \left[[A]\begin{Bmatrix} u_{o,x} \\ v_{o,y} \end{Bmatrix} \right] dydx = \left(\frac{1}{ab}\right)[A]\begin{Bmatrix} \int_0^b [u(x=a)-u(x=0)]dy \\ \int_0^a [v(y=b)-v(y=0)]dx \end{Bmatrix} \tag{4.49}$$

Notice that $u(x=a)$, $u(x=0)$, $v(y=b)$ and $v(y=b)$ are all zero for simply-supported boundary conditions then the first set of terms on the right side of equation (4.49) may be neglected and the coefficients to the complimentary function become

$$\begin{aligned} C_{mn}^1 \quad &= \sum_m \sum_n W_{mn}^2(t) \left[\frac{1}{8} A_{11}\left(\beta_n^2 + \alpha_m^2 v\right) \right. \\ &- \left(\frac{A_{11}\left(\beta_n^2 - \alpha_m^2 \upsilon\right)}{16a\alpha_m^2} \right) \sin[2a\alpha_m] \\ &+ \left(\frac{\left(\frac{1}{a_{11}}\right)\alpha_m^2 + A_{11}\left(\beta_n^2 - \alpha_m^2 \upsilon\right)}{16b\beta_n^2} \right) \sin[2b\beta_n] \\ &\left. - \left(\frac{A_{11}\left(\beta_n^2 + \alpha_m^2 \upsilon\right)}{32ab\alpha_m\beta_n} \right) \sin[2a\alpha_m] \sin[2b\beta_n] \right] \\ &= \sum_m \sum_n W_{mn}^2(t)\overline{C}_{mn}^1 \end{aligned} \tag{4.50}$$

$$
\begin{aligned}
C_{mn}^{2} &= \sum_{m}\sum_{n} W_{mn}^{2}(t)\Bigg[\frac{1}{8}A_{11}\left(\alpha_m^2+\beta_n^2 v\right) \\
&+\left(\frac{\left(\frac{1}{a_{11}}\right)\beta_n^2 + A_{11}\left(\alpha_m^2-\beta_n^2 \upsilon\right)}{16a\alpha_m^2}\right)\sin[2a\alpha_m] \\
&-\left(\frac{A_{11}\left(\alpha_m^2-\beta_n^2\upsilon\right)}{16b\beta_n^2}\right)\sin[2b\beta_n] \\
&-\left(\frac{A_{11}\left(\alpha_m^2+\beta_n^2\upsilon\right)}{32ab\alpha_m\beta_n^2}\right)\sin[2a\alpha_m]\sin[2b\beta_n]\Bigg] \\
&= \sum_{m}\sum_{n} W_{mn}^{2}(t)\overline{C}_{mn}^{2}
\end{aligned}
\qquad (4.51
$$

Notice that in (4.50) and (4.51), the *sin* terms become

$$
\begin{aligned}
\sin[2a\alpha_m] &= \sin\left[2a\frac{m\pi}{a}\right] = \sin[2m\pi] = 0 \quad \text{for m} = 1, 2, 3, \cdots, \infty \\
\sin[2b\beta_n] &= \sin\left[2b\frac{n\pi}{b}\right] = \sin[2n\pi] = 0 \quad \text{for n} = 1, 2, 3, \cdots, \infty
\end{aligned}
$$

and the coefficients become

$$
\begin{aligned}
C_{ij}^{1} &= W^2(t)\frac{1}{8}A_{11}\left(\beta_n^2+\alpha_m^2 v\right) \\
&= W^2(t)\overline{C}_{ij}^{1}
\end{aligned}
\qquad (4.52)
$$

$$
\begin{aligned}
C_{ij}^{2} &= W^2(t)\frac{1}{8}A_{11}\left(\alpha_m^2+\beta_n^2 v\right) \\
&= W^2(t)\overline{C}_{ij}^{2}
\end{aligned}
\qquad (4.53)
$$

Now that the coefficients for the complimentary function are defined, an expression exists for the static stress function, *Φ(x,y)*. With the approximations for the transverse displacement *W(x,y)*, equation (4.37), and the static stress function with the appropriate coefficients, equation (4.44), the equation of motion describing the transverse displacement of a thin laminate plate with all edges simply supported may be revisited as

$$I_O \frac{\partial^2 W}{\partial t^2} + D_{11}\left(\frac{\partial^4 W}{\partial x^4} + 2\frac{\partial^4 W}{\partial x^2 \partial y^2} + \frac{\partial^4 W}{\partial x^4}\right)$$
$$= Q + \left[p(x, y) + \Phi_{xx} w_{yy} + \Phi_{yy} w_{xx} - 2\Phi_{xy} w_{xy}\right] \tag{4.54}$$

and put in the form of a reduced-order model. If equations (4.37) and (4.44) are inserted into (4.54), (4.54) becomes

$$\begin{aligned}
&\sum_m \sum_n [[\sin(\alpha_m x)\sin(\beta_n y)] && * \frac{d^2 W_{mn}(t)}{dt^2} \\
&+ \left[(\alpha_m^2 + \beta_n^2)^2 D_{11} \sin(\alpha_m x)\sin(\beta_n y)\right] && * W_{mn}(t) \\
&\Big[(\beta_n^2 \overline{C}_{ij}^1 + \alpha_m^2 \overline{C}_{ij}^2)\sin(\alpha_m x)\sin(\beta_n y) && \\
&+ \frac{(\alpha_m^4 + \beta_n^4)}{8a_{11}}\cos(2\alpha_m x)\sin(\alpha_m x)\sin(\beta_n y) && \\
&+ \frac{(\alpha_m^4 + \beta_n^4)}{8a_{11}}\cos(2\beta_n y)\sin(\alpha_m x)\sin(\beta_n y)\Big] && * W_{mn}^3(t) \\
& && = Q]
\end{aligned} \tag{4.55}$$

In order to apply Galerkin's method, a technique for approximating the solution of a differential eigenvalue problem, an error function or residual is defined from equation (4.55) as

$$R = \sum_m \sum_n \left[c_1 \frac{d^2 W_{mn}(t)}{dt^2} + c_2 W_{mn}(t) + c_3 W_{mn}^3(t) - Q\right] \tag{4.56}$$

If a set of weighting functions are defined as

$$W_{WeightFcn}(x, y) = \sum_p^\infty \sum_q^\infty \sin(\alpha_p x)\sin(\beta_q y) \tag{4.57}$$

and the residual is multiplied by the weighting functions and integrated over the plate boundaries, the coefficients to equations (4.55) and (4.56) become

$$c_1 = \sum_m \sum_n \int_0^a \int_0^b [\sin(\alpha_m x)\sin(\beta_n y)]\sin(\alpha_p x)\sin(\beta_q y) dydx \tag{4.58}$$

$$c_2 = \sum_m \sum_n \int_0^a \int_0^b \left[\left(\alpha_m^2 + \beta_n^2\right)^2 D_{11} \sin(\alpha_m x)\sin(\beta_n y)\right] * \sin(\alpha_p x)\sin(\beta_q y) dydx]$$

$$c_3 = \sum_m \sum_n \int_0^a \int_0^b \Big[-\left(\beta_n^2 \overline{C}_{ij}^1 + \alpha_m^2 \overline{C}_{ij}^2\right) \sin(\alpha_m x)\sin(\beta_n y) + \frac{\beta_n^4}{8a_{11}} \cos(2\alpha_m x)\sin(\alpha_m x)\sin(\beta_n y) + \frac{\alpha_m^4}{8a_{11}} \cos(2\beta_n y)\sin(\alpha_m x)\sin(\beta_n y)\Big] * \sin(\alpha_p x)\sin(\beta_q y) dydx$$

$$q = \sum_m \sum_n \int_0^a \int_0^b Q \sin(\alpha_p x)\sin(\beta_q y) dydx$$

$$c_1 \quad = I_o * \begin{cases} \frac{a*b}{4} & \text{for p = m, q = n} \\ 0 & \text{otherwise} \end{cases}$$

$$c_2 = \left(\alpha_m^2 + \beta_n^2\right)^2 D_{11} \begin{cases} \frac{ab}{4} & \text{for p = m, q = n} \\ 0 & \text{otherwise} \end{cases}$$

$$c_3 = -\left(\alpha_m^2 C_{mn}^2 + \beta_n^2 C_{mn}^1\right)^2 \begin{cases} \frac{ab}{4} & \text{for p = m, q = n} \\ 0 & \text{otherwise} \end{cases}$$
$$-\frac{\beta_n^2}{16a_{11}} \begin{cases} \frac{ab}{4} & \text{for p = m, q = n} \\ 0 & \text{otherwise} \end{cases}$$
$$-\frac{\alpha_m^2}{16a_{11}} \begin{cases} \frac{ab}{4} & \text{for p = m, q = n} \\ 0 & \text{otherwise} \end{cases}$$
$$= -\frac{1}{16}\left[\left(\frac{\left(\alpha_m^4 + \beta_n^4\right)}{a_{11}}\right) + 2A_{11}\left(\alpha_m^4 + \beta_n^4 + 2\alpha_m^2\beta_n^2\upsilon\right)\right]$$
$$* \begin{cases} \frac{ab}{4} & \text{for p = m, q = n} \\ 0 & \text{otherwise} \end{cases}$$

$$q \quad = \frac{16}{9\pi^2} Q \begin{cases} \frac{ab}{4} & \begin{matrix} \text{p} = 1,3,5,\cdots & p = q \\ \text{q} = 1,3,5,\cdots & p \neq q \end{matrix} \\ 0 & \textit{elsewhere} \end{cases} \tag{4.59}$$

Noticing that $\frac{ab}{2}$ can be cancelled from every coefficient in equation (4.59), then the reduced-order model, from the equilibrium equation (4.54), becomes

$$I\frac{d^2W_{mn}(t)}{dt^2} + \left[\left(\alpha_m^2 + \beta_n^2\right)^2 D_{11}\right]W_{mn}(t)$$
$$+\frac{1}{16}\left[\left(\frac{\left(\alpha_m^4 + \beta_n^4\right)}{a_{11}}\right) + 2A_{11}\left(\alpha_m^4 + \beta_n^4 + 2\alpha_m^2\beta_n^2\upsilon\right)\right]W_{mn}^3(t)$$
$$= \frac{16}{9\pi^2} q$$

$$c_1 \frac{d^2 W_{mn}(t)}{dt^2} + c_2 W_{mn}(t) + c_3 W_{mn}^3(t) = Q \tag{4.60}$$

Equation (4.60) is also known as the Düffing oscillator because of the cubic stiffness term, $W_{mn}^3(t)$. The method of multiple scales may be used to obtain an analytical approximation for a solution of this system if the nonlinearity is weak.

4.7 Special Case: Composite Laminate Plate With All Edges Clamped

Following the special case of a thin laminate plate with all edges simply supported, in this Section a reduced-order model will be developed for a plate with all edges clamped (Figure 4.3).

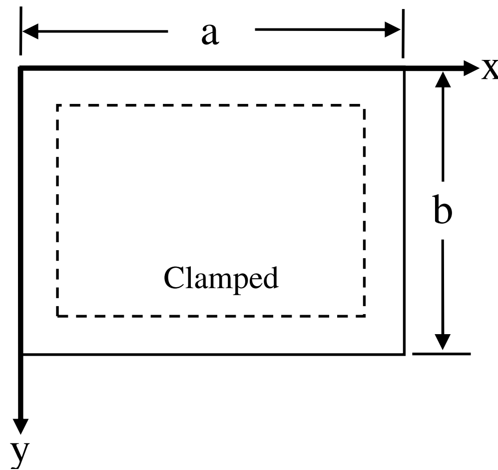

Figure 4.3: Thin laminate plate with clamped boundaries.

The boundary conditions for a clamped plate are

$$\begin{array}{llll} w(0,y,t)=0 & w(a,y,t)=0 & w(x,0,t)=0 & w(x,b,t)=0 \\ \dfrac{\partial w(0,y,t)}{\partial x}=0 & \dfrac{\partial w(a,y,t)}{\partial y}=0 & \dfrac{\partial w(x,0,t)}{\partial y}=0 & \dfrac{\partial w(x,b,t)}{\partial y}=0 \end{array} \tag{4.61}$$

For the clamped case, equation (4.32) will not satisfy the boundary conditions given in (4.61). If the Navier method is applied to the clamped case, the transverse displacement of the thin plate is defined as

$$W(x,y,t)=\sum_{m}^{\infty}\sum_{n}^{\infty}W_{mn}(t)\sin^2(\alpha_m x)\sin^2(\beta_n y) \tag{4.62}$$

$$\alpha_m=\frac{m\pi}{a} \quad \beta_n=\frac{n\pi}{b}$$

If the transverse displacement of equation (4.62) is inserted into the first set of boundary conditions in equation (4.61), that is, those at x = 0

$$\begin{array}{l} w(0,y)=W_{mn}(t)\sin^2(\alpha_m 0)\sin^2(\beta_n y)=0 \\ \dfrac{\partial w(0,y)}{\partial x}=2\alpha_m W_{mn}(t)\cos(\alpha_m 0)\sin(\alpha_m 0)\sin^2(\beta_n y)=0 \end{array} \tag{4.63}$$

and the second set of boundary conditions at $x = a$,

$$\begin{array}{l} w(a,y)=W_{mn}(t)\left[\sin^2(\alpha_m a)\right]\sin^2(\beta_n y)=0 \\ \dfrac{\partial w(a,y)}{\partial x}=2\alpha_m W_{mn}(t)\cos(\alpha_m a)\left[\sin(\alpha_m a)\right]\sin^2(\beta_n y)=0 \end{array} \tag{4.64}$$

Similarly, it can be verified that the boundary conditions at y = 0 and y = b are satisfied. Clearly equation (4.62) satisfies the boundary conditions for a clamped plate. If equation (4.62) is inserted into (4.31),

$$
\begin{aligned}
\Phi_{xxxx} + 2\Phi_{xxyy} + \Phi_{yyyy} &= \left(\frac{1}{a_{11}}\right)\left[\left(\frac{\partial^2 w}{\partial x \partial y}\right)^2 - \frac{\partial^2 w}{\partial x^2}\frac{\partial^2 w}{\partial y^2}\right] \\
&= \left(\frac{1}{4a_{11}}\right)\alpha_m^2\beta_n^2 W^2(t)(\\
&2\cos(2\alpha_m x) - 2\cos(4\alpha_m x) \\
&+ 2\cos(2\beta_n y) - 2\cos(4\beta_n y) \\
&+ \cos(2\alpha_m x - 4\beta_n y) \\
&- 2\cos(2\alpha_m x - 2\beta_n y) \\
&+ \cos(4\alpha_m x - 2\beta_n y) \\
&- 2\cos(2\alpha_m x + 2\beta_n y) \\
&+ \cos(4\alpha_m x + 2\beta_n y) \\
&\cos(2\alpha_m x + 4\beta_n y))
\end{aligned} \tag{4.65}
$$

Similar to the procedure followed in the previous case of simply-supported boundary conditions,

$$
\begin{aligned}
\Phi_P(x, y) &= F_{1mn}\cos(2\alpha_m x) + F_{2mn}\cos(4\alpha_m x) \\
&+ F_{3mn}\cos(2\beta_n y) + F_{4mn}\cos(4\beta_n y) \\
&+ F_{5mn}\cos(2\alpha_m x - 4\beta_n y) + F_{6mn}\cos(2\alpha_m x - 2\beta_n y) \\
&+ F_{7mn}\cos(4\alpha_m x - 2\beta_n y) + F_{8mn}\cos(2\alpha_m x + 2\beta_n y) \\
&+ F_{9mn}\cos(4\alpha_m x + 2\beta_n y) + F_{10mn}\cos(2\alpha_m x + 4\beta_n y)
\end{aligned} \tag{4.66}
$$

$$
\begin{aligned}
F_{1mn} &= \frac{\beta_n^2}{32a_{11}\alpha_m^2}W_{mn}^2(t) & F_{2mn} &= -\frac{\beta_n^2}{512a_{11}\alpha_m^2}W_{mn}^2(t) \\
F_{3mn} &= \frac{\alpha_m^2}{32a_{11}\beta_n^2}W_{mn}^2(t) & F_{4mn} &= -\frac{\alpha_m^2}{512a_{11}\beta_n^2}W_{mn}^2(t) \\
F_{5mn} &= \frac{\alpha_m^2\beta_n^2}{64a_{11}(\alpha_m^2 + 4\beta_n^2)^2}W_{mn}^2(t) & F_{6mn} &= -\frac{\alpha_m^2\beta_n^2}{32a_{11}(\alpha_m^2 + \beta_n^2)^2}W_{mn}^2(t) \\
F_{7mn} &= \frac{\alpha_m^2\beta_n^2}{64a_{11}(4\alpha_m^2 + \beta_n^2)^2}W_{mn}^2(t) & F_{8mn} &= -\frac{\alpha_m^2\beta_n^2}{32a_{11}(\alpha_m^2 + \beta_n^2)^2}W_{mn}^2(t) \\
F_{9mn} &= \frac{\alpha_m^2\beta_n^2}{64a_{11}(4\alpha_m^2 + \beta_n^2)^2}W_{mn}^2(t) & F_{10mn} &= \frac{\alpha_m^2\beta_n^2}{64a_{11}(\alpha_m^2 + 4\beta_n^2)^2}W_{mn}^2(t)
\end{aligned}
$$

From equation (4.66), the particular solution Φ_P exists, but does not satisfy boundary conditions. Again, the complimentary function is chosen following He, [15], [16] and [17], as

$$\Phi_C(x, y) = \frac{1}{2} C_{mn}^1 x^2 + \frac{1}{2} C_{mn}^2 y^2 \tag{4.67}$$

and the complete solution to the compatibility equation becomes

$$\begin{aligned} \Phi(x, y) \quad &= \sum_m \sum_n \frac{1}{2} C_{mn}^1 x^2 + \frac{1}{2} C_{mn}^2 y^2 \\ &F_{1mn} \cos(2\alpha_m x) + F_{2mn} \cos(4\alpha_m x) \\ &+ F_{3mn} \cos(2\beta_n y) + F_{4mn} \cos(4\beta_n y) \\ &+ F_{5mn} \cos(2\alpha_m x - 4\beta_n y) + F_{6mn} \cos(2\alpha_m x - 2\beta_n y) \\ &+ F_{7mn} \cos(4\alpha_m x - 2\beta_n y) + F_{8mn} \cos(2\alpha_m x + 2\beta_n y) \\ &+ F_{9mn} \cos(4\alpha_m x + 2\beta_n y) + F_{10mn} \cos(2\alpha_m x + 4\beta_n y) \end{aligned} \tag{4.68}$$

Applying boundary conditions for a clamped plate, the coefficients of the complimentary function are

$$\begin{Bmatrix} C_{mn}^2 \\ C_{mn}^1 \end{Bmatrix} = \left(\frac{1}{ab}\right) \int_0^a \int_0^b \left[[A] \begin{Bmatrix} \frac{1}{2} w_x^2 \\ \frac{1}{2} W_y^2 \end{Bmatrix} - \begin{Bmatrix} \Phi_{P,yy} \\ \Phi_{P,xx} \end{Bmatrix} \right] dydx \tag{4.69}$$

and the coefficients to the complimentary function become

$$\begin{aligned} C_{mn}^1 \quad &= \sum_m \sum_n \frac{3}{32} A_{11} \left(\beta_n^2 + \alpha_m^2 \upsilon\right) W_{mn}^2(t) \\ C_{mn}^2 \quad &= \sum_m \sum_n \frac{3}{32} A_{11} \left(\alpha_m^2 + \beta_n^2 \upsilon\right) W_{mn}^2(t) \end{aligned} \tag{4.70}$$

Now that the coefficients are known, a complete expression exists for the approximation of the static stress function Φ. With the approximations for W and Φ, the equation of motion describing the transverse displacement of a thin laminate plate with all edges clamped may be revisited as

$$
\begin{aligned}
&I_O \frac{\partial^2 W}{\partial t^2} + D_{11}\left(\frac{\partial^4 W}{\partial x^4} + 2\frac{\partial^4 W}{\partial x^2 \partial y^2} + \frac{\partial^4 W}{\partial x^4}\right) \\
&= Q + \left[p(x, y) + \Phi_{xx} w_{yy} + \Phi_{yy} w_{xx} - 2\Phi_{xy} w_{xy}\right]
\end{aligned}
\tag{4.71}
$$

and put in the form of a reduced-order model. If equations (4.62) and (4.68) are inserted into (4.71), and Galerkin's method is applied with the weighting functions as

$$
W_{WeightFcn}(x, y) = \sum_{p}^{\infty} \sum_{q}^{\infty} \sin^2(\alpha_p x) \sin^2(\beta_q y) \tag{4.72}
$$

(4.71) becomes

$$c_1 \frac{d^2 W_{mn}(t)}{dt^2} + c_2 W_{mn}(t) + c_3 W_{mn}^3(t) - Q = 0$$

$$c_1 = I_o$$

$$c_2 = \frac{16}{9}\left(3\alpha_m^4 + 2\alpha_m^2\beta_n^2 + 3\beta_n^4\right)D_{11}$$

$$c_3 = -\frac{1}{144}\left(\frac{17\beta_n^4 + \alpha_m^4\left(17 + 8\beta_n^4\left(\frac{4}{\left(\alpha_m^2 + \beta_n^2\right)^2} + \frac{1}{\left(4\alpha_m^2 + \beta_n^2\right)^2} + \frac{1}{\left(\alpha_m^2 + 4\beta_n^2\right)^2}\right)\right)}{a_{11}}\right.$$
$$\left. 18A_{11}\left(\alpha_m^4 + \beta_n^4 + 2\alpha_m^2\beta_n^2 \upsilon\right)\right)$$

$$Q = \frac{16}{9}q$$

(4.73)

The different coefficients in equations (4.73) have been determined by using Mathematica (see appendices). Equation (4.73) is the reduced-order model, the undamped Düffing oscillator, describing the transverse displacement of thin laminate plate with all edges clamped. The method of multiple scales may be used to obtain an analytical approximation for a solution of this system if the nonlinearity is weak. In this chapter, a methodology has been illustrated to obtain reduced-order models for dynamic analysis of composite plate structures with simply-supported and clamped boundaries.

5 FABRICATION OF MEMS DEVICES AND EXPERIMENTAL ARRANGEMENTS

In this chapter, thin-film deposition, device design and layouts, and fabrication and release processes with application to MEMS devices are discussed. During thin-film deposition, stress measurements are taken via wafer bow stress measurements. In addition, the thickness of each of these films is taken via a Woollam Ellipsometer. An optical profilometer is used to determine deflection profiles of all these devices. Finally, the experimental setup used to collect frequency response data is presented.

5.1 Fabrication of MEMS Devices

5.1.1 Thin-film Deposition

For the purpose of this work, piezoelectric microresonators were fabricated at the Army Research Laboratory in Adelphi, MD. Each of these resonators consists of four thin-film layers. To begin fabrication, a baseline wafer bow measurement is taken of the bare silicon wafer via the Tencor FLX-2908 instrument. This measurement is used in the calculation of the stress that accrues in the deposition of the first thin-film layer. Next, a silicon dioxide layer is deposited via plasma enhanced chemical vapor deposition (PECVD). PECVD is a process that utilizes radio-frequency (*RF*) plasma to transfer energy into reactant gases, which allows the substrate to remain at lower temperatures in comparison to other processes. Precise temperature control of the substrate-surfaces aids

in the quality of the deposited films [1]. The SiO_2 layer and substrate are then rapid thermal annealed at 700˚C for 60 seconds, the oxide layer thickness is measured via the Woolam Ellipsometer, and a wafer bow measurement is taken over the top of the SiO_2 layer. An extremely thin titanium layer is then sputtered to the SiO_2 layer in order to aid in adhesion with the subsequent sputtered platinum layer. The thickness of the combined titanium/platinum is measured via the Woollam eillipsometer as well as the wafer bow measurements made by using the Tencor FLX – 2908. The third layer to be deposited is a PZT layer. This deposition process begins using a syringe to deposit the PZT solution onto a stationary wafer. The wafer is then spun and put on a hot plate for pyrolysis and then a crystallization process is performed via rapid thermal annealing [2]. These three processes are repeated until the desired PZT layer thickness is reached. Again the thickness and wafer bow measurements are taken via the Woollan ellipsometer and the Tencor FLX-2908. Finally, the top platinum layer is deposited with thicknesses and wafer bow measurements taken as before.

5.1.2 Device Layouts

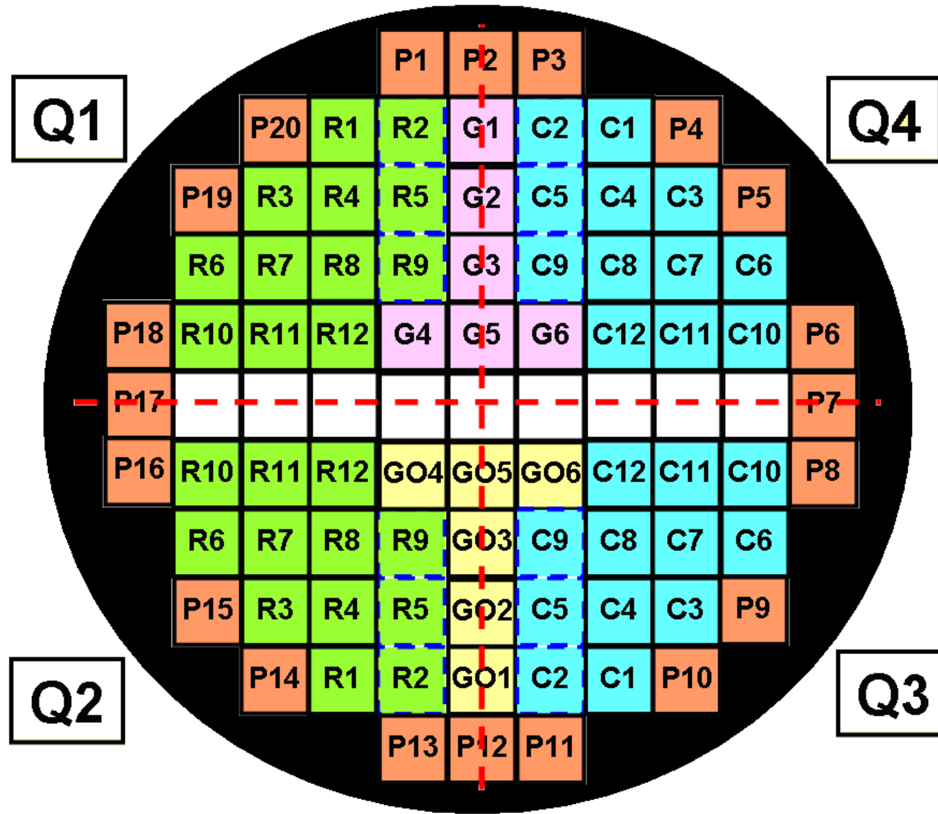

Figure 5.1: Device layout in grid pattern on silicon wafer.

Devices are initially laid out in a grid pattern on a silicon wafer (Figure 5.1). In Figure 5.1, the wafer is divided into four quadrants designated by Q1, Q2, Q3, and Q4. The green squares on the left side represent the various sized PZT clamped-clamped resonators. The blue squares on the right represent PZT cantilevers. The light yellow squares represent gold structures, and the orange squares represent plate-like structures. For purpose of study in this work, squares R2, R5, R9, C2, C5, and C9 are full stack resonators (SiO_2 - Ti/Pt – PZT - Pt), numbers 1, 4, and 8 are trilayered resonators consisting of SiO_2 - Ti/Pt – PZT, numbers 10, 11, and 12 are bilayered resonators consisting of SiO_2 - Ti/Pt and numbers 3, 6 and 7 are single layered silicon resonators.

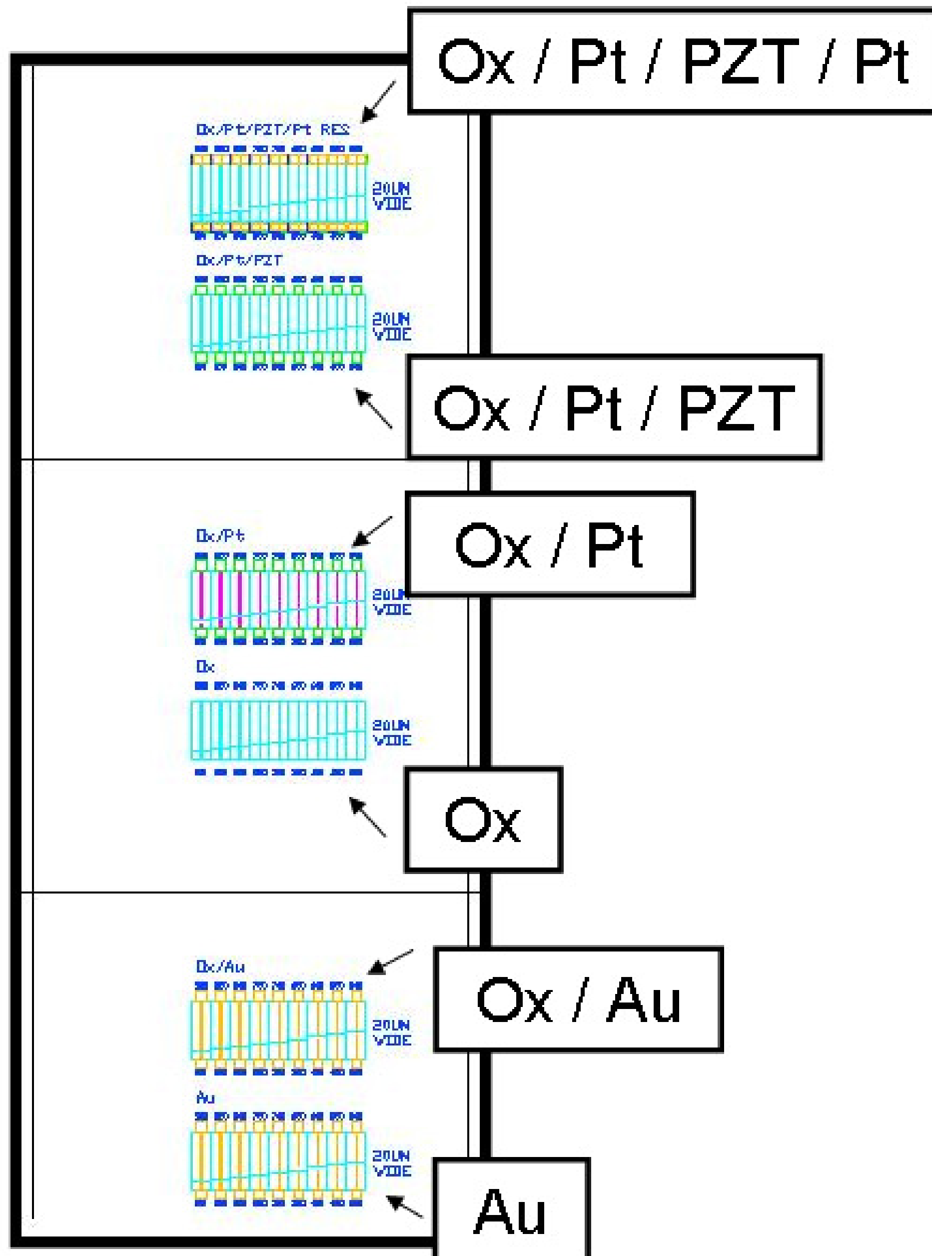

Figure 5.2: Varying layered cantilevered resonators.

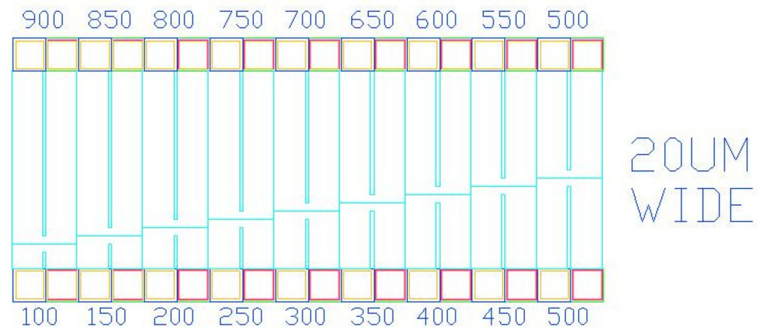

Figure 5.3: 20 μm wide PZT cantilevers with lengths varying from 100 to 900 μm long.

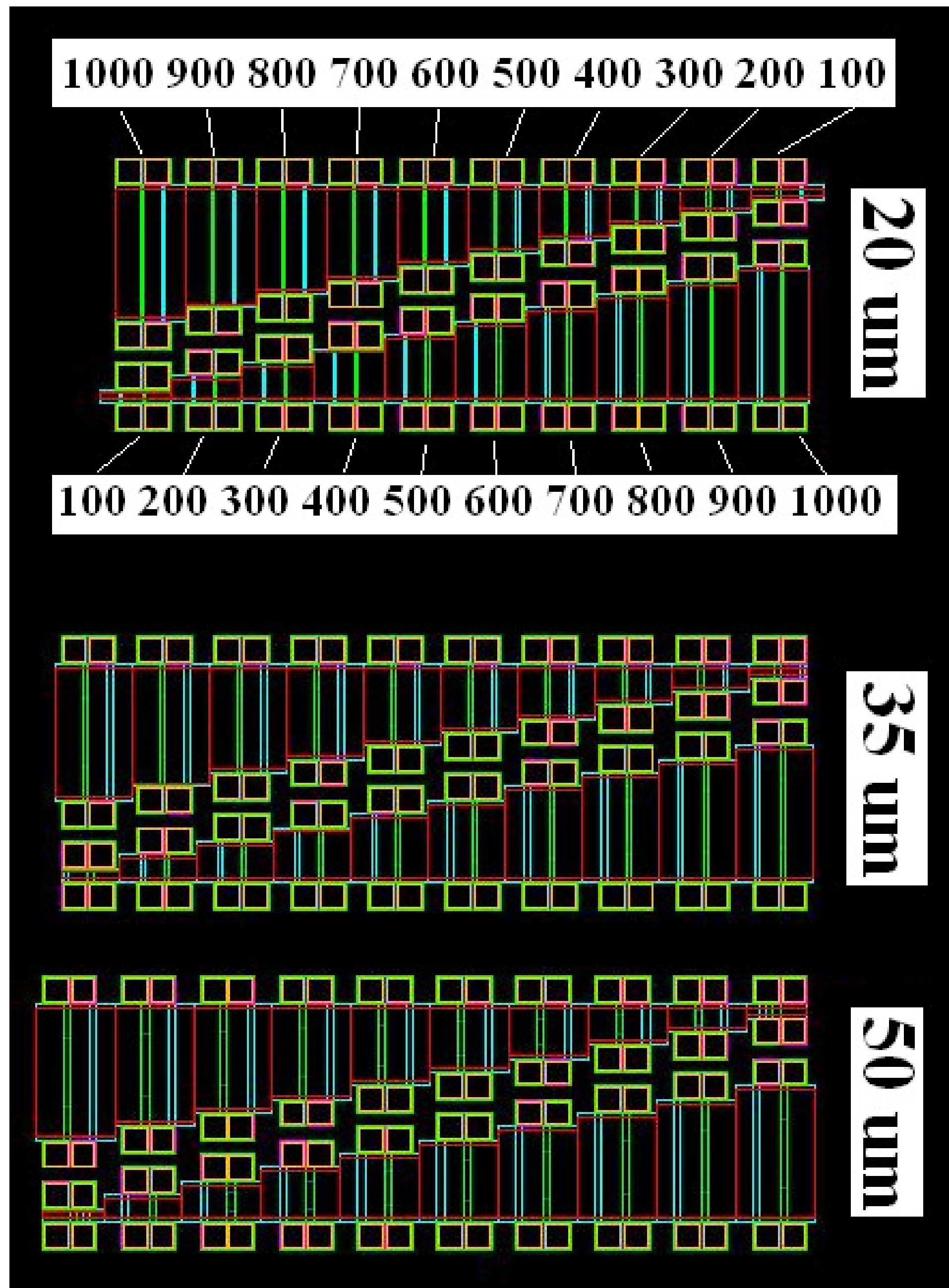

Figure 5.4: Die representation of microresonators. Three rows of 20, 35 and 50 μm wide resonators ranging in lengths of 100 μm to 1000 μm are present.

Figure 5.2 and Figure 5.3 are AutoCad representations of cantilevered resonators. These figures demonstrate the layout of the cantilevers on each die. Each die contains three blocks of devices (Figure 5.4). Each block represents a width set with the different widths being 20 μm, 35 μm and 50 μm wide. Resonator lengths are ranging from 100 μm to 1000 μm. The full stack PZT resonators are pictured as the thin green beams. The thin blue beams beside the PZT resonators are single layered, SiO_2 resonators (Figure 5.5). A SiO_2 resonator is placed next to each PZT resonator in order to determine whether the PZT resonator is fully released. SiO_2 resonators are nearly transparent and identifying whether they are partially or fully released under a microscope is relatively simple (Figure 5.6). Once the SiO_2 resonators are released, the PZT resonators are assumed released as well.

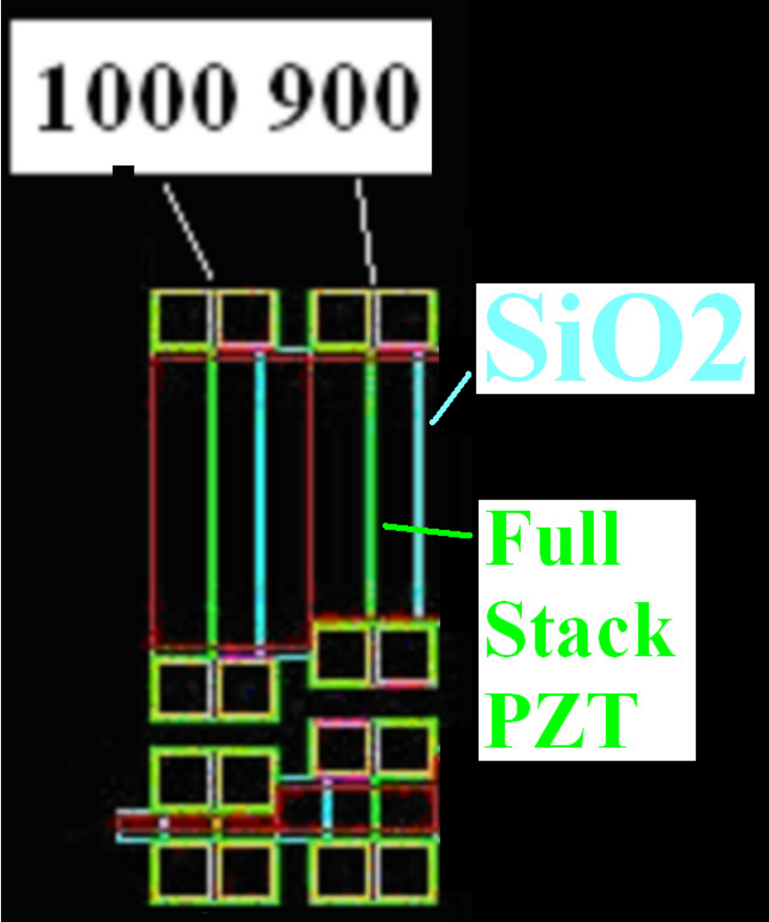

Figure 5.5: Schematic exhibiting SiO_2 and PZT resonators.

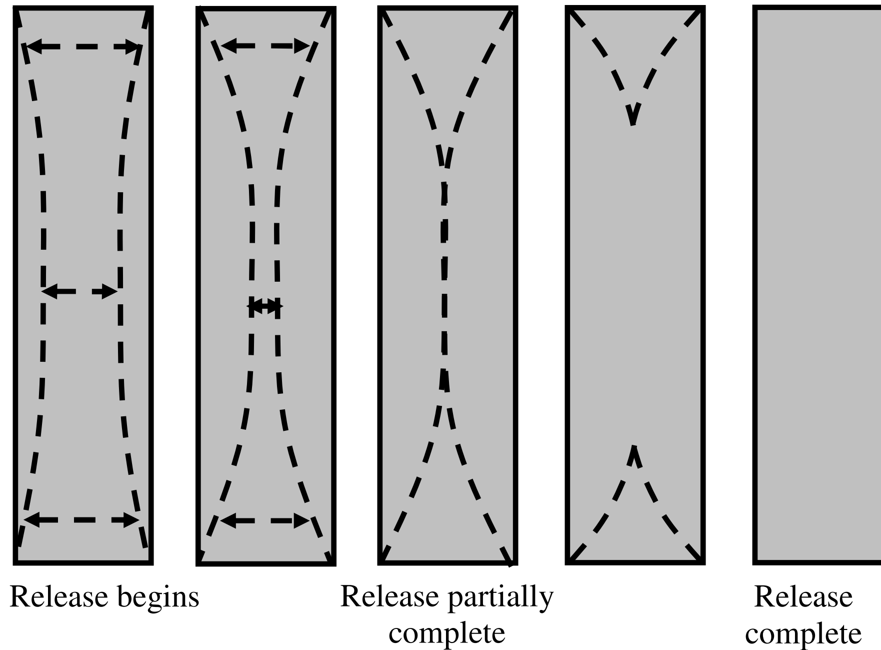

Figure 5.6: Silicon resonator exhibiting various stages of release.

5.1.3 Fabrication / Release Processes

After thin-film deposition and device design and layouts are complete, a six mask set is used to shape, fabricate and release the MEMS devices. The devices are fabricated such that in each quarter, there are three die and with each devoted to single layered SiO_2 resonators, bilayered SiO_2/TiPt resonators, trilayered SiO_2/TiPt/PZT and full stack PZT, SiO_2/TiPt/PZT/Pt resonators. Each one of the masks is designed in AUTOCAD such that it contributes to the formation and shaping of the device through each of the deposited thin-film layers as well as the release of the entire structure.

To begin, the first mask is used to pattern the top platinum electrode of the PZT structure. The platinum surface is typically patterned with photoresist, to define the shape of the top electrode. The unwanted Pt is then removed via an ion milling process. The formation of

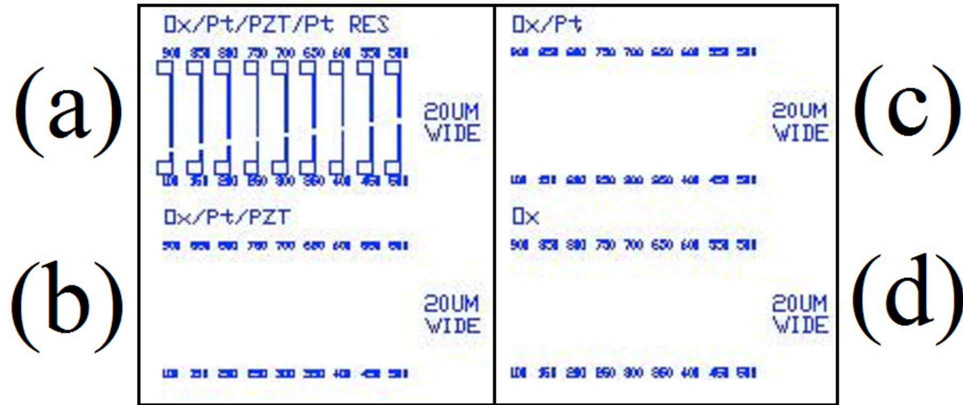

Figure 5.7: Mask #1 defining the top electrode area. (a) Full stack cantilevered resonators with top platinum electrode. (b), (c), (d) SiO_2/TiPt/PZT, SiO_2/TiPt, SiO_2 cantilever with no top electrode layer.

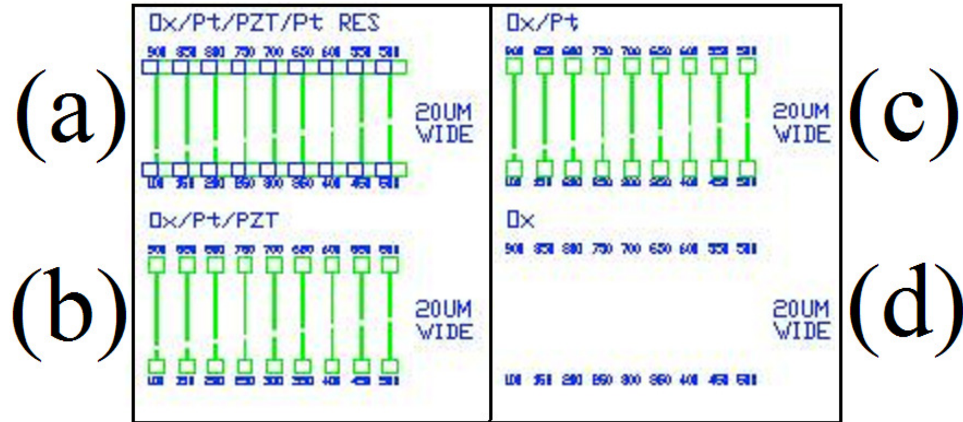

Figure 5.8: Mask #2 defining PZT and bottom Pt area to be ion milled.

the top electrode is clearly seen in Figure 5.7 (a). In Mask #2, the definition of the PZT and the bottom Pt area to be ion milled can be seen. Mask #3 defines area for wet etching and PZT removal. Wet etching, also known as chemical etching, involves solutions of diluted chemicals to dissolve substrates. In Figure 5.8, the green lines are used to show the protection for the inside areas from material removed and leaving only SiO_2 in the

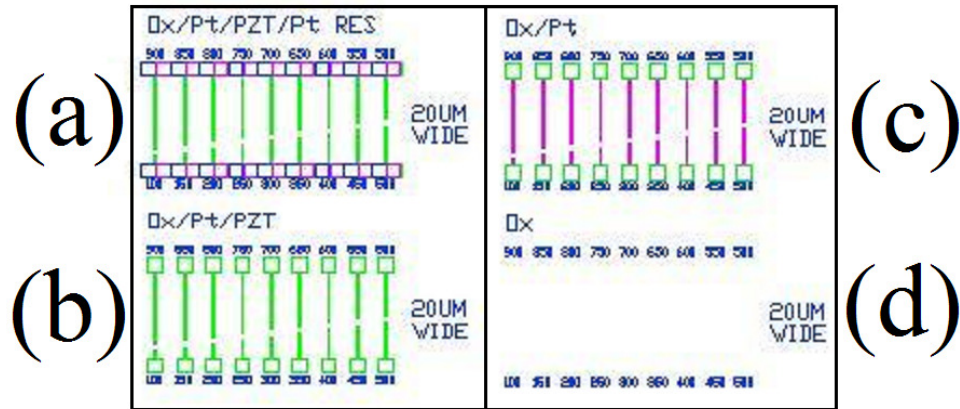

Figure 5.9: Mask #3 defining area for wet etching and PZT removal.

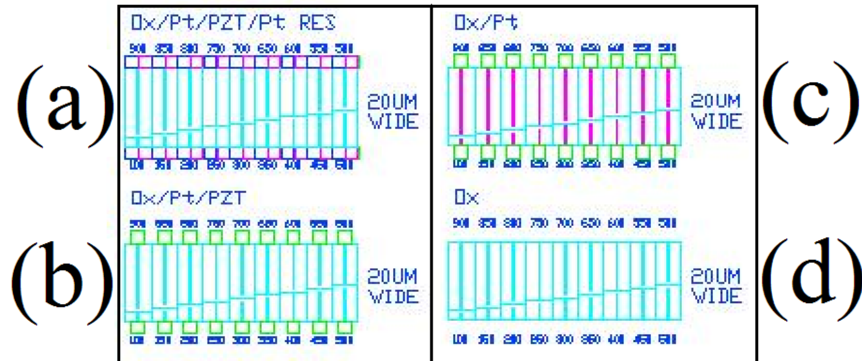

Figure 5.10: Mask #4 defining area for etching SiO_2.

outside areas. In Figure 5.8 (d), the PZT layer is clearly removed leaving only SiO_2 to create the single layered cantilevered resonators.

The final step is the application of Mask #4 for the final etching of the SiO_2 layer (Figure 5.10). In Figure 5.10, all the cantilevered resonators have been shaped and formed. However, they are unreleased, meaning the bottom SiO_2 layer is still in contact with the wafer substrate. The fifth and final mask protects the entire resonator from being etched or damaged. A XeF_2 etch is applied in such a manner that the substrate is removed

downward, and underneath the resonator as well (Figure 5.11) [2]. After some time has passed, the wafer is removed from the etch, put under a micro scope and devices are examined in a manner as shown in Figure 5.6. Once its clear the neighboring SiO_2 resonator is fully released, its assumed that the other resonators containing the same geometries are also fully released (Figure 5.12).

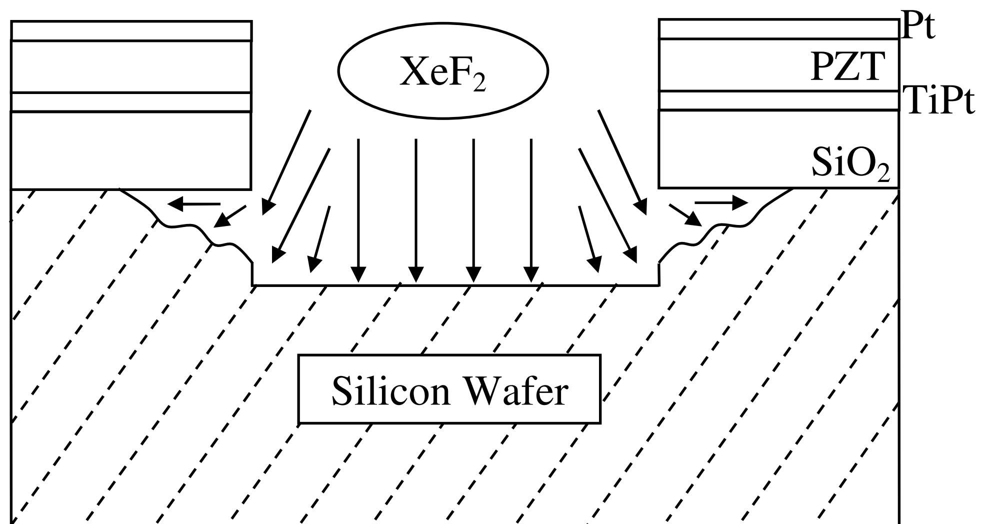

Figure 5.11: XeF_2 etching releasing resonators.

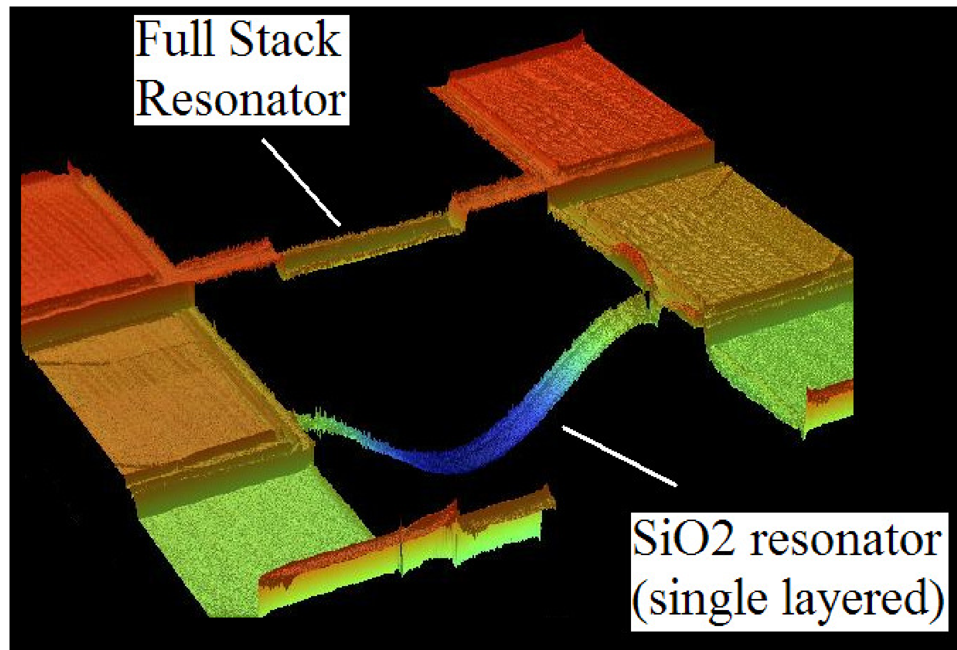

Figure 5.12: Full stack resonator and SiO_2 resonator post-fabrication and release.

5.2 Wafer Bow Stress Measurements

During fabrication of multi-layered structures, thin-film layers are deposited, and wafer-bow stress measurements are made via the equipment shown (Tencor FLX-2908) in Figure 5.13

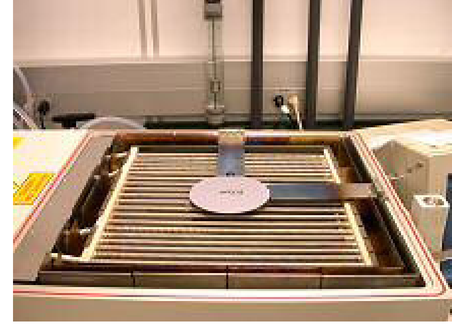

Figure 5.13: Instrumentation used for wafer bow measurement in thin-films [2].

Initially a wafer is placed on quartz pegs as shown in Figure 5.13 on the right. A laser then scans the surface of the wafer in the direction of the heating elements. Once the scan is complete, a radius of curvature is returned. The wafer is rotated 90˚ and scanned again. Once four scans are complete (360˚), the wafer is removed and a thin-film is deposited. On completion of the deposition, the wafer is returned to the Tencor FLX – 2908 and scanned again. At each of the four points, a change in radius of curvature is calculated, and then a thin-film stress value may be calculated via Stoney's formula.

5.3 Woollam Ellipsometer

Thin-film thicknesses were measured via an ellipsometer at the Army Laboratory in Adephi, MD. An example of an ellipsometer is shown in Figure 5.14.

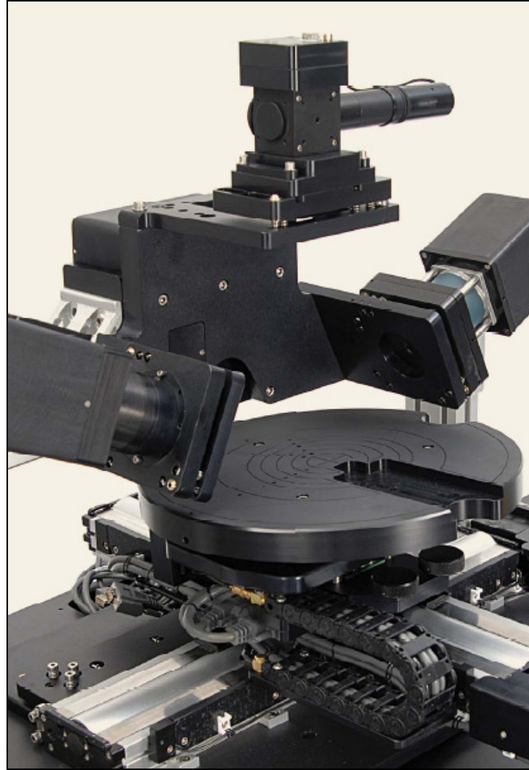

Figure 5.14: Woollam Ellipsometer used for measuring thin-film thicknesses [40].

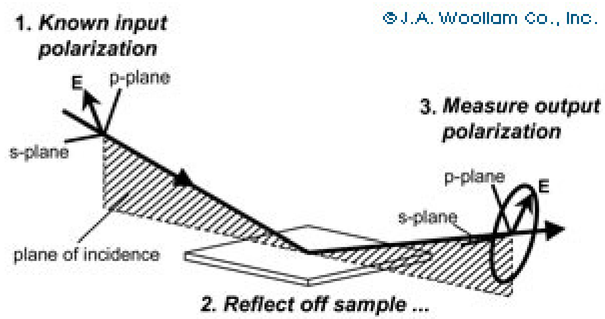

Figure 5.15: Typical ellipsometry configuration, where linearly polarized light is reflected from the sample surface and the polarization change is measured to determine sample response [40].

Ellipsometry measures a change in polarization as light reflects or transmits from a material structure. The polarization change is represented as an amplitude ratio, Ψ, and the phase difference, Δ. The measured response depends on optical properties and the thickness of individual materials [40]. An illustration of ellipsometry is shown in Figure 5.15. Primary tools for collecting the data are a light source, polarization generator, sample, polarization analyzer, and detector. The ellipsometry measure changes in light polarization to determine the sample material's properties such as film thickness. The film thickness is then determined by the interference between light reflecting from the surface and light traveling through the film. Depending on relative phase change of the rejoining light to the surface reflection, interference can be defined as constructive or destructive. The interference involves both amplitude and phase information. Ellipsometry is typically used for films whose thickness ranges from sub-nanometers to a few microns. As films become thicker, interference oscillations become increasingly difficult to resolve. Thickness measurements require that a portion of the light pass through the entire film and return to the surface. If the material absorbs the light, thickness measurements by optical instruments will be limited to thin, semi-opaque layers. For metals with strong tendencies to absorb light, the maximum thickness tends to be 100 nm to circumvent this problem [40].

5.4 Optical Profilometer

MEMS resonators deflections and curvatures are measured via the Veeco Optical Profilometer at the Army Research Laboratory in Adelphi, MD.

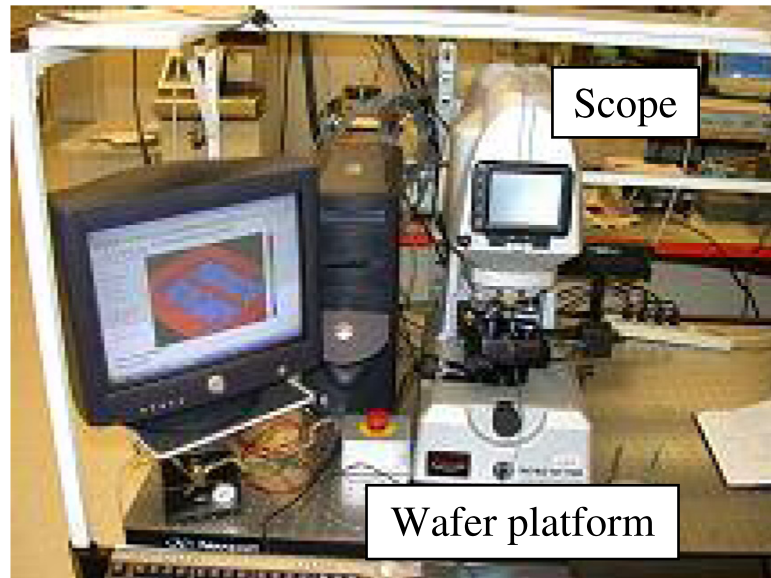

Figure 5.16: Veeco optical profilometer [2].

White light is reflected from the sample combined with light from a reference mirror to produce a fringe pattern over the devices and the wafer, which the system measures [2]. Fringes are seen in only a very small depth of field and by knowing the relative z position of the sample; the system can determine the vertical position of each point on the sample [2]. This system has a vertial range of up to 2 mm and a resolution of 3nm.

In addition to the optical profilometer used at the Army Research Laboratory, an additional optical profilometer, a TM1200 system, was utilized via the Sensors and Actuators Laboratory in the Department of Mechanical Engineering at the University of Maryland.

5.5 Dynamic Experiment Setup

Dynamic experiments were conducted at the Maryland MEMS Laboratory, Department of Mechanical Engineering, University of Maryland. Resonators are placed in a vacuum chambered probe station, with a probe on each the top and bottom electrodes (Figure 5.17). An electric current is applied and a sine sweep output of the resonator is determined via the spectrum analyzer. A laser Doppler vibrometer is positioned in the center of each resonator examined, and used to measure the velocity of the top surface as its vibrating.

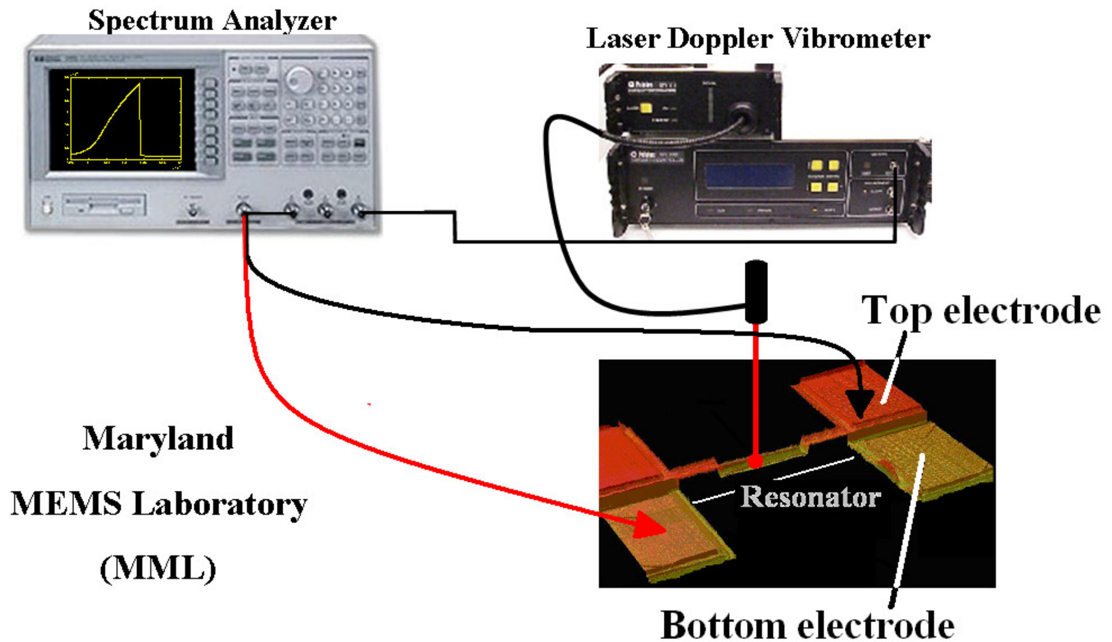

Figure 5.17: Experimental set for dynamic experiments at the Maryland MEMS Laboratory.

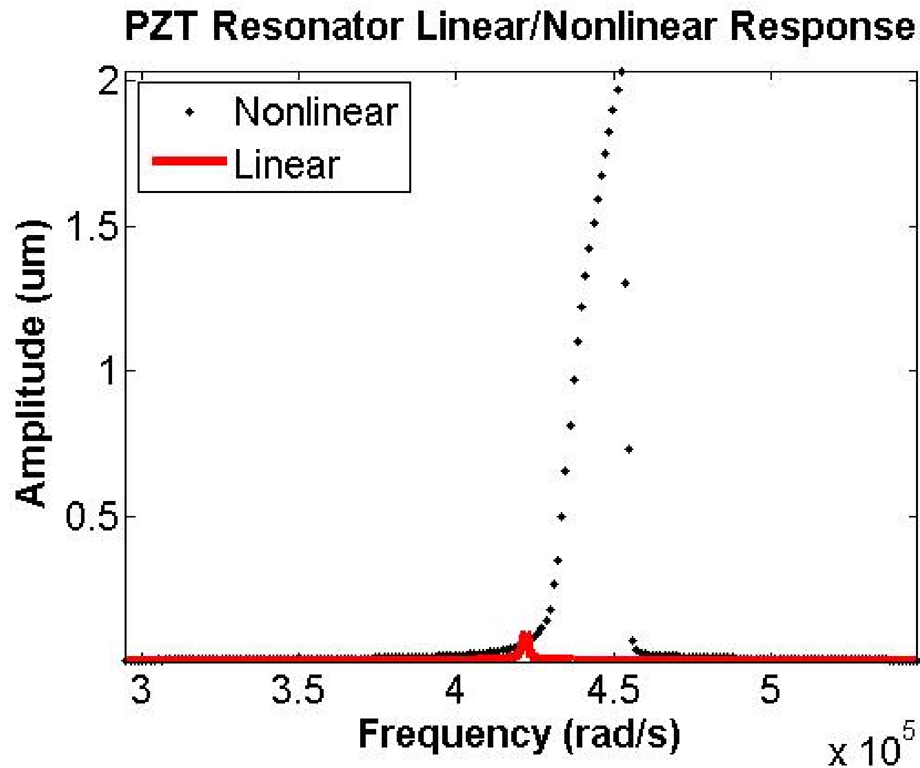

Figure 5.18: Linear and nonlinear frequency response of a PZT resonator, 900 μm long, 35 μm wide.

From initial sine sweeps of the resonators, the frequency response data showed decidedly linear characteristics (red solid line in Figure 5.18). Typically, PZT devices are put through a polarization procedure before usage. This is because PZT material is made up of domains of cells with dipole moments aligned in the same directions. However, these directions can change from one region to another. To align all dipoles in all regions, a large current is sent through the PZT resonator which aligns these dipole moments, which in the end, make these devices work more effectively. However, once poling is complete, sine sweeps are conducted again, and the response clearly becomes nonlinear and exhibits Düffing behavior as shown in Figure 5.18.

6 RESIDUAL STRESS INDUCED DEFORMATION IN MEMS CANTILEVERS

When the length of a plate is much longer than the plate width, the loading is such that the displacement w in the vertical direction is a function of the plate's length L, along the x-axis. In this case, the variables of displacement, u, v, and w are functions of x only (Figure 6.1). In this case, spatially one-dimensional analysis of the laminated plate structure as a laminated beam, can be carried out on the basis of classical laminated plate theory. Here, this type of analysis is carried out to determine the deformation fields.

In this chapter, a description of a MEMS PZT cantilevered structure is presented. The laminate stiffness and residual force and moments are given. Residual stress induced deformation is discussed as is the neutral axis location and its effect on residual stress deformation, force and moments and laminate stiffness calculations.

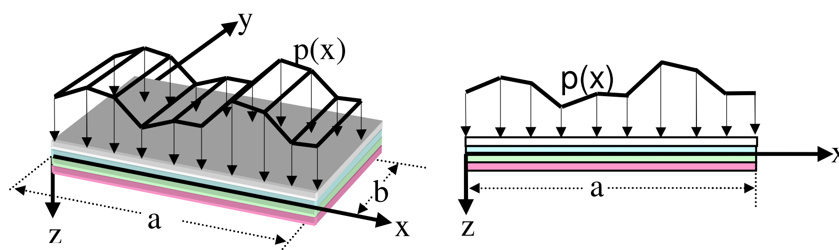

Figure 6.1: Composite laminate plate resolved to a laminate beam for spatially one dimensional analysis.

6.1 MEMS Cantilever Description

Beginning with a silicon wafer, SiO_2 is deposited, followed by sputtered titanium and platinum, followed by spun PZT, and completed with a final layer of sputtered platinum. Through several fabrication and release processes, the MEMS cantilever in its true form is produced (Figure 6.2).

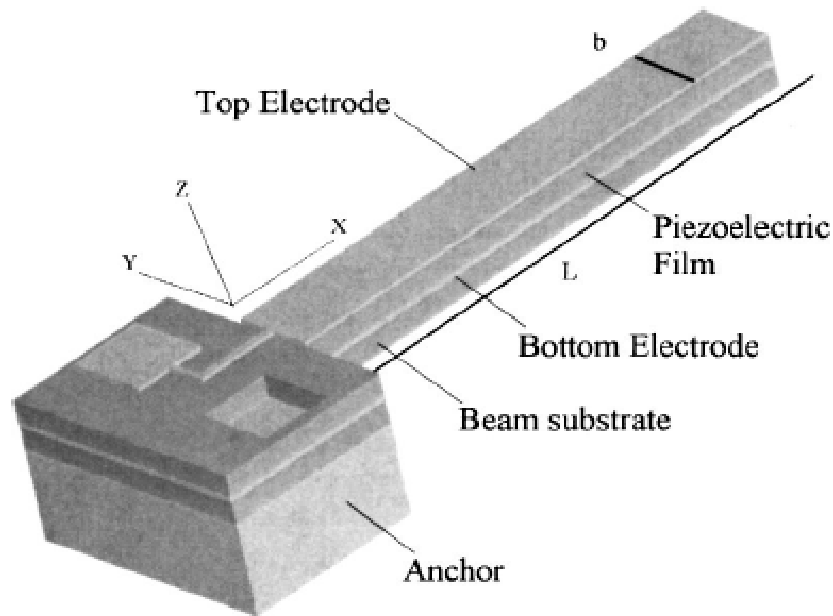

Figure 6.2: PZT cantilever [6].

6.2 One-Dimensional Analysis of MEMS Cantilevers

In general, the stresses under consideration for a single laminate element is shown in Figure 6.3

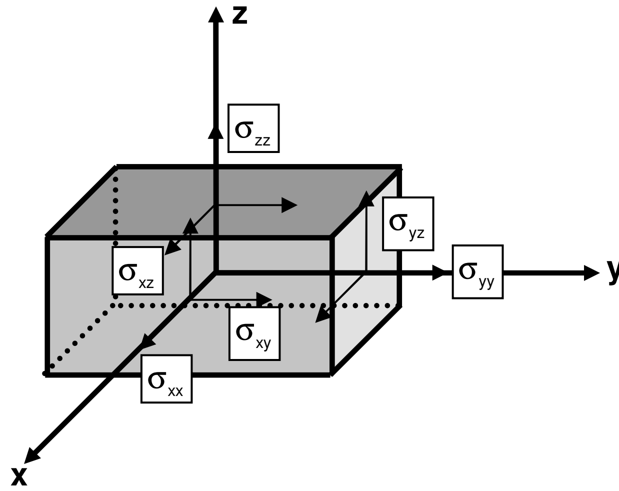

Figure 6.3: Lamina exhibiting stresses defined via Hooke's Law.

Thin beams in bending are usually modeled under the basis of the Euler-Bernoulli theory. According to this theory, the strains, ε_{yy}, ε_{zz}, and ε_{yz}, are assumed zero for any stress state. If one considers a Timoshenko beam, the strain ε_{xx} is nonzero, and the strains ε_{xy} and ε_{xz} are considered to be small, but nonzero. In Euler-Bernoulli's theory, all strains are assumed to be zero, except the axial strain along the beam's length, ε_{xx}. This theory can be used to carry out one-dimensional analysis. In the rest of this Section, this theory is used. To obtain the constitutive equations describing a laminated composite beam, first revisit equations describing the classical laminated plate. Since the main concern is analyses along the length of the MEMS cantilever, all derivatives with respect to y are set to zero, and equations become

$$\frac{\partial^2 M_{xx}}{\partial x^2} + N(w_o) + q - I_o \frac{\partial^2 w_o}{\partial t^2} = \left(-I_2 + \frac{I_1^2}{I_0} \right) \frac{\partial^2}{\partial t^2} \left(\frac{\partial^2 w_o}{\partial x^2} \right) + \frac{I_1}{I_0} \left(\frac{\partial^2 N_{xx}}{\partial x^2} \right) \quad (6.1)$$

$$N(w_o) = \frac{\partial}{\partial x}\left(N_{xx} \frac{\partial w_o}{\partial x} \right) = \frac{\partial N_{xx}}{\partial x}\frac{\partial w_o}{\partial x} + N_{xx}\frac{\partial^2 w_o}{\partial x^2} \tag{6.2}$$

The nonlinear strains and curvatures become

$$\begin{aligned} M_y &= -(EI)\frac{\partial^2 w}{\partial x^2}\left(1 + \left(\frac{\partial w}{\partial x}\right)^2\right)^{-\frac{3}{2}} \\ &= -(EI)\frac{\partial^2 w}{\partial x^2}\left(1 - \frac{3}{2}\left(\frac{\partial w}{\partial x}\right)^2\right) \end{aligned} \tag{6.3}$$

$$\{\varepsilon_{xx}^{o}\} = \left\{ \frac{\partial u_o}{\partial x} + \frac{1}{2}\left(\frac{\partial w_o}{\partial x}\right)^2 \right\} \tag{6.4}$$

and the force-strain and moment-curvature relations and stiffnesses are defined as

$$\begin{Bmatrix} N_{xx} \\ M_{xx} \end{Bmatrix} = \begin{bmatrix} A & B \\ B & D \end{bmatrix} \begin{Bmatrix} \varepsilon_{xx}^{o} \\ \kappa \end{Bmatrix} \tag{6.5}$$

Equations (6.1) through (6.5) effectively describe the transverse displacement of a MEMS cantilever based on classical laminate plate theory and Euler-Bernoulli beam assumptions.

6.3 MEMS Cantilever Laminate Stiffness and Residual Force/Moment Description

The MEMS cantilever shown in Figure 6.2 can now be modeled as an asymmetric laminated beam with multiple isotropic layers.

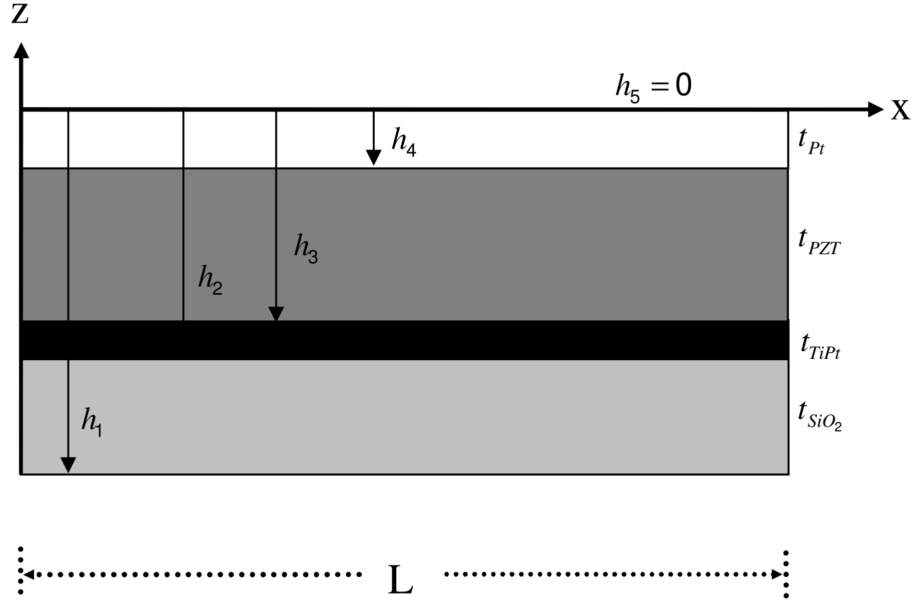

Figure 6.4: Asymmetric laminate schematic of MEMS cantilever.

The zero axis is taken from the top of the cantilever and the neutral axis is not taken into consideration here. In general, the stiffnesses can be determined as

$$
\begin{aligned}
A = (EA)_{tot} &= \sum_{k=1}^{N} bE_k (h_{k+1} - h_k) \\
B = (ES)_{tot} &= \frac{1}{2}\sum_{k=1}^{N} bE_k (h_{k+1}^2 - h_k^2) \\
D = (EI)_{tot} &= \frac{1}{3}\sum_{k=1}^{N} bE_k (h_{k+1}^3 - h_k^3)
\end{aligned}
\tag{6.6}
$$

And h_k are clearly defined by the laminate thicknesses. Residual forces and moments are defined as

$$
\begin{aligned}
N_R &= \sum_{k=1}^{n} bE_k(z)\Lambda_k(z)(h_{k+1} - h_k) \\
M_R &= \sum_{k=1}^{n} bE_k(z)\Lambda_k(z)\left(\frac{h_{k+1}^2}{2} - \frac{h_k^2}{2}\right)
\end{aligned}
\tag{6.7}
$$

where h_k is defined the same as the laminate stiffnesse, b is the cantilever width, E is material Young's modulus value and Λ_k is the laminate layer's residual strain. The residual strain, Λ_k, is experimentally measured input.

6.4 Residual Stress Induced Deformation and Preliminary Results

Residual stress induced deformation can initially be predicted via the force-strain and moment-curvature relations. When residual stress induced force and moments are taken into consideration, the force-strain and moment curvature relation can be written as

$$\begin{Bmatrix} N_R \\ M_R \end{Bmatrix} = \begin{bmatrix} A & B \\ B & D \end{bmatrix} \begin{Bmatrix} \varepsilon^o_{xx} \\ \kappa \end{Bmatrix} \tag{6.8}$$

and solving for the curvature relation results in

$$\{\kappa_{xx}\} = \left\{ \frac{d^2 w}{dx^2} \left(1 + \left(\frac{dw}{dx} \right)^2 \right)^{-\frac{3}{2}} \right\} = \left(\frac{1}{AD - B^2} \right) \left(AM_R - BN_R \right) \tag{6.9}$$

The right side of (6.9) is constant whereas the left side is a nonlinear second order differential equation with respect to the transverse displacement and the beam's length. For purpose of analysis in this Section, equation (6.9) can be broken into four equations as

$$\frac{\partial^2 w}{\partial x^2} = \left(\frac{AM_R - BN_R}{AD - B^2} \right) \Rightarrow \text{COUPLED}$$

$$\frac{\partial^2 w}{\partial x^2} = \left(\frac{M_R}{D} \right) \Rightarrow \text{UNCOUPLED} \left([B] = 0 \right) \tag{6.10 a,b}$$

$$\frac{\partial^2 w}{\partial x^2} \left(1 + \left(\frac{\partial w}{\partial x} \right)^2 \right)^{-\frac{3}{2}} = \left(\frac{AM_R - BN_R}{AD - B^2} \right) \Rightarrow \text{COUPLED}$$

$$\frac{\partial^2 w}{\partial x^2} \left(1 + \left(\frac{\partial w}{\partial x} \right)^2 \right)^{-\frac{3}{2}} = \left(\frac{M_R}{D} \right) \Rightarrow \text{UNCOUPLED} \left([B] = 0 \right) \tag{6.11a,b}$$

Equations (6.10 a,b) and (6.11 a,b) effectively describe the transverse displacement of a thin laminate beam. The stiffnesses and residual force and moments are calculated via the formulae given in *Section 6.3* where the *h's* are formulated from using Figure 6.4. In Figure 6.4, the zero axis is taken from the top of the beam and the neutral axis is not taken into consideration, and the extensional, bending and coupling stiffnesses are solved for. (6.10 a,b) and (6.11a,b) are solved for the cases of when the coupling stiffness, *B*, is zero and nonzero to highlight the importance of including or excluding the coupling stiffness.

An exact solution can be found for (6.10 a,b), by integrating the $\partial^2 w / \partial x^2$ twice and applying boundary conditions for a clamped-free beam leading to

$$W(x) = \frac{1}{2} \kappa x^2 \tag{6.12}$$

If $x = L$

$$W(L) = \frac{1}{2}\kappa L^2 \tag{6.13}$$

and then equation (6.13) is the solution for the tip deflection of a cantilevered beam. The nonlinear version of the deflection profile is solved by using the *4th order Runge Kutta method*.

Preliminary results, which describe the residual stress induced deformation of a MEMS cantilever are obtained through comparison of solutions from equations (6.10 a,b) and (6.11 a,b) with experimental data obtained from the Army Research Laboratory (ARL), Adelphi, Maryland. Four wafers with MEMS cantilevers were obtained from the ARL (fabrication described in Chapter 5) and the results from one wafer are shown. As the thin-film layers were laid on each of the wafers, the residual stress and the thin-film layer thicknesses were measured. In addition to these parameters, three different sets of material properties (Young's modulus) were used. Each of the wafers has multiple cantilevers of different lengths. After each of the cantilevers was released, the tip displacement was measured with an optical profilometer. The residual stress and layer thickness values were used in calculating the residual stress induced force and moments. The thickness and Young's Modulus values resulted in two sets of stiffness values that are used to verify the analytical model. Finally, after the linear and nonlinear curvature relation are solved, the values calculated for the tip displacements of MEMS cantilevers were compared with the values experimentally measured via the optical microscope. In Figure 6.5, the tip deflections are compared with analytical result obtained from the linear and nonlinear curvature relations. If it is assumed that coupling exists between the extensional and bending stiffness components, from Figure 6.5, it is seen that

linear/nonlinear solutions to the beam's curvature are nearly exact. These two solutions clearly fit the experimental data better than if zero coupling was assumed. In Figure 6.6, the coupled curvatures produce a closer fit to the experimental data than the uncoupled curvatures. In both Figure 6.5 and Figure 6.6, though the coupled

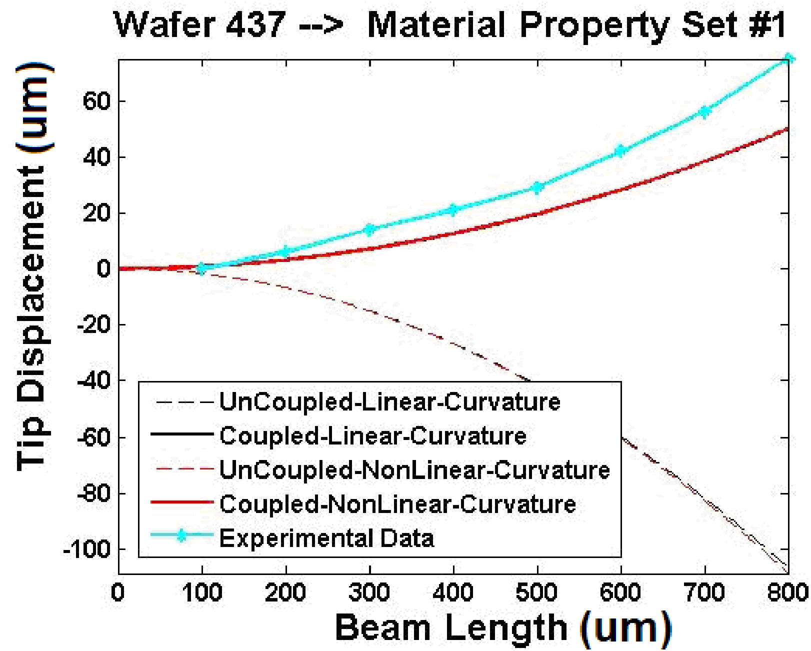

Figure 6.5: Tip deflections for MEMS cantilevers.

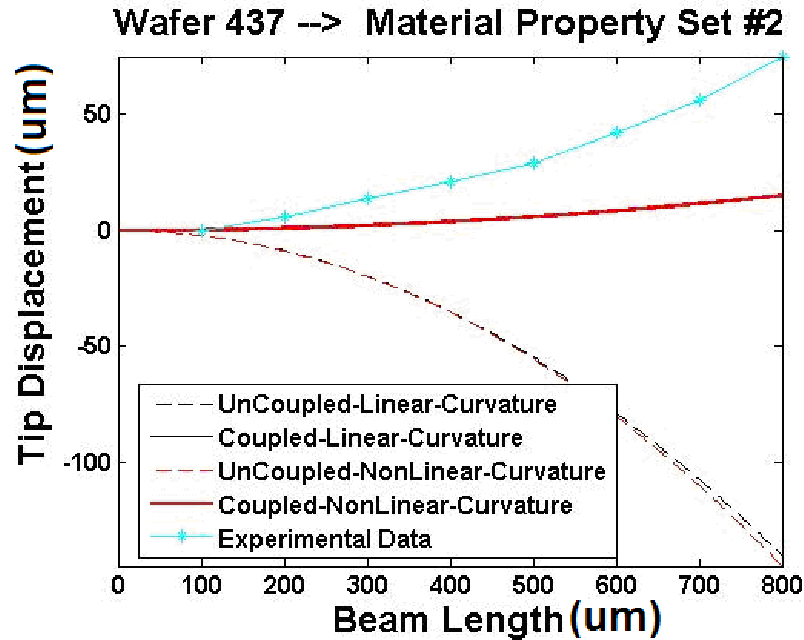

Figure 6.6: Tip deflections for MEMS cantilevers.

curvatures are a better fit, solutions fit neither set of experimental data well. This results will be used as the motivation for Chapter 7.

6.5 Neutral Axis Location and Its Effect on Residual Stress Deformation, Residual Force, Moment and Laminate Stiffness Calculations

In calculating the tip deflections of Figure 6.5 and Figure 6.6, the curvatures in equation (6.13) come from calculations in (6.10 a,b) and (6.11 a,b). These curvatures consist of extensional stiffness $[EA]$, bending stiffness , $[EI]$, coupled stiffnesses $[ES]$, and the residual force and moments. How these parameters are calculated can have a varying effect on the curvature. In this Section, the procedure developed in Section 3.5 to calculate stiffnesses in a laminate regardless of symmetry in laminate layers is used to

analyze laminate stiffnesses and residual force and moments excluding coupling stiffnesses and including the neutral axis location. This method is also compared to the standard method of calculating the stiffnesses, forces and moments presented in Sections 3.2, 3.3, and 3.4 that includes the coupling stiffnesses and excludes the neutral axis location.

First, consider the layout of Figure 6.7

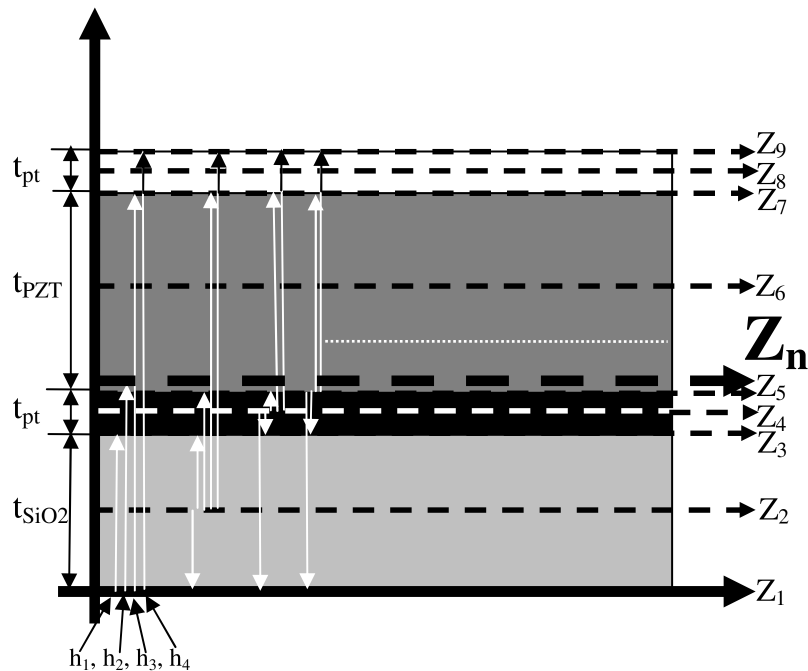

Figure 6.7: Laminate beam showing neutral axis location, Z_n and various other locations for the zero axis starting position.

The laminate beam in Figure 6.7 shows the neutral axis location of the beam as well as several zero axis starting positions ($Z_1,\ldots,Z_9$). Each one of these starting positions are placed throughout the beam in such a way as to map the location's effect on the stiffness,

force, moment and curvature calculations. From each of these starting positions, a set of *h's* are defined Table 6.1 as

Table 6.1: *h* locations for various zero axis starting positions (μm)

	h_1	h_2	h_3	h_4	h_5	h_6
Z_1	0	t_{sio2}	$t_{sio2}+t_{pt}$	$t_{sio2}+t_{pt}+t_{PZT}$	$t_{sio2}+t_{pt}+t_{PZT}+t_{pt}$	
Z_2	$-1/2*t_{sio2}$	0	$1/2*t_{sio2}$	$1/2*t_{sio2}+t_{pt}$	$1/2*t_{sio2}+t_{pt}+t_{PZT}$	$1/2*t_{sio2}+t_{pt}+t_{PZT}+t_{pt}$
Z_3	$-t_{sio2}$	0	$t_{sio2}+t_{pt}$	$t_{sio2}+t_{pt}+t_{PZT}$	$t_{sio2}+t_{pt}+t_{PZT}+t_{pt}$	
Z_4	$-(1/2*t_{pt}+t_{SiO2})$	$-(1/2*t_{pt})$	0	$(1/2*t_{pt})$	$(1/2*t_{pt}+t_{PZT})$	$(1/2*t_{pt}+t_{PZT}+t_{pt})$
Z_5	$-(t_{pt}+t_{SiO2})$	$-(t_{pt})$	0	t_{PZT}	$t_{PZT}+t_{pt}$	
Z_6	$-(1/2*t_{PZT}+t_{pt}+t_{SiO2})$	$-(1/2*t_{PZT}+t_{pt})$	$-(1/2*t_{PZT})$	0	$(1/2*t_{PZT})$	$(1/2*t_{PZT}+t_{pt})$
Z_7	$-(t_{PZT}+t_{pt}+t_{SiO2})$	$-(t_{PZT}+t_{pt})$	$-(t_{PZT})$	0	t_{pt}	
Z_8	$-(1/2*t_{pt}+t_{PZT}+t_{pt}+t_{sio2})$	$-(1/2*t_{pt}+t_{PZT}+t_{pt})$	$-(1/2*t_{pt}+t_{PZT})$	$-(1/2*t_{pt})$	0	$(1/2*t_{pt})$
Z_9	$-(t_{pt}+t_{PZT}+t_{pt}+t_{sio2})$	$-(t_{pt}+t_{PZT}+t_{pt})$	$-(t_{pt}+t_{PZT})$	$-(t_{pt})$	0	

Table 6.2: Zero axis positions (μm)

$Z_1 = 0$	$Z_6 = t_{sio2}+ t_{pt}+t_{PZT}/2$
$Z_2 = t_{sio2}/2$	$Z_7 = t_{sio2}+ t_{pt}+t_{PZT}$
$Z_3 = t_{sio2}$	$Z_8 = t_{sio2}+ t_{pt}+t_{PZT}+t_{pt}/2$
$Z_4 = t_{sio2}+ t_{pt}/2$	$Z_9 = t_{sio2}+ t_{pt}+t_{PZT}+t_{pt}$
$Z_5 = t_{sio2}+ t_{pt}$	Z_n = Neutral Axis Location

and the zero axis positions in relation to the laminate thicknesses for the *h's* in Table 6.1 are listed in Table 6.2.

The stiffnesses, forces and moments are calculated first, about the listed zero axis positions. Then, the tip deflections are calculated similar to those used to generate the results of Figure 6.5 and Figure 6.6. The results obtained are shown in Figure 6.8.

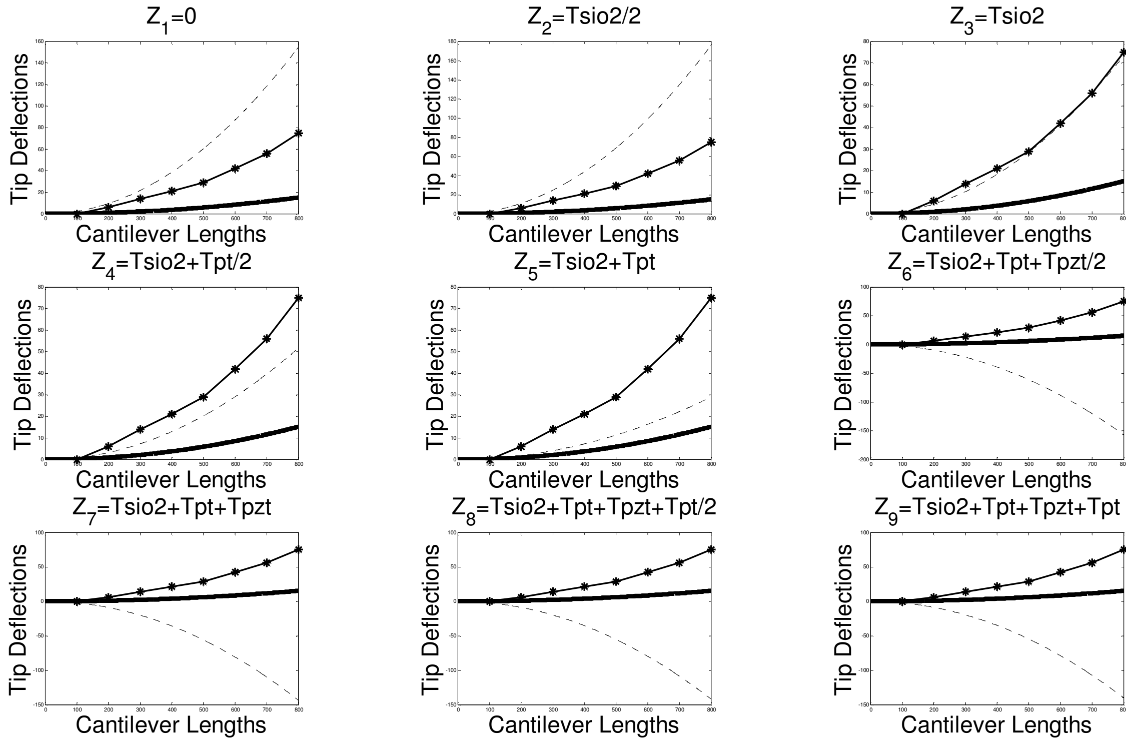

Figure 6.8: Cantilever deflections (μm) versus cantilever lengths (μm) for nine different zero axis locations, and three stiffness methods (Coupled – straight black line, Uncoupled – dashed line, Neutral axis – straight black line included, Experimental Data - dotted).

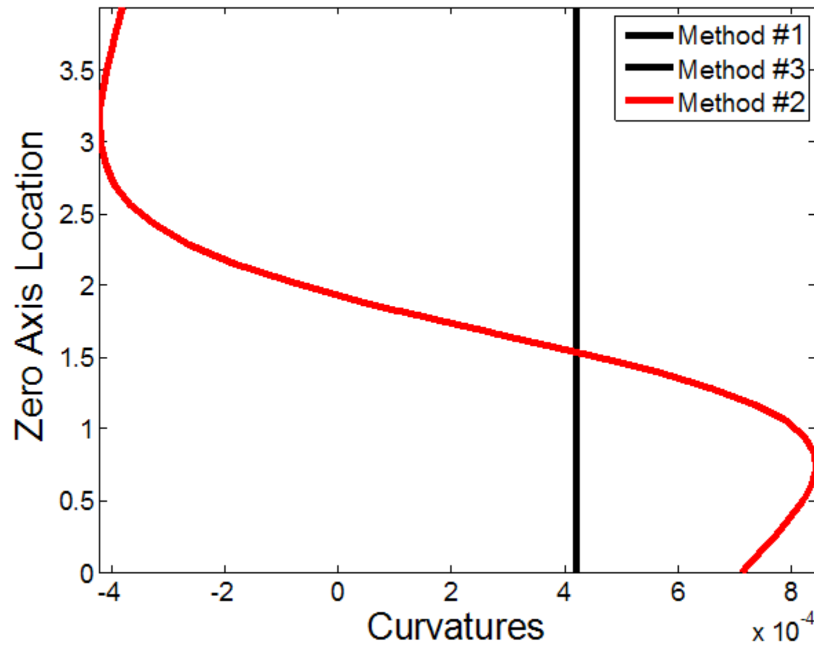

Figure 6.9: Zero axis locations (μm) versus curvatures taken from thin laminate curvature calculations from equations 6.14.

When considering coupled, uncoupled and neutral axis included stiffnesses, the general curvature formula considered is

$$\begin{aligned}
&Method\#1 \quad \frac{\partial^2 w}{\partial x^2} = \left(\frac{AM_R - BN_R}{AD - B^2}\right) \Rightarrow \text{COUPLED} \\
&Method\#2 \quad \frac{\partial^2 w}{\partial x^2} = \left(\frac{M_R}{D}\right) \Rightarrow \text{UNCOUPLED} \\
&Method\#3 \quad \frac{\partial^2 w}{\partial x^2} = \left(\frac{M_R}{D}\right) \Rightarrow \text{NEUTRAL AXIS INCLUDED}
\end{aligned} \tag{6.14}$$

In equation (6.14), the only difference between Method #1 and Method #2 is that in Method #2 the coupled stiffness is assumed zero. Method #1 and Method #2 do not take the neutral axis into consideration as does Method #3. In method three, the coupling stiffness naturally becomes zero and may be dropped (derived in Section 3.5) from

equations of motion. Several conclusions can be drawn from the figures in Figure 6.8. First, that Method #1 and Method 3 have the exact same solution which is also shown in Figure 6.9 where the curvatures are plotted (represented by the black line). In addition, no matter the location of the zero axis, the curvatures do not vary and produce the exact same solutions. However, the uncoupled solution of Method #2 varies in curvature and deflections and should never be used in these types of calculations. Finally, since Method #1 and Method #3 produce the same solutions, Method #3 would be more ideal to use in modeling because it enables the coupling terms to always be neglected. Method 3, in a sense, takes an asymmetric laminate and makes it a symmetric laminate about its neutral axis, thereby allowing for the neglect of coupling stiffness terms.

In addition, Methods 1 and 3 have been plotted for the stiffness, force and moments for a varying zero axis in Figure 6.10 to Figure 6.19. Though they produce the same curvature values as was shown in Figure 6.9, there is large variations in individual laminate layer values. In Figure 6.10 and Figure 6.11, the coupling stiffnesses are plotted. As seen from Figure 6.10, when the zero axis changes, the stiffness values also change. In addition, the composite coupling stiffness changes over a very large range, -60 N/μm^2 to 40 N/μm^2. In comparison, Method #3 whose results are pictured in 6.11 clearly show that though the individual layer coupling stiffnesses are nonzero, that the composite stiffness is always zero, enabling that stiffness to be neglected. Figure 6.12 and Figure 6.13 show the exact same result for both methods when calculating the extensional stiffness. This is because the neutral axis location cancels out when calculating Method #2, thereby making the extensional stiffness not dependent on neutral axis location. In Figure 6.14, there is a large difference and variation in the determined values of the

bending stiffnesses for each layer, the composite structure, compared to the results of Figure 6.15. Figure 6.16 and Figure 6.17 show similar results for the residual moments. The residual forces in Figure 6.18 and Figure 6.19 show the exact same result, smiliar to the results from the extensional stiffness calculations, because the residual force calculation is not dependent on the neutral axis location. In conclusion, both methods accurately calculate the same curvatures and deflections. However, Method #3 should be more widely used for isotropic composite laminates because the coupling stiffness may be neglected allowing one to deal with a simpler form of the governing equation of motion.

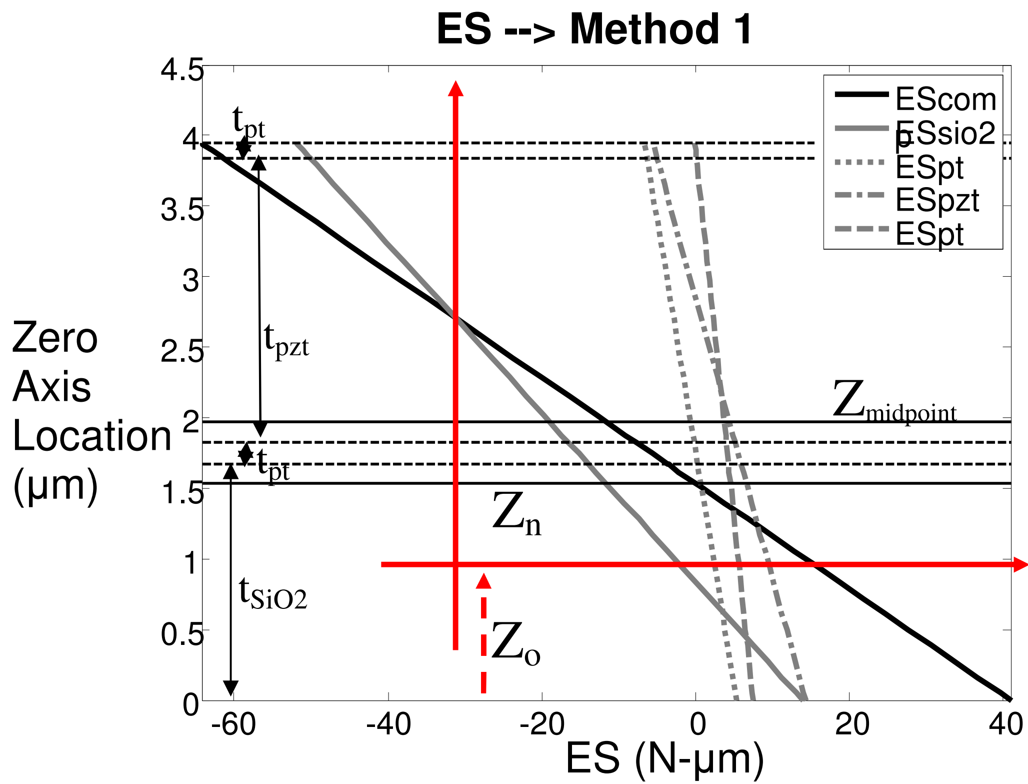

Figure 6.10: Coupling stiffnesses *B* for each individual laminate layer calculated via Method #1 for any zero axis position. ES_{SiO2} is the coupling stiffness for the SiO_2 layer, ES_{Pt} is the coupling stiffness for the platinum layer, ES_{PZT} is the coupling stiffness for the PZT layer, ES_{Pt} is the coupling stiffness for the top Pt layer.

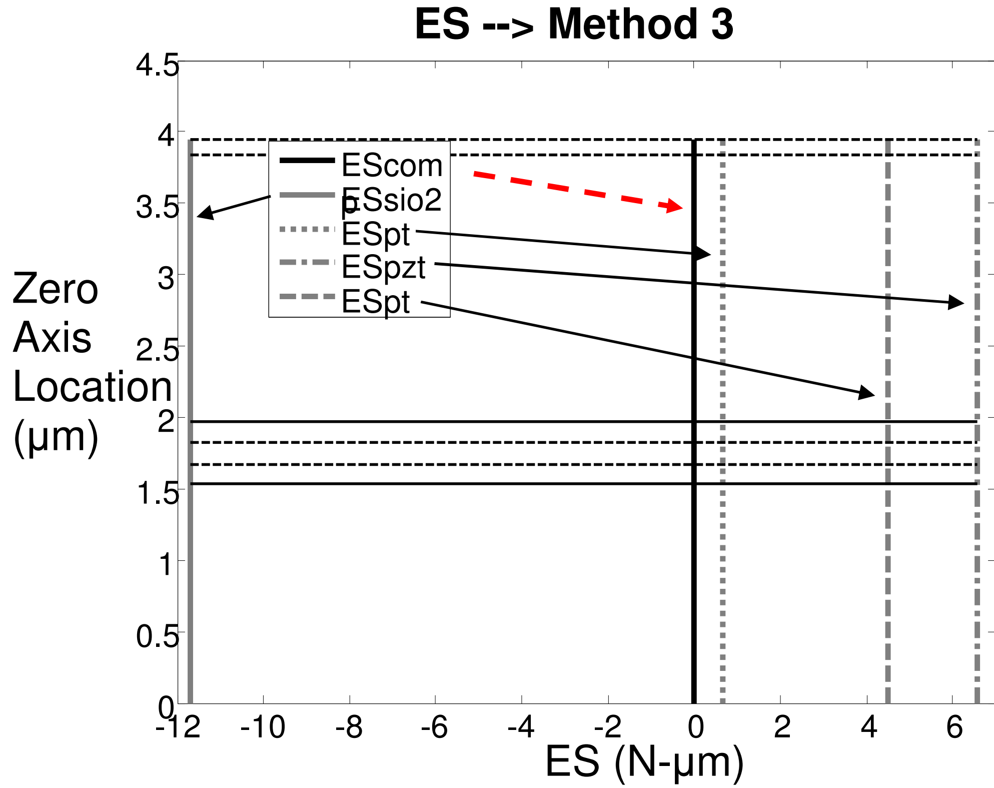

Figure 6.11: Coupled stiffnesses $[B]$ are zero (composite) and calculated via Method #3. ES_{SiO2} is the coupling stiffness for the SiO_2 layer, ES_{Pt} is the coupling stiffness for the platinum layer, ES_{PZT} is the coupling stiffness for the PZT layer, ES_{Pt} is the coupling stiffness for the top Pt layer.

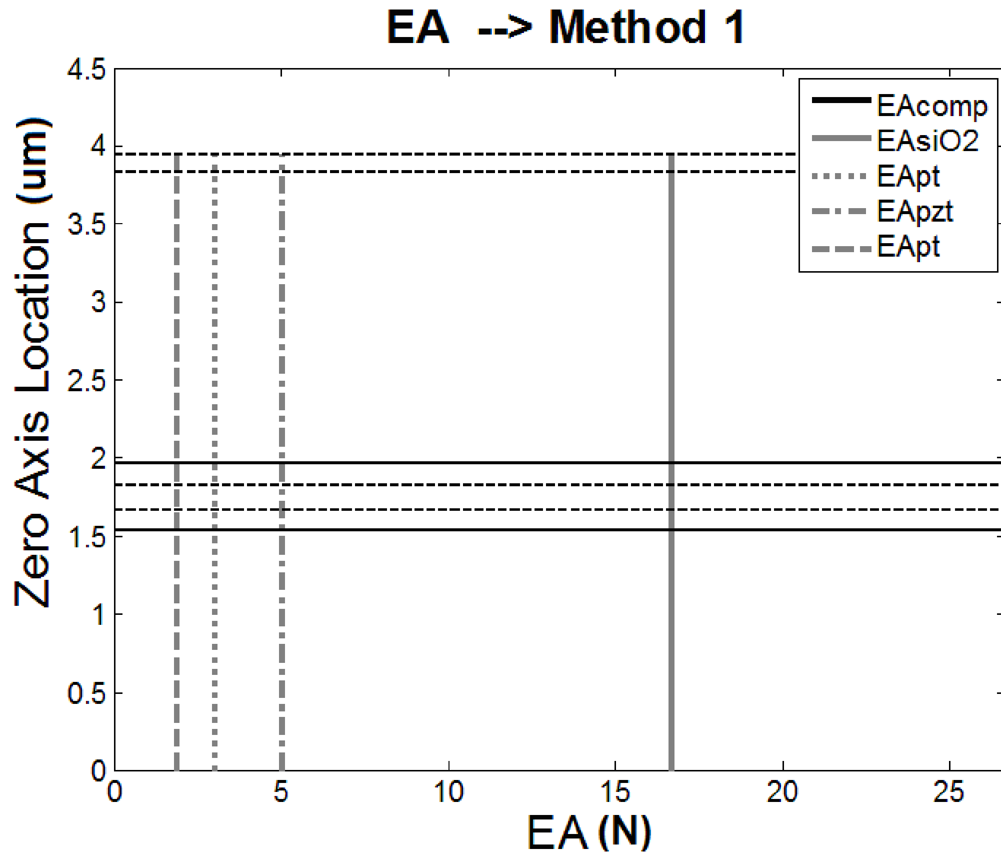

Figure 6.12: Extensional stiffnesses calculated via Method #1. EA_{SiO2} is the extensional stiffness for the SiO_2 layer, EA_{Pt} is the extensional stiffness for the platinum layer, EA_{PZT} is the extensional stiffness for the PZT layer, EA_{Pt} is the extensional stiffness for the top Pt layer.

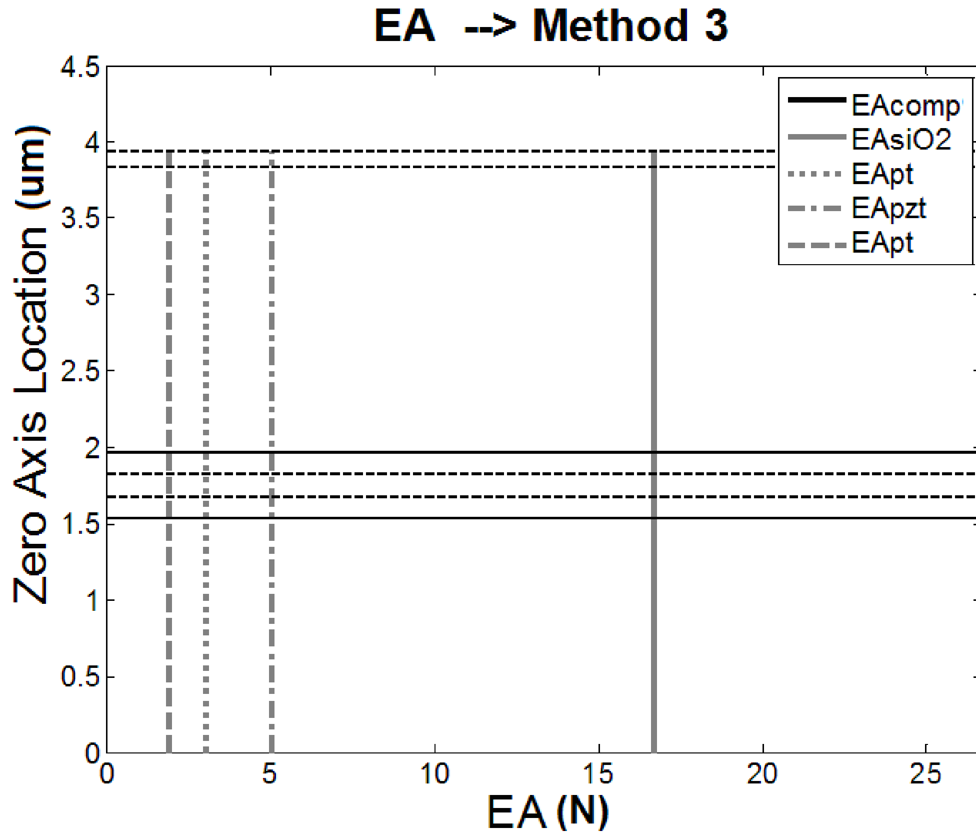

Figure 6.13: Extensional stiffnesses calculated via Method #3. EA_{SiO2} is the extensional stiffness for the SiO_2 layer, EA_{Pt} is the extensional stiffness for the platinum layer, EA_{PZT} is the extensional stiffness for the PZT layer, EA_{Pt} is the extensional stiffness for the top Pt layer.

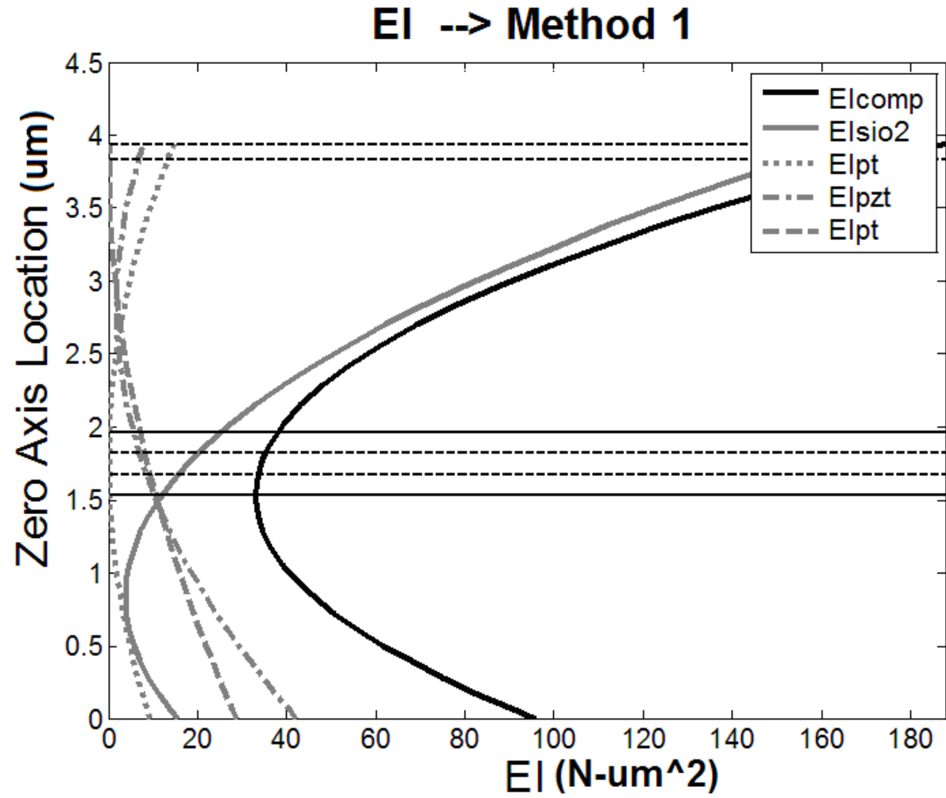

Figure 6.14: Bending stiffnesses calculated via Method #1. EI_{SiO2} is the bending stiffness for the SiO_2 layer, EI_{Pt} is the bending stiffness for the platinum layer, EI_{PZT} is the bending stiffness for the PZT layer, EI_{Pt} is the bending stiffness for the top Pt layer.

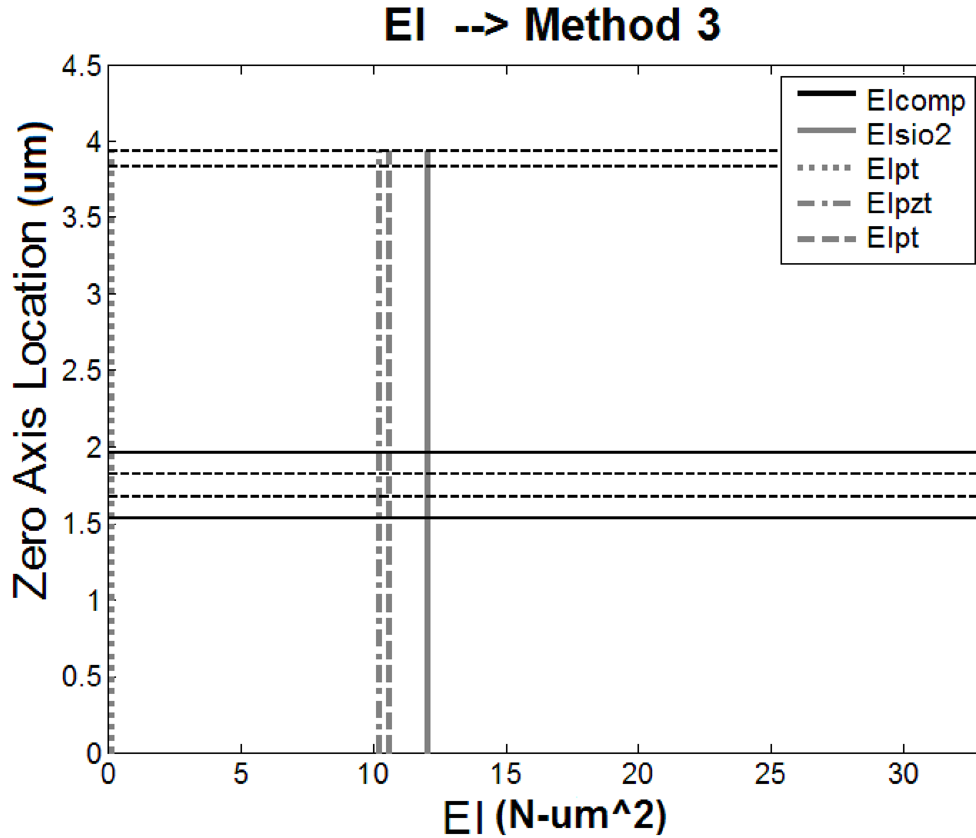

Figure 6.15: Bending stiffnesses calculated via Method #1. EI_{SiO2} is the bending stiffness for the SiO_2 layer, EI_{Pt} is the bending stiffness for the platinum layer, EI_{PZT} is the bending stiffness for the PZT layer, EI_{Pt} is the bending stiffness for the top Pt layer.

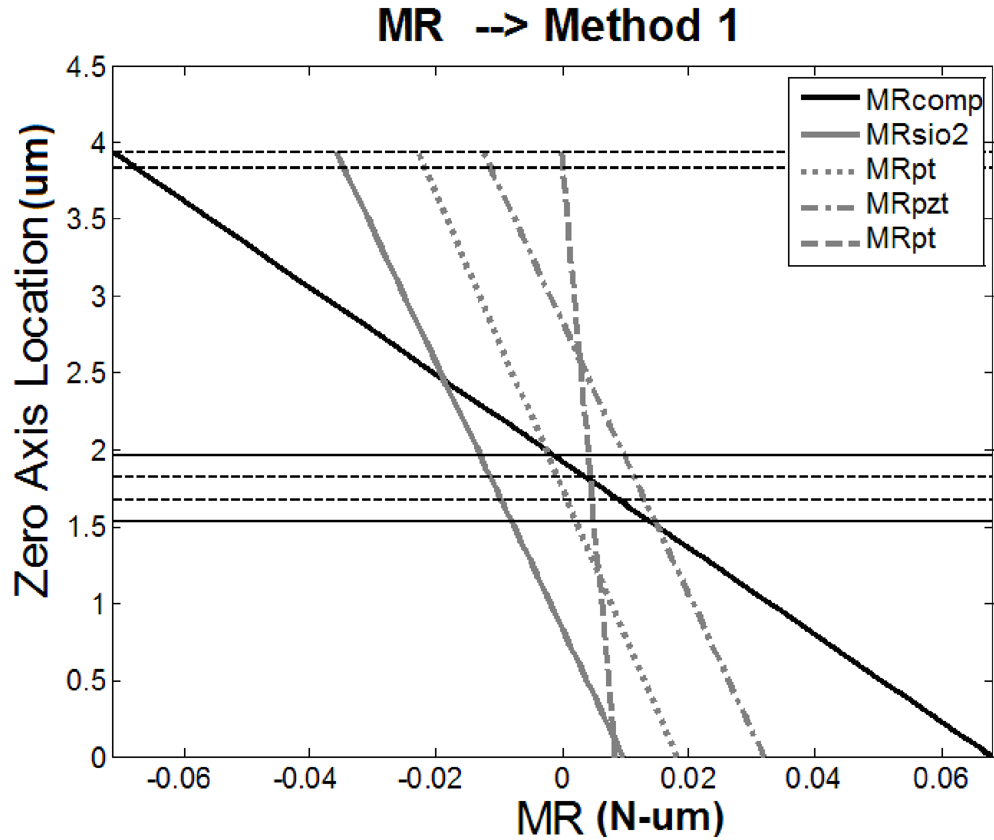

Figure 6.16: Residual moments calculated via Method #1. MR_{SiO2} is the residual moment for the SiO_2 layer, MR_{Pt} is the residual moment for the platinum layer, MR_{PZT} is the residual moment for the PZT layer, MR_{Pt} is the residual moment for the top Pt layer.

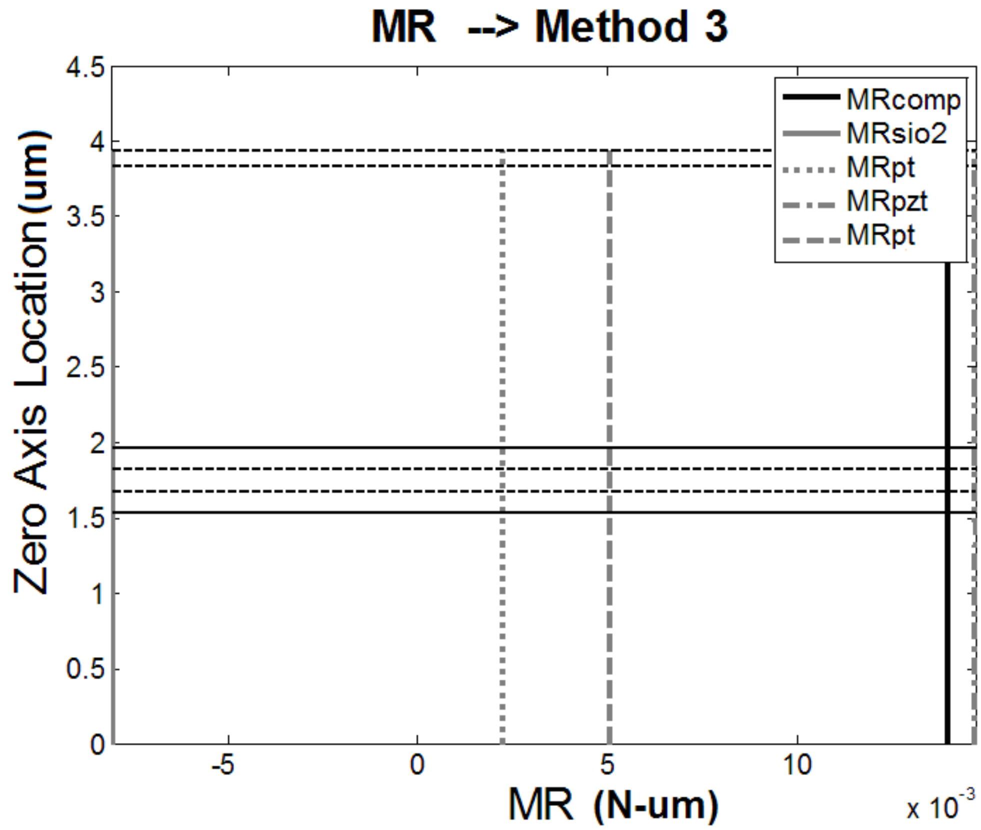

Figure 6.17: Residual moments calculated via Method #3. MR_{SiO2} is the residual moment for the SiO_2 layer, MR_{Pt} is the residual moment for the platinum layer, MR_{PZT} is the residual moment for the PZT layer, MR_{Pt} is the residual moment for the top Pt layer.

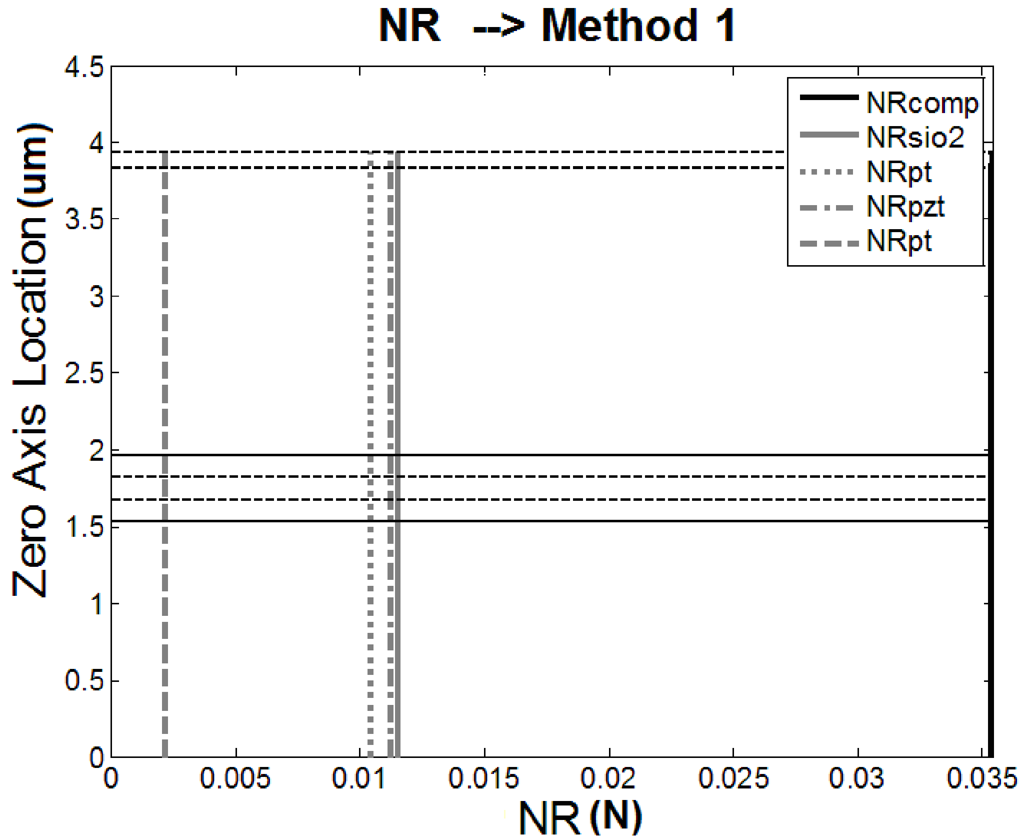

Figure 6.18: Residual forces calculated via Method #1. NR_{SiO2} is the residual force for the SiO_2 layer, NR_{Pt} is the residual force for the platinum layer, NR_{PZT} is the residual force for the PZT layer, NR_{Pt} is the residual force for the top Pt layer.

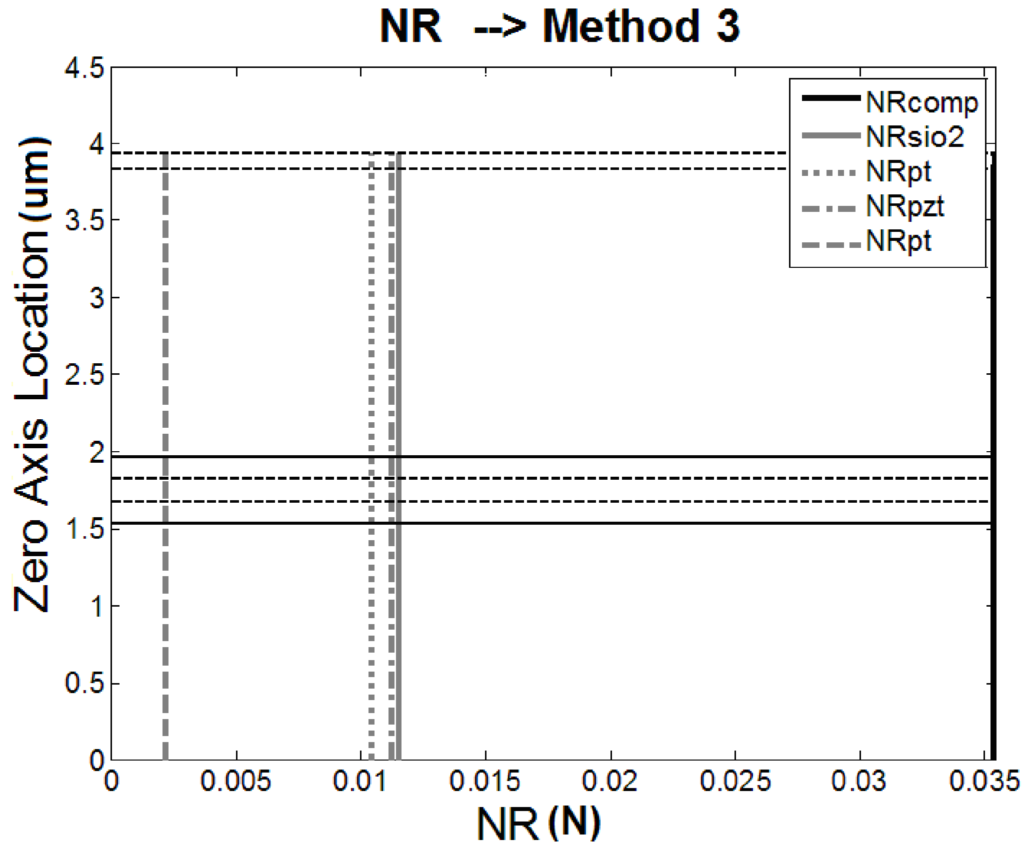

Figure 6.19: Residual forces calculated via Method #3. NR_{SiO2} is the residual force for the SiO_2 layer, NR_{Pt} is the residual force for the platinum layer, NR_{PZT} is the residual force for the PZT layer, NR_{Pt} is the residual force for the top Pt layer.

7 CHARACTERIZATION OF RESIDUAL STRESSES IN MEMS DEVICES

The stress that occurs during thin-film deposition, fabrication and release processing can induce structural defects and impede device performance. Modeling residual stress can be an extremely difficult task. In prior studies, the focus has primarily been on residual-stress measurements in thin-films as they are being deposited and prior to the release of a particular device. In this chapter, residual stresses in MEMS resonators are characterized pre- and post-micro-machining and release of the structures via several static and dynamic techniques.

7.1 Static Technique: Wafer Bow Measurements and Stoney's Formula

During fabrication of multi-layered structures, thin-film layers are deposited, and wafer-bow measurements are taken to measure the residual stress in each layer by using the instrumentation shown in Figure 5.13 [2]. In the experiments, first an initial radius of curvature R_1 on the substrate is measured. After deposition of a thin-film, the radius of curvature of the wafer is changed due to the residual stress. The measurement system is again used to measure the radius of curvature R_2 after the thin-film deposition, and the radius of curvature is then defined and calculated from

$$R = \frac{R_1 R_2}{R_1 - R_2} \tag{7.1}$$

Once the radius of curvature R is known, the residual thin-film stress is determined from Stoney's formula; that is,

$$\sigma_{ave} = \frac{Eh^2}{(1-\upsilon)6t}\frac{1}{R} \tag{7.2}$$

In equation (7.2), σ_{ave} is the average thin-film stress, E is the Young's modulus, is the Poisson's ratio, and t is the thickness. The *average* is used because in most cases, one scan across the wafer is not sufficient. The wafer is scanned initially, then rotated and scanned again at 45º, 90º, and 135º angles. The average of all of these measurements is then determined. This technique determines the individual material layer stresses, and to find a composite value, a volumetric average is taken. Since these residual stress measurements are determined before fabrication, photo patterning or release steps have occurred, the stress values are assumed to be the residual stress values before a device is released. However, though this stress value clearly characterizes thin-film stress and stress in a MEMS device prior to fabrication and release, this value is often used as the residual stress value that that exists in MEMS device post-release. The following Sections will characterize the stress post-release.

7.2 Static Technique: Residual Stress Identification in MEMS Cantilevers

Past work related to residual stress in MEMS cantilevers had focused more on modeling the deflection profiles produced by the stress rather than predicting the stress and understanding the deflections it produces. Pulskamp *et al.* [6] observed severe deflections in micro cantilevers post-fabrication and release processing

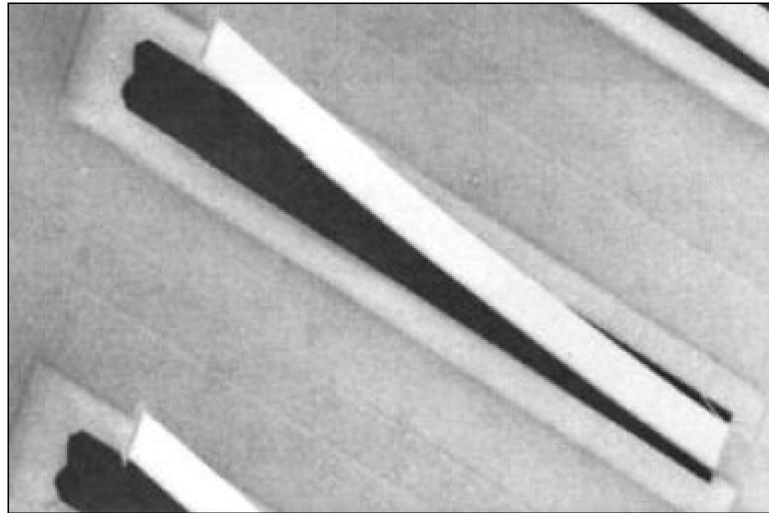

Figure 7.1: MEMS cantilevers exhibiting large curvatures.

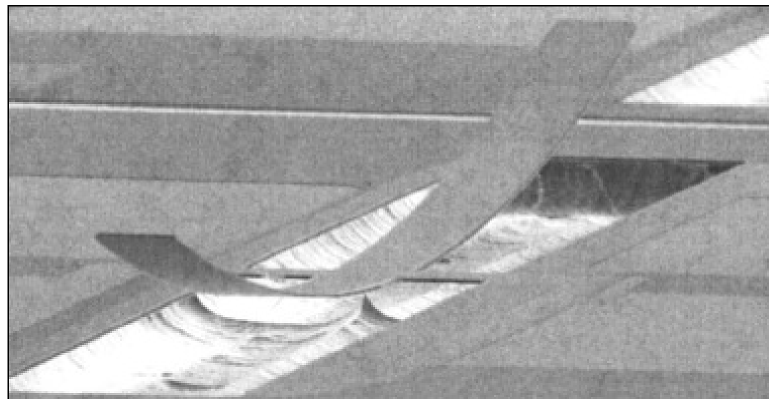

Figure 7.2: MEMS cantilevers exhibiting large curvatures.

Pulskamp *et al.* utilized a linear and nonlinear beam curvature model to predict the static transverse deflection of these cantilevers. Residual stress measurements were taken via the Tencor FLX-2908 bow measurements and Stoney's formula (Sections 5.2, 5.4, 7.1) a the Army Research Laboratory. These stress measurements were taken during thin-film deposition and it was assumed that the stress that exists in each cantilever post-fabrication and release processing. In addition, these stress measurements were inserted into the beam curvature models and used as the driving force for the deflections that occurred in the cantilevers. Pulskamp *et al.* models showed good correlation between analytical and experimental data.

Based of Pulskamp's model and the work completed in Chapter 6, a technique to predict residual stress in MEMS cantilevers is presented in this Section. To begin, residual stress induced deformation can be predicted via the force-strain and moment-curvature relations as

$$\left\{ \begin{Bmatrix} N_{xx} \\ M_{xx} \end{Bmatrix} + \begin{Bmatrix} N_R \\ M_R \end{Bmatrix} \right\} = \begin{bmatrix} EA & EI \\ EI & ES \end{bmatrix} \begin{Bmatrix} \varepsilon_{xx} \\ \kappa_{xx} \end{Bmatrix} \quad (7.3)$$

where $\{N_{xx} \quad M_{xx}\}$ are force and moments resultants induced by a general stress field. Furthermore, $\{N_R \quad M_R\}$ are force and moment resultants produced by a residual stress field respectively. $[EA]$, $[EI]$ and $[ES]$ are the extensional, coupling and bending stiffnesses. If is assumed that all outside stresses are zero, besides residual stress acting in the MEMS cantilever, then the strains and curvatures of equation (7.4) may be solved as

$$\begin{Bmatrix} \varepsilon_{xx} \\ \kappa \end{Bmatrix} = \left(\frac{1}{(EA)(EI) + ES^2} \right) \begin{Bmatrix} (EI)N_R - (ES)M_R \\ (EA)M_R - (ES)N_R \end{Bmatrix} \tag{7.4}$$

and the curvature relation becomes

$$\kappa = \frac{(EA)M_R - (ES)N_R}{(EA)(EI) + ES^2} = \frac{d^2 w}{dx^2} \tag{7.5}$$

If equation (7.5) is integrated twice, stiffness methodologies and calculations of Sections 3.5 and 6.5 are applied, the tip deflections of MEMS cantilevers may be modeled and solved for as

$$W(L) = W_{tipdeflection} = \frac{1}{2}\frac{M_R}{EI}L^2 = \frac{1}{2}\kappa L^2 \tag{7.6}$$

In general, if the laminate layer stresses are known, then the residual moment maybe calculated as

$$M_R = \sum_{k=1}^{4} \sigma_k \frac{b}{2}\left(h_{k+1}^2 + h_k^2\right) \tag{7.7}$$

In addition, a structure's composite residual moment maybe be calculated as

$$M_R = N_R d = \left(\frac{1}{2} w_c t_c^2\right)\sigma_c \tag{7.8}$$

where N_R is the residual force, d is the moment arm, w_c is the width of the cross-Section of the beam, t_c is the thickness or height of the cross-Section and σ_c is the composite residual stress that acts in the axial direction along a beam length.

Table 7.1: Residual stress range (MPa) for identification scheme

	LowerBound	UpperBound
Composite Residual Stress	-2000 MPa	2000 MPa

To begin the residual stress identification scheme, equation (2.8 will be used in calculation of the beam curvature in equation (2.6. The composite residual stress in equation (2.8 will be chosen in a range given in Table 7.1. The residual stresses observed in the materials used in PZT structures can very dramatically in each individual layer, a micro structure as a whole as well as wafer to wafer and run to run as thin-films are being deposited and devices are fabricated and released. Though these stresses can vary dramatically, they still vary within a range. The range chosen in Table 7.1 is chosen initially to encompass all possible composite stresses that might occur in a PZT structure.

Once the composite residual stress is defined, this stress is inserted into equation (7.8) to calculate the composite residual moment; the composite moment is then inserted into equation (7.6) to calculate the cantilever's tip deflection. This tip deflection is then compared to and experimentally measured tip deflection of a PZT cantilever with the same dimensions and material parameters. An error function is defined and calculated as

$$error(n) = \left| W_{tip_analytical}(n) - W_{tip_experimental}(n) \right| \tag{7.9}$$

where $W_{tip_analytical}$ is the solution produced via equation (7.6) and $W_{tip_experimental}$ are experimentally measured tip deflections measured experimentally. By using this scheme, an error value is calculated for every stress value chosen in the range defined in Table 7.1. The minimal error out of all calculated is located, and the composite residual stress

that produces that minimal error, is assumed to be the device residual stress value post-fabrication and release processing. An important note to make is here is to calculate the residual moment via the composite residual moment formula of (7.8). If equation (7.7) is used, instead of needing one composite residual moment value for the entire structure, four individual moment values will be needed to accurately describe each laminate layer in the PZT structure. There can possibly be an infinite number of combinations of laminate layer residual moments that can produce one composite residual moment value. For this reason, the main focus of this technique will be using the composite values.

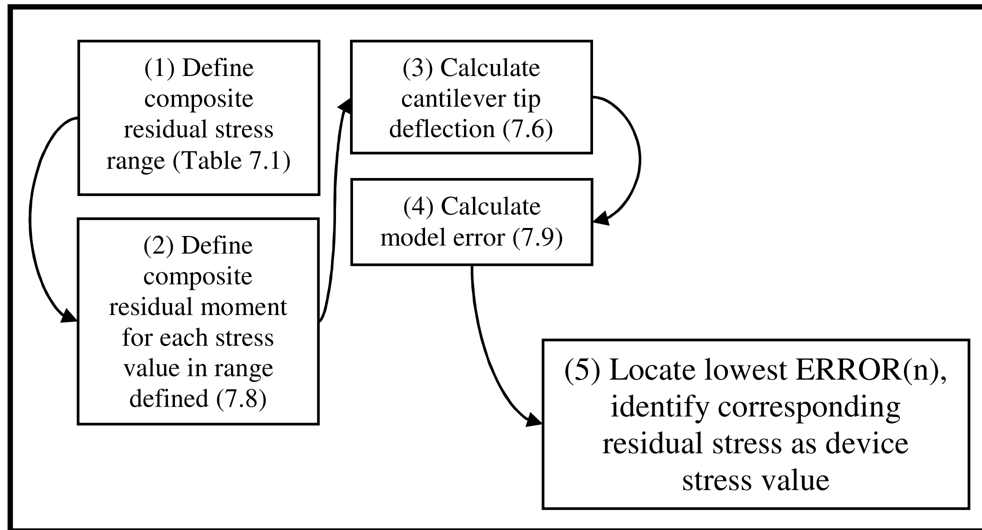

Figure 7.3: Residual stress identification process.

7.3 Dynamic Technique: Parametric Identification of MEMS Resonators

In this Section, the development of a dynamic technique related to the parametric identification of MEMS resonators is presented. Dick *et al*. ([10], [41]) observed that frequency-response data obtained from piezoelectric micro-scale resonators revealed nonlinear characteristics. These resonators are multi-layered structures with the mid-Section typically having three layers and each of the end Sections having four layers. Such a clamped-clamped resonator is shown in Figure 7.4.

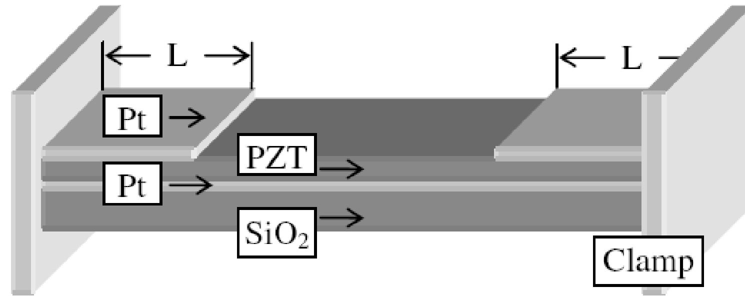

Figure 7.4: Schematic of a clamped-clamped micro resonator with partial top platinum layers.

The governing equation for the transverse displacement of a section of the resonator in Figure 7.4 can be written as

$$\begin{aligned} &\rho A_n W_{n,tt}(x,t) + cW_{n,t}(x,t) + \left(EI_n W_{n,xx}(x,t)\right)_{,xx} \\ &-\left[P + \frac{EA}{2l}\int_{l_{n-1}}^{l_n} \left(W_{n,x}(x,t)\right)^2 dx\right] W_{n,xx}(x,t) \\ &= M_1(t)\frac{d^2}{dx^2}\left[u(x) - u\left(x - \frac{l}{4}\right)\right] \end{aligned} \tag{7.10}$$

In equation (7.10), W_n is the transverse displacement field in the nth Section of the structure, x is the horizontal position along the length of the resonator, ρA_n is the mass per

unit length of the nth Section, P is the axial force, A_n is the area of the nth cross-Section, M_1 is the moment term due to the distributed piezoelectric actuation and u is the unit step function that is used to describe the localized actuation.

To reduce equation (7.10) to the reduced-order model form of the Düffing oscillator, a single mode approximation is assumed as

$$W(x,t) = z(x)\phi(t) \tag{7.11}$$

where W is the transverse displacement, z is the time dependent amplitude and $\Phi(x)$ is the beam deflection profile or mode shape, which depends on the boundary conditions. After inserting equation (7.11) into equation (7.10), the equilibrium equation is reduced by using the first order approximation to produce the Düffing oscillator as

$$\overline{m}\ddot{z} + \overline{c}\dot{z} + kz + \alpha * z^3 = F * cos(\omega * t) \tag{7.12}$$

where $\overline{m}$ is the modal mass, $\overline{c}$ is the modal damping, $\overline{k}$ is the linear stiffness coefficient, α is the nonlinear stiffness coefficient, F is the forcing amplitude and ω is the excitation frequency. Carrying out a weakly nonlinear analysis by using the method of multiple scales leads to the approximate solution

$$z(t) = a(t)\cos(\omega t - \gamma) + H.O.T. \tag{7.13}$$

where the amplitude and phase are governed by

$$\begin{aligned} \dot{a}(t) &= -\mu a(t) + K\sin(\gamma(t)) \\ a(t)\dot{\gamma}(t) &= \sigma a(t) - \frac{3}{8}\alpha a^3(t) + K\cos(\gamma(t)) \end{aligned} \tag{7.14}$$

In equation (7.14), σ is a detuning parameter. The fixed point equations for this system can be combined to produce the frequency – response equation

$$\left(\mu^2 + \left(\sigma - \frac{3}{8}\alpha a_0^2\right)^2\right)a_0^2 = K \tag{7.15}$$

The Jacobian matrix can be constructed, and shown that the critical points need to satisfy equation (7.15) as well as

$$\mu^2 + \left(\sigma - \frac{3}{8}\alpha a_0^2\right)\left(\sigma - \frac{3}{9}\alpha a_0^2\right) = 0 \tag{7.16}$$

As described in the work of Dick *et al.* ([10], [41]), on the basis of the frequency-response of equation (7.16), the experimental frequency-response data is curve fit by using a least-squares scheme to determine the different parameters including linear stiffness, nonlinear stiffness, damping coefficient, and the forcing factor. In Figure 7.5, representative frequency-response curves (red) are shown along with the corresponding response curve (blue) obtained when one of the parameters in (7.16) is varied. The blue curves in Figure 7.5(a) correspond to the case when damping is decreased from the nominal case. The blue curves in Figure 7.5 (b), (c), and (d) correspond to cases where the linear stiffness has been increased from the nominal case, the nonlinear stiffness has been increased from the nominal case, and the forcing amplitude has been decreased, respectively.

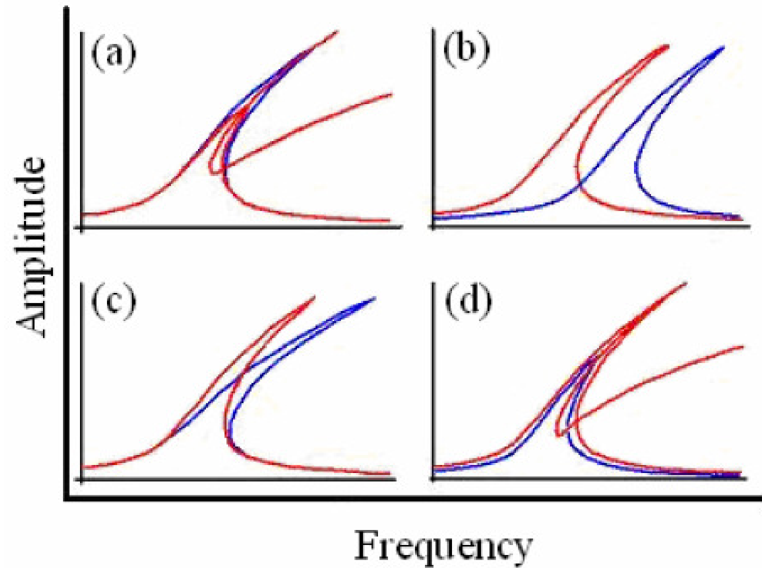

Figure 7.5: Representation frequency-response curves that aid in determining various parameters: (a) sensitivity to damping, (b) sensitivity to linear stiffness, (c) sensitivity to nonlinear stiffness and (d) sensitivity to forcing amplitude.

By using the least-squares method, the corresponding parameters in the forced Düffing oscillator are determined. Once these parameters are known, a finite element model is used to determine the modal mass and the axial force P. The axial force, P, is then adjusted until the fundamental frequency of the model matches the identified fundamental frequency. Once the axial force is known, the residual stress at a location along the resonator can be calculated.

The equations and parametric identification scheme presented in this Section is implemented for the purpose of measuring the residual stress in resonators. As previously mentioned, residual stresses in resonators are typically measured via wafer-bow measurements. However, these measurements are taken during fabrication as thin-films

are being deposited and before the resonator is released. It's often assumed that the residual stress measured via wafer-bow measurements does not change after the resonator is released. This Section will aid in characterizing residual stress in a micro resonator, after it has been released and during a frequency-response.

7.4 Static technique: Parametric Identification of MEMS Resonators

In this Section, the resonator of interest is the clamped-clamped structure shown in Figure 7.4. The resonator can be thought of as a long thin structure under a compressive load (Figure 7.6). This clamped-clamped structure is assumed to be subjected to an axial load caused by residual stress. This residual stress or axial force (N_R) induces bending in resonators. The equation of motion describing the static deflection profile of the resonator given in Section 2.1 reads as

$$\frac{d^4 w}{dx^4} + \left(\frac{N_R}{EI}\right)\frac{d^2 w}{dx^2} = 0 \tag{7.17}$$

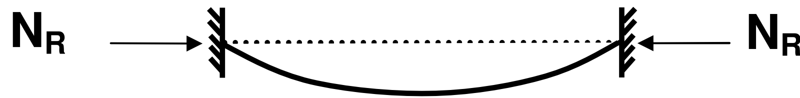

Figure 7.6: Resonator treated as a long thin structure under a compressive load.

where N_R is the axial force residual produced via residual stress and EI is the flexural rigidity or bending stiffnesses. Equation (7.17) produces the characteristic equation

$$m^4 + \left(\frac{N_R}{EI}\right)m^2 = 0 \tag{7.18}$$

which contains two repeated roots and a pair of complex conjugate roots. This, in turn, produces a solution to static deflection profile of equation (7.17)

$$W(x,t) = c_1 + c_2 x + c_3\, sin\left(\sqrt{\frac{N_{RS}}{EI}}x\right) + c_4\, cos\left(\sqrt{\frac{N_{RS}}{EI}}x\right) \tag{7.19}$$

The boundary conditions for a clamped-clamped beam are given by

$$\begin{array}{ll} x = 0 & x = L \\ W(x=0,t) = 0 & W(x=L,t) = 0 \\ W_x(x=0,t) = 0 & W_x(x=L,t) = 0 \end{array} \tag{7.20}$$

When the first set of boundary conditions are applied at x = 0, the first two coefficients are solved for as

$$\begin{aligned} c_1 &= -c_4 \\ c_2 &= -c_3\sqrt{\frac{N_{RS}}{EI}} \end{aligned} \tag{7.21}$$

Inserting these coefficients into (7.19)

$$W(x,t) = c_3\left(\sin\left(\sqrt{\frac{N_{RS}}{EI}}x\right) - \sqrt{\frac{N_{RS}}{EI}}x\right) + c_4\left(\cos\left(\sqrt{\frac{N_{RS}}{EI}}x\right) - 1\right) \tag{7.22}$$

and applying the first of the second set of boundary conditions results in an expression for c_3 as

$$c_3 = c_4 \frac{\left(\cos\left(L\sqrt{\frac{N_{RS}}{EI}}\right) - 1\right)}{L\sqrt{\frac{N_{RS}}{EI}} - \sin\left(L\sqrt{\frac{N_{RS}}{EI}}\right)} \tag{7.23}$$

If the first three coefficients are inserted into the second boundary condition at $x = L$, the result is the following characteristic equation as

$$cos(\beta_n) + \frac{1}{2}\beta_n\, sin(\beta_n) - 1 = 0 \quad \beta_n = L\sqrt{\frac{N_{RS}}{EI}} \tag{7.24}$$

Equation (7.24) is solved by applying the biSection method for an infinite number of roots, the first being determined as $\beta_1 = 6.2768$. For this value, the residual force, moment and stress value may be calculated from the following equation as

$$\mathrm{N_{RS}} = \frac{\mathrm{EI}}{\mathrm{L^2}}\mathrm{B_1^2} = \frac{\mathrm{EI}}{\mathrm{L^2}}(6.2768)^2 = 39.3982\frac{\mathrm{EI}}{\mathrm{L^2}} \tag{7.25}$$

$$M_{RS} = N_{RS} d = \left(B_1^2 \frac{EI}{L^2}\right)\left(\frac{1}{2}t\right) = \frac{B_1^2 (EI) t}{2L^2} \tag{7.26}$$

$$\sigma_{RS} = \frac{N_{RS}}{A_C} = \left(B_1^2 \frac{EI}{L^2}\right)\left(\frac{1}{tw}\right) = \frac{B_1^2 EI}{twL^2} \tag{7.27}$$

These force, moment and stresses are known as the buckling forces, moments and stresses due to residual stress. From this, the buckling residual stresses will be compared to similar results in previous Sections.

In addition to calculating and comparing the buckling stresses, a procedure is also included here to approximate the fourth coefficient of the deflection profile based off of

the first buckling mode as well as experimentally measured center resonator deflections. To begin, insert the three known coefficients into equation (7.19) as well as the center length, $x = L/2$

$$
\begin{aligned}
W(x,t) &= c_4\left[-1-\left[\frac{\left(\cos\left(L\sqrt{\frac{N_{RS}}{EI}}\right)-1\right)}{L\sqrt{\frac{N_{RS}}{EI}}-\sin\left(L\sqrt{\frac{N_{RS}}{EI}}\right)}\right]\frac{L}{2}\sqrt{\frac{N_{RS}}{EI}}\right. \\
&\quad+\left[\frac{\left(\cos\left(L\sqrt{\frac{N_{RS}}{EI}}\right)-1\right)}{L\sqrt{\frac{N_{RS}}{EI}}-\sin\left(L\sqrt{\frac{N_{RS}}{EI}}\right)}\right]\sin\left(\sqrt{\frac{N_{RS}}{EI}}\frac{L}{2}\right) \\
&\quad\left.+\cos\left(\sqrt{\frac{N_{RS}}{EI}}x\right)\right]
\end{aligned}
\tag{7.28}
$$

which can be simplified to

$$
\begin{aligned}
W_{centerdeflection} &= c_4\left[-1-\underbrace{\left[\frac{(\cos(\beta_n)-1)}{\beta_n-\sin(\beta_n)}\right]\frac{\beta_n}{2}}_{c_2}\right. \\
&\quad+\underbrace{\left[\frac{(\cos(\beta_n)-1)}{\beta_n-\sin(\beta_n)}\right]}_{c_3}\sin\left(\frac{\beta_n}{2}\right) \\
&\quad\left.+\cos\left(\frac{\beta_n}{2}\right)\right]
\end{aligned}
\tag{7.29}
$$

where the center deflection is that of an experimentally measured resonator. Some important observations can be made concerning equation (7.29). If the first buckling

mode is considered, then $\beta_1 = 6.2768$. This value is very close to 2π. Because of this, $cos(2\pi) = 1$ and both c_2 and c_3 go to zero. Equation (7.29) reduces to

$$W_{centerdeflection} = c_4\left[\cos\left(\frac{\beta_n}{2}\right) - 1\right] \quad (7.30)$$

Again, if $\beta_1 = 6.2768$, then $cos(\beta_n / 2) \cong cos(2 * \pi / 2) = cos(\pi) = -1$ and the fourth and final coefficient of the deflection profile may be solve for as

$$c_4 = -\frac{1}{2} W_{centerdeflection} \quad (7.31)$$

8 COMPARISON OF TECHNIQUES, DISCUSSION AND RESULTS

In this chapter, different methods that can be used to determine the residual stress values in a composite MEMS structure have been discussed. Analytical and experiment results produced from Sections 7.1 through 7.4 are presented, by using these methods. These results help understand the residual stress state before release and post-release.

8.1 Results From Wafer Bow Measurements and Stoney's Formula

During resonator/cantilever fabrication, thin-film layers were deposited and wafer bow curvature measurements were taken via the Tencor FLX-2908 (Section 5.2, Figure 5.13) and converted to residual thin-film stress measurements via Stoney's formula (Section 7.1). Representative results are shown in Table 8.1.

Table 8.1: Results from wafer bow measurements and Stoney's formula

Orientation Degrees	Film Layer	Stress MPa	Thickness A
0	SiO2	-164.5	-5278
45	SiO2	-108.5	-5278
90	SiO2	-85.8	-5278
135	SiO2	-93.8	-5278
	Average thin-film residual stress	-113.15 MPa	

Orientation degrees	Film Layer	Stress MPa	Thickness A
0	Pt	342.7	-1884
45	Pt	342	-1884
90	Pt	347.7	-1884
135	Pt	342.8	-1884
	Average thin-film residual stress	343.8 MPa	

Orientation Degrees	Film Layer	Stress MPa	Thickness A
0	PZT	135.5	-5202
45	PZT	125	-5202
90	PZT	130.6	-5202
135	PZT	133.6	-5202
	Average thin-film residual stress	131.18 MPa	

Orientation degrees	Film Layer	Stress MPa	Thickness A
0	Top Pt	52.8	-1050
45	Top Pt	69.6	-1050
90	Top Pt	60.6	-1050
135	Top Pt	66.4	-1050
	Average thin-film residual stress	62.35 MPa	

In table 8.1, the layer stress values for each orientation are shown. Though there are some differences for each layer's differing orientations, the average value is taken and assumed to be that layer's residual thin-film stress value. The composite stress for all four laminate layers is calculated via a volumetric average and given in Table 8.2. This composite stress value is that of the four thin laminate layers that are initially deposited on the wafer, and before fabrication and release processes begin. The results from the three techniques presented in Sections 7.2 to 7.4 be used will characterize residual stresses post processing in individual devices.

Table 8.2: Thin-film layer stresses and composite stress calculation

Material	Thickness (μm)	Stress N/μm^2
SiO_2	.5278	-113.15e-06
Pt	1884	343.8e-06
PZT	5202	131.18e-06
Pt	1050	62.35e-06
	Composite Residual Stress	59.5169

8.2 Results From the Static Technique Applied to MEMS Cantilevers

The static technique of Section 7.2 is applied to PZT cantilevered devices taken from five wafers with differing thicknesses, wafer bow results, and cantilever length and widths. The cantilever dimensions are given in Table 8.3 to Table 8.5. Post-fabrication and release, the cantilevers in the following table are scanned via the optical profilometer shown in Section 5.4. A typical scan is shown in Figure 8.3 and Figure 8.4. From these scans, deflections profiles were saved, and cantilever tip deflections were extracted and inserted into the technique from Section 7.2 in order to extract individual device residual stress values. These cantilever tip deflections are shown in Figure 8.1 and Figure 8.2. The straight lines in these figures represent analytically predicted model deflections, driven by residual stress value taken during thin-film deposition (composite stress values calculated for each wafer, Table 8.1 and Tabel 8.2). Clearly the model predicted profiles via wafer bow measurements and Stoney's formula do not match the experimental data well. The technique of Section 7.2 is applied; the composite residual stress is varied until the deflection profile matches experimental data with the lowest error. This lowest error indicates that the corresponding residual stress is the individual device stress value post-fabrication and release. Results for individual cantilevered devices are shown in Figure 8.5. For cantilevers on the same wafer, wafer #5, two widths sets corresponding to 20 μm and 35 μm cantilevers are compared. There are some slight differences in the stress values produced with each set. However, regardless of the width, nearly the same residual stress value is produced for each individual length. This indicates that the width effect does not affect the cantilever deflection and residual stress values as assumed through Euler-Bernoulli beam theory. In comparison to other wafers of cantilevers of

different length and width sets, there are some noticeable differences in the residual stress values produced. Wafers #1 through #4 have cantilevers of similar lengths and widths. However, there are differences in the individual thin-film layer thicknesses for each of those wafers. If Table 8.6 is examined, it can be seen that the SiO_2 and *PZT* are the two layers, whose values vary with thickness. If wafer #3 and wafer #4 are compared, the residual stress values are similar for each length, with a difference of approximately 5 MPa for each length in each set. When examining the layer thicknesses, one can see that the SiO_2 layer thickness for wafer #4 is over two times that of wafer #3. This thicker thin-film layer clearly produced lower stress values. The major difference in comparisons of all the wafers, is the laminate layer thicknesses driving the deflection profiles and the corresponding residual stress values.

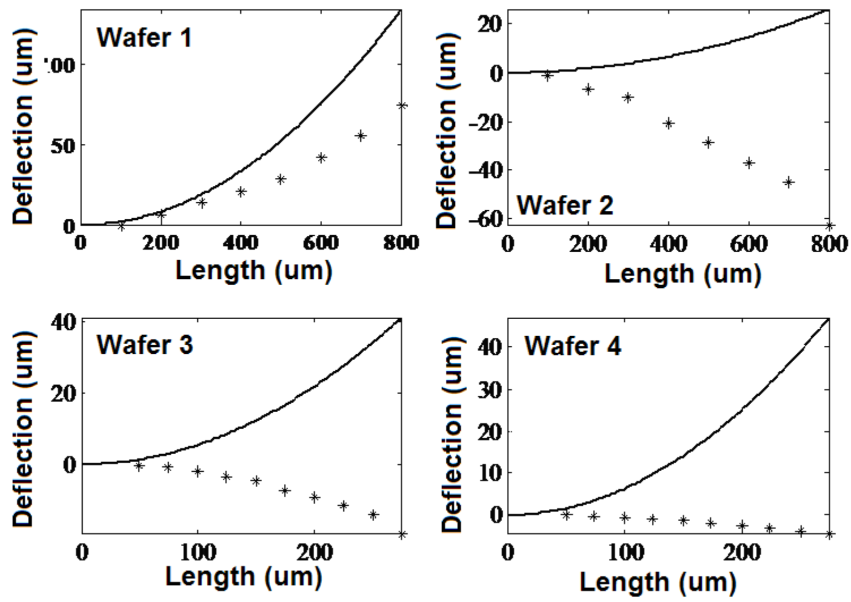

Figure 8.1: Cantilever tip deflection data. Asterisks represent experimentally measured tip deflections; straight line represents analytically predicted tip deflections.

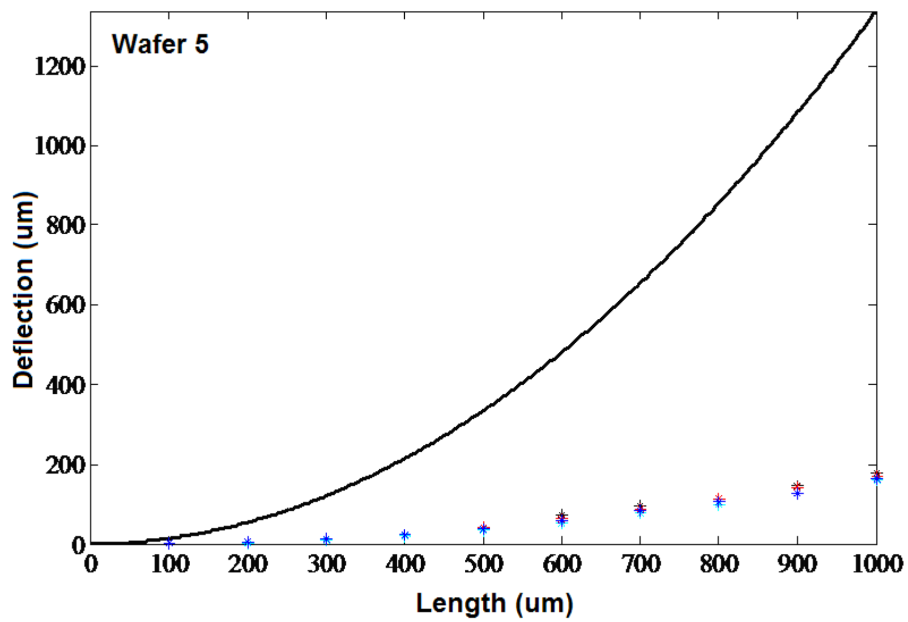

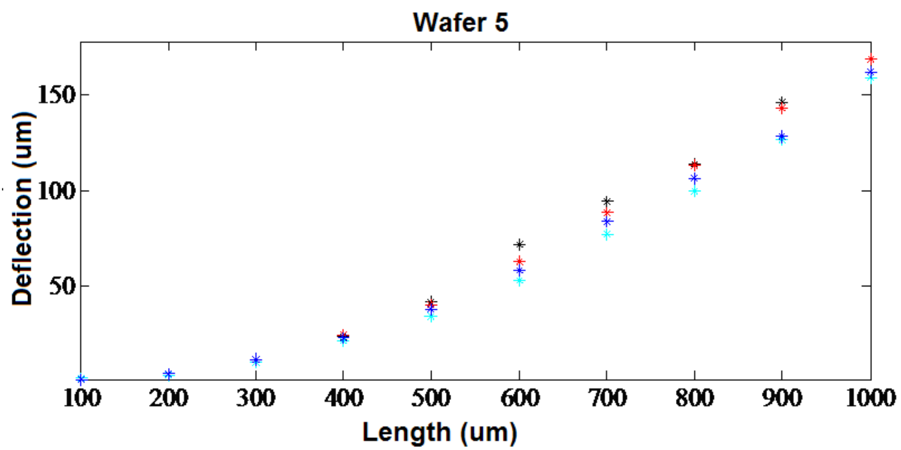

Figure 8.2: Cantilever tip deflection data. Asterisks represent experimentally measured tip deflections, straight line represents analytically predicted tip deflections.

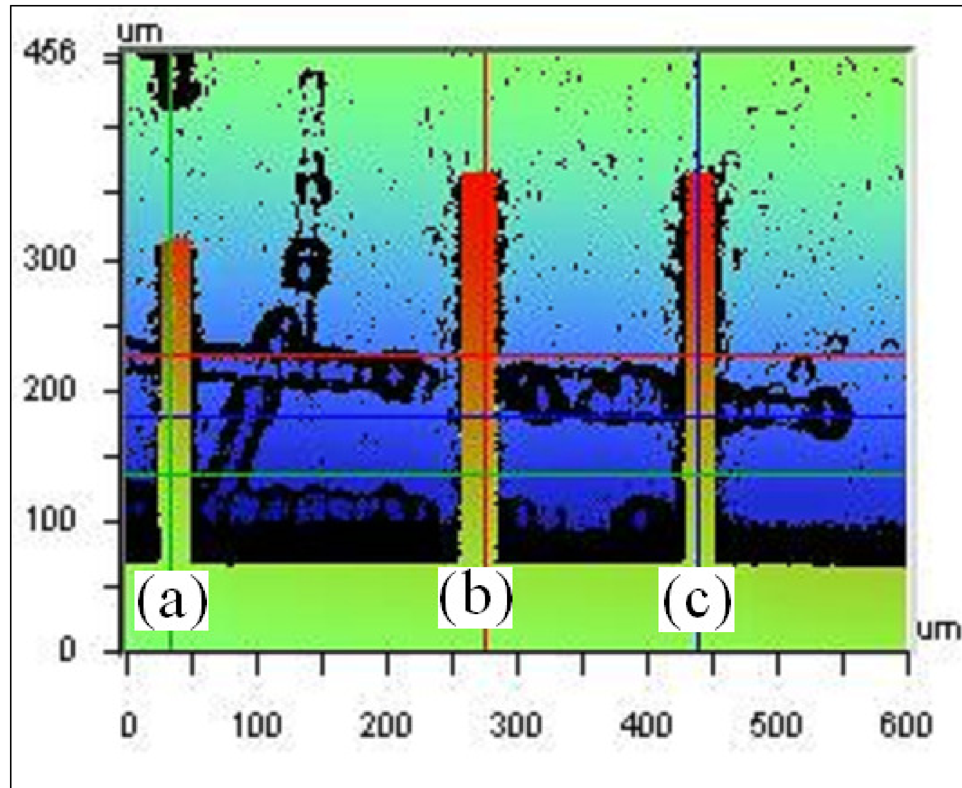

Figure 8.3: Optical profilometer scan of three cantilevered resonators. (a) 250 μm long, 20 μm wide PZT resonator. (b) 300 μm long, 20 μm wide PZT resonator. (c) 300 μm long, 20 μm wide SiO_2 resonator. Obtained via optical profilometer at the Army Research Laboratory, Adelphi, MD.

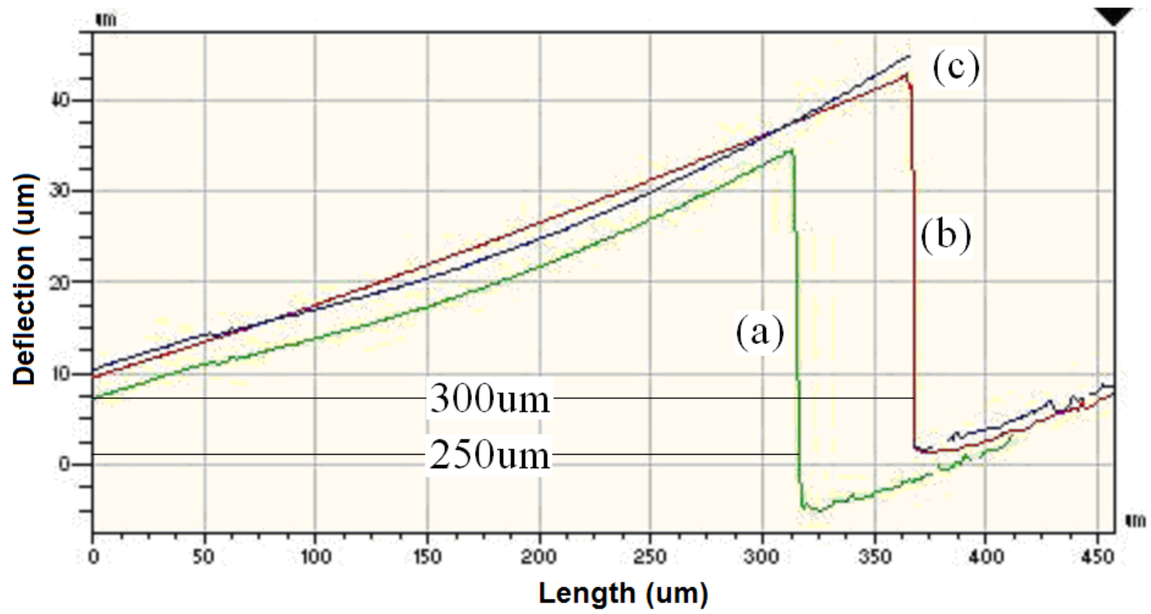

Figure 8.4: Y Profile from optical profilometer scan. . Obtained via optical profilometer at the Army Research Laboratory, Adelphi, MD.

Table 8.3: Wafer #1 and Wafer #2: cantilever widths, lengths, tip deflections.

Wafer #1 (μm)			Wafer #2 (μm)		
Width	length	tipdeflection	width	length	tipdeflection
100	100	0	100	100	-1.2
100	200	6	100	200	-6.9
100	300	14	100	300	-10.4
100	400	21	100	400	-20.8
100	500	29	100	500	-28.9
100	600	42	100	600	-37
100	700	56	100	700	-45.1
100	800	75	100	800	-62.5

Table 8.4: Wafer #3 and Wafer #4: cantilever widths, lengths, tip deflections.

Wafer #3 (μm)			Wafer #4 (μm)		
width	length	tipdeflection	width	length	tipdeflection
100	50	-0.3	100	50	0
100	75	-0.9	100	75	-0.2
100	100	-2.1	100	100	-0.6
100	125	-3.5	100	125	-1.1
100	150	-4.7	100	150	-1.3
100	175	-7.1	100	175	-1.9
100	200	-9.3	100	200	-2.5
100	225	-11.6	100	225	-3.2
100	250	-14.3	100	250	-3.8
100	275	-19.3	100	275	-4.4

Table 8.5: Wafer #5: cantilever widths, lengths, tip deflections.

Width (μm)	Length (μm)	Tipdeflection (μm)	Width (μm)	Length (μm)	Tipdeflection (μm)
20	100	1.6	35	100	1.5
20	200	4.0	35	200	3.6
20	300	10.1	35	300	11.3
20	400	23.7	35	400	23.8
20	500	41.5	35	500	40.3
20	600	72.1	35	600	62.4
20	700	94.1	35	700	88.3
20	800	114.3	35	800	113.0
20	900	146.3	35	900	143.2
20	1000	177.9	35	1000	169.2

width	length	tipdeflection	width	length	tipdeflection
20	100	1.2	35	100	1.1
20	200	2.8	35	200	3.8
20	300	9.9	35	300	11.2
20	400	21.1	35	400	22.9
20	500	33.7	35	500	37.5
20	600	53.1	35	600	57.8
20	700	76.9	35	700	83.6
20	800	99.4	35	800	106.3
20	900	126.8	35	900	128.3
20	1000	159.5	35	1000	162.4

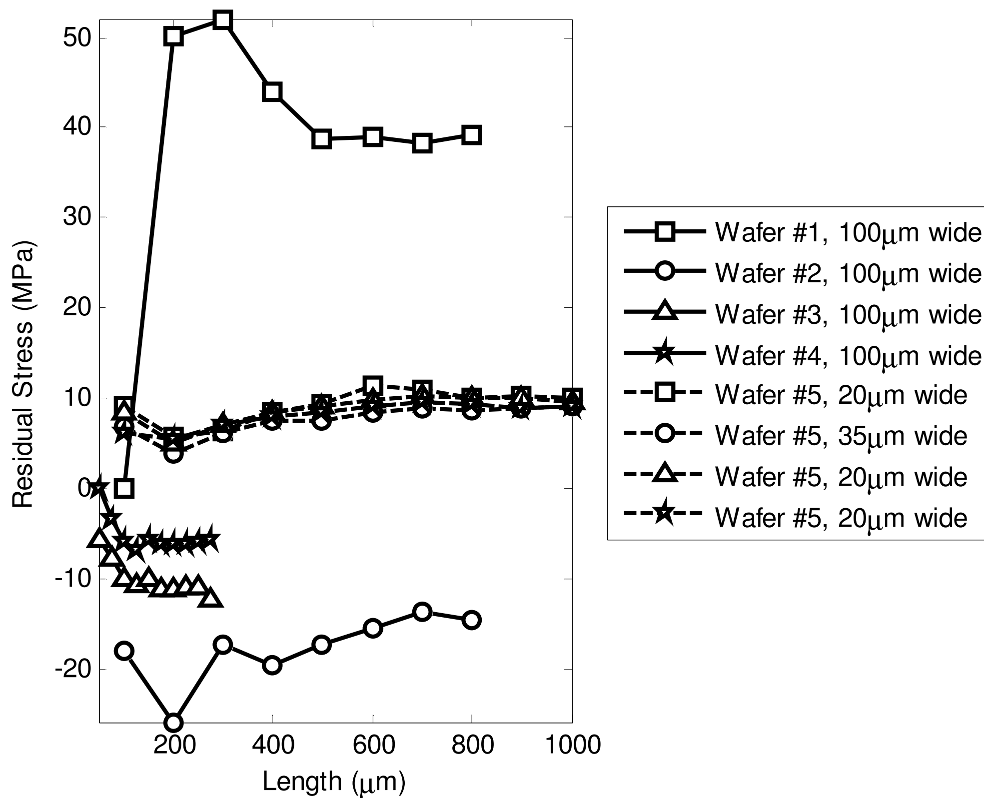

Figure 8.5: Composite residual stresses for individual cantilevered devices approximated from the static technique given in Section 7.2.

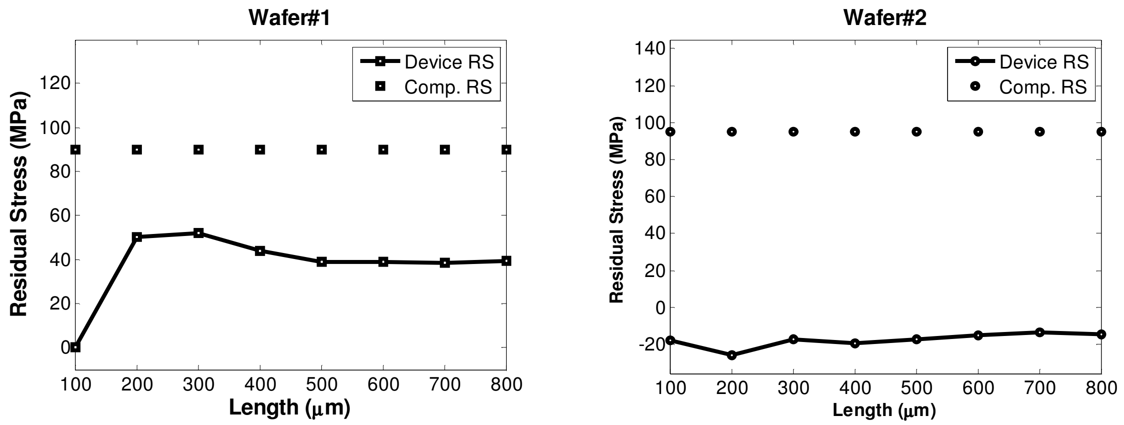

Figure 8.6 (a) & (b): Individual wafer composite residual stress (*Comp. RS*) in comparison to cantilevered device residual stress (*Device RS*).

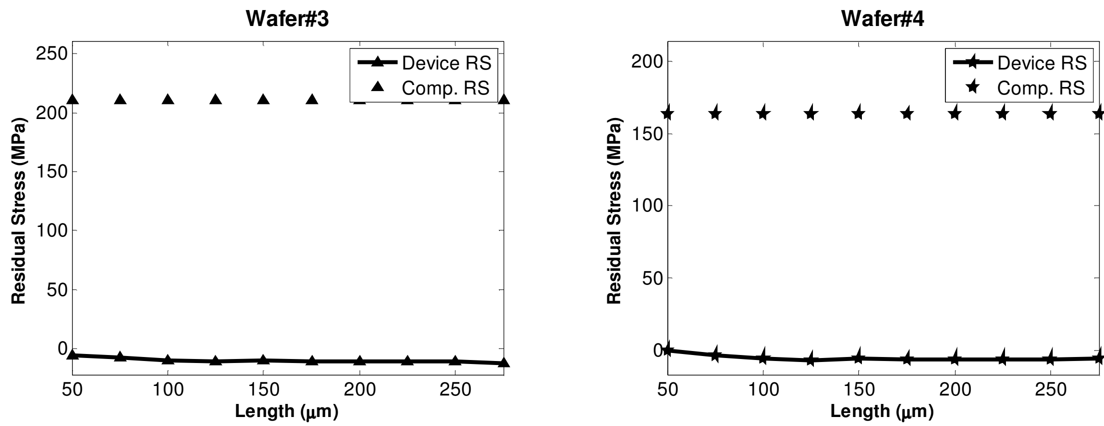

Figure 8.7 (a) & (b): Individual wafer composite residual stress (*Comp. RS*) in comparison to cantilevered device residual stress (*Device RS*).

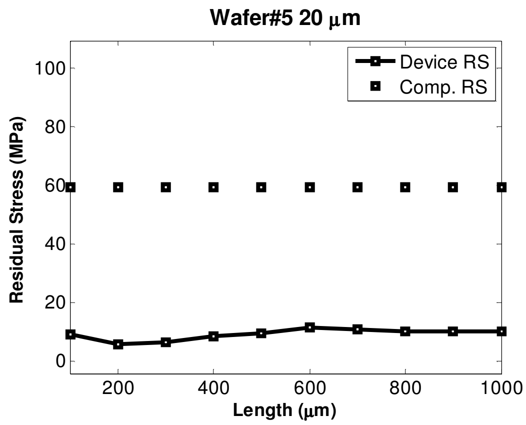

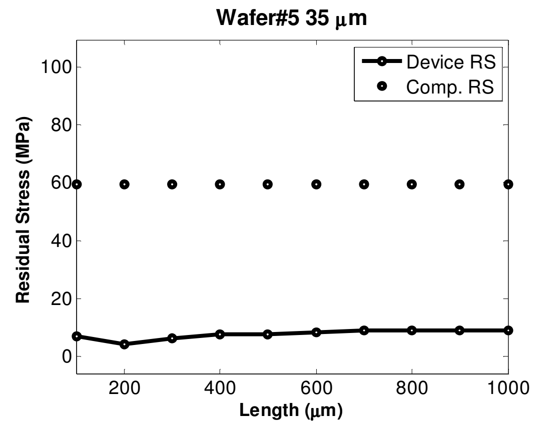

Figure 8.8 (a) & (b): Individual wafer composite residual stress (*Comp. RS*) in comparison to cantilevered device residual stress (*Device RS*).

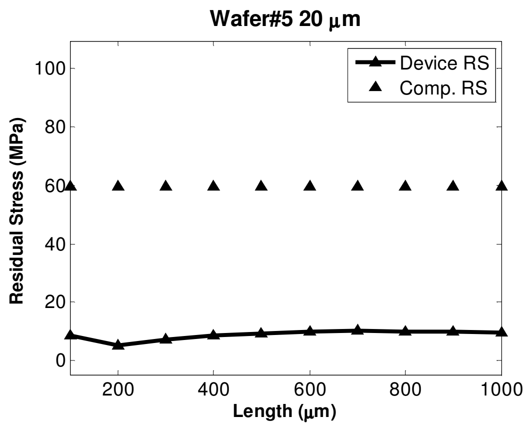

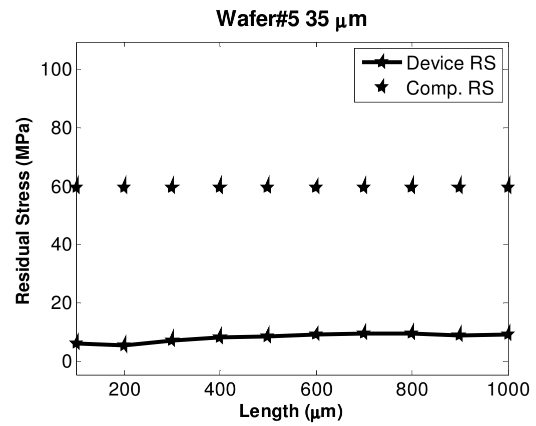

Figure 8.9 (a) & (b): Individual wafer composite residual stress (*Comp. RS*) in comparison to cantilevered device residual stress (*Device RS*).

Table 8.6: Thin-film layer thicknesses by wafer (μm).

Wafer	SiO_2	Pt	PZT	Pt
Wafer#1	1.6688	0.16	2.0145	0.1
Wafer#2	0.737	0.16	1.461	0.1
Wafer#3	0.5122	0.1	0.5006	0.105
Wafer#4	1.1177	0.1	0.4948	0.105

8.3 Results From Dynamic Technique Applied to MEMS Clamped-Clamped Resonators

The dynamic technique of Section 7.3 is applied to PZT clamped-clamped devices through the experimental arrrangement described in Section 5.5. From initial sine sweeps of the resonators, the frequency-response was decidedly linear (red line in Figure 8.10). Typical PZT devices are usually poled (send current through device for small length of time to align all dipoles in PZT material). A current of 10V was passed through the resonator for 10 minutes, the sine sweep was repeated. The frequency-response, after poling, now exhibits the nonlinear behavior as exhibited by a Düffing oscillator.

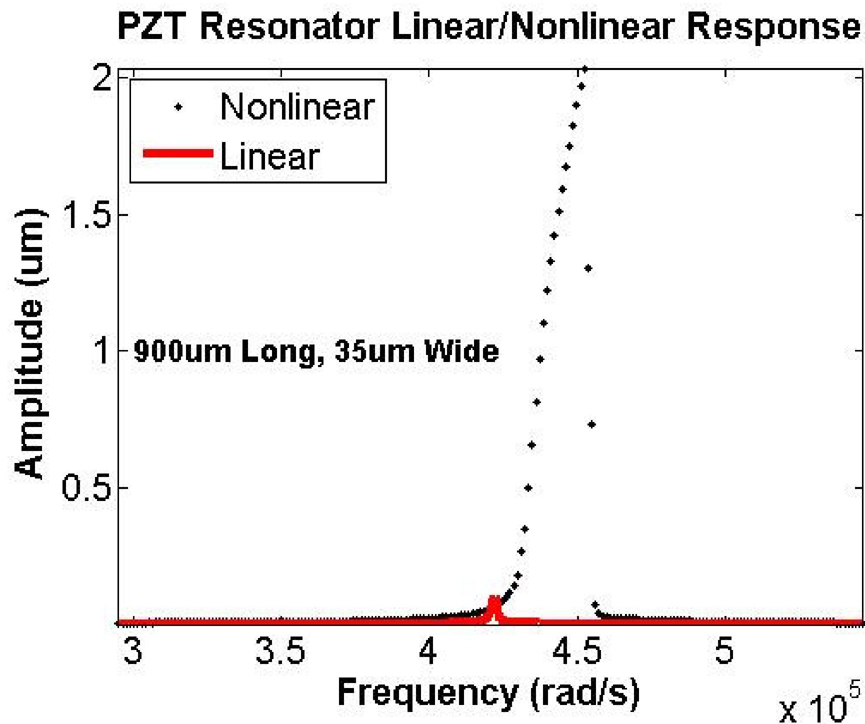

Figure 8.10: Linear and nonlinear frequency-response of a PZT resonator, 900 μm long and 35 μm wide.

Frequency-response data for resonators of lengths varying between 300 μm and 1000 μm as well as two width sets, 20 μm and 35 μm wide were taken post poling of the devices. The analytical model was fit to the experimental data and system parameters (mass, linear and nonlinear stiffness coefficients, damping coefficients, forcing factor, and axial force) were determined (Figure 8.11). In addition, the RMS error was calculated and ranged from 1.5 nm to 25 nm. Since most deflection amplitudes were over 1000 μm, a maximum error of 25 nm was considered extremely small in comparison. The final results from this technique are shown in Figure 8.12 and Figure 8.13. In Figure 8.12, the axial force for two width Sections are shown and compared to the axial force produced via the dynamic technique for two different width sets, 20 μm and 35 μm wide. The axial forces are dependent on the width of these structures. However, when using these forces to calculate the residual stress values, the width is not a factor. The residual stress value for each device is not dependent on width but dependent on its length (Figure 8.13.).

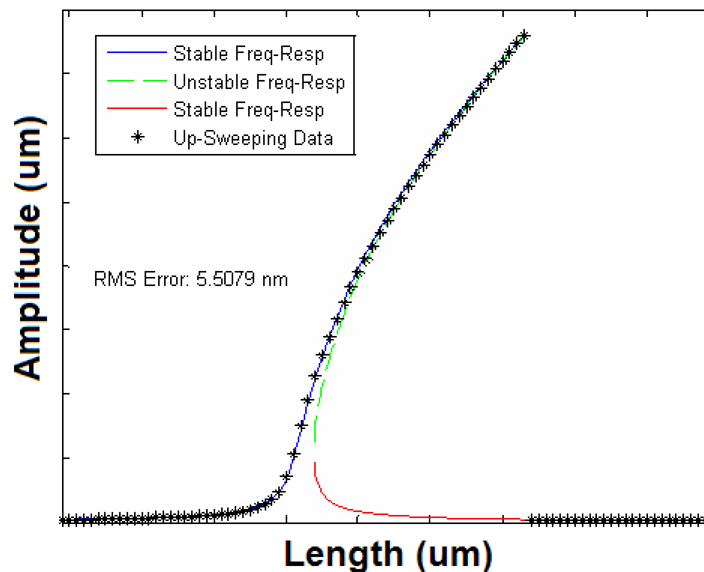

Figure 8.11: Sample results obtained from the dynamic technique for a single resonator.

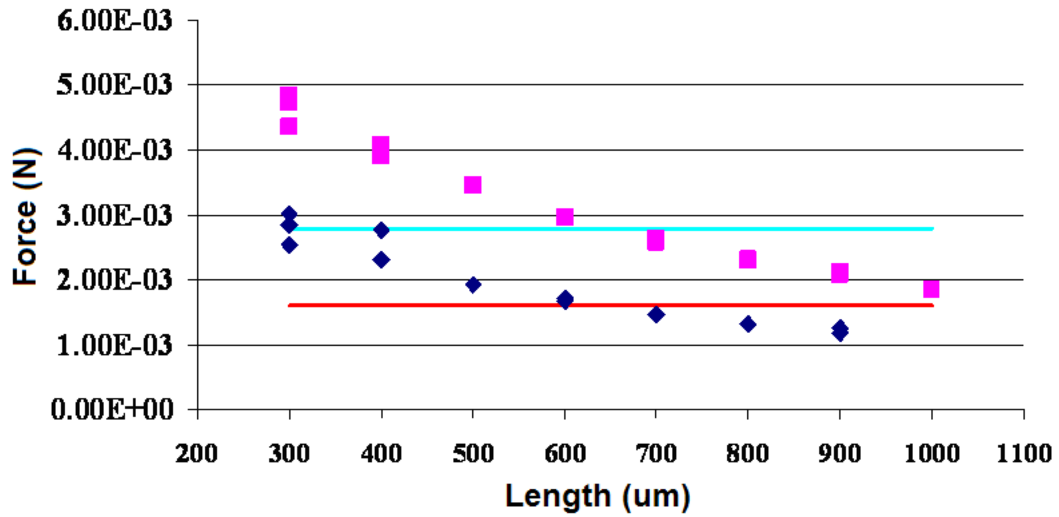

Figure 8.12: Axial force calculated via the dynamic technique for varying lengths and widths (squares) and the axial force calculated via wafer bow measurements and Stoney's formula.

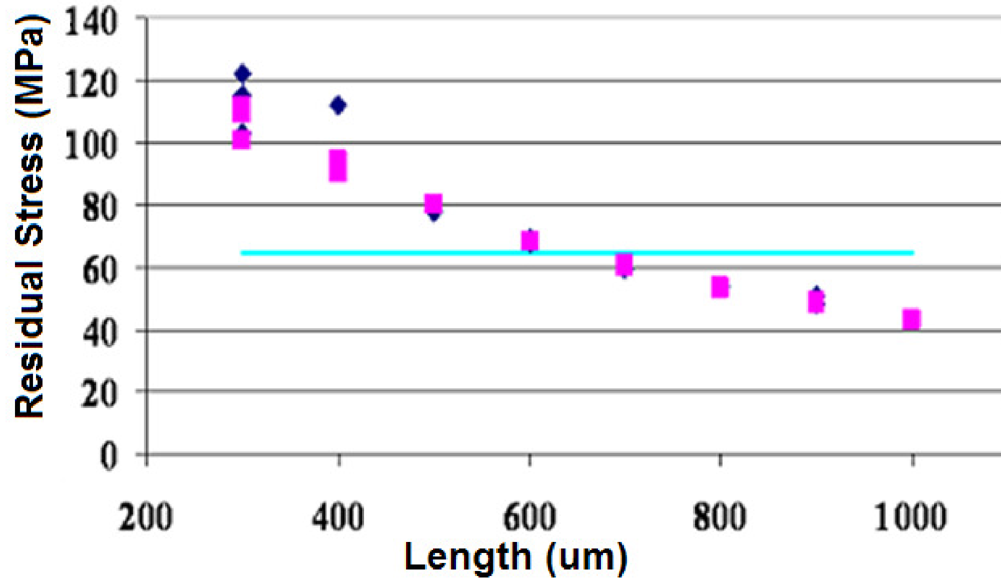

Figure 8.13: Residual stress calculated via the dynamic technique for varying lengths and widths (squares) and the axial force calculated via wafer bow measurements and Stoney's formula.

8.4 Results From the Static Technique: Parametric Identification of MEMS Resonators

Results in this Section are obtained via the application of the Section 7.4. Again, the same resonators from Sections 7.3 and 8.3 are examined. These resonators have varying lengths between 300 μm to 1000 μm as well as two width sets, 20 μm and 35 μm. Each of these resonators was examined under the optical profilometer (Section 5.4). A deflection profile was measured and the analytical mode was fit to the experimental data (center deflections of these resonators), from which device residual stress measurements resulted. Two representative results are shown in Figure 8.14 exhibit results from this technique. Beginning with a zero residual stress value (flat resonator), the residual stress is increased until the shape of the deflection profile matches that of experiment. As a result of fabrication and release processing, micro resonators are often deflected because of residual stress. However, when the resonators in this study were fabricated and released, they were with zero deflections, the center deflection was flat or zero.

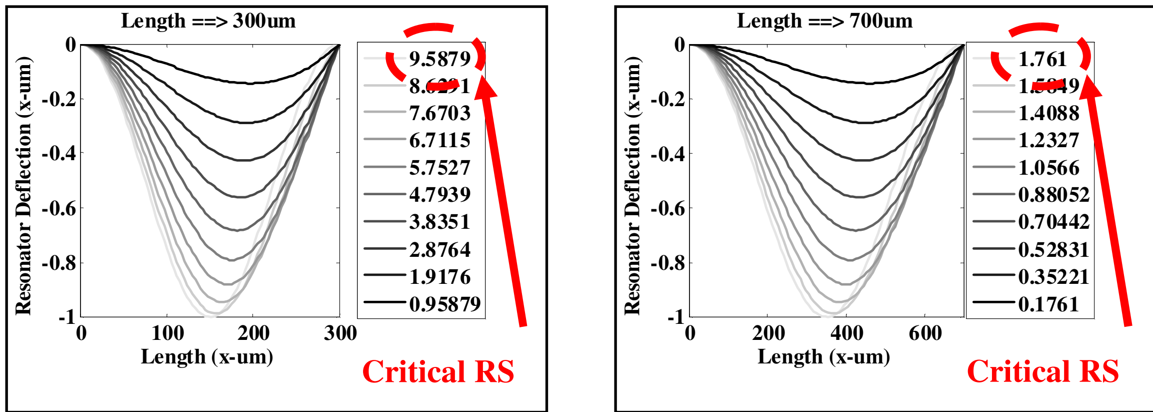

Figure 8.14:Deflection profiles for a 300 μm and 700 μm long resonators under various levels of residual stress.

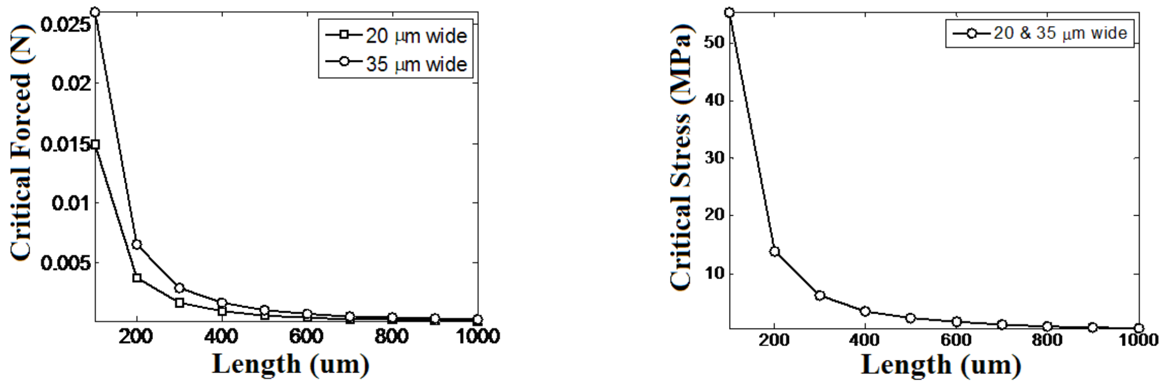

Figure 8.15 (a,b): Critical force and residual stresses obtained from the static technique of Section 7.4.

From Section 7.4, the solution to the critical equation takes the form of $\beta_n = L\sqrt{N_{RS} / EI} = 6.2768$, then the critical force and residual stress values may be solved for as in equations (7.25) through (7.29). The obtained results and are shown in Figure 8.15 (a,b). Clearly, the force is width dependent, as was previously shown, and the residual stress is independent of a device's width.

Finally, the results in this Section are compared to the dynamic technique of Section 7.3 and the wafer bow/Stoney's formula results of Section 7.1 in Figure 8.16. The results from Section 7.4 are considered the buckling forces and stresses. Clearly, wafer bow / Stoney's formula produce much higher values than the buckling values, thereby inducing buckling in these resonators.

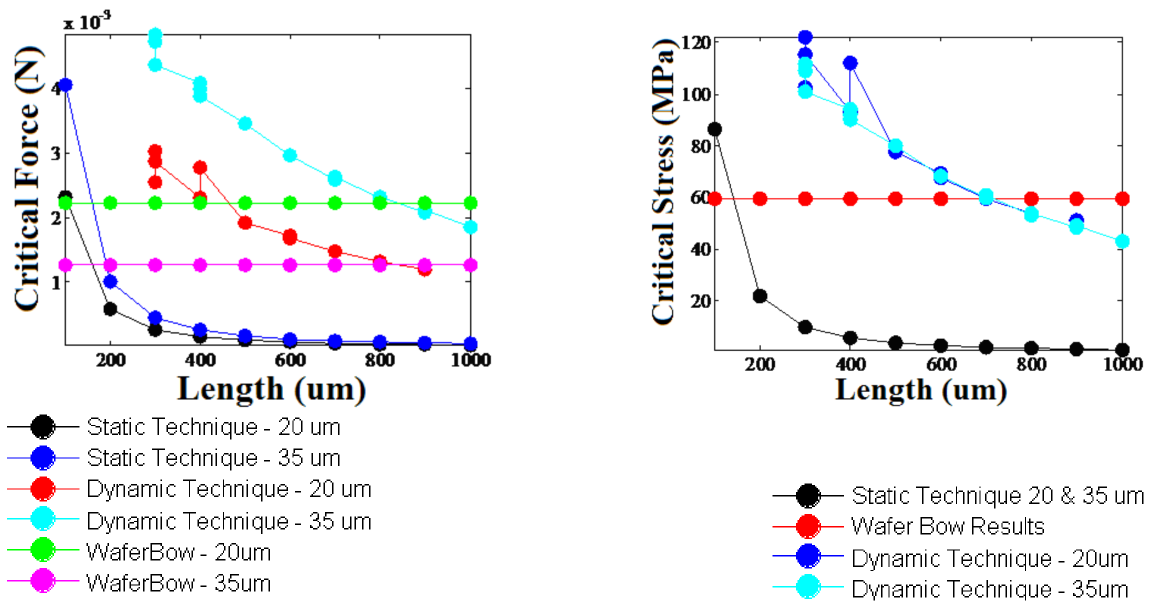

Figure 8.16 (a,b): Axial force and residual stress results for Stoney's formula, the dynamic technique of Section 7.3 and the static technique of Section 7.4.

9 SUMMARY, CONCLUDING REMARKS AND SUGGESTIONS FOR FUTURE WORK.

Through this dissertation effort, many contributions have been made in developing reduced-order models for composite structures such as micro-scale devices and characterizing residual stresses these devices.

9.1 Plate-Like Structure Modeling and Reduced-Order Methodologies

Within this dissertation, plate and micro-scale structures are studied. An analytical model has been developed to describe the behavior of thin composite laminate plates. In order to create a reduced-order model from the equilibrium equation of a plate, an expression for the plate mode shapes is needed. Because an exact solution for these mode shapes does not exist, the Navier method has been applied to develop an expression for the mode shapes of a plate with all edges either simply supported or clamped. These approximations satisfy the boundary conditions. In addition, because of midplane stretching, the equilibrium equation for the considered plate is highly nonlinear. This nonlinearity involves a static stress function that describes the midplane stress field. In order to ensure compatibility of strains, the compatibility equation is applied leading to a linear fourth order differential equation in terms of the static stress function. This differential equation is solved in two parts, producing a complimentary solution and a particular solution to the problem. In order to solve for the coefficients to the

complimentary solution, this procedure is heavily dependent on the boundary conditions used. Once an expression for the static stress function is determined, the governing equation describing the plate's transverse displacement is put in the form of a reduced-order model called the Duffing oscillator.

9.2 Isotropic Laminate Stiffness Calculations

In addition, these plate-like structures are asymmetric isotropic laminates. When considering an asymmetric laminate, material properties, thicknesses and structures are not symmetric about the laminate's center line. Because of this, coupling stiffness occurs and can add complicated nonlinear terms to an equation of motion. In addition, the placement for the zero axis is also critical in calculating isotropic laminate stiffness calculations (Figure 9.1).

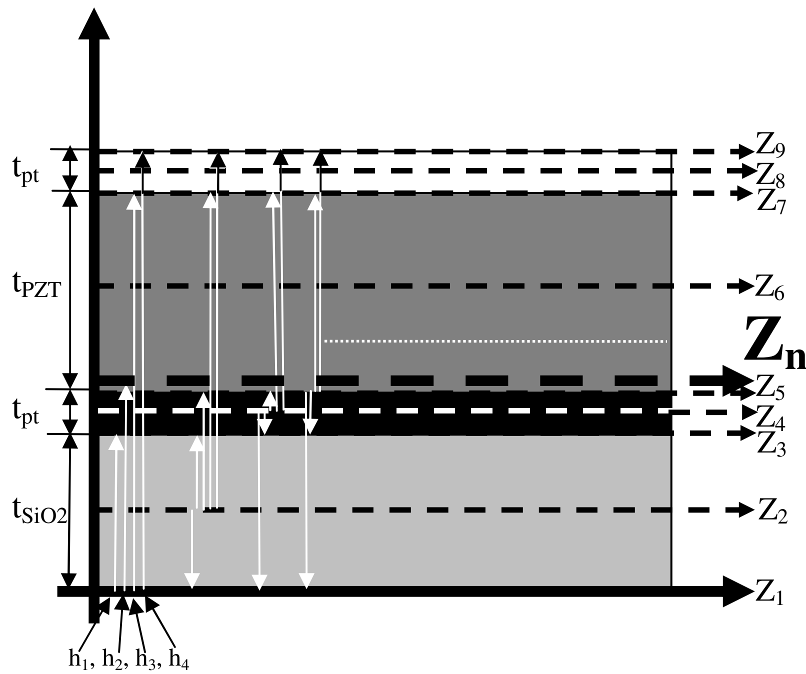

Figure 9.1: Laminate beam showing neutral axis location, Z_n and various other locations for the zero axis starting position.

It was demonstrated that placing the start/zero axis at different locations through the laminate in Figure 9.1 can change the value of the coupling stiffness and the bending stiffness. However, an important observation was made when the zero axis was placed at the position of the laminate's neutral axis location. The coupling stiffness was zero no matter what the other parameters were in the calculations. With this observation, a procedure was developed to calculate multi layer composite laminate stiffness about the neutral axis location. In this procedure, the coupling stiffness is always zero and in a sense, makes the asymmetric laminate an equivalent symmetric laminate about its neutral axis.

9.3 Characterization of Residual Stress Induced Deformation in Plate and Micro-Scale Structures.

Parametric identification techniques were developed to identify system parameters and to characterize residual stress induced deformation in plate and micro-scale structures. The first technique was based of a linear curvature model and describes the curvature of a cantilevered resonator. Cantilevers were fabricated and their deflection profiles were measured via an optical profilometer at the Army Research Laboratory. These profiles were compared to the analytical model, and the residual stress was varied until the model matched the experimental data. These residual stress values were then considered the individual device residual stress values post-fabrication and release. These stress values were then compared to wafer bow measurements collected during thin-film deposition, and before fabrication and release processing began. The individual device residual values were considerably lower than that of the wafer bow measurements. This is attributed to the fact that when a cantilever is released, three sides and its underneath are released from the wafer. This in a sense, causes a stress relaxation in the cantilever thereby making the device values post-fabrication and release have much lower values than that of the wafer bow measurements. A final observation is that the individual cantilever stress values are clearly length dependent, but not width dependent for the sets studied.

The second technique used in the work was that of Dick *et al.* This technique is a dynamic technique that analyzes the nonlinear frequency-response of clamped-clamped micro resonators. A nonlinear beam model is developed and put in a reduced-order form of the Duffing oscillator. From this model, an identification technique is developed, in

which the model system parameters are adjusted until the nonlinear frequency-response matches that taken during experiments. From this, the axial force is determined and thereby the residual stress in the resonator. Once each device was tested, it was scanned under the optical profilometer, and determined that their was no change in device deformations. Finally, these stresses were compared to that of wafer bow measurements, and were much closer in value than the cantilever. This was attributed to the fact that two sides are clamped, and less area of the resonator has been stress relaxed.

The final technique is also applied to a clamped-clamped resonator. This technique is a static technique. The linear static equilibrium equation is solved for the beam mode shapes and the critical buckling force and residual stresses are calculated. It was determined that the shape of the deflection profile was clearly dependent on residual stress, but the amplitude was not. The results from this Section were compared to those obtained by using the of wafer bow measurements and the dynamic technique. The individual device buckling stresses were much lower than the previous two, indication that wafer bow stresses and that of the dynamic technique are high enough to induce buckling.

From these identification techniques, several accomplishments have been made. First, this is the first characterization of residual stresses in individual device PZT cantilevers and resonators post-fabrication and post-release of the devices. This is important accomplishment to note because it makes clear that wafer bow measurements, though accurately describing stresses in thin-films, do not accurately describe the stress in devices post-fabrication and release processing. In addition, the necessity of linear and nonlinear modeling and identification techniques has been shown.

9.4 Summary/Contributions and Suggestions for Future Work

From the work presented in this dissertation, there are several interesting observations and contributions obtained from this work:

Is a plate model necessary in describing and analyzing the static and dynamic behavior of MEMS devices?

- Not necessarily. With all the devices that I worked on, though the dimensions indicated that a plate model would be necessary, the data and results clearly showed that a plate model was not necessary and the width effect could be neglected.
- For a small subset of the cantilevered devices, the data might be better explained by a plate model.
- Experimental observations included curved cross-sections: plate models can be used here.

Does the residual stress in an individual device depend on width, length, material thickness, or Young's modulus?

- Clearly the residual stress is length dependent and in some cases dependent on thin-film thickness. It was shown for various widths that the width effect may be neglected

How does characterization work for multilayer structures?

- I determined that characterization of micro-scale structures can be done in several steps. Static techniques were applied to analyze residual stress via deflection or curvature measurements, dynamic techniques were applied to analyze stresses that occurred during harmonic excitations. In addition, the necessity of using a linear or nonlinear model was clearly demonstrated

Does residual stress values change from thin film deposition to post-fabrication and release processing?

- I clearly showed that residual stress approximations in thin films do not hold true for individual device stress values post-fabrication and release processing. Individual device characterization needs to be done for the purpose of building a body of work that will enable future predictions of device stress, curvatures and performance capabilities

From the work presented in this dissertation, there are several interesting and necessary topics for future work that include the following:

- Development of approximations for plate mode shapes that satisfy the boundary conditions for a clamped-clamped and cantilevered plate. Besides the dimensions of some of the micro-scale devices in this work fit that of a plate-like structure, curvatures across the width-span of some devices has been observed in experiments as well as across the length. This would indicate that plane strain conditions cannot be satisfied and

that the axial residual force that occurs along a beam's length is not equivalent to that across its width and further needs to be studied.

- In this work, the composite residual stress in full stack PZT resonators has been characterized. However, there can be an infinite number of combinations of residual stress values for individual laminate layer stress values that can make up the composite stress value for an individual structure. These individual layer values are what drive the composite stress value and the overall deformation of the micro-scale structure.
- Additional techniques are needed to fully characterize residual stress in micro-scale structures.
  - During the dynamic testing of the clamped-clamped resonators, linear frequency-responses were initially observed. A technique similar to the dynamic technique present from Dick *et al*. needs to be developed to characterize the residual stress during linear frequency-responses and compared to that of the dynamic technique in this work.
  - The dynamic techniques discussed in this work and in future work should be applied to cantilevered micro-scale structures as well.
  - An additional static technique is needed to analyze electrically induced buckling in MEMS cantilevers and resonators.
- In addition to residual stress characterization, parametric dependencies should be further examined related to a beam or plates width, length, thicknesses and material Young's modulus values.

A1 REDUCED-ORDER MODELS FOR PLATE-LIKE STRUCTURES: METHODOLOGY UTILIZING OPPOSING BEAM MODES

Main Purpose: To reduce governing equation of motion of a composite laminate plate to the form of the Düffing oscillator.

- Variables in the governing equation for a plate are not separable, so approximations are needed for transverse deflection *W* and static stress function *Φ*.

GOVERNING EQUATION OF MOTION

$$I_o \frac{\partial^2 W}{\partial t^2} + D_{11} * \left[\frac{\partial^4 W}{\partial x^4} + 2 * \frac{\partial^4 W}{\partial x^2 \partial y^2} + \frac{\partial^4 W}{\partial y^4} \right] - \left[N(\phi, W) + q \right] = 0$$

$$N(\phi, W) = \left(\frac{\partial^2 \Phi}{\partial x^2} \frac{\partial^2 w}{\partial y^2} + \frac{\partial^2 \Phi}{\partial y^2} \frac{\partial^2 w}{\partial x^2} - 2 \frac{\partial^2 \Phi}{\partial x \partial y} \frac{\partial^2 w}{\partial x \partial y} \right)$$

$I_o \Rightarrow$ Inertia

$W \Rightarrow$ Transverse Deflection

$D_{11} \Rightarrow$ bending stiffness

$N(\phi, W) \Rightarrow$ Nonlinear Stretching

$N(\phi, W) = \phi_{xx} W_{yy} + \phi_{yy} W_{xx} - 2 * \phi_{xy} W_{xy}$

$\phi \Rightarrow$ Static Stress Function

$q \Rightarrow$ Outside Forces

COMPATIBILITY EQUATION

$$\frac{\partial^2 \varepsilon_x}{\partial y^2} + \frac{\partial^2 \varepsilon_y}{\partial x^2} - \frac{\partial^2 \varepsilon_{xy}}{\partial x \partial y} = \left(\frac{\partial^2 w}{\partial x \partial y} \right)^2 - \frac{\partial^2 w}{\partial x^2} \frac{\partial^2 w}{\partial y^2}$$

With *Static Stress Function* Φ

$$\Phi_{xxxx} + 2 * \Phi_{xxyy} + \Phi_{yyyy} = \left(\frac{1}{a_{22}} \right) * \left(\left(\frac{\partial^2 w}{\partial x \partial y} \right)^2 - \frac{\partial^2 w}{\partial x^2} \frac{\partial^2 w}{\partial y^2} \right)$$

where a_{22} is extensional stiffness for an isotropic unsymmetric laminate

PROCEDURE FOR REDUCING EQUATION OF MOTION TO DÜFFING FORM

(1) Define approximation for transverse displacement *W*

$$W(x,y,t)=\sum_{i=1}^{\infty}\sum_{j=1}^{\infty}W_{ij}(t)*X_i(x)*Y_j(y)$$

- Transverse deflection is comprised of opposing general beam modes.

  $$X_i(x)=x_1\sin(B_i*x)+x_2\cos(B_i*x)+x_3\sinh(B_i*x)+x_4\cosh(B_i*x)$$
  $$Y_j(y)=y_1\sin(B_j*y)+y_2\cos(B_j*y)+y_3\sinh(B_j*y)+y_4\cosh(B_j*x)$$

- The coefficients to the trigonometric and hyperbolic function are general and can be changed to fit whatever beam mode is being considered. For example, if a clamped-clamped plate was being considered,

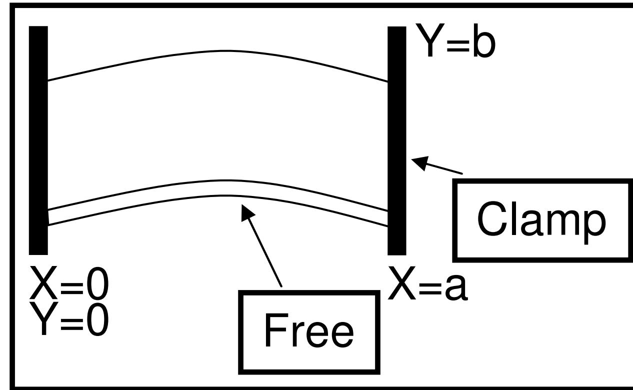

- Transverse deflection for a plate under these boundary conditions is comprised of a clamped-clamped beam and a free-free beam.

  $$X(\tilde{x})=\left[(\sin((\beta*L)*\tilde{x})-\sinh((\beta*L)*\tilde{x})) -\left[\frac{\sinh(\beta*L)+\sin(\beta*L)}{\cosh(\beta*L)+\cos(\beta*L)}\right]*(\cos((\beta*L)*\tilde{x})-\cosh((\beta*L)*\tilde{x}))\right]$$

  $$Y(\tilde{y})=\left[\left(\frac{\cosh(\beta L)-\cos(\beta L)}{\sinh(\beta L)-\sin(\beta L)}\right)*(\sin((\beta*L)*\tilde{y})+\sinh((\beta*L)*\tilde{y})) +(\cos((\beta*L)*\tilde{y})+\cosh((\beta*L)*\tilde{y}))\right]$$

  then the transverse deflection becomes

  $$W(x,y,t)=\sum_{i=1}^{\infty}\sum_{j=1}^{\infty}W_{ij}(t)*X_i(x)*Y_j(y)$$

- **For the purpose of this work, will keep opposing beam modes in the general form**

  $$X_i(x)=x_1\sin(B_i*x)+x_2\cos(B_i*x)+x_3\sinh(B_i*x)+x_4\cosh(B_i*x)$$
  $$Y_j(y)=y_1\sin(B_j*y)+y_2\cos(B_j*y)+y_3\sinh(B_j*y)+y_4\cosh(B_j*x)$$

  in order to reduce the equation of motion to the Düffing form that will work for multiple boundary conditions, not one case at a time.

(2) Insert the approximation for the transverse displacement *W* into the compatibility equation, and solve for the static stress function *Φ*.

a. Solve for the static stress function, solve for the particular solution first.
b. Then solve for the complimentary solution to ensure that *Φ* satisfies the boundary conditions.

(3) Once expressions for Φ and W are known, insert into the equation of motion.
(4) Define residual, apply Galerkin's procedure, integrate over boundaries and the Düffing form will result
(5) Want a reduced-order model to find frequency responses of various plates, with application to MEMS cantilevered and clamped-clamped devices.

A2 MATLAB PROGRAM: CRITICAL FORCE AND STRESSES

This program plots the data in **Figure 8.15**

```
clear all
close all
clc


YM=[0.100000    0.190000    0.025000    0.190000];
b=[20 35];
TH=[0.5270 0.1880 0.5202 0.1050];
h=[0 TH(1) (TH(1)+TH(2))...
   (TH(1)+TH(2)+TH(3))...
   (TH(1)+TH(2)+TH(3)+TH(4))];
[ST20]=...
   StiffnessForceMoments3(YM,h,b(1));
[ST35]=...
   StiffnessForceMoments3(YM,h,b(2));

B1=6.2768;
L=100:100:1000;

for incL=1:length(L)
   Nrs20(incL)=ST20(3)*B1^2/L(incL)^2;
   Nrs35(incL)=ST35(3)*B1^2/L(incL)^2;
   Ors20(incL)=ST20(3)*B1^2/(L(incL)^2*sum(TH)*b(1));
   Ors35(incL)=ST35(3)*B1^2/(L(incL)^2*sum(TH)*b(2));
end

figure(1)
axes('FontSize',16,'FontName','TimesNewRoman','FontWeight','bold')
plot(L,Nrs20*10,'ks-','MarkerFaceColor',[1 1 1],...
   'MarkerSize',8,...
   'LineWidth',2); hold on;
plot(L,Nrs35*10,'ko-','MarkerFaceColor',[1 1 1],...
   'MarkerSize',8,...
   'LineWidth',2); hold on;
xlabel('Length \mum','FontSize',16,'FontWeight','bold')
ylabel('Critical Force (N)','FontSize',16,'FontWeight','bold')
legend('20 \mum wide','35 \mum wide')
axis tight

figure(2)
axes('FontSize',14,'FontName','TimesNewRoman')
```

```
plot(L,Ors20*10^6,'ko-','MarkerFaceColor',[1 1 1],...
   'MarkerSize',8,...
   'LineWidth',2);
xlabel('Length \mum','FontSize',16,'FontWeight','bold')
ylabel('Critical Stress (MPa)','FontSize',16,'FontWeight','bold')
legend('20 & 35 \mum wide')
axis tight
```

A3 MATLAB PROGRAM: CALCULATING RESIDUAL STRESS VALUES FROM SECTION 7.1

```
clear all
close all
clc

YM=[0.100000   0.190000  0.025000  0.190000];
for incW=8
    clear x W
    if incW==1
        %%% analying wafer, 437
        L=100:100:800;
        W437=[0 6 14 21 29 42 56 75];
        b=100;
        TH=[1.6688  0.16 2.0145    0.1];
        h=[0 TH (1) (TH (1)+TH (2))...
                   (TH (1)+TH (2)+TH (3))...
                 (TH (1)+TH (2)+TH (3)+TH (4))];
        RS=[0.000069 0.000651 0.000056 0.000215];
    elseif incW==2
        %%% analying wafer, 469
        L=100:100:800;
        W469=[-1.2 -6.9 -10.4 -20.8 -28.9 -37 -45.1 -62.5];
        b=100;
        TH=[0.737 0.16 1.461 0.1];
        h=[0 TH (1) (TH (1)+TH (2))...
                   (TH (1)+TH (2)+TH (3))...
                 (TH (1)+TH (2)+TH (3)+TH (4))];
        RS=[0.00005 0.00071   0.00006   -0.00005];
    elseif incW==3
        %%% analying wafer, 1287
        L=50:25:275;
        W1287=[-0.3 -0.9 -2.1 -3.5 -4.7 -7.1 -9.3 -11.6 -
14.3 -19.3];
        b=100;
        TH=[0.5122  0.1  0.5006    0.105];
        h=[0 TH (1) (TH (1)+TH (2))...
                   (TH (1)+TH (2)+TH (3))...
                 (TH (1)+TH (2)+TH (3)+TH (4))];
        RS=[0.0001090.00112   0.000134  0.000208];
    elseif incW==4
        %%% analying wafer, 1288
        L=50:25:275;
```

```
        W1288=[0 -0.2 -0.6 -1.1 -1.3 -1.9 -2.5 -3.2 -3.8 -
4.4];
        b=100;
        TH=[1.1177  0.1  0.4948    0.105];
        h=[0 TH (1) (TH (1)+TH (2))...
                  (TH (1)+TH (2)+TH (3))...
                (TH (1)+TH (2)+TH (3)+TH (4))];
        RS=[0.0000980.00111   0.000123  0.000146];
    elseif incW==5
        L=100:100:1000;
        W1780_W20set1=[1.6 4.0 10.1 23.7 41.5 72.1 94.1
114.3 146.3 177.9];
        b=20;
        TH=[0.5270 0.1880 0.5202 0.1050];
        h=[0 TH (1) (TH (1)+TH (2))...
                  (TH (1)+TH (2)+TH (3))...
                (TH (1)+TH (2)+TH (3)+TH (4))];
        RS=[-0.00011320 0.00034380 0.00013118 0.00006235];
    elseif incW==6
        L=100:100:1000;
        W1780_W35set1=[1.5 3.6 11.3 23.8 40.3 62.4 88.3
113.0 143.2 169.2];
        b=35;
        TH=[0.5270 0.1880 0.5202 0.1050];
        h=[0 TH (1) (TH (1)+TH (2))...
                  (TH (1)+TH (2)+TH (3))...
                (TH (1)+TH (2)+TH (3)+TH (4))];
        RS=[-0.00011320 0.00034380 0.00013118 0.00006235];
    elseif incW==7
        L=100:100:1000;
        W1780_W20set2=[1.2 2.8 9.9 21.1 33.7 53.1 76.9 99.4
126.8 159.5];
        b=20;
        TH=[0.5270 0.1880 0.5202 0.1050];
        h=[0 TH (1) (TH (1)+TH (2))...
                  (TH (1)+TH (2)+TH (3))...
                (TH (1)+TH (2)+TH (3)+TH (4))];
        RS=[-0.00011320 0.00034380 0.00013118 0.00006235];
    elseif incW==8
        L=100:100:1000;
        W1780_W35set2=[1.1 3.8 11.2 22.9 37.5 57.8 83.6
106.3 128.3 162.4];
        b=35;
        TH=[0.5270 0.1880 0.5202 0.1050];
        h=[0 TH (1) (TH (1)+TH (2))...
                  (TH (1)+TH (2)+TH (3))...
                (TH (1)+TH (2)+TH (3)+TH (4))];
        RS=[-0.00011320 0.00034380 0.00013118 0.00006235];
    end

    [ST]=...
        StiffnessForceMoments3 (YM,RS,h,b);
    % Ors=(-2000:10:2000)*10^-6;
```

```
    % Ors=(35:.002:55)*10^-6; % W437 range
    % Ors=(-55:.005:-5)*10^-6; % W469 range
    % Ors=(-30:.005:0)*10^-6; % W1287
    % Ors=(-30:.005:0)*10^-6;% W1288
    Ors=(0:.005:20)*10^-6;

    for incL=1:length (L)
        for incOrs=1:length (Ors)
            W (incOrs)=((1/4)*(b*sum (TH)*L (incL)^2)/ST
(3))*Ors (incOrs);
            if incW==1
                Err (incOrs)=abs (W (incOrs)-W437 (incL));
            elseif incW==2
                Err (incOrs)=abs (W (incOrs)-W469 (incL));
            elseif incW==3
                Err (incOrs)=abs (W (incOrs)-W1287 (incL));
            elseif incW==4
                Err (incOrs)=abs (W (incOrs)-W1288 (incL));
            elseif incW==5
                Err (incOrs)=abs (W (incOrs)-W1780_W20set1
(incL));
            elseif incW==6
                Err (incOrs)=abs (W (incOrs)-W1780_W35set1
(incL));
            elseif incW==7
                Err (incOrs)=abs (W (incOrs)-W1780_W20set2
(incL));
            elseif incW==8
                Err (incOrs)=abs (W (incOrs)-W1780_W35set2
(incL));
            end
            incOrs
        end
        figure (1)
        plot (Ors,Err,' k-');hold on
        [t1,t2]=min (Err);
        RSdevice (incL)=Ors (t2);
    end
    figure (2)
    plot (L,RSdevice*10^6,' k*-')

end
```

A4 MATLAB PROGRAM: BISECTION METHOD FOR ROOTS IN SECTION 7.4

```
clear all
close all
clc

x=sym('x','real');
F=2*cos(x)+(x)*sin(x)-2;

a=.1;  b=.2;
x=a; Fa=eval(F);
x=b; Fb=eval(F);
incR=1;

while incR<=30
   incR
   incIT=1; incMd=1;
   while incIT<=1000
      c=(a+b)/2;
      d=[incIT incMd incR vpa(a,2) vpa(b,2) vpa(c,8) vpa(Fa*Fb,4)];
      if Fa*Fb<0%then bisection method on this range valid
         c=(a+b)/2; %calculate midpoint
         x=c; Fc=eval(F);
         if abs(Fc)<.000000001 %if this is the case, have root at c
            Roots(incR)=c;
            incR=incR+1;
            break
         else            %if not the case, evaluate F and create new ranges
            if Fa*Fc<0%left half interval
               b=c; x=b; Fb=eval(F);%rename b as midpoint c
            elseif Fb*Fc<0 %right half interval
               a=c; x=a; Fa=eval(F);%rename a as midpoint c
            end
         end
         incMd=incMd+1;
      else%if range not valid, then increments b until it is
         b=b+.2; x=b; Fb=eval(F);
         bHold=b;
         incIT=incIT+1;
      end
   end
   a=bHold;  x=a;  Fa=eval(F);
   b=bHold+.2;  x=b;  Fb=eval(F);
end
save Roots Roots
```

```
plot(Roots,'k*')
```

A5 MATHEMATICA SPREADSHEET: REDUCED-ORDER MODEL FOR PLATE WITH ALL EDGES SIMPLY-SUPPORTED (INPUTS ONLY)

```
PARTICULAR AND COMPLIMENTARY SOLNS FOR STATIC STRESS FCN Φ
PARTICULAR AND COMPLIMENTARY SOLNS FOR STATIC STRESS FCN Φ
PARTICULAR AND COMPLIMENTARY SOLNS FOR STATIC STRESS FCN Φ
PARTICULAR AND COMPLIMENTARY SOLNS FOR STATIC STRESS FCN Φ
Clear[Am,Ap,Bn,Bq,m,n,p,q]
In[]:  w=W[t]*Sin[Am*x]*Sin[Bn*y]
In[]:  CompEqnRS=(1/a11)*((D[w,x,y])^2-D[w,x,x]*D[w,y,y])
In[]:  Expand[TrigReduce[CompEqnRS]]
In[]:  PartSoln=F1*Cos[2 Am x]+F2*Cos[2 Bn y]
In[]:  CompEqnLS=D[PartSoln,x,x,x,x]+2*D[PartSoln,x,x,y,y]+D[PartSoln,y,y,y,y]
In[]:  Solve[16 Am^4 F1==(Am^2 Bn^2  W[t]^2)/(2 a11),F1]
In[]:  F1=(Bn^2 W[t]^2)/(32 a11 Am^2)
In[]:  Solve[16 Bn^4 F2 ==(Am^2 Bn^2*W[t]^2)/(2 a11),F2]
In[]:  {{F2=(Am^2 W[t]^2)/(32 a11 Bn^2)}}
In[]:  PartSoln
In[]:  ComplSoln=(1/2)*C1*x^2+(1/2)*C2*y^2
In[]:
In[]:
In[]:  A={{A11,v*A11},{v*A11,A11}}
In[]:  Coeff=(1/(a b))
Integrate[Factor[Expand[TrigReduce[A.{{1/2*(D[w,x])^2},{1/2*(D[w,y])^2}}-
{{D[PartSoln,x,x]},{D[PartSoln,x,x]}}]]]],{x,0,a},{y,0,b}]
In[]:  C1=Expand[Coeff[[2,1]]]
In[]:  C2=Expand[Coeff[[1,1]]]
In[]:  Am=m π/a
In[]:  Bn=n π/b
In[]:  m=1
In[]:  n=1
In[]:  Factor[C1]
In[]:  Factor[C2]
In[]:  Clear[Am,Bn,m,n]
In[]:  c1=Factor[1/8 A11 Bn^2 W[t]^2+1/8 A11 Am^2 v W[t]^2]
In[]:  c2=Factor[1/8 A11 Am^2 W[t]^2+1/8 A11 Bn^2 v W[t]^2]
In[]:  ComplSoln=(1/2)*c1*x^2+(1/2)*c2*y^2
In[]:  CompatibilityEqn=ComplSoln+PartSoln
In[]:  Φssfcn=ComplSoln+PartSoln
In[]:  COEFFICIENTS TO DUFFING OSCILLATOR
In[]:  COEFFICIENTS TO DUFFING OSCILLATOR
In[]:  COEFFICIENTS TO DUFFING OSCILLATOR
In[]:
In[]:
In[]:
```

```
In[]:  w=W[t]*Sin[Am*x]*Sin[Bn*y]
In[]:  Φssfcn=1/16 A11 (Bn^2+Am^2 v) x^2 W[t]^2+1/16 A11 (Am^2+Bn^2 v) y^2 W[t]^2+(Bn^2 Cos[2 Am x] W[t]^2)/(32 a11 Am^2)+(Am^2 Cos[2 Bn y] W[t]^2)/(32 a11 Bn^2)
In[]:  WeigthFcn=Sin[Ap*x]*Sin[Bq*y]
In[]:  a1=Io*D[w,t,t]*WeigthFcn
In[]:  Ap=Am
In[]:  Bq=Bn
In[]:  a1
In[]:  Expand[Integrate[a1,{x,0,a},{y,0,b}]]
In[]:  A=1/4 a b Io
In[]:
In[]:
In[]:
In[]:
In[]:  Clear[Ap,Am]
In[]:  w=W[t]*Sin[Am*x]*Sin[Bn*y]
In[]:  Φssfcn=1/16 A11 (Bn^2+Am^2 v) x^2 W[t]^2+1/16 A11 (Am^2+Bn^2 v) y^2 W[t]^2+(Bn^2 Cos[2 Am x] W[t]^2)/(32 a11 Am^2)+(Am^2 Cos[2 Bn y] W[t]^2)/(32 a11 Bn^2)
In[]:  WeigthFcn=Sin[Ap*x]*Sin[Bq*y]
In[]:  b1=TrigReduce[D11*(D[w,x,x,x,x]+2*D[w,x,x,y,y]+D[w,y,y,y,y])*WeigthFcn]
In[]:  b2=Expand[Integrate[b1,{x,0,a},{y,0,b}]]
In[]:  Clear[Ap,Bq,Am, Bn]
In[]:  m=1
In[]:  n=2
In[]:  p=3
In[]:  q=4
In[]:  Ap=p*π/a
In[]:  Bq=q*π/b
In[]:  Am=m*π/a
In[]:  Bn=n*π/b
In[]:  b2
In[]:  Clear[Ap,Bq,Am, Bn,m,n,p,q]
In[]:  Ap=Am
In[]:  Bq=Bn
In[]:  b1=TrigReduce[D11*(D[w,x,x,x,x]+2*D[w,x,x,y,y]+D[w,y,y,y,y])*WeigthFcn]
In[]:  b3=Expand[Integrate[b1,{x,0,a},{y,0,b}]]
In[]:  Am=m*π/a
In[]:  Bn=n*π/b
In[]:  n=1
In[]:  m=1
In[]:  Factor[b3]
In[]:  Clear[Ap,Bq,Am, Bn,m,n,p,q]
In[]:  Factor[1/4 a Am^4 b D11 W[t]+1/2 a Am^2 b Bn^2 D11 W[t]+1/4 a b Bn^4 D11 W[t]]
In[]:  B=1/4 a b (Am^2+Bn^2)^2
In[]:
In[]:
```

```
In[]:
In[]:  Clear[Ap,Bq,Am, Bn,m,n,p,q]
In[]:  w=W[t]*Sin[Am*x]*Sin[Bn*y]
In[]:  Φssfcn=1/16 A11 (Bn^2+Am^2 v) x^2 W[t]^2+1/16 A11 (Am^2+Bn^2 v) y^2 W[t]^2+(Bn^2
Cos[2 Am x] W[t]^2)/(32 a11 Am^2)+(Am^2 Cos[2 Bn y] W[t]^2)/(32 a11 Bn^2)
In[]:  Clear[Φssfcn,C1,C2,F1,F2]
In[]:  Φssfcn=1/2 C1  x^2+1/2 C2 y^2+F1*Cos[2 Am x]+F2*Cos[2 Bn y]
In[]:  WeigthFcn=Sin[Ap*x]*Sin[Bq*y]
In[]:  Expand[(D[Φssfcn,x,x]*D[w,y,y]+D[Φssfcn,y,y]*D[w,x,x]-
2*D[Φssfcn,x,y]*D[w,x,y])*WeigthFcn]
In[]:  c1=TrigReduce[Expand[(D[Φssfcn,x,x]*D[w,y,y]+D[Φssfcn,y,y]*D[w,x,x]-
2*D[Φssfcn,x,y]*D[w,x,y])*WeigthFcn]]
In[]:  c2=Expand[Integrate[c1,{x,0,a},{y,0,b}]]
In[]:  Clear[Am,Ap,Bn,Bq,m,n,p,q]
In[]:  Collect[Collect[Collect[c2,F1],C1],C2]
In[]:  Ap=p*π/a
In[]:  Bq=q*π/b
In[]:  Am=m*π/a
In[]:  Bn=n*π/b
In[]:  Collect[Collect[Collect[c2,F1],C1],C2]
In[]:  m=1
In[]:  n=2
In[]:  p=4
In[]:  q=7
In[]:  Ap=p*π/a
In[]:  Bq=q*π/b
In[]:  Am=m*π/a
In[]:  Bn=n*π/b
In[]:
In[]:  c2
In[]:  Clear[Am,Ap,Bn,Bq,m,n,p,q]
In[]:  Ap=Am
In[]:  Bq=Bn
In[]:  c2=Expand[Integrate[c1,{x,0,a},{y,0,b}]]
In[]:  Collect[Collect[Collect[Collect[c2,C1],C2],F1],F2]
In[]:  m=1
In[]:  n=2
In[]:  Clear[m,n]
In[]:  Am=m*π/a
In[]:  Bn=n*π/b
In[]:  Collect[Collect[Collect[Collect[c2,C1],C2],F1],F2]
In[]:  Clear[Ap,Bq,Am, Bn,m,n,p,q]
In[]:  Collect[Collect[Collect[Collect[c2,C1],C2],F1],F2]
In[]:  CC=Factor[C2 (-1/4 a Am^2 b W[t])+C1 (-1/4 a b Bn^2 W[t])+F1 (-1/2 a Am^2 b Bn^2
W[t])+F2 (-1/2 a Am^2 b Bn^2 W[t])]
In[]:  F1=(Bn^2 W[t]^2)/(32 a11 Am^2)
```

```
In[]:  F2=(Am^2 W[t]^2)/(32 a11 Bn^2)
In[]:  C1=Factor[1/8 A11 Bn^2 W[t]^2+1/8 A11 Am^2 v W[t]^2]
In[]:  C2=Factor[1/8 A11 Am^2 W[t]^2+1/8 A11 Bn^2 v W[t]^2]
In[]:  Simplify[CC*4/(a b)]
In[]:  CC
In[]:  Simplify[1/8 A11 Bn^2 (Bn^2+Am^2 v) W[t]^2+1/8 A11 Am^2 (Am^2+Bn^2 v) W[t]^2]
In[]:
In[]:
In[]:
In[]:  Clear[Am,Ap,Bn,Bq,m,n,p,q]
In[]:  q1=f WeigthFcn
In[]:  q2=TrigReduce[Integrate[q1,{x,0,a},{y,0,b}]]
In[]:  Ap=p π/a
In[]:  Bq=q π/b
In[]:  q2
In[]:  p=3
In[]:  q=3
In[]:  q2*(4/(a b))
In[]:
```

A6 MATHEMATICA SPREADSHEET: REDUCED-ORDER MODEL FOR PLATE WITH ALL EDGES CLAMPED (INPUTS ONLY)

```
Clear[Am,Ap,Bn,Bq,m,n,p,q,c1,c2,F1,F2,C1,C2]
In[]:  w=W[t]*Sin[Am*x]^2*Sin[Bn*y]^2
In[]:  CompEqnRS=(1/a11)*((D[w,x,y])^2-D[w,x,x]*D[w,y,y])
In[]:  Expand[TrigReduce[CompEqnRS]]
In[]:  PartSoln=F1 Cos[2 Am x]+F2  Cos[4 Am x]+F3 Cos[2 Bn y]+F4 Cos[4 Bn y]+F5
Cos[2 Am x-4 Bn y]+F6 Cos[2 Am x-2 Bn y]+F7 Cos[4 Am x-2 Bn y]+F8  Cos[2 Am
x+2 Bn y]+F9 Cos[4 Am x+2 Bn y]+F10 Cos[2 Am x+4 Bn y]
In[]:  CompEqnLS=D[PartSoln,x,x,x,x]+2*D[PartSoln,x,x,y,y]+D[PartSoln,y,y,y,y]
In[]:
Collect[Collect[Collect[Collect[Collect[Collect[Collect[Collect[Collect[Collect[CompEq
nLS,F1],F2],F3],F4],F5],F6],F7],F8],F9],F10]
In[]:  Expand[TrigReduce[CompEqnRS]]
In[]:  Solve[16 Am^4 F1 Cos[2 Am x]==(Am^2 Bn^2 Cos[2 Am x] W[t]^2)/(2 a11),F1]
In[]:  Solve[256 Am^4 F2 Cos[4 Am x]==-(Am^2 Bn^2 Cos[4 Am x] W[t]^2)/(2 a11),F2]
In[]:  Solve[16 Bn^4 F3 Cos[2 Bn y]==(Am^2 Bn^2 Cos[2 Bn y] W[t]^2)/(2 a11),F3]
In[]:  Solve[256 Bn^4 F4 Cos[4 Bn y]==-(Am^2 Bn^2 Cos[4 Bn y] W[t]^2)/(2 a11),F4]
In[]:  Solve[F5 (16 Am^4 Cos[2 Am x-4 Bn y]+128 Am^2 Bn^2 Cos[2 Am x-4 Bn y]+256
Bn^4 Cos[2 Am x-4 Bn y])==(Am^2 Bn^2 Cos[2 Am x-4 Bn y] W[t]^2)/(4 a11),F5]
In[]:  Solve[F6 (16 Am^4 Cos[2 Am x-2 Bn y]+32 Am^2 Bn^2 Cos[2 Am x-2 Bn y]+16 Bn^4
Cos[2 Am x-2 Bn y])==-(Am^2 Bn^2 Cos[2 Am x-2 Bn y] W[t]^2)/(2 a11),F6]
In[]:  Solve[F7 (256 Am^4 Cos[4 Am x-2 Bn y]+128 Am^2 Bn^2 Cos[4 Am x-2 Bn y]+16
Bn^4 Cos[4 Am x-2 Bn y])==(Am^2 Bn^2 Cos[4 Am x-2 Bn y] W[t]^2)/(4 a11),F7]
In[]:  Solve[F8 (16 Am^4 Cos[2 Am x+2 Bn y]+32 Am^2 Bn^2 Cos[2 Am x+2 Bn y]+16 Bn^4
Cos[2 Am x+2 Bn y])□-(Am^2 Bn^2 Cos[2 Am x+2 Bn y] W[t]^2)/(2 a11),F8]
In[]:  Solve[F9 (256 Am^4 Cos[4 Am x+2 Bn y]+128 Am^2 Bn^2 Cos[4 Am x+2 Bn y]+16
Bn^4 Cos[4 Am x+2 Bn y])==(Am^2 Bn^2 Cos[4 Am x+2 Bn y] W[t]^2)/(4 a11),F9]
In[]:  Solve[F10 (16 Am^4 Cos[2 Am x+4 Bn y]+128 Am^2 Bn^2 Cos[2 Am x+4 Bn y]+256
Bn^4 Cos[2 Am x+4 Bn y])==(Am^2 Bn^2 Cos[2 Am x+4 Bn y] W[t]^2)/(4 a11),F10]
In[]:  F1=(Bn^2 W[t]^2)/(32 a11 Am^2)
In[]:  F2=-(Bn^2 W[t]^2)/(512 a11 Am^2)
In[]:  F3=(Am^2 W[t]^2)/(32 a11 Bn^2)
In[]:  F4=-(Am^2 W[t]^2)/(512 a11 Bn^2)
In[]:  F5=(Am^2 Bn^2 W[t]^2)/(64 a11 (Am^2+4 Bn^2)^2)
In[]:  F6=-(Am^2 Bn^2 W[t]^2)/(32 a11 (Am^2+Bn^2)^2)
In[]:  F7=(Am^2 Bn^2 W[t]^2)/(64 a11 (4 Am^2+Bn^2)^2)
In[]:  F8=-(Am^2 Bn^2 W[t]^2)/(32 a11 (Am^2+Bn^2)^2)
In[]:  F9=(Am^2 Bn^2 W[t]^2)/(64 a11 (4 Am^2+Bn^2)^2)
In[]:  F10=(Am^2 Bn^2 W[t]^2)/(64 a11 (Am^2+4 Bn^2)^2)
In[]:
In[]:  A={{A11,v*A11},{v*A11,A11}}
In[]:  Coeff=(1/(a b))
Integrate[Factor[Expand[TrigReduce[A.{{1/2*(D[w,x])^2},{1/2*(D[w,y])^2}}-
{{D[PartSoln,x,x]},{D[PartSoln,x,x]}}]]]],{x,0,a},{y,0,b}]
```

```
In[]:  C1=Expand[Coeff[[2,1]]]
In[]:  C2=Expand[Coeff[[1,1]]]
In[]:  m=2
In[]:  n=5
In[]:  Am=m □/a
In[]:  Bn=n □/b
In[]:  Factor[C1]
In[]:  Factor[C2]
In[]:  Clear[Am,Bn,m,n]
In[]:  c1=(3/32)*A11*(Bn^2+Am^2*v)*W[t]^2
In[]:  c2=(3/32)*A11*(Am^2+Bn^2*v)*W[t]^2
In[]:  ComplSoln=(1/2)*c1*x^2+(1/2)*c2*y^2
In[]:  □ssfcn=ComplSoln+PartSoln
In[]:  COEFFICIENTS TO DUFFING OSCILLATOR
In[]:  COEFFICIENTS TO DUFFING OSCILLATOR
In[]:  COEFFICIENTS TO DUFFING OSCILLATOR
In[]:
In[]:
In[]:
In[]:  Clear[c1,c2,F1,F2,F3,F4,F5,F6,F7,F8,F9,F10]
In[]:  Clear[Am,Ap,Bn, Bq, m,n, p ,q]
In[]:  w=W[t]*Sin[Am*x]^2*Sin[Bn*y]^2
In[]:  □ssfcn=(1/2)*c1*x^2+(1/2)*c2*y^2+F1 Cos[2 Am x]+F2  Cos[4 Am x]+F3 Cos[2
Bn y]+F4 Cos[4 Bn y]+F5 Cos[2 Am x-4 Bn y]+F6 Cos[2 Am x-2 Bn y]+F7 Cos[4 Am
x-2 Bn y]+F8  Cos[2 Am x+2 Bn y]+F9 Cos[4 Am x+2 Bn y]+F10 Cos[2 Am x+4 Bn y]
In[]:  WeigthFcn=Sin[Ap*x]^2*Sin[Bq*y]^2
In[]:  a1=Io*D[w,t,t]*WeigthFcn
In[]:  Ap=Am
In[]:  Bq=Bn
In[]:  a1
In[]:  a2=Expand[Integrate[a1,{x,0,a},{y,0,b}]]
In[]:  m=2
In[]:  n=4
In[]:  Am=m □/a
In[]:  Bn=n □/b
In[]:  a2
In[]:  A=9/64 a b Io
In[]:
In[]:
In[]:
In[]:
In[]:  Clear[Am,Ap,Bn, Bq, m,n, p ,q]
In[]:  w=W[t]*Sin[Am*x]^2*Sin[Bn*y]^2
In[]:  WeigthFcn=Sin[Ap*x]^2*Sin[Bq*y]^2
In[]:  b1=TrigReduce[D11*(D[w,x,x,x,x]+2*D[w,x,x,y,y]+D[w,y,y,y,y])*WeigthFcn]
In[]:  b2=Expand[Integrate[b1,{x,0,a},{y,0,b}]]
```

In[]: Clear[Ap,Bq,Am, Bn]
In[]: m=1
In[]: n=2
In[]: p=3
In[]: q=4
In[]: Ap=p*□/a
In[]: Bq=q*□/b
In[]: Am=m*□/a
In[]: Bn=n*□/b
In[]: b2
In[]: Clear[Ap,Bq,Am, Bn,m,n,p,q]
In[]: Ap=Am
In[]: Bq=Bn
In[]: b1=TrigReduce[D11*(D[w,x,x,x,x]+2*D[w,x,x,y,y]+D[w,y,y,y,y])*WeigthFcn]
In[]: b3=Expand[Integrate[b1,{x,0,a},{y,0,b}]]
In[]: Am=m*□/a
In[]: Bn=n*□/b
In[]: n=1
In[]: m=1
In[]: Factor[b3*(1/A)]
In[]: Expand[b3*(1/A)]
In[]: Clear[Ap,Bq,Am, Bn,m,n,p,q]
In[]: Factor[1/4 a Am^{4} b D11 W[t]+1/2 a Am^{2} b Bn^{2} D11 W[t]+1/4 a b Bn^{4} D11 W[t]]
In[]: B=1/4 a b (Am^2+Bn^2)^{2}
In[]:
In[]:
In[]:
In[]: Clear[Ap,Bq,Am, Bn,m,n,p,q]
In[]: w=W[t]*Sin[Am*x]*Sin[Bn*y]
In[]: □ssfcn=1/16 A11 (Bn^{2}+Am^{2} v) x^{2} W[t]^{2}+1/16 A11 (Am^{2}+Bn^{2} v) y^{2} W[t]^{2}+(Bn^{2} Cos[2 Am x] W[t]^{2})/(32 a11 Am^{2})+(Am^{2} Cos[2 Bn y] W[t]^{2})/(32 a11 Bn^{2})
In[]: Clear[□ssfcn,C1,C2,F1,F2]
In[]: □ssfcn=1/2 C1 x^{2}+1/2 C2 y^{2}+F1*Cos[2 Am x]+F2*Cos[2 Bn y]
In[]: WeigthFcn=Sin[Ap*x]*Sin[Bq*y]
In[]: Expand[(D[□ssfcn,x,x]*D[w,y,y]+D[□ssfcn,y,y]*D[w,x,x]-2*D[□ssfcn,x,y]*D[w,x,y])*WeigthFcn]
In[]: c1=TrigReduce[Expand[(D[□ssfcn,x,x]*D[w,y,y]+D[□ssfcn,y,y]*D[w,x,x]-2*D[□ssfcn,x,y]*D[w,x,y])*WeigthFcn]]
In[]: c2=Expand[Integrate[c1,{x,0,a},{y,0,b}]]
In[]: Clear[Am,Ap,Bn,Bq,m,n,p,q]
In[]: Collect[Collect[Collect[c2,F1],C1],C2]
In[]: Ap=p*□/a
In[]: Bq=q*□/b
In[]: Am=m*□/a
In[]: Bn=n*□/b
In[]: Collect[Collect[Collect[c2,F1],C1],C2]

```
In[]:  m=1
In[]:  n=2
In[]:  p=4
In[]:  q=7
In[]:  Ap=p*□/a
In[]:  Bq=q*□/b
In[]:  Am=m*□/a
In[]:  Bn=n*□/b
In[]:
In[]:  c2
In[]:  Clear[Am,Ap,Bn,Bq,m,n,p,q]
In[]:  Ap=Am
In[]:  Bq=Bn
In[]:  c2=Expand[Integrate[c1,{x,0,a},{y,0,b}]]
In[]:  Collect[Collect[Collect[Collect[c2,C1],C2],F1],F2]
In[]:  m=1
In[]:  n=2
In[]:  Clear[m,n]
In[]:  Am=m*□/a
In[]:  Bn=n*□/b
In[]:  Collect[Collect[Collect[Collect[c2,C1],C2],F1],F2]
In[]:  Clear[Ap,Bq,Am, Bn,m,n,p,q]
In[]:  Collect[Collect[Collect[Collect[c2,C1],C2],F1],F2]
In[]:  CC=Factor[C2 (-1/4 a Am^2 b W[t])+C1 (-1/4 a b Bn^2 W[t])+F1 (-1/2 a Am^2 b Bn^2
W[t])+F2 (-1/2 a Am^2 b Bn^2 W[t])]
In[]:  F1=(Bn^2 W[t]^2)/(32 a11 Am^2)
In[]:  F2=(Am^2 W[t]^2)/(32 a11 Bn^2)
In[]:  C1=Factor[1/8 A11 Bn^2 W[t]^2+1/8 A11 Am^2 v W[t]^2]
In[]:  C2=Factor[1/8 A11 Am^2 W[t]^2+1/8 A11 Bn^2 v W[t]^2]
In[]:  Simplify[CC*4/(a b)]
In[]:  CC
In[]:  Simplify[1/8 A11 Bn^2 (Bn^2+Am^2 v) W[t]^2+1/8 A11 Am^2 (Am^2+Bn^2 v) W[t]^2]
In[]:
In[]:
In[]:
In[]:  Clear[Am,Ap,Bn,Bq,m,n,p,q]
In[]:  q1=f WeigthFcn
In[]:  q2=TrigReduce[Integrate[q1,{x,0,a},{y,0,b}]]
In[]:  Ap=p □/a
In[]:  Bq=q □/b
In[]:  q2
In[]:  p=3
In[]:  q=3
In[]:  q2*(4/(a b))
In[]:
```

REFERENCES

[1] Koch, R. (1994). "The intrinsic stress of polycrystalline and epitaxial thin metal films," J. Phys.: Condens. Matter 6, pp. 9519-9550.

[2] Piekarski, B. H. (2005). Lead Zirconate Titanate Thin-films for Piezoelectric Actuation and Sensing of MEMS resonators. Ph.D. Dissertation, Department of Mechanical Engineering, University of Maryland, College Park, MD

[3] Fang, W. and Wickert, J. A. (1994). Post-buckling of micromachined beams. J. Micromech. Microeng. Vol. 4, pp. 116-122.

[4] Fang, W. and Wickert, J. A. (1995). Comments on Measureing thin-film stresses using bi-layer micromachined beams. J. Micromech. Microeng. Vol. 5, pp. 276-281.

[5] Fang, W. and Wickert, J. A. (1996). Determining mean and gradient stresses in thin-films using micromachined cantilevers. J. Micromech. Microeng. Vol. 6, pp. 301-309.

[6] Pulskamp. J. S., Smith, G., Wickenden, A., Polcawich, R., Piekarski, B., and Dubey, M. (2003). "Mitigation of Residual Film Stress Deformation in Multi-Layer MEMS Cantilever Devices," J. Vac. Sci. Technol., B 21(6), pp. 2482 - 2486.

[7] Fang, W., Lee, C.-H. and Hu, H-Hua. (1999). On the buckling behavior of micromachined beams. J. Micromech. Microeng. Vol. 9, pp. 236-244.

[8] Vechery, M., Dick, A., Balachandran, B., and Dubey, M. (2008). Pre and Post Machining and Release Residual Stresses in Microelectromechanical Systems. Proceedings of SPIE 2008 Conference, San Diego, CA, March 2008.

[9] Taher, M. and Saif, A. (2000). On a Tunable Bistable MEMS - Theory and Experiment. Journal of Microelectromechanical Systems, Vol. 9, No. 2, pp. 157-170.

[10] Dick, A. J., Balachandran, B., DeVoe, D. L. and Mote Jr., C. D. (2005). Parametric Identification of Piezoelectric Micro-scale Resonators. ENOC-2005, Eindhoven, Netherlands.

[11] Hou, M. T-K. and Chen, R. (2003). Effect of width on the stress-induced bending of micromachined bilayer cantilevers. J. Micromech. Microeng. Vol. 13, pp. 141-148.

[12] Hou, M. T-K. and Chen, R. (2004). A new residual stress measurement method using ultra-wide micromachined bilayer cantilevers. J. Micromech. Microeng. Vol. 14, pp. 490-496.

[13] Suhir, E. (1992). "Nonlinear Dynamic Response of a Flexible Thin Plate to Constant Acceleration Applied to Its Support Contour, with Application to Printed Circuit Boards, Used in Avionic Packaging," International Journal of Solids and Structures, Vol. 29, No. 1, 1992, pp. 41 – 55.

[14] Suhir, E. (1992). "Response of a Flexible Printed Circuit Board to Periodic Shock Loads Applied to its Support Contour," Journal of Applied Mechanics, Vol. 59, pp. 253 -259.

[15] He. X. (2000). "A Theoretical Framework for the Dynamic Analysis of a Printed Wiring Board Under Mechanical and Thermal Loading," Ph.D. thesis, Department of Mechanical Engineering, Georgia Institute of Technology, December.

[16] He. X, and Fulton, R. E. (2003). "Nonlinear Dynamics Analysis of a Laminated Printed Wiring Board," Journal of Electronic Packaging, Vol. 124, pp. 77 - 84.

[17] He, X. and Stallybrass, M. (2002). "Drop induced impact response of a printed wiring board," International Journal of Solids and Structures, Vol. 39, No. 24, pp. 5979 - 5991.

[18] Stoney, G. G. (1909). The Tension of Metallic Films deposited by Electrolysis. Proc. R. Soc. London, Ser., Vol. A82, pp. 172-175.

[19] Chen, K. S. and Ou, K. S. (2002). "Modification of Curvature-Based Thin-Film Residual Stress Measurement for MEMS Applications," Journal of Micromechanics and Microengineering, Vol. 12, pp. 917-924.

[20] Brenner, A. and Senderoff, S. (1949). Calculation of stress in electrodeposits from the curvature of a plated strip. J. Res. Natl. Bur. Stand, Vol.42, pp. 105-123.

[21] Atkinson, A. (1995). Macro- and microstress analysis in sol-gel derived Pb (ZrxTi1-x)O3 thin-films. Br. Ceram. Proc. Vol. 54, pp. 1-7.

[22] Freund, L. B., Floro, J. A., and Chasen, E. (1999). Extensions of the Stoney formula for substrate curvature to configurations wth thin substrates or large deformations. Applied Physics Letters, Vol. 24(14), pp. 1987-1989.

[23] Klein, C. A. (2000). How accurate are Stoney's equation and recent modifications. Journal of Applied Physics. Vol. 88, No. 9, pp. 5487-5489.

[24] Zhang, X., Chen, K-S., Ghodssi, R., Ayon, A. A. and Spearing, S. M. (2001). Residual Stress and fracture in thick tetraethylorthosilicate (TEOS) and silane-based PECVD oxide films. Sensors and Actuators, Vol. A, No. 91, pp. 373-380.

[25] Zhang, X., Chen, K-S. and Spearing, S. M. (2002). Residual Stress and Fracture of Thick Dielectric Films For Power MEMS Applications. 2002 IEEE, pp. 164-167.

[26] Zhang, X., Chen, K-S. and Spearing, S. M. (2003). Thermo-mechanical behavior of thick PECVD oxide films for power MEMS applications. Sensors and Actuators. Vol. A, No. 103, pp. 263-270.

[27] Nicu, L., Temple-Boyer, P., Bergaud, C., Scheid, E. and Martinez, A. (1999). Energy study of buckled micromachinged beams for thin-film stress measurements applied to SiO2. J. Micromech. Microeng. Vol. 9, pp. 414-421.

[28] Min, Y-H. and Kim, Y-K. (2000). In situ measurement of residual stress in micromachined thin-films using a specimen with composite-layered cantilevers. J. Micromech. Microeng. Vol. 10, pp. 314-321.

[29] Piekarski, B., DeVoe, D., Dubey, M., Kaul, R. and Conrad, J. Surface micromachined piezoelectric resonant beam filters. Sensors and Actuators. Vol. A, No. 91, pp. 313-320.

[30] Jaksic, N. and Boltezar, M. (2002). An Approach to Parameter Identification for a Single-Degree-of-Freedom Dynamical System Based on Short Free Acceleration Response. Journal of Sound and Vibration. Vol. 250, No. 3, pp. 465-483.

[31] Yahiaoui, R. and Bosseboeuff, A. (2004). Cantilever beams: Modelling of the dynamical behavior and material characterization. 5th Int. Conf. on Thermal and Mechanical Simulation and Experiments in Micro-electronics and Micro-Systems, IEEE 2004.

[32] Ayela, F. and Fournier, T. (1998). An experimental stufy of anharmonic mciromachinged silicon resonators. Meas. Sci. Technol. Vol. 9, pp. 1821-1830.

[33] Malatkar, P. and Nayfeh, A. (2003). A Parametric Identification Technique for Single-Degree-of-Freedom Weadly Nonlinear Systems with Cubic Nonlinearities. Journal of Vibration and Control. Vol. 9, pp. 317-336.

[34] Szilard, R. (2004). Theories and Applications of Plate Analysis. John Wiley & Sons, Inc., New Jersey.

[35] Reddy, J. N. (2004). Mechanics of Laminated Composite Plates and Shells, Theory and Analysis. CRC Press, Washington D. C., 2004.

[36] Jones, R. M. (1999). Mechanics of Composite Materials. Taylor & Francis, Pennsylvania

[37] Meirovitch, L. (2001). Fundamentals of Vibrations. McGraw Hill, New York.

[38] Rao, J. S., (1992). Computational Mechanics in Aerospace Engineering. AIAA.

[39] Hsu, T.-R. (2002). MEMS & Microsystems Design and Manufacture. McGraw Hill, Boston.

[40] http://www.jawoollam.com/

[41] Dick, A. J. (2007) Advantageous Utilization of Nonlinear Phenomena in Micro-Structures and Macro-Structures. Ph.D. Dissertation, Department of Mechanical Engineering, University of Maryland, College Park, MD.

[42] Abu-Salih, S. and Elata, D. (2003). Electromechanical Buckling of a Pre-Stressed Layer Bonded to an Elastic Foundation. Abstracted to subbmuitted to MSM 2004 as oral presentation and to Israel MOMS 2003 as poster.

[43] Allen, M. G., Mehregany, R. T. and Senturia, S. D. (1987). Microfabricated structures for the in situ measurment of residual stress, Young's modulus, and iltimate strain of thin-films. Appl. Phys. Lett., Vol. 51, No. 4, pp. 241-243.

[44] Atkinson, A. (1995). Macro- and microstress analysis in sol-gel derived Pb (ZrxTi1-x)O3 thin-films. Br. Ceram. Proc. Vol. 54, pp. 1-7.

[45] Baker, M. S., de Boer, M. P., Smith, N. F., Warne, L. K. and Sinclair, M. B. (2002). Intergrated Meausrment - Modeling Approaches for Evaluating Residual Stress Using Micromachined Fixed-Fixed Beams. Journal of Microelectromechanical Systesm. Vol. 11, No. 6, pp. 743-753.

[46] Ballestra, A., Brusa, E., De Pasquale, G. Munteanu, M. Gh. and Soma, A. (2008). RF-MEMS beam components: FEM modelling and experimental identification of pull-in in presense of residual stress. DTIP 2008, Nice, France.

[47] Barker, N. S. and Rebeiz, G. M. (1998). Distributed MEMS True-Time Delay Phase Shifters and Wide-Band Switches. IEEE Transactions on Microwave Theory and Techniques. Vol. 46, No. 11, pp. 1881-1890.

[48] Bathe, J. (1996). Finite Element Procedures. Prentice Hall, New Jersey.

[49] Batra, R. C., Porfiri, M. and Spinello, D. (2006). Electromechanical Model of Electrically Actuated Narrow Microbeams. Journal of Microelectromechanical Systems. Vol. 15, No. 5, pp. 1175-1189.

[50] Biebl, M., Mulhern, G. T. and Howe, R. T. (1995). In Situ Phosphorus-doped polysilicon for integrated MEMS. The 8th International Conference on Solid-State Sensors and Actuators, and Eurosensors IX. Stockholm, Sweden.

[51] Brenner, A. and Senderoff, S. (1949). Calculation of stress in electrodeposits from the curvature of a plated strip. J. Res. Natl. Bur. Stand, Vol.42, pp. 105-123.

[52] Brusa, E. Gaspera, A. D. and Munteanu, M. Gh. (2008). Validation of Compact Models of Microcantilever Actuators for RF-MEMS Application. DTIP 2008, Nice, France.

[53] Chan, E. K. L. (2000). Characterization and Modeling of Electrostatically Actuated Polysilicon Micromechanical Devices. PhD. Dissertation, Department of Electrical Engineering, Stanford University.

[54] Chen, S., Baughn, T. V., Yao, Z. J. and Goldsmith, C. L. (2002). A New In Situ Residual Stress Measurement Method for a MEMS Thin Fixed-Fixed Beam Structure. Journal of Microelectromechanical Systems. Vol. 11, No. 4, pp. 309-316.

[55] hen, K.-S., Chen, T. Y-F., Chuang, C-C. and Lin, I-K. (2004). Full-Field Wafer Level Thin-film Stress Measurement by Phase-Stepping Shadow Moire. IEEE Transactions on Components and Pckaging Technologies. Vol. 27, No. 3, pp. 594-601.

[56] hen, R. T., Nguyen, H. and Wu, M. C. (1999). A low voltage micromachined optical switch by stress-induced bending. Twelfth IEEE International Conference on Micro Electro Mechanical Systems. Orlando, FL, pp. 424-428.

[57] Chen, K. S. and Ou, K. S. (2002). "Modification of Curvature-Based Thin-Film Residual Stress Measurement for MEMS Applications," Journal of Micromechanics and Microengineering, Vol. 12, pp. 917-924.

[58] Chen, K-S. and Ou, K-S. (2007). Development and verification of 2D dynamic electromechanical coupling solver for micro-electrostatic-actuator applications. Sonsors and Actuators. Vol. A, No. 136. pp. 403-411.

[59] Chen, K-S., Zhang, X. and Spearing, S. M. (2001). Processing if Thick Dielectric Films for Power MEMS: Stress and Fracture. Mat. Res. Soc. Symp. Proc. Vol. 657, pp. EE8.4.1-EE8.4.6

[60] Chiao, M. and Lin, Liwei. Self-Buckling of Micromachined Beams Under Resistive Heating. Journal of Microelectromechanical Systems. Vol. 9, No. 1, pp. 146-151.

[61] Daniel, I. M., Wang, T. M., and Gotro, J. T. (1990). "Thermomechanical Behavior of Multilayer Structures in Microelectronics," Journal of Electronic Packaging – Vol. 112, pp. 11 - 15.

[62] Denhoff, M. W. (2003). A measurement of Young's modulus and residual stress in MEMS bridges using a surface profiler. Journal of Micromechanics and Microengineering. Vol. 13, pp. 686-692.

[63] Elata, D. Modeling the Electromechanical Response of Electrostatic Actuators. MEMS/NEMS handbook techniques and applications. Vol. 4, pp. 1085-1111.

[64] Elata, D. and Abu-Salih, S. (2005). "Analysis of a Novel Method for Measuring Residual Stress in Micro-Systems," J. Micromech. Microeng. Vol. 15, pp. 921 – 927.

[65] Fang, W., Tsai, H-C. and Lo, C-Y. (1999). Sensors and Actuators. Vol. 77, pp. 21-27.

[66] Freund, L. B., Floro, J. A., and Chasen, E. (1999). Extensions of the Stoney formula for substrate curvature to configurations wth thin substrates or large deformations. Applied Physics Letters, Vol. 24(14), pp. 1987-1989.

[67] Fu, X-A., Jezeski, R. Zorman, C. A. and Mehregany, M. (2004). Use of deposition pressure to control residual stress in polycyrstalline SiC films. Applied Physics Letters, Vol. 84, No. 3, pp. 341-343

[68] Gianchandani, Y. B. and Najafi, K. (1996). Bent-Beam Strain Sensors. Journal of Microelectromechanical Systems. Vol. 5, No. 1, pp. 52-58.

[69] Han, L. H., and Lu, T. J. (2004). "Modeling and Optimal Design of Multilayer Cantilever Microactuators," Mat. Res. Soc. Symp. Proc. – Vol. 795, pp. 473 - 478, Materials Research Society.

[70] He, X. and Stallybrass, M. (2002). "Drop induced impact response of a printed wiring board," International Journal of Solids and Structures, Vol. 39, No. 24, pp. 5979 - 5991.

[71] Hill, M., O'Mahony, C. O. and Mathewson, A. (2002). Investigation of performance and reliability of post-CMOS metal/oxide MEMS structures. Proc. Micromechanics Europe, Sinai, Romania.

[72] Hou, M. T-K. and Chen, R. (2003). Effect of width on the stress-induced bending of micromachined bilayer cantilevers. J. Micromech. Microeng. Vol. 13, pp. 141-148.

[73] Hou, M. T-K. and Chen, R. (2004). A new residual stress measurement method using ultra-wide micromachined bilayer cantilevers. J. Micromech. Microeng. Vol. 14, pp. 490-496.

[74] Hu, Y-C., Lin, J-H., Huang, K-Y. and Chuang, W-C. (2008). An electrical testing method of the structural material of micro devices. Proceedings of the d3rd IEEE Int. Conf. on Namo/Micro Engineered and Molecular Systems. Sanya, China.

[75] Huang, S. H., Li, X., Song, Z., Wang, Y., Yang, H., Che, L. and Jiao, J. (2005). A high-performance micromachined piezoresistive accelerometer with axially stressed tiny beams. J. Micromech. Microeng. Vol. 15, pp. 993-1000.

[76] Huang, S. H. and Zhang, X. (2006). Extension of the Stoney Formula for film-substrate systems with gradient stress for MEMS applications. J. Micromech. Microeng. Vol. 16, pp. 382-389.

[77] Huang, S. and Zhang, X. (2005). An analysis of elastic deformation induced by gradient residual stresses in multilayered MEMS structures. Proceedings of IMECE2005, Orlando, Florida.

[78] Huang, S. and Zhang, X. (2006). Extension of the Stoney formula for film-substrate systems with gradient stress for MEMS applications. J. Micromech. Microeng. Vol. 16, pp. 382-389.

[79] Huang, S. and Zhang, X. (2007). Gradient residual stress induced elastic deformation of multilayer MEMS structures. Sensors and Actuators. Vol. A, No. 134, pp. 177-185.

[80] Jeong, J. H., Baik, Y. J., and Kwon, D. (2002). "An Analytical Model for Intrinsic Residual Stress Effect on Out-of-Plane Deflection in Chemical-Vapor-Deposited Free-Standing Thick Film," Mat. Res. Soc. Symp. Proc., Vol. 695., pp. L6.20 - L6.6

[81] Jeong, J. H., and Kwon, D. (2002). "Analytical Model for Intrinsic Residual Stress Effects and Out-of-Place Deflection in Free-Standing Thick Films," Journal of Applied Physics, Vol. 91, No. 10, pp. 6333 - 6340.

[82] Jeong, J-H, Kwon, D., Lee, W-S. and Baik, Y-J. (2001). Intrinsic stress in chemical vapor deposited diamond films: An analytical amodel for the plastic

deformation of the Si Substrate. Journal of Applied Physics. Vol. 90, No 3, pp. 1227-1236.

[83] Jeong, J. H., Kwon, D., Lee, J. K., Lee, W. S., and Baik, Y. J., (2000). "Micromechanical Analysis of Residual Stress Effect in CVD-Processed Diamond Wafer," Mat. Res. Soc. Symp. Proc. Vol. 594, pp. 343 - 348, Materials Research Society.

[84] Joachim, D. and Lin, L. (2003). Characterization of Selective Polysilicon Deposition for MEMS Resonators Tuning. Journal of Microelectromechanical Systems. Vol. 12, No. 2, pp. 193-200.

[85] Jones, R. M. (1999). Mechanics of Composite Materials. Taylor & Francis, Pennsylvania

[86] Kang, T. J., Kim, J. G., Lee, J. S. Lee, J. H., Hahn, J. H., Lee, H. Y. and Kim, Y. H. (2005). Low-thermal-budget and selective relaxation of stress gradients in gold micro-cantilever beams using ion implantation. J. Micromech. Microeng. Vol. 15, pp. 2469-2478.

[87] Kawski, J. L. and Flood, J. (1993). Cumulative Thin-film Stress from Wafer Fabrication Processes and its Effect on Post Backgrind Wafer Shape. IEEE/SEMI Advanced Semiconductor Manufacturing Conference.

[88] Knapp, J. A. and de Boer, M. P. (2002). Mechanics of Microcantilever Beams Subject to Combined Electrostatic and Adhesive Forces. Journal of Microelectromechanical Systems. Vol. 11, No. 6, pp. 754-764.

[89] Knight, R. R. (2005). The Analysis and Testing of MEMS and Macro-scale Piezoelectric Devices. Master's Thesis, Mechanical Engineering, University of Pittsburg.

[90] Kobrinsky, M. J., Deutsch, E. R. and Senturia, S. D. (2000). Effect of Support Compliance and Residual Stress on the Shape of Doubly Supported Surface-Micromachined Beams. Journal of Microelectromechanical Systems. Vol. 9, No. 3, pp. 361-369.

[91] Koch, R. (1994). "The intrinsic stress of polycrystalline and epitaxial thin metal films," J. Phys.: Condens. Matter 6, pp. 9519-9550.

[92] Kuang, J-H. and Chen, C-J. (2004). Dynamic characteristics of shaped micro-actuators solved using the differential quadrature method. J. Micromech. Microeng. Vol. 14, pp. 647-655.

[93] Kuang, J-H. and Chen, C-J. (2005). The nonlinear electrostatic behavior for shpaed electrode actuators. International Journal of Mechanical Sciences. Vol. 47, pp. 1172-1190.

[94] Laconte, J., Iker, F., Jorez, S., Andre, N., Proost, J., Pardoen, T., Flandre, D. and Raskin, J-P. (2004). Microelectronic Engineering. Vol. 76, pp. 219-226.

[95] Legtenberg, R., Gilbert, J. and Senturia, S. D. (19997). Electrostatic Curved Electrode Actuators. Journal of Microelectomechanical Systems. Vol. 6, No. 3, pp. 257-265.

[96] Li, H. and Balachandran, B. (2006). Buckling and Free Oscillations of Composite Microresonators. Journal of Microelectromechanical Systems. Vol. 15, No. 1, pp. 42-51.

[97] Lin, H-Y. and Fang, W. (2000). Rib-reinforced micromachined beam and its applications. J. Micromech. Microeng. Vol. 10, pp. 93-99.

[98] Lishchynska, M., Cordero, N., Slattery, O. and O'Mahony, C. (2005). Modelling electrostatic behavior of microcantilevers incorporating residual stress gradient and non-ideal anchors. J. Micromech. Microeng. Vol. 15, pp. S10-S14.

[99] Masters, N. D., de Boer, M. P., Jensen, B. D., Baker, M. S., and Koester, D. (2001). Side-by-Side Comparison of Passive MEMS Strain Test Structures Under Residual Compression. Mechanical Properties of Structural Films, STP 1413, S. B. Brown and C. L. Muhlstein, Eds., American Properties for Testing and Materials, West Conshohocken, PA.

[100] Mayr, S. G. and Samwer, K. (2001). "Model for Intrinsic Stress Formulation in Amorphous Thin-films," The American Physical Society, Physical Review Letters, Vol. 87, No. 3, 036105-1 to 036105-1.

[101] Michael, A., Kwok, C. Y., Yu, K. and Mackenzie, M. R. (2008). A Novel Bistable Two-way Actuated Out-of-Plane Electrothermal Microbridge. Journal of Microelectromechanical Systems, Vol. 17, No. 1, pp. 58-69.

[102] Min, Y-H. and Kim, Y-K. (1998). Design and fabrication of a polysilicon micro mirror with a flat surface by gold metallization. Broadband Optical Networks and Technologies: An Emerging Reality/Optical MEMS/Smart Pixels/Organic Optics and Optoelectronics, 1998 IEEE/LEOS Summer Topical Meetings.

[103] Min, Y-H. and Kim, Y-K. (1999). Modeling, design, fabrication and measurement of a single layer polysilicon micromirror with initial curvature compensation. Sensors and Actuators. Vol. 78, pp. 8-17.

[104] Min, Y-H. and Kim, Y-K. (2000). In situ measurement of residual stress in micromachined thin-films using a specimen with composite-layered cantilevers. J. Micromech. Microeng. Vol. 10, pp. 314-321.

[105] Nayfeh, A. H., and Balachandran, B. (1995). Applied Nonlinear Dynamics. John Wiley & Sons, Inc., New York.

[106] Nayfeh, A. H., and Mook, D. T. (1979). Nonlinear Oscillations. John Wiley & Sons, Inc., New York.

[107] Nayfeh, A. H., Younis, M. I. and Abdel-Rahman, E. M. (2005). Reduced-Order Models for MEMS Applications. Nonlinear Dynamics. Vol. 41, pp. 211-236.

[108] Nicu, L., Temple-Boyer, P., Bergaud, C., Scheid, E. and Martinez, A. (1999). Energy study of buckled micromachinged beams for thin-film stress measurements applied to SiO2. J. Micromech. Microeng. Vol. 9, pp. 414-421.

[109] Pan, C. S. and Hsu, W. (1999). A Microstructure for in situ Determination of Residual Strain. Journal of Microelectromechanical Systems. Vol. 8, No. 2, pp. 200-207.

[110] Park, S. (2005). A Study on Buckled-Beam Actuators For RF MEMS Applications. Master's Thesis, Electrical Engineering, Louisiana State University

[111] Pasupuleti, A., Sahin, F., Raisanen, A., Hebding, J. L., Walter, W. W. and Hirschman, K. D. (2005). Predicting the Mechanical Behavior of Self-Deformed Micromachined Cantilevers. 6th Int. Conf. on Thermal, Mechanical and Multiphysics Simulation and Experiments in Micro-Electronics and Micro-Systems, EuroSimE IEEE 2005.

[112] Peroulis, D., Pacheco, S. P., Sarabandi, K. and Katehi, L. P. B. (2001). Alleviating the Adverse Effects of Residual Stress in RF MEMS Switches. 2001 European Microwave Conference

[113] Peroulis, D., Pacheco, S. P., Sarabandi, K. and Katehi, L. P. B. (2003). Electromechanical Considerations in Developing Low-Voltage RF MEMS Switches. IEEE Transactions on Microwave Theory and Techniques. Vol. 51, No. 1, pp. 259-270.

[114] Phillips, M. A., Ramaswamy, V., Clemens, B. M. and Nix, W. D. (2000). "A Model for Calculating Substrate Curvature During Coalescence of Pt Islands

on an Amorphous Substrate," Mat. Res. Soc. Symp. Proc., Vol. 578, pp. 39 - 44, Materials Research Society.

[115] Piekarski, B., DeVoe, D., Dubey, M., Kaul, R. and Conrad, J. Surface micromachined piezoelectric resonant beam filters. Sensors and Actuators. Vol. A, No. 91, pp. 313-320.

[116] Porfiri, M. (2008). Vibrations of parallel arrays of electrostatically actuated microplates. Journal of Sound and Vibration, Vol. 315, pp. 1071-1085.

[117] Li, H., Preidikman, S., Balachandran, B. and Mote Jr., C. D. (2006). Nonlinear free and forced oscillations of piezoelectric microresonators. J. Micromech. Microeng. Vol. 16, pp. 356-367.

[118] Qui, J., Lang, J. H. and Slocum, A. H. (2001). A centrally-clamped parallel-beam bistable MEMS mechanism. IEEE 2001.

[119] Qui, J., Lang, J. H. and Slocum, A. H. (2004). A Curved-Beam Bistable Mechanism. Journal of Microelectromechanical Systems, Vol. 13, No. 2, pp. 137-146.

[120] Rao, J. S., (1992). Computational Mechanics in Aerospace Engineering. AIAA.

[121] Sattler, R., Voigt, P., Pradel, H. and Wachutka, G. Innovative design and modelling of a micromechanical relay with electrostatic actuation. J. Micromech. Microeng. Vol. 11, pp. 428-433.

[122] Sglavo, V. M., Bonafini, M., and Prezzi, A. (2004). "Procedure for Residual Stress Profile Determination by Curvature Measurements," Mechanics of Materials, Vol. 37, pp. 887 – 898.

[123] Sglavo, V. M., Paternoster, M. and Bertoldi, M. (2005). Tailored Residual Stresses in High Reliability Alumina-Mullite Ceramic Lamiantes. J. Am. Ceram. Soc. Vol. 88, No. 10, pp.p 2826-2832.

Sinclair, M. (2002). A high frequency resonant scanner using thermal actuation. 2002 IEEE.

[124] Tran, M. D., Poublan, J. and Dautzenberg, J. H. (1997). A practical method for the determination of the Young's modulus and residual stresses of PVD thin-films. Thin Solid Films. Vol. 308-309, pp. 310-314.

[125] Trevino, J., Fu, X-A., Mehregany, M. and Zorman, C. (2005). Low-Stress, heavily-doped polycrystalline silicon carbide for MEMS applications. 2005 IEEE.

[126] Vechery, M., Dick, A., Balachandran, B., and Dubey, M. (2007). Comparison of Techniques for Measurement of Residual Stresses in Multilayered Micro-Electro-Mechanical Devices. Proceedings of SPIE 2007 Conference, San Diego, CA, March 2007.

[127] Vechery, M., Dick, A., Currano, L., Dubey, M., and Balachandran (2006). Static and Dynamic Techniques for Residual Stress Measurements in Microelectromechanical Systems. Proceedings of 2006 ASME IMECE Conference, Chicago, Illinois, 5-10 November 2006.

[128] Ventsel, E., and Krauthammer, T. (2001). Thin Plates and Shells: Theory, Analysis, and Applications. Marcel Dekker, New York.

[129] Wang, X., Wang, J., Zhao, M-H. and Zhang, T-Y. (2005). Microbridge Testing on Symmetrical Trilayer Films. Journal of Microelectromechanical Systems. Vol. 14, No. 3, pp. 634-645.

[130] Wickenden, A. E., Currano, L. J., Takacs, T., Pulskamp, J., Dubey, M., Hullavarad, S., and Vispute, R. D. (2003). "The Effect of Microstructures on AlN MEMS Resonator Response," Integrated Ferroelectrics, Vol. 54, pp. 565-574.

[131] Withers, P. J. and Bhadeshia, H. K. D. H. (2001). Residual Stress, Part 2 - Nature and Origins. Materials Science and Technology. Vol. 17, pp. 366-375.

[132] Withers, P. J. and Bhadeshia, H. K. D. H. (2001). Residual Stress, Part 1 - Measurement Techniques. Materials Science and Technology. Vol. 17, pp. 355-365.

[133] Yahiaoui, R. and Bosseboeuff, A. (2004). Cantilever beams: Modelling of the dynamical behavior and material characterization. 5th Int. Conf. on Thermal and Mechanical Simulation and Experiments in Micro-electronics and Micro-Systems, IEEE 2004.

[134] Yee, Y., Park, M. and Chun, K. (1998). A Sticking Model of Suspended Polysilicon Microstructure Including Residual Stress Gradient and Postrelease Temperature. Journal of Microelectromechanical Systems, Vol. 7, No. 3, pp. 339-344.

[135] Yin, W-L. (1991). Thermal Stresses and Free-Edge Effects in Laminated Beams: A Variational Approach Using Stress Functions. Transactions of ASME, Vol. 113, pp. 68-75.

1

[136] Yin, W-L. (1994). Simple Solutions of the Free-Edge Stresses in Composite Laminates under Thermal and Mechanical Loads. Journal of Composite Materials, Vol. 28, No. 6, pp. 573-586.

[137] Zhang, X., Chen, K-S., Ghodssi, R., Ayon, A. A. and Spearing, S. M. (2001). Residual Stress and fracture in thick tetraethylorthosilicate (TEOS) and silane-based PECVD oxide films. Sensors and Actuators, Vol. A, No. 91, pp. 373-380.

[138] Zhang, X., Chen, K-S. and Spearing, S. M. (2002). Residual Stress and Fracture of Thick Dielectric Films For Power MEMS Applications. 2002 IEEE, pp. 164-167.

[139] Zhang, X., Chen, K-S. and Spearing, S. M. (2003). Thermo-mechanical behavior of thick PECVD oxide films for power MEMS applications. Sensors and Actuators. Vol. A, No. 103, pp. 263-270.

[140] Zhou, Y., Yang, C-S., Chen, J-A., Ding, G-F., Ding, W., Wang, L., Wang, M-J., Zhang, Y-M. and Zhang, T-H. (2004). Measurement of Young's modulus and residual stress of copper film electroplated on silicon wafer. Thin Solid Films. Vol. 460, pp. 175-180.

[141] Zhu, Y. and Espinosa, H. D. (2004). Effect of temperature on capacitive RF MEMS switch performance - a coupled - field analysis. Journal of Microelectromechanical Systems. Vol. 14, pp. 1270-1279.